論文 / 著書情報
Article / Book Information

題目(和文)	水平2方向入力を受ける免震構造に設置されたU型鋼材ダンパーの信頼性
Title(English)	Reliability of U-shaped steel dampers as seismic isolation devices for base-isolated structures subjected to biaxial excitation
著者(和文)	Ene Diana
Author(English)	Diana Ene
出典(和文)	学位:博士（工学）, 学位授与機関:東京工業大学, 報告番号:甲第10201号, 授与年月日:2016年3月26日, 学位の種別:課程博士, 審査員:山田 哲,坂田 弘安,山中 浩明,寒野 善博,吉敷 祥一
Citation(English)	Degree:, Conferring organization: Tokyo Institute of Technology, Report number:甲第10201号, Conferred date:2016/3/26, Degree Type:Course doctor, Examiner:,,,,
学位種別(和文)	博士論文
Type(English)	Doctoral Thesis

Doctoral Thesis, 2016

Reliability of U-shaped Steel Dampers as Seismic Isolation Devices for Base-Isolated Structures Subjected to Biaxial Excitation

水平2方向入力を受ける免震構造に設置されたU型鋼材ダンパーの信頼性

by Diana Ene

Tokyo Institute of Technology

Table of Contents

I. Background

II. Fidelity of $D_2{}^u - J_f$ Interaction Curve for the Case of Seismic Excitation

III. Simple Hysteretic Model for U-shaped Steel Dampers

IV. Reliability of U-shaped Steel Dampers as Seismic Isolation Devices for Base-Isolated Structures Subjected to Biaxial Excitation

V. Comparison between One-directional and Bidirectional Damage Evaluation Approaches

VI. Conclusions

Acknowledgements

I would like to express my deepest gratitude to all those who made it possible for me to complete this doctoral thesis:

Satoshi Yamada, Professor in Tokyo Institute of Technology, my academic advisor, for giving me the opportunity to continue my research as a doctoral student. Professor Yamada graciously advised me through my doctoral course, offering me – at the same time – the invaluable experience of making my own mistakes, which helped me improve both as a researcher and as a human being. I also owe Professor Yamada the honor of having introduced me to the elite world of structural engineering by presenting me with numerous opportunities to participate to various conferences. Moreover, I consider myself very fortunate for having received his guidance not only about my research, but also regarding the difficulties of finding employment in Japan.

Shoichi Kishiki, Associate Professor in Tokyo Institute of Technology, for the guidance in conducting experimental tests, writing journal papers and for sharing his opinions and research results on U-shaped steel dampers. I am also deeply grateful for his time to show me the testing facilities of Osaka Institute of Technology where he was a lecturer for several years.

Yu Jiao, Assistant Professor in Tokyo University of Science, without whose advice and support I really doubt I could have made it through some of the most difficult times during my doctoral course. By sharing her own experiences as a female foreigner researcher, Professor Jiao inspired and motivated me towards achieving my goals.

Professor ***Hiroaki Yamanaka***, Professor ***Hiroyasu Sakata*** and Associate Professor ***Yoshihiro Kanno***, for taking the time to examine my thesis, and for their invaluable advice that helped me improve my research.

Takanori Ishida, Assistant Professor of Yamada lab, for his advice on my presentations, both in English and in Japanese. I also am deeply grateful for his guidance as my tutor in various matters starting from the very day I met him. I am looking forward to the opportunity to work with him in the future, since Professor Ishida is one of the most reliable and earnest persons I have ever met.

Otone Ibayashi, Secretary of Yamada lab, for the sincere kindness and consideration I have always been treated with, as well as for helping me with all the paper work. Furthermore, for her relentless aid in making friends and communicate to the rest of the Yamada lab members – from the very first day I came to Japan up to now. Words fail to describe how grateful I am to Mrs. Ibayashi for being there for me every time, in spite of her own personal problems.

Norihito Miki, my doctoral colleague in Yamada lab, with whom I shared both happy and difficult times. I wish to express my gratitude for helping me with my presentations in Japanese and for teaching me interesting things about Japanese culture. Moreover, I will take this opportunity to thank him for sending every year a box of みかん to Yamada lab – I am a very big fan of fruits and I have always appreciated his kind gesture.

Ryohei Kobayashi, former graduate student in Yamada lab (2015), and my 後輩, for working together on similar research topics. I am deeply grateful for his diligent work and help with my experiments.

Kazuhiko Tomatsu, D1 student in Yamada lab, for his help with different occasions such as my experimental tests and organizing barbeques and various conferences and events. I wish him the best of luck with his research and a bright future and career.

Donsoku Lee, D1 student in Yamada lab, for his kindness and support when I was going through difficult times. I really appreciate his positive attitude and determination to achieve his goals. I wish him all the best in fulfilling his dreams.

Ryo Chugun, M2 student in Yamada lab, for his relentless determination in communicating with me in English and making me feel included. I deeply appreciate his kindness and thoughtfulness, especially when sending e-mails in which he always translated the contents in English.

Takumi Kobayashi, Bunpei Yasuda, M2 students in Yamada lab, for offering me their help with various documents I had to fill in Japanese and giving me the opportunity to learn about their research.

Kohei Kubota, Masahiro Nohsho, former graduate students in Yamada lab (2015) for their valuable help with my loading tests and for kindly explaining to me their research topics in English when I didn't understand the Japanese terminology.

Kei Tanaka, Yoshiki Nishizaki, Tomoaki Goso, M1 students in Yamada lab, for their help with various tasks such as cleaning the experimental facilities, barbeques and arranging the room for my presentation. I wish them all the best of luck in finding their dream jobs.

Yoshinao Konishi, Norihisa Kawamura, Masao Terashima, Yuuma Hoashi, Nippon Steel & Sumikin Welding Co., Ltd., Tokyo; *Toyoki Kuroiwa*, Nippon Steel & Sumikin Welding Co., Ltd., US; for the help and guidance throughout all my experimental tests, for providing the specimens and other pieces of equipment required for my tests and for the financial support during the experimental test at the University of California San Diego.

Ion Simulescu, former professor in Technical University of Civil Engineering Bucharest, and my academic advisor for my Bachelor thesis, for whom I have the deepest respect and gratitude. Professor Simulescu has offered me tremendous moral support and advice on my career from my first year in college up to the present day.

Dai Takayama, without whose moral support I wouldn't have been able to finish the present research. He has been there for me every step, sharing both the success and the difficulties, never tired, never complaining, always listening and giving me good advice even when he himself was extremely busy.

In the end, I would like to thank my father and my sister for being so understanding and supportive regarding my leaving to and studying in Japan which is so far away from home. I know it hasn't been easy on either of them and I hope one day I can repay them for all they did for me.

Chapter I

Background

I.1. Introduction on seismic isolated structures

Devastating effects of strong motion earthquakes from historic times up to the present day were reported in numerous catalogs and studies. Among these events, the 1868 Arica earthquake in Peru (now Chile), the 1896 Sanriku, 1923 Kanto earthquakes in Japan, the 1906 San Francisco earthquake in the United States, and the 1908 Messina earthquake in Italy had a particular impact in shaping a new concept for construction of buildings and other structures. This concept is called "earthquake-resistant design", and aims at reducing the destructive effects on structures, protecting, thus, the human life. By definition, an earthquake-resistant building is a structure able to withstand a certain level of lateral force without posing any life-threatening situations.

Tremendous progress has been made from the early stages of earthquake-resistant design to the current design codes, and various techniques were proposed to improve the performance of structures under seismic excitation. One of the newest techniques is seismic isolation. The first official record on its concept dates more than 100 years ago and it is a patent obtained in 1909 by J.A. Calantarients, a medical doctor from Northern England [I.1]. He was the first to acknowledge that by introducing a layer that decouples the upper-structure from the foundation, the former experiences a fairly smaller amount of shocks and vibrations than otherwise, thus rendering it safer in the event of an earthquake. Usually, the targeted performance of the upper-structure subjected to frequent events (level L1) is the elastic range, meaning that no damage is allowed in the structural members. The main difference between seismic isolation and other conventional earthquake-resistant techniques is that the latter is based on decreasing the seismic demand rather than increasing the capacity.

The performance of seismic isolated structures under strong motions was verified with several occasions among which the 1994 Northridge (US), the 1995 Kobe and the 2011 Tohoku (Japan) earthquakes are worth noting. One famous example is the University of Southern California (USC) hospital – a base-isolated structure with lead-rubber bearings – which performed remarkably well during the 1994 Northridge strong motion event. The building was extensively instrumented by the California Strong Motion Instrumentation Program soon after its completion in 1991. The data registered during Northridge earthquake revealed that the peak roof acceleration was reduced almost to half with respect to the registered peak ground acceleration, while the peak drift was less than 30% of the code specification [I.2]. In Japan, the efficiency of seismic isolation technique was confirmed during the 1995 Kobe earthquake, when two base-isolated buildings in the northern part of Kobe city performed very well despite being subjected to severe ground motions. One of the buildings was the computer center of the Ministry of Post and Telecommunications, while the other one was a testing facility of a construction company. This success convinced the structural engineers of the remarkable earthquake resistance of seismic isolated structures and as a result, the number of base-isolated structures rapidly increased in the following years. At the time of Tohoku earthquake, there were approximately 3000 seismic isolated structures and

4500 single housing units in Japan. Despite the extremely large magnitude of this event, the National Institute for Land and Infrastructure Management reported that no structural damage was observed [I.3].

The first attempts to generate an isolation effect, involved applying a thick layer of an appropriate material capable of free interstitial movement (ex: sand) between two smooth surfaces, one being the foundation and the other the upper-structure. Nowadays, there is a large variety of devices, generally referred to as "seismic isolation devices" which can easily fulfill this function due to their high compressive strength and low lateral stiffness (e.g.: natural rubber bearings, sliding bearings, friction pendulums etc). The resulting isolation system does not dissipate the earthquake-induced energy, but rather deflects it through the dynamics of the whole system which means that in theory no damping is required (Naiem *et al.*) [I.1]. However, since large displacements can occur at this level, it is likely that they cannot be accommodated within the available space. Hence it is necessary to introduce dampers to dissipate the earthquake energy, consequently reducing the displacements. The present work focuses on U-shaped steel dampers – one of the several types of isolation devices – and its behavior under biaxial seismic excitation.

I.2. U-shaped steel dampers and other seismic isolation devices

In practical design, when deciding the isolation system to be adopted for a specific building, besides the characteristics of the structural system, many other factors such as cost-efficiency ratio, maintenance cost, possibility of easy replacement, durability of the seismic isolation devices *etc* have to be considered. That is the reason why it is important to investigate more than one solution for the isolation system, compare the results, and eventually adopt the optimal one.

Seismic isolation devices are installed between the upper-structure and the foundation to reduce the effect of ground shaking by lengthening the fundamental period of the structure. They are classified into two main categories:

1. ***Isolators***: devices that decouple the upper-structure from the foundation
2. ***Dampers***: devices that reduce the displacements occurring at the level of the isolation layer

I.2.1. Isolators

The modern devices included in the first category – isolators – are usually made of alternating layers of natural rubber and steel plates inserted to improve the compressive stiffness and reduce the bulging of the rubber. There is a considerable variety of such devices among which the most commonly used are: (a) laminated rubber bearings (Fig. I-1), (b) lead-plug rubber bearings (Fig. I-2), and (c) friction pendulums (simple or triple, Fig. I-3). Other devices are elastomeric rubber bearings, high-damping rubber bearings, elastic sliders, rolling sliders etc. All these devices are usually installed under vertical load bearing members – such as columns – to safely transmit the weight of the upper-structure to the foundation.

The main common characteristics of the isolators are the following:

- ***High compressive stiffness*** to transfer the vertical loads from the upper-structure.
- ***Low lateral stiffness*** to reduce the response of the upper-structure under seismic excitation by allowing large relative displacements in the isolation layer.
- ***High restoring force ability*** to ensure that the upper-structure has no (or very small) residual deformations after a seismic event.

The lateral stiffness of an isolator is a sensitive aspect, since it should balance two important requirements: (1) resist frequent wind loads without displacing from the initial position, and (2) allow large displacements under seismic excitation in order to protect the upper-structure from damage. In addition, for the second requirement it is also necessary to ensure that the isolator does not lose its capacity to transmit vertical loads when subjected to significantly large displacements, or otherwise the upper-structure becomes unstable and may overturn.

Another important issue for isolators is that sometimes their maximum displacements cannot be accommodated in the available space. Therefore, to solve this problem, the common solution is to introduce dampers in order to limit the maximum displacements. For lead-rubber bearings, however, it is worth mentioning that the lead plug was introduced with the specific goal to achieve higher damping reducing – thus – the displacements. However, Kalpakidis and Constantinou (2009) have found that the energy dissipated per cycle and the characteristic strength of these isolators were reduced as a result of heating of the lead core under increasing number of loading cycles [I.4].

Triple friction pendulum isolators are commonly adopted in USA due to the fact that their characteristics can be adjusted to meet a large variety of design requirements for different types of seismic isolated structures. Nevertheless, they have two main disadvantages: (1) design process is significantly complicated, and (2) presence of considerable residual displacements [I.5].

I.2.2. Dampers

In Japan, in the recent years (2007 ~ 2011), the elastomeric and laminated rubber bearings represented 53% from the total number of seismic isolation devices mainly because of their cost effectiveness and low maintenance [I.6]. However, these types of isolators exhibit large displacements under extreme loadings. As a result, the most commonly adopted solution in Japan is a combination between these devices and different types of dampers.

The main roles of dampers are as follows:

- Dissipate the earthquake-induced energy and consequently reduce the displacements of the isolation layer
- Prevent (or reduce) torsional effects in the isolation layer

Unlike isolators, the variety of dampers is rather limited, with only two well-known types: (1) hysteretic, and (2) viscous. The object of the present study – U-shaped steel dampers (Fig. I-4) – is included in the first category, together with U-shaped lead dampers (Fig. I-5). Both damper types dissipate the earthquake-induced energy by acquiring large plastic deformations. Viscous dampers are usually employed to resist strong wind loads and frequent (small intensity) earthquakes (Fig. I-6).

U-shaped lead dampers present the advantage that pure lead has a low yield stress and very high ductility with minimal strain hardening. However, when subjected to a large number of small-amplitude cycles (caused by wind or traffic vibrations), fatigue cracks appear on the surface, affecting the damping properties of lead dampers. In addition, lead is an extremely heavy material and the significant dimensions of these devices render them quite inconvenient to be handled on construction sites.

The main advantage of U-shaped steel dampers over other hysteretic devices is that they are low-maintenance and easy to replace if necessary. Moreover, different sizes (Table I-1) and configurations (units of 4, 6, or 8 elements) are available, which allows meeting different design targets.

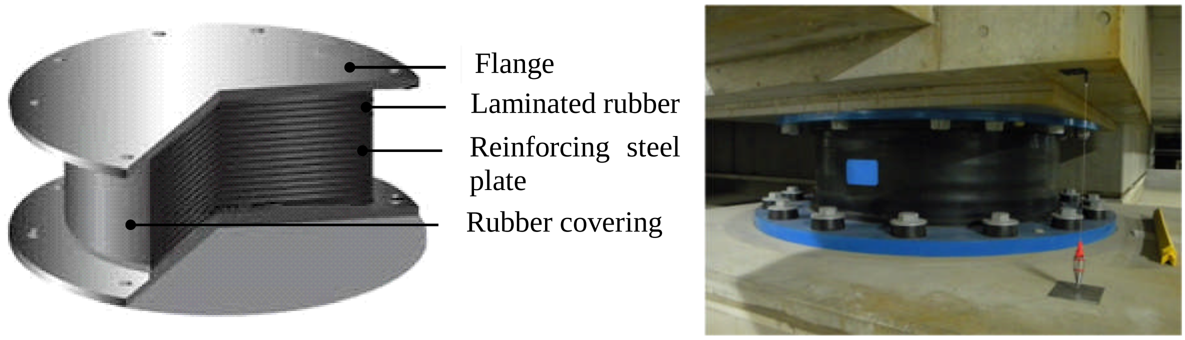

(a) Inside view [I.7]

(b) Photo (Tokyo Institute of Technology J2 building)

Figure I-1. Laminated rubber bearing.

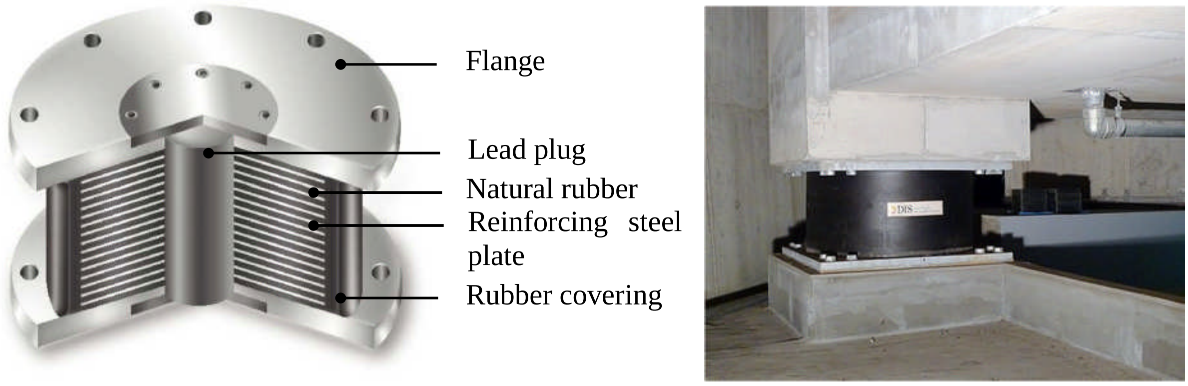

(a) Inside view [I.8]

(b) Photo [I.9]

Figure I-2. Lead-plug rubber bearing.

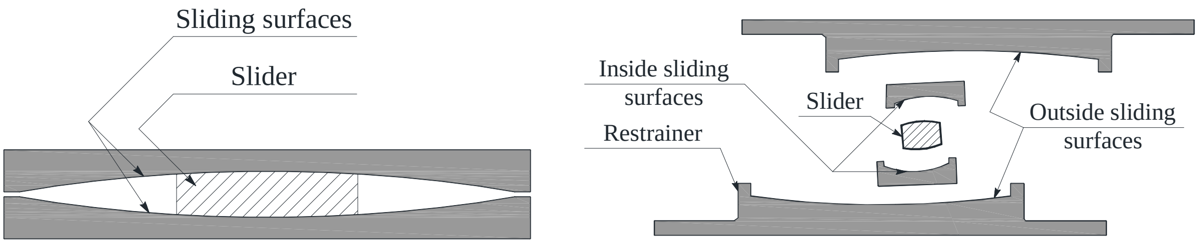

(a) Simple friction pendulum (inside view) [I.10]

(c) Triple friction pendulum (inside view) [I.5]

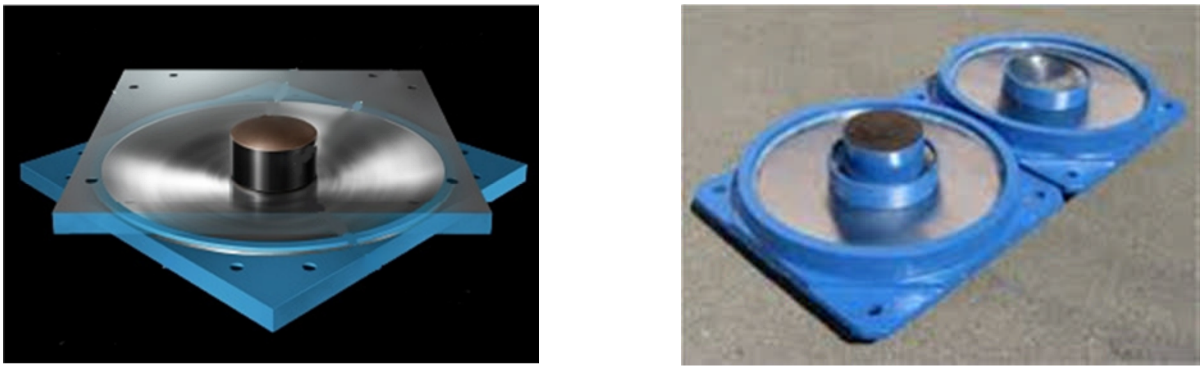

(b) Simple friction pendulum (photo) [I.11]

(d) Triple friction pendulum (photo) [I.12]

Figure I-3. Friction pendulum (simple and triple).

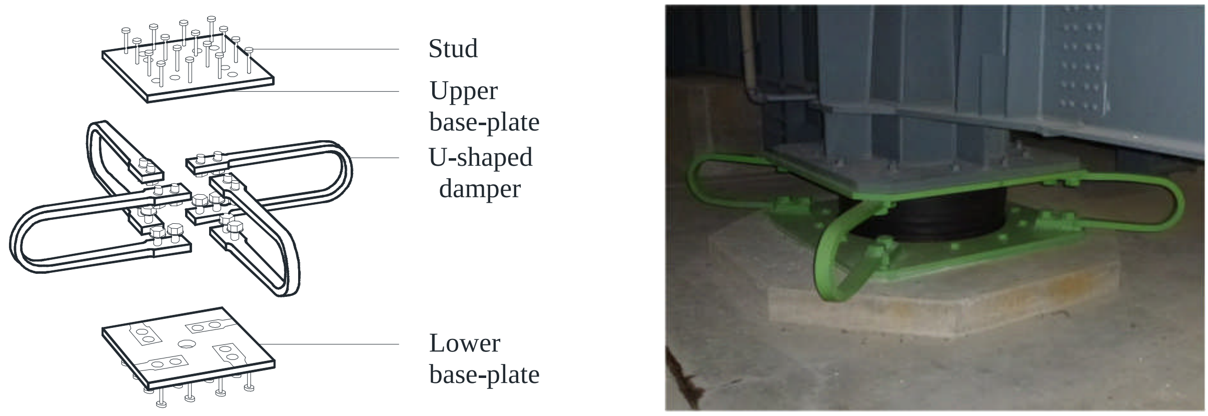

(a) Unit of 4 elements (b) Unit of 4 elements + isolator

Figure I-4. U-shaped steel dampers.

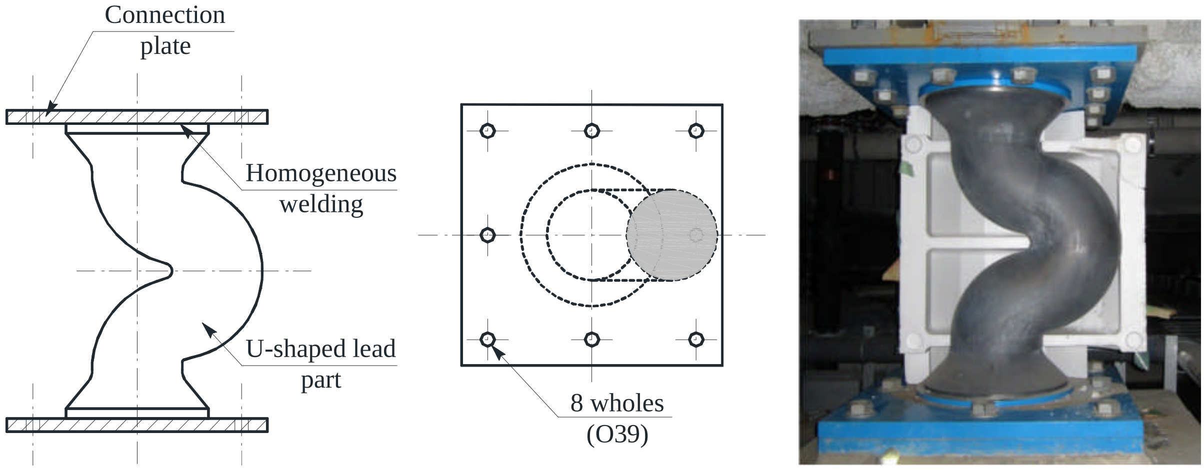

(a) Configuration (b) Photo

Figure I-5. U-shaped lead damper.

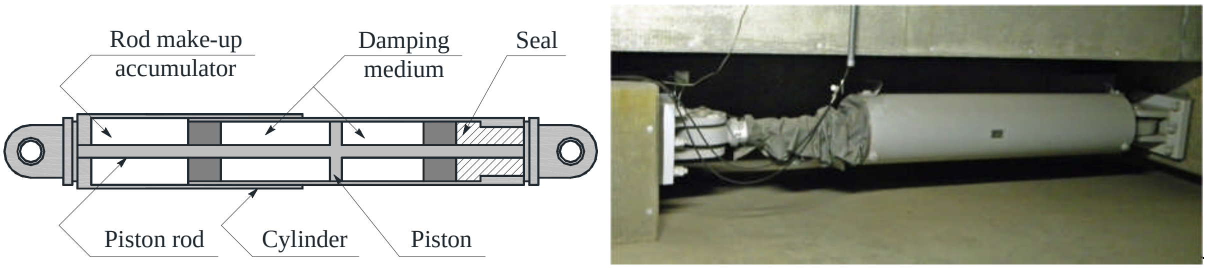

(a) Configuration (b) Photo (Tokyo Tech, J2 building)

Figure I-6. Viscous damper.

Table I-1. Geometric characteristics of different U-shaped damper sizes

Size	L [mm]	h [mm]	t [mm]	w [mm]	δ_{20} (*) [mm]	δ_{max} (**) [mm]
UD40	611	231	28	60	400	550
UD45	758	284	36	74	450	650
UD50	882	335	40	87	500	750
UD55	983	374	45	97	550	850
UD60	1199	453	55	118	600	1000

(*) 20 cycles before fracture; (**) 5 cycles before fracture

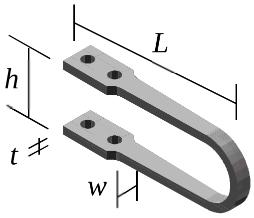

I.3. Fatigue behavior of U-shaped steel dampers under one-directional loading

In technical literature, the term "fatigue" is used to describe failure of a metallic element under repeated alternating or cyclic stresses. It is a progressive failure that starts with the appearance of microscopic cracks which propagate slowly until critical size is reached, then at a much higher rate, causing unstable behavior and eventually fracture. The fatigue strength is governed by three variables: (1) number of cycles of loading N, (2) difference between minimum and maximum stress, and (3) initial size of a flaw (*e.g.* extremely small crack). In structural engineering, there are two types of fatigue, depending on the number of cycles of loading N: (1) high-cycle fatigue ($N > 10^5$), and (2) low-cycle fatigue. High-cycle fatigue essentially occurs for elastic deformations and is generally investigated for bridges. Low-cycle fatigue involves plastic deformations and high stress levels at a low number of loading cycles. Seismic isolation devices are subjected to large plastic deformations in the event of a strong shaking, therefore the low-cycle fatigue behavior of U-shaped steel dampers is of interest.

The low-cycle fatigue behavior of U-shaped steel dampers is one of their most important characteristics, as it is vital to ensure they are able to fulfill their function without reaching premature failure during a strong motion event. In testing the performance of seismic isolation devices, generally the first step is to investigate the behavior under one-directional loading, with the purpose of obtaining information about basic aspects such as stability of hysteretic loops, displacement thresholds defining changes in stiffness, sensitivity to loading direction and loading speed, fracture mode etc.

The behavior of U-shaped steel dampers under one-directional loading was studied by Kishiki *et al.* (2008) and Jiao *et al.* (2015) [I.13][I.14]. Both studies confirmed that the dampers exhibit high ductility and large plastic deformation capacity before reaching fracture. Ductile cracks propagate slowly until the complete separation of the specimen into two different parts. This is reflected in the fracture surface (Fig. I-7) which is not a smooth one (as it is the case for brittle fracture), but it presents numerous cup-like depressions called dimples.

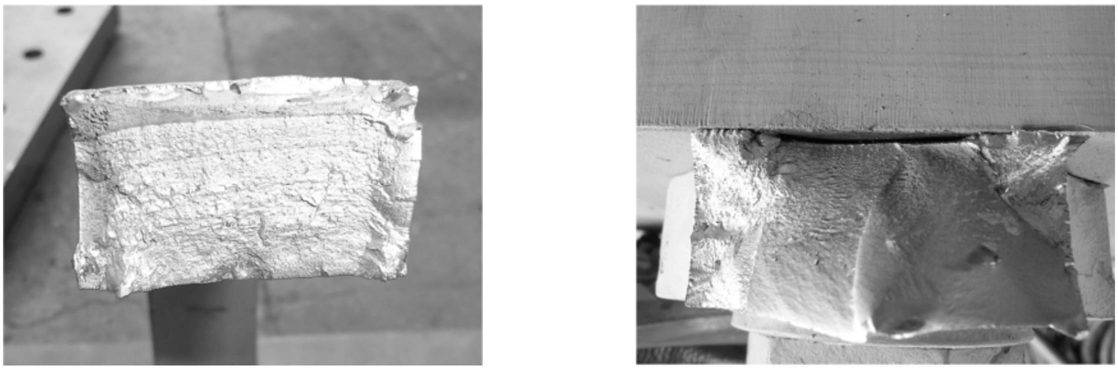

(a) Specimen loaded at 0° direction (b) Specimen loaded at 90° direction

Figure I-7. Fracture surfaces for specimens under one-directional loading (ductile fracture).

The other aspects of the behavior of U-shaped steel dampers under one-directional loading were investigated by Kishiki *et al.* and Jiao *et al.* by considering the effect of following parameters:

1. Loading direction (direction along which loading is applied)
2. Amplitude of the displacement history
3. Size of the damper elements
4. Loading speed
5. Initial temperature

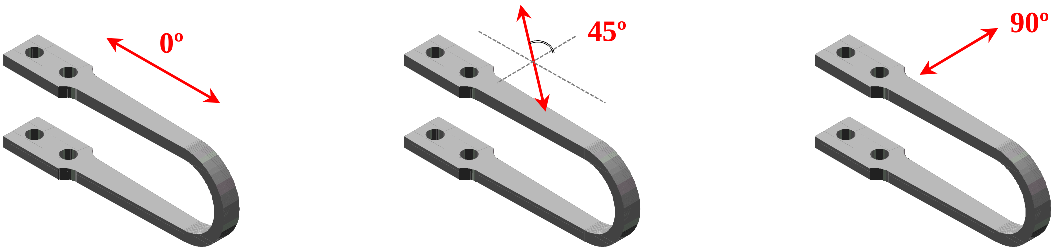

(a) 0° direction (b) 45° direction (c) 90° direction

Figure I-8. Main loading directions.

Kishiki *et al.* (2008) have tested reduced and full-scale single U-shaped steel dampers, considering all the above parameters, except the initial temperature. The specimens were tested until fracture, exhibiting stable behavior until the moment of occurrence of large ductile cracks. Three important findings were reported: (1) the plastic deformation capacity (fatigue life) of a single damper element is influenced by the combination of loading direction (Fig. I-8) and displacement amplitude, (2) accounting for similarity principle – *i.e.* suppressing the effect of different specimen sizes – the peak-to-peak shear deformation angle γ_t proved suitable to evaluate the fatigue life, and (3) loading speed has negligible effect on the yield strength and initial stiffness. Based on these findings, Kishiki *et al.* (2012)[I.15] have proposed a set of Manson-Coffin-type fatigue evaluation curves for 0° and 90° directions that allow estimating the damage of a damper knowing its displacement history through employing Miner's rule. The fatigue evaluation curves as well as the characteristic deformed shapes of the dampers under various loading directions are discussed in *Section I.3.1.*

The influence of loading speed on the energy dissipation capacity of U-shaped steel dampers was investigated by Jiao *et al* [I.14]. Full-scale specimens grouped 2-by-2 and placed on orthogonal directions were tested quasi-statically and dynamically. The maximum loading speed varied between 16(mm/s) (quasi-static) and 524(mm/s) (dynamic). The results – within the range of the considered parameters – the hysteretic behavior of the dampers under dynamic loading was slightly better than that under quasi-static loading. This finding allows drawing the important conclusion that by neglecting the influence of the loading speed, the behavior of the dampers is evaluated on the conservative side.

I.3.1. One-directional low-cycle fatigue evaluation curves

For metallic elements expected to suffer several stress reversals during their useful life, their low-cycle fatigue behavior requires particular attention. In the event of a strong ground motion, U-shaped steel dampers are subjected to a considerable number of such stress reversals, usually at significant displacement amplitudes. Therefore it is important to develop a method to estimate their damage under such conditions.

Manson-Coffin-type relations are widely adopted to estimate the fatigue life of metallic elements. For constant amplitude loading, they relate the stress amplitude to the number of cycles until fracture N_f. Depending on the stress amplitudes expected for the considered metallic element, there may be necessary to conduct an extensive amount of experimental tests in order to obtain a reasonable accuracy for Manson-Coffin relations.

Unlike conventional metallic members (such as beams designed to work in plastic range, steel braces etc.) that usually suffer stress reversals with relatively small amplitudes, the loading histories of U-shaped steel dampers – expressed in terms of relative displacement between their top and bottom base-plates (δ in Fig. I-9) – are between few to several hundred millimeters (for the largest damper size may even reach 1.00(m)). Since these relative displacements depend on the size of the damper, the peak-to-peak shear deformation angle γ_t – computed as the ratio between the total displacement amplitude δ_t and the height of the damper h (Eq. (I.1)) – is adopted to suppress this effect.

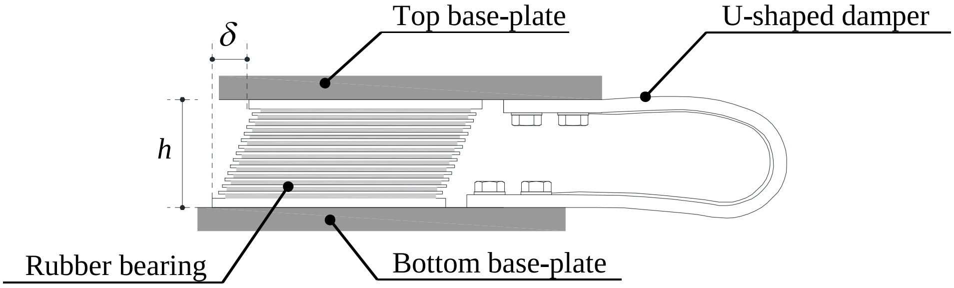

Figure I-9. Deformed shape under loading at 0° direction.

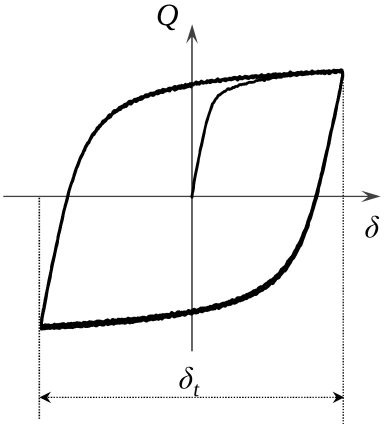

Figure I-10. Definition of total displacement amplitude δ_t.

$$\gamma_t = \frac{\delta_t}{h} \tag{I.1}$$

where δ_t is the total displacement amplitude; h is the height of the damper.

By employing γ_t, Manson-Coffin relations independent on the dimensions of the specimen can be constructed. This represents the great advantage that a single relation can be used to describe the behavior of any damper size, reducing, thus, the number of specimens required to obtain a fatigue curve with satisfying accuracy.

The valuable work of Kishiki *et al.* (2008, 2012) provided a significant database that allowed tracing two fatigue evaluation curves, one for loading at 0° direction (Eq. (I.2)), the other for loading at 90° direction (Eq. (I.3)) [I.13][I.15]. The necessity of two fatigue evaluation curves instead of a single one was dictated by the difference observed in the ultimate plastic deformation capacity of specimens loaded at 0° direction and of those loaded at 90° direction. This difference is caused by the fact that plastic deformations concentrate at different locations on the specimen, depending on: (a) loading direction, and (b) displacement amplitude (Fig. I-12).

$${}_{0^\circ}\gamma_t = 2370 \cdot {}_{0^\circ}N_f^{-0.66} \qquad \left(20\% \le {}_{0^\circ}\gamma_t \le 500\%\right) \tag{I.2}$$

$${}_{90^\circ}\gamma_t = 2535 \cdot {}_{90^\circ}N_f^{-0.55} \qquad \left(20\% \le {}_{90^\circ}\gamma_t \le 253.5\%\right) \tag{I.3a}$$

$${}_{90^\circ}\gamma_t = 2370 \cdot {}_{90^\circ}N_f^{-0.23} \qquad \left(253.5\% < {}_{90^\circ}\gamma_t \le 500\%\right) \tag{I.3b}$$

where the subscripts "0°", "90°" refer to the direction at which loading is applied (Fig. I-8)
N_f is the number of cycles to fracture (at constant amplitude)
γ_t is the peak-to-peak shear deformation angle (Eq. (I.1)).

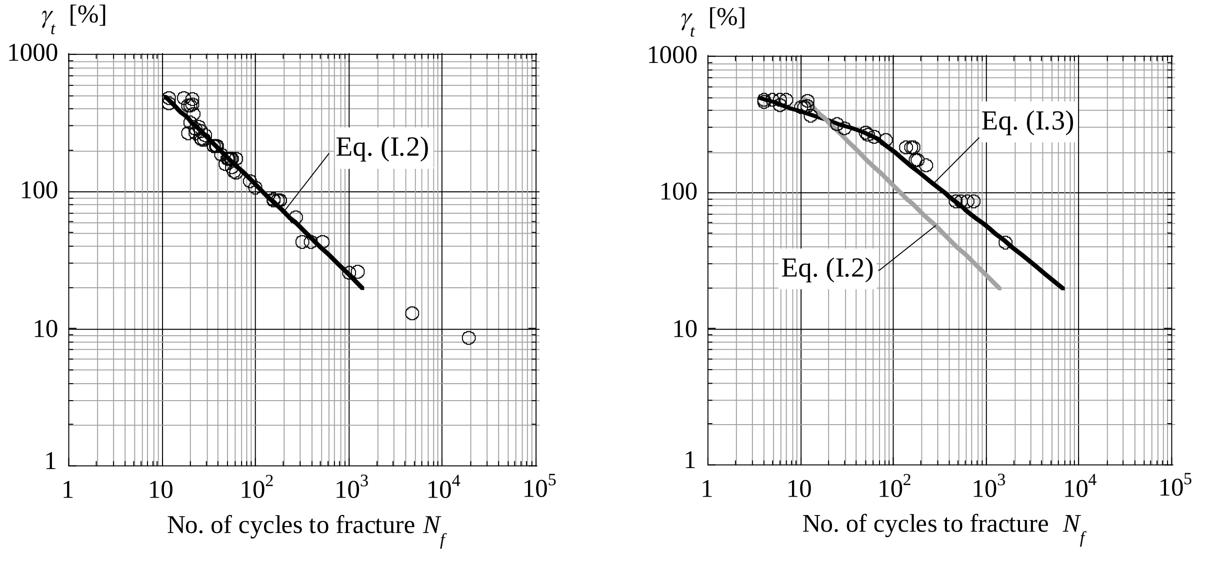

(a) 0° direction (b) 90° direction

Fig. I-11. One-directional low-cycle fatigue evaluation curves [I.15].

Deformed shapes for loading at 0° and 90° directions

The deformations of U-shaped steel dampers when loaded at 0° direction, respectively at 90° direction are explained in Fig. I-11 where a unit of 4 UD40 elements is shown. Displacement is induced in the positive sense of *x* axis, therefore, the dampers parallel to *x* axis (hereafter named *x* dampers) are loaded at their 0° direction, while those parallel to *y* axis (*y* dampers) are loaded at their 90° direction. In Fig. I-11 it can be observed that *x* dampers have an in-plane deformations, being mainly subjected to bending and, depending on the displacement amplitude at which the cyclic loading is conducted, load concentration zones appear on the flat part of the specimens (shown with red). As for *y* dampers, they are subjected to warping torsion in the cross-sections near the connection to the jigs (both up and down). This is caused by the large out-of-plane deformations of the specimens. The locations where stress concentrates for each damper are shown with red in Fig. I-11. These are the locations at which fracture under cyclic loading usually occurs [I.13], which raises the question whether – given the fact that the displacement of the isolation layer is bidirectional – the same statement can be made about U-shaped steel dampers subjected to bidirectional loading histories. This is a very important aspect because it can affect the energy dissipation characteristics of the dampers. The first step towards assessing this problem was conducted by Kishiki *et al.* (2012) who tested 29 UD40 elements using simple bidirectional loading histories (circle, ellipse). The results are briefly presented in Section I.4.

The one-directional low-fatigue cycle fatigue evaluation curves proposed by Kishiki *et al.* describe the behavior of the dampers when they exhibit either purely in-plane or out-of-plane deformations. Further on, the damage of the dampers is estimated using Miner's rule, as explained in the next section.

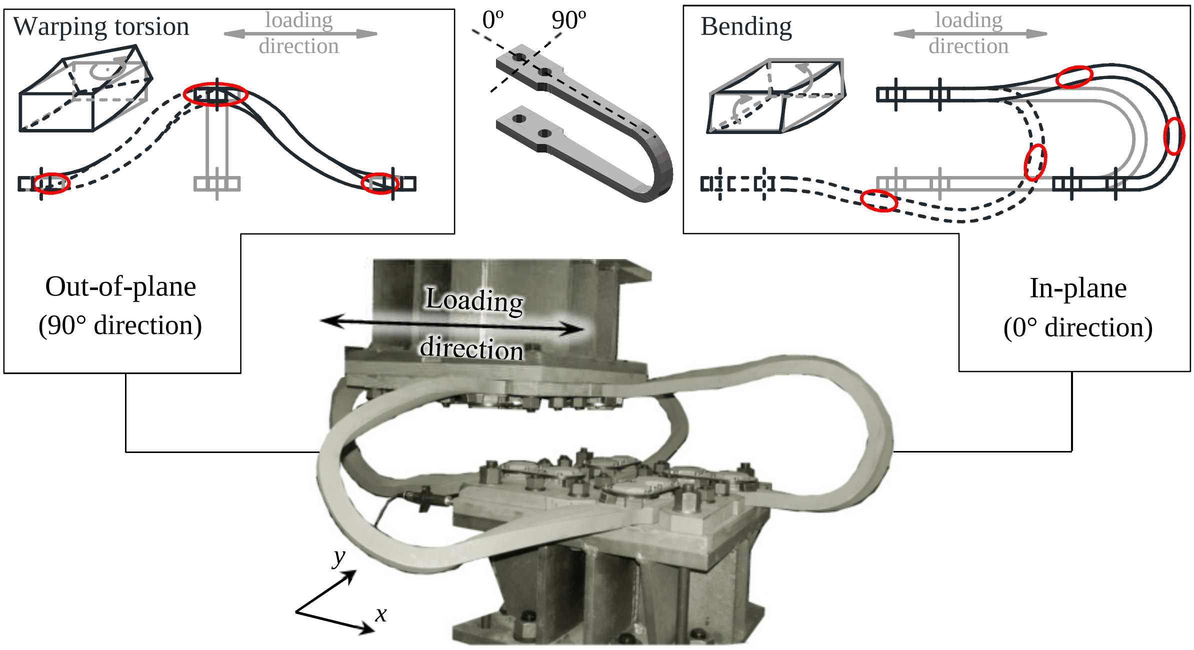

Figure I-12. Deformed shape of a unit of 4 UD40 dampers.

I.3.2. One-directional damage evaluation method

Manson-Coffin type fatigue evaluation curves are generally used in combination with Miner's rule to estimate the damage of the targeted specimen. According to Miner's rule, the damage under a loading history with various amplitudes is accumulated in the following way:

$$D = \sum_i \frac{n_i}{N_{f,i}} \tag{I.4}$$

where n_i is the frequency of cycles with amplitude A_i

N_f is the number of cycles to fracture under cyclic loading at amplitude A_i.

The limit value of the damage index D is 1.0, when the specimen is considered to have reached fracture. For U-shaped steel dampers, due to the fact that there are two fatigue evaluation curves, it results that two damage indices can be computed given a considered one-directional loading sequence by simply applying it at 0° direction (D_{0°) or at 90° direction (D_{90°). The *Design Recommendations for Base-Isolated Structures* [I.16] stipulate that the maximum damage index should be considered when checking the design of isolation layers for which U-shaped steel dampers are used (Eq. (I.5)):

$$D = \max\left(D_{0^\circ}, D_{90^\circ}\right) \quad (<1.0) \tag{I.5}$$

where D is the maximum one-directional cumulative damage index

D_{0°, D_{90° are the one-directional cumulative damage indices when loading along 0° direction (Eq. (I.2)), respectively along 90° direction (Eq. (I.3)).

However, by conducting a set of bidirectional loading tests using simple histories (circles, ellipses), Kishiki *et al.* found that the ultimate inelastic deformation capacity of the dampers decreases because of the influence of torsional stresses in the steel bar induced by the relative displacement between the two fixed ends of the specimen. This raised awareness on the fact that the one-directional approach may overestimate the inelastic deformation capacity of U-shaped steel dampers, which leads to unsafe design. For this reason, Kishiki *et al.* (2012) proposed an empirical method to evaluate the damage of the dampers under bidirectional loadings. This method is briefly introduced in the next section.

I.4. $D_2^u - J_f$ interaction curve for fatigue behavior of U-shaped steel dampers under simple bidirectional loading

Using simple bidirectional histories (Fig. I-13), Kishiki *et al.* (2012) have shown that the basic bidirectional behavior of U-shaped steel dampers is significantly different than their one-directional behavior, because the ultimate inelastic deformation capacity decreases when subjected to biaxial loading. This decrease is caused by the complex torsion stresses that appear in the steel bar as a result of the bidirectional displacement history. In other words, a specimen subjected to bidirectional displacement will reach an earlier fracture than a specimen subjected to one-directional displacement with the same amplitude. In addition, the following differences were found by comparison to the behavior under one-directional histories:

1. Depending on the shape and amplitude of the loading history, respectively on the loading sense, severe residual out-of-plane deformations were observed. Under loading in reverse sense these deformations were – to some extent – reversed.
2. Because of the extreme out-of-plane deformations, contact between the dampers and the loading jigs occurred.

Kishiki *et al.* proved that the ultimate inelastic deformation capacity depends on both the displacement amplitude and on the in-plane rotation angle described by the loading history with respect to the initial position of the undeformed specimen. An evaluation method taking into account these two aspects was proposed based on two indices: (1) bidirectional cumulative damage index D_2, and (2) empirical sway-motion index J_f. Further on, using these two indices, an interaction curve was traced as the lower bound of the test results. The basic notions about each index are presented below.

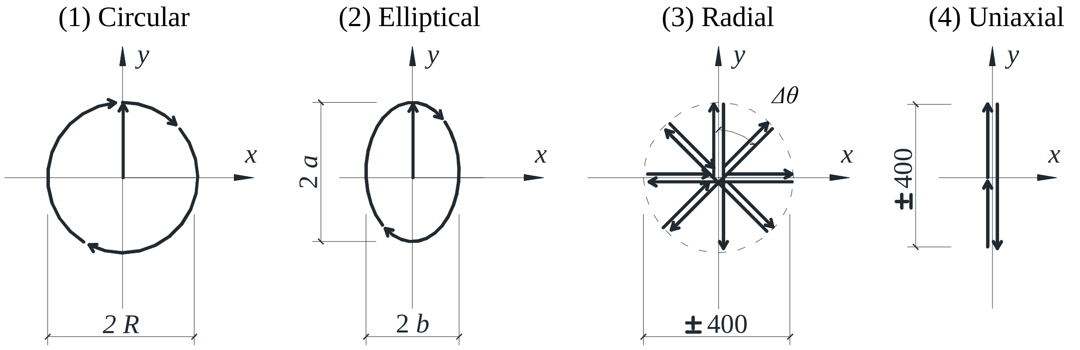
(1) Circular (2) Elliptical (3) Radial (4) Uniaxial

Constant radius at:
R=150, 200, 250, 300, 350 mm

Incremental radius at:
R=50~250 mm

Constant b:
a=400, b=50, 100 mm
a=300, b=50, 100 mm

Incremental b:
a=400, b=50~150

$\Delta\theta = 15.0, 22.5, 45.0(°)$

Loading on y axis or on x axis

Figure I-13. Simple bidirectional loading histories conducted by Kishiki *et al.* (2012) [I.15].

I.4.1. Bidirectional cumulative damage index D_2

The bidirectional cumulative damage index D_2 was proposed by Kishiki *et al.* (2012) to evaluate the damage induced to a U-shaped steel damper by a bidirectional displacement orbit. To illustrate how D_2 is obtained, let us consider a circular displacement orbit of radius R, for which the value R was reached by loading on y direction (Fig. I-14). The displacement is decomposed on two orthogonal directions, x and y components δ_x, δ_y. If a damper is placed parallel to the input direction of δ_x, as shown in Fig. I-14, it will suffer in-plane damage (at its 0° direction) caused by δ_x, and out-of-plane damage (at its 90° direction) caused by δ_y. Therefore the two one-directional fatigue evaluation curves (Eq. (I.2), (I.3)) can be applied to compute the damage indices ${}_xD_{0^\circ}$, respectively ${}_yD_{90^\circ}$. Assuming that the total bidirectional damage of a U-shaped steel damper can be expressed by using the two previously defined low-cycle fatigue evaluation curves, the bidirectional cumulative damage index D_2 is obtained by adding the damage index at 0° to that at 90° (Eq. (I.6)):

$$D_2 = \underbrace{\sum_{i=1}^{n} \frac{n_i}{{}_{0^\circ}N_{f,i}}}_{D_{0^\circ}} + \underbrace{\sum_{j=1}^{m} \frac{n_j}{{}_{90^\circ}N_{f,j}}}_{D_{90^\circ}} \tag{I.6}$$

where n, m are the total number of cycles of δ_x, respectively δ_y

n_i, n_j are the frequencies of each amplitude on each direction (x and y)

${}_{0^\circ}N_{f,i}$, ${}_{90^\circ}N_{f,j}$ are the number of cycles to fracture under each displacement amplitude obtained from Eq. (I.2) and (I.3).

The limit value of D_2 index (after which the dampers are considered fractured) is the $D_2^u - J_f$ interaction curve and is discussed in Section I.4.3.

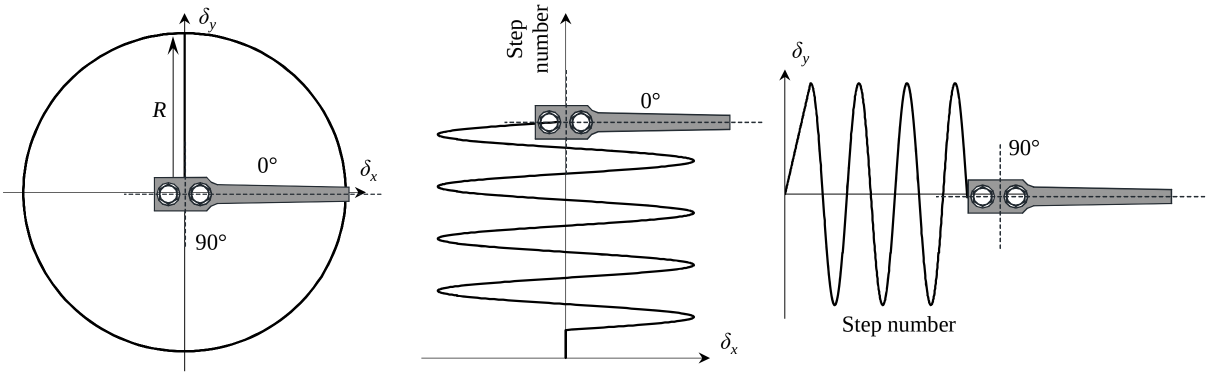

(a) Bidirectional displacement history (b) Damage at 0° (${}_xD_{0^\circ}$) (c) Damage at 90° (${}_yD_{90^\circ}$)

Figure I-14. Computation of the bidirectional cumulative damage index D_2.

I.4.2. Sway-motion index J_f and contact index J_c

As mentioned above, Kishiki *et al.* (2012) found that the reduction of the ultimate inelastic deformation capacity of U-shaped steel dampers under bidirectional loading depends on the shape and amplitudes of the loading history, and on the loading sense. The sway-motion index J_f was proposed empirically as a measure of the interaction between the displacement amplitude and the in-plane rotation angle described by the loading history with respect to the initial position of the undeformed specimen (Eq. (I.7)). The larger the value of J_f, the more complex the shape of the displacement orbit is, or the larger the number of conducting loading cycles is; moreover, for one-directional loading J_f is 0, since there is no rotation about the initial position, but only translation ($\Delta\varphi = 0$).

In the physical sense, J_f is an indirect measure of the out-of-plane deformations of the dampers. A large value of J_f (>15(rad)) implies that the specimen was significantly affected by torsional stresses. This is described by the D_2^u – J_f interaction curve (see next section).

$$J_f = \sum_{i=1}^{n-1} \left(\gamma_i \cdot \gamma_{i+1} \cdot \frac{\gamma_i + \gamma_{i+1}}{2} \cdot \left| \Delta\varphi_i \right| \right) \tag{I.7}$$

where J_f (rad) is the sway-motion index evaluating the torsion-induced reduction of the cyclic deformation capacity of a damper under a bidirectional displacement orbit

n is the total number of loading steps

γ_i is the shear deformation angle (the ratio between the radius at a given step, R_i and the height of the damper, h)

$\Delta\varphi_i$ is the incremental angle between 2 consecutive steps, "i" and "i+1" (Fig. I-15).

It is worth noting that the value of the sway-motion index does not depend on the step increment (number of steps n), but on the total cumulative rotation angle φ.

In addition to the sway-motion index J_f, it is worth mentioning the contact index J_c defined by Kishiki *et al.* to estimate the contact timing (between the damper and the loading jigs). The J_c index is defined using the same equation as J_f index, where the incremental angle is taken with its sign. The limit value of J_c was found to be ±26.8(rad) and needs to be verified for the case of realistic loading histories.

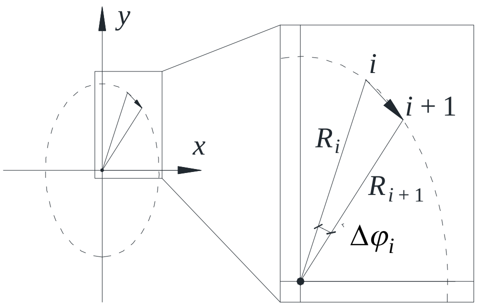

Figure I-15. Computation of the sway-motion index J_f.

I.4.3. D_2^u – J_f interaction curve

Using the displacement histories shown in Fig. I-13, Kishiki *et al.* tested 29 full-scale specimens (UD40 size). For each specimen, the values of the two proposed indices (D_2 and J_f) at the moment of fracture were computed and plotted against each other as shown in Fig. I-16. It can be easily observed that, as J_f increases, the corresponding values of D_2 decrease, which means that the ultimate inelastic deformation capacity decreases, and the specimens fracture at values of D_2 less than 1.0. To account for this phenomenon, the D_2^u – J_f interaction curve was defined as the lower limit of the test results (Eq. (I.8)):

$$D_2^u = \left| \begin{array}{ll} 1.0 & \left(\quad J_f \le 15 \right) \\ 1.6 - 0.04 \cdot J_f & \left(15 < J_f \le 30 \right) \\ 0.4 & \left(30 < J_f \right) \end{array} \right. \tag{I.8}$$

where J_f is the sway-motion index measured in radians

D_2^u is the maximum allowable bidirectional cumulative damage index before fracture.

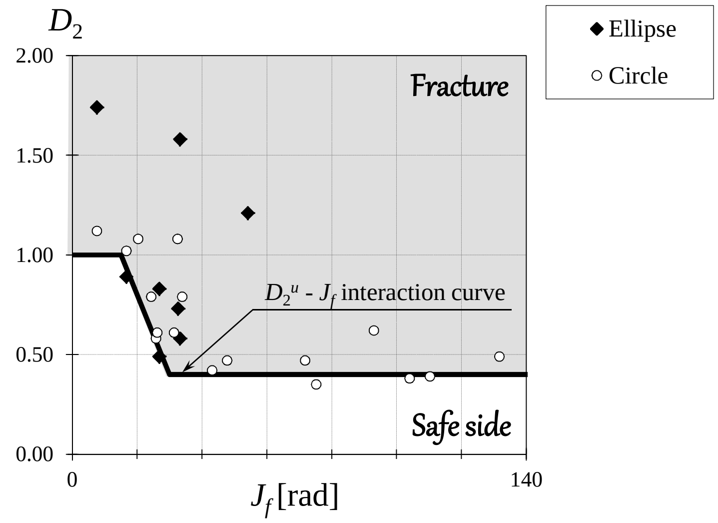

Figure I-16. D_2^u – J_f interaction curve and previous test results [I.15].

It can be noticed that for J_f greater than 60(rad), the lower limit is dictated exclusively by specimens subjected to circular loading patterns. Consequently, the question whether the proposed interaction curve is suitable to estimate the ultimate inelastic deformation of U-shaped steel dampers under realistic bidirectional histories raises. The answer to this question is an extremely important issue, because it may confirm or infirm not only the fidelity of the interaction curve, but also the suitability of the proposed indices (D_2 and J_f) in assessing the damage level of a U-shaped steel damper under random bidirectional loadings.

I.5. Research objectives

During a ground motion, seismic isolated buildings are – as any other type of structures – subjected to biaxial excitation. As a result, large (several tens of centimeters) bidirectional displacements occur in the isolation layer, where the earthquake-induced energy is dissipated by allowing a certain degree of damage of the isolation devices. The reliability of these devices under such conditions is – therefore – of crucial importance.

In the present study, the reliability of U-shaped steel dampers under realistic bidirectional loading histories is investigated. To this purpose, the following objectives are targeted:

1. By conducting a set of dynamic test with realistic bidirectional histories (determined through nonlinear response analysis):
    a. Assess the fidelity of the $D_2^u - J_f$ interaction curve [I.15] in estimating the ultimate inelastic deformation capacity of dampers subjected to *realistic bidirectional* loading histories (***Chapter II***).
    b. Investigate the reliability of the dampers under several strong motion events (***Chapter II***).
2. Propose an analytical model able to accurately simulate the behavior of the dampers under bidirectional loading (***Chapter III***).
3. By conducting a set of nonlinear time-history analyses, assess the reliability of the dampers under various seismic hazard levels ranging from frequent to extremely rare events. Based on the results, derive fragility curves relating certain damage levels of the dampers to a selected intensity measure of the ground motion (***Chapter IV***).
4. Identify the differences between the damage evaluation methodology generally adopted in typical design practices in Japan and the bidirectional approach employed in the present study. Further on, conduct a quantitatively investigation on whether the former provides unsafe results as compared to the latter, and decide whether this can represent a real dangerous situation in the practical use of U-shaped steel dampers (***Chapter V***).

References:

[I.1] Naeim, F., Kelly, J. M., 1999. Design of Seismic Isolated Structures: From Theory to Practice, John Wiley & Sons, Inc., United States of America, pp. 1-23;

[I.2] Nagarajaiah, S., Xiaohong, S., 2000. Response of base-isolated USC hospital building in Northridge earthquake, *Journal of Structural Engineering* ***126***, No. 10, October, 2000;

[I.3] National Institute for Land and Infrastructure Management (NILIM) and Building Research Institute (BRI), 2011. Summary of the Field Survey and Research on "The 2011 off the Pacific coast of Tohoku Earthquake" (the Great East Japan Earthquake), Response of seismically isolated buildings (accessed on December 6th 2013) http://www.kenken.go.jp/english/contents/topics/20110311/0311summaryreport.html;

[I.4] Kalpakidis, I.V., Constantinou, M.C., 2009. Effects of heating on the behavior of lead-rubber bearings. I: Theory, *Journal of Structural Engineering ASCE* ***135***, pp. 1440-1449;

[I.5] Becker, T.C., Mahin, S., 2012. Experimental and analytical study of the bidirectional behavior of the triple friction pendulum isolator, *Earthquake Engineering and Structural Dynamics* ***41***, pp. 355-373;

[I.6] 日本建築センター：ビルディング レター;

[I.7] www.bpress.cn (accessed on 2015.09.09);

[I.8] www.taiwanpillar.com.tw (accessed on 2015.09.09);

[I.9] www.tokyo-office-guide.net (accessed on 2015.09.09);

[I.10] 中村秀司，西本晃治，長谷川 久巳，中村博志．2015. 球面すべり支承（SSB）の繰り返しによる温度上昇と摩擦係数の予測（その1, その2, その3, その4），日本建築学会大会学術講演梗概集（関東）2015年　9月；

[I.11] http://www.sumitomo-siporex.co.jp/product/seismically/product/lead_damper.html (accessed on 2015.11.20);

[I.12] onlinelibrary.wiley.com (accessed on 2015.09.09);

[I.13] 吉敷 祥一，大河原 勇太，山田 哲，和田 章：免震構造用U字形鋼材ダンパーの繰り返し変形性能に関する研究，日本建築学会構造系論文集　第73巻 第624号, pp.333-340, 2008.2;

[I.14] Jiao, Y., Kishiki, S., Yamada, S., Ene, D., Konishi, Y., Hoashi, Y., Terashima, M., 2015 Low cyclic fatigue and hysteretic behavior of U-Shaped steel dampers for seismically isolated buildings under dynamic cyclic loadings, *Earthquake Engineering and Structural Dynamics* ***44***, pp.1523-1538;

[I.15] 吉敷 祥一，高山 大，山田 哲，ENE Diana，小西克尚，川村典久，寺嶋正雄：水平2方向載荷下における繰り返し変形性能に関する実験：免震構造用U字形鋼材ダンパーの水平2方向特性（その1），日本建築学会構造系論文集　第680号, pp.1579-1588, 2012.10;

[I.16] 日本建築学会 2013：免震構造設計指針.

Chapter II

Fidelity of $\mathbf{D}_2 - J_f$ Interaction Curve for the Case of Seismic Excitation

II.1. Introduction

II.2. Nonlinear time-history analysis for experimental plan

- II.2.1. Ground motion set
- II.2.2. Analytical model
- II.2.3. Preliminary analysis
- II.2.4. Analytical results
- II.2.5. Loading protocols

II.3. Bidirectional dynamic loading tests

- II.3.1. Specimens and loading facilities
- II.3.2. Test results

II.4. Bidirectional quasi-static loading tests

- II.4.1. Loading protocols
- II.4.2. Specimens and loading facilities
- II.4.3. Test results
- II.4.3. Comparison between dynamic and quasi-static loading tests

II.5. Summary

II.1. Introduction

By conducting one-directional and bidirectional tests with simple displacement loading histories and comparing the results, Kishiki *et al.* (2008, 2012) proved that the ultimate inelastic deformation capacity of U-shaped steel dampers under bidirectional loading is reduced as a result of the torsional stresses induced in the specimen by the relative displacement between its upper and lower parts [II.1][II.2]. This reduction was found to be dependent on the characteristics of the displacement history (amplitude, shape, loading sense). An interaction curve able to take into account these aspects was proposed based on the bidirectional cumulative damage index D_2 and sway-motion index J_f as the lower bound of the obtained test results (Eq.(I.8)) [II.2]. However, the fidelity of both D_2 and especially J_f, as well as that of the $D_2^u - J_f$ interaction curve have to be verified against realistic displacement loading histories to confirm that the damage of U-shaped steel dampers subjected to seismic excitation can be estimated by using this approach.

The main objective of the present chapter is – thus – to assess whether the above mentioned damage evaluation method is suitable to estimate with sufficient reliability and satisfying accuracy the damage of U-shaped steel dampers subjected to seismic excitation. To this purpose, the following steps are conducted:

1. Propose a realistic set of bidirectional displacement histories by conducting nonlinear time-history analysis and simulate the bidirectional response of an isolation layer.
2. Using the bidirectional displacement histories established at the previous step, conduct a set of dynamic loading tests on full-size specimens until fracture (units of 4, respectively 8 UD50 dampers) and compare the results with the $D_2^u - J_f$ interaction curve.
3. Investigate the effect of loading speed for the case of bidirectional loading by conducting another set of tests (quasi-static) and comparing the results with those obtained in the previous step (force – deformation relations, respectively values of D_2 and J_f).

In addition, the validity of the similitude principle which employs the height of the dampers (proposed by Kishiki *et al.* for computing the peak-to-peak shear deformation angle γ_t) in describing the force – deformation relations of different damper-sizes is assessed.

Another aspect investigated in this chapter is the contact occurrence, first identified by Kishiki *et al.* (2012), who found that severe out-of-plane deformations caused by loading in a single sense (clockwise or counterclockwise), the initial shape of the dampers becomes distorted, causing contact with the loading jigs. This aspect was carefully observed both during the dynamic and quasi-static loading tests with realistic bidirectional displacement histories.

II.2. Nonlinear time-history analysis for experimental plan

To achieve the main objective of this chapter, a set of realistic bidirectional displacement histories has to be established. For this purpose, a set of ground motions and an analytical model are required. These are described in the present section. Moreover, it is necessary to estimate the damage of U-shaped steel dampers by using the bidirectional cumulative damage index D_2 and sway-motion index J_f. In addition, having established the loading protocol, the minimum expected ultimate inelastic deformation capacity of the specimens is predicted at the intersection with the interaction curve. The contact occurrence is investigated by computing the contact index J_c and comparing it to the limit value (28.6(rad)) [II.2].

II.2.1. Ground motion set

A set of 21 strong ground motions from 10 different seismic events from all over the world were selected to evaluate the induced bidirectional damage of U-shaped steel dampers (Table II-1). Both horizontal components of each ground motion were considered. In addition, the three recordings typically adopted in design of buildings in Japan (Taft, El Centro, Hachinohe) were also employed. The acceleration time-histories are shown in Fig. II-1. It can be noted that long-period events (Tohoku → Fukushima, Sendai, Iwaki, Koriyama) as well as near-fault events with pulse-like contents (Northridge → Newhall, Olive View; Kocaeli → Yarimca) are adopted.

It is worth noting that the Ishinomaki hospital recording of Tohoku 2011 earthquake was selected here in spite of its small intensity, because the monitored building is a seismic isolated structure for which U-shaped steel dampers were used.

II.2.2. Analytical model

The analytical model is an idealization of a base-isolated structure where the upper structure is modeled as a rigid body. This is permitted due to the fact that generally the fundamental vibration mode of a base-isolated structure is the one that dictates the response of the whole system, which is concentrated at the level of the isolation layer. Therefore, a single mass system with two degrees of freedom is adopted. The latter are conferred by employing a multiple shear spring (MSS) element proposed by Wada (1989) [II.3]. Details about the MSS model are given in ***Chapter IV***.

The restoring force characteristics of the system are obtained by superimposing the behavior of a unit of 4 damper elements to that of a rubber bearing. The assumed hysteretic behavior for the damper unit is a linear elastic – perfectly plastic one, with an initial stiffness k_e^d equal to 10540(kN/m) and a yield strength Q_y^d equal to 294(kN).

The maximum considered displacement is $\delta_{\max}$ = 400(mm) and the corresponding equivalent vibration period T_{eq} is set to 4.0(sec). The maximum base shear strength $Q_{\max}$ of the isolation layer is set to 10% of the total weight of the structure. At the maximum displacement δ_{max}, the contribution of the dampers to the restoring force characteristics of the system is $0.3 \cdot Q_{max}$., while that of the rubber bearing is $0.7 \cdot Q_{max}$.

The selected values for δ_{max} and T_{eq} are the most frequent ones for seismic isolated structures built in the last 10 years as reported by the Building Letters [II.4] (see ***Chapter IV***).

Table II-1. Ground motion set for experimental plan

Earthquake				Station		*PGV* [cm/s]	
No.	M	Year	Name	Full name	Abv.	*C*1 (*)	*C*2 (*)
1	9.0	2011	Tohoku	JMA Sendai	JS	53.3	54.5
2				K-net Koriyama	KY	43.6	60.4
3				K-net Fukushima	FS	30.1	24.9
4				K-net Iwaki	IK	34.5	63.0
5				Ishinomaki hospital	IH	12.6	33.0
6	7.3	1999	Chi-Chi	TCU078	CA	42.0	33.0
7				TCU129	CB	55.4	51.0
8	7.6	1999	Kocaeli	Yarimca	YP	88.8	88.7
9	7.2	1995	Kobe	JMA Kobe	KB	78.0	89.3
10				JR Takatori	TK	122.0	122.7
11				Port Island	KP	52.0	90.9
12				Osaka Nanko-Port	NP	21.8	24.5
13				Amagasaki	AM	85.9	49.6
14				NTT Kobe	NT	87.2	28.8
15	6.7	1994	Northridge	Newhall	NH	74.8	96.8
16				Olive View	SO	78.0	129.2
17	6.9	1989	Loma Prieta	Agnews hospital	AG	28.9	17.6
18	6.1	1980	Victoria	Chihuahua	CH	24.8	15.6
19	7.3	1968	Tokachi-Oki	Hachinohe	HC	37.0	34.6
20	7.3	1952	Kern County	Taft	TF	17.5	18.2
21	6.9	1940	Imperial Valley	El Centro	EL	48.8	38.1

(*) *C*1 stands for seismic horizontal component 1, *C*2 – for the horizontal component 2.

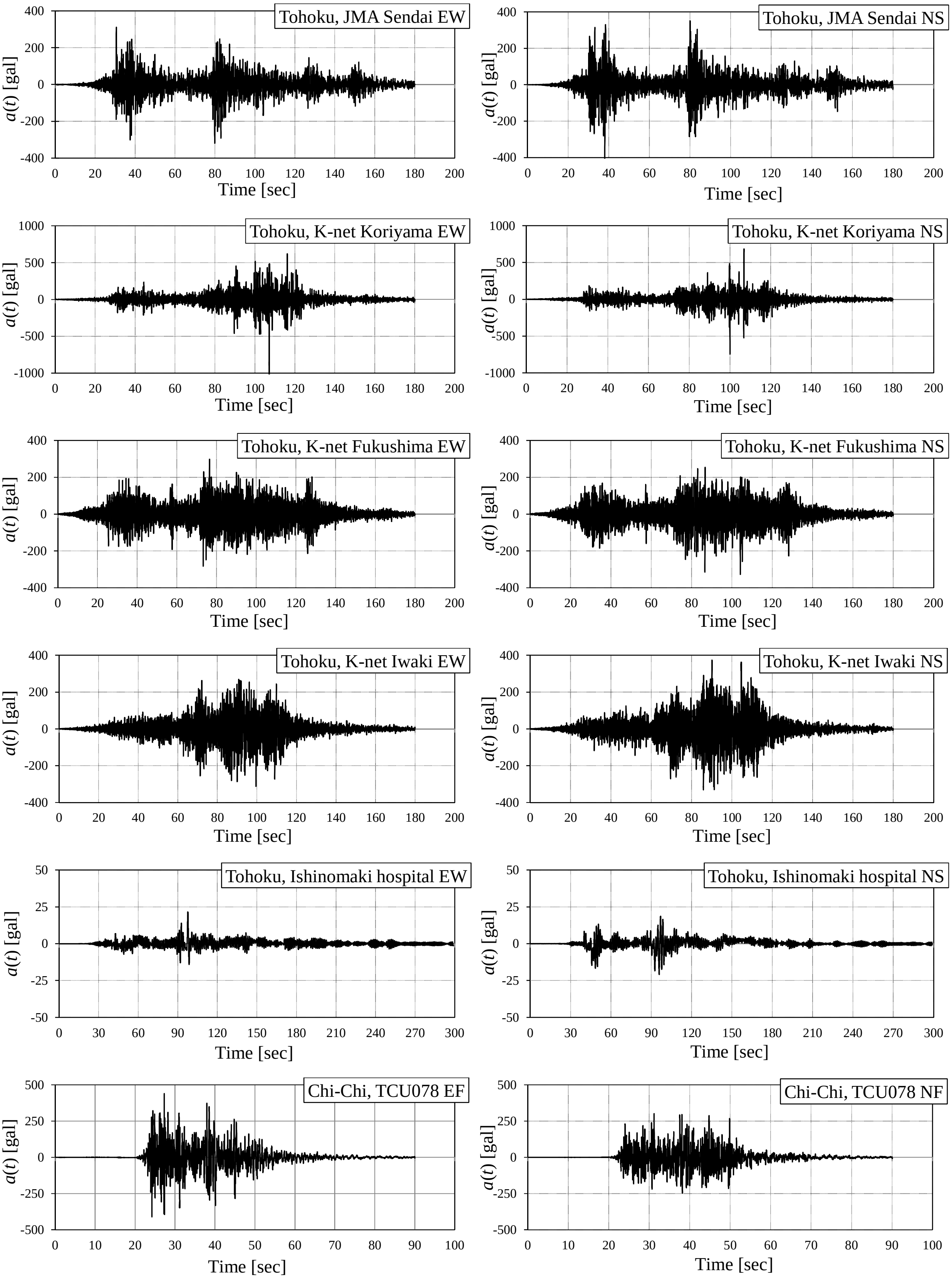

Figure II-1. Acceleration time-histories for experimental plan (1).

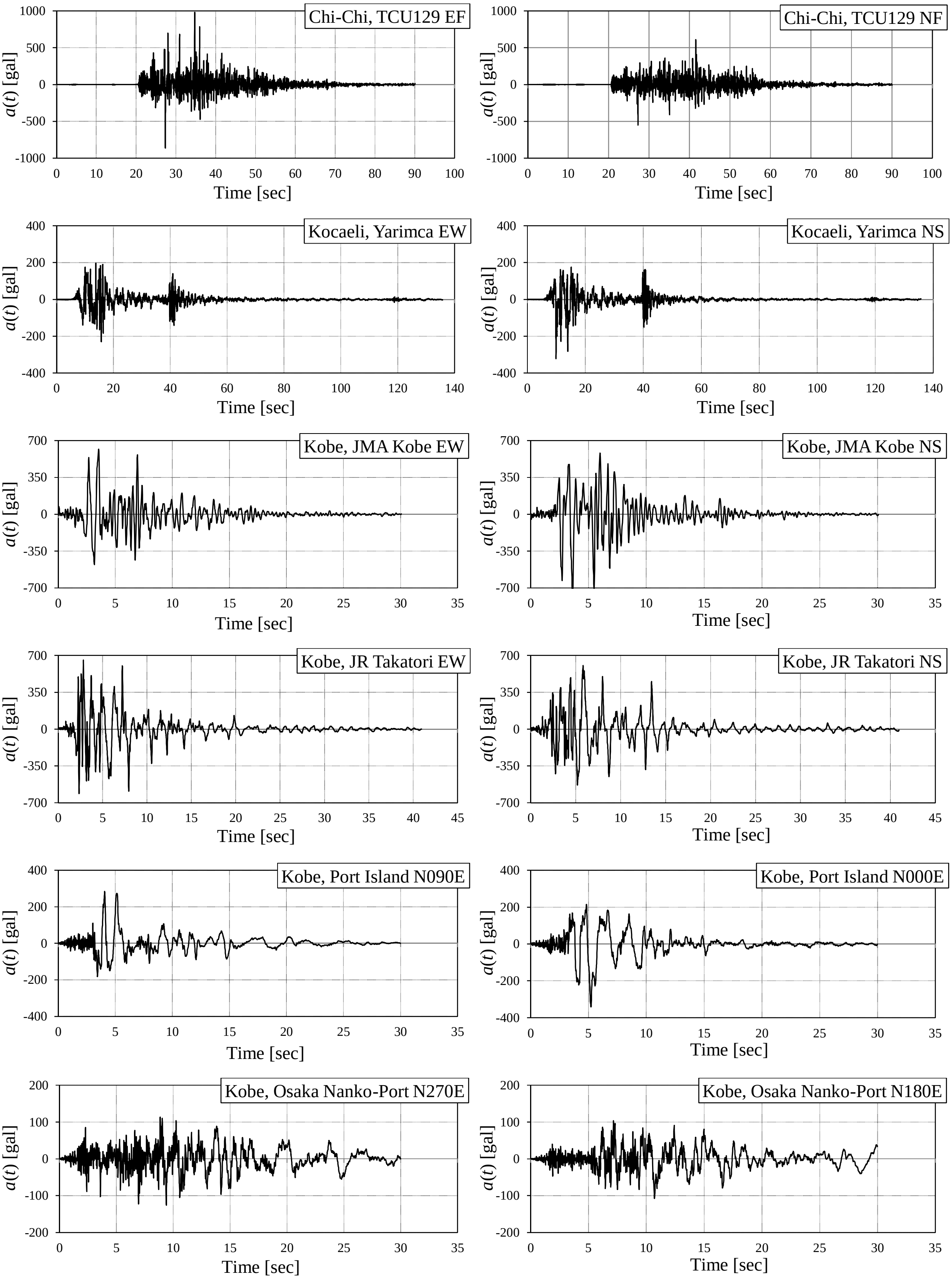

Figure II-1. Acceleration time-histories for experimental plan (2).

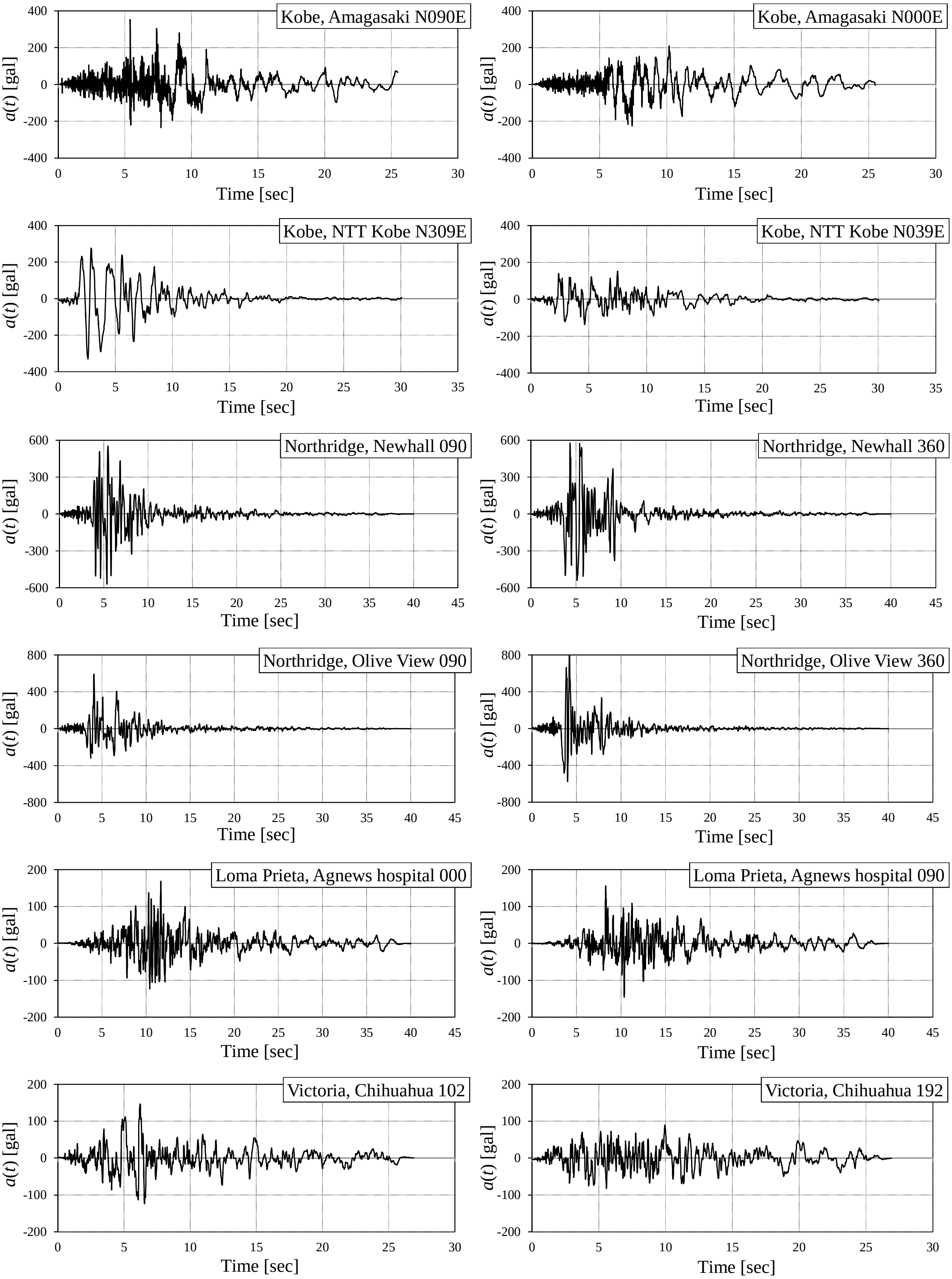

Figure II-1. Acceleration time-histories for experimental plan (3).

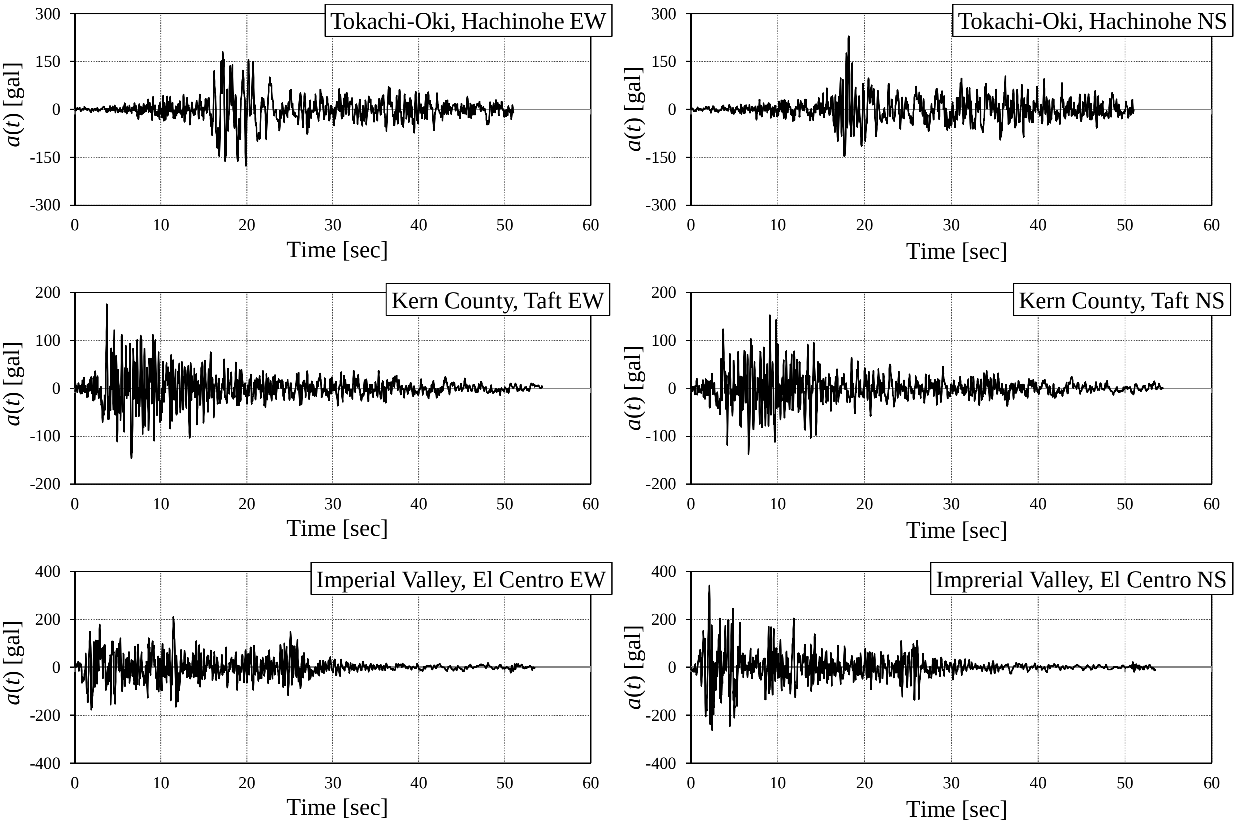

Figure II-1. Acceleration time-histories for experimental plan (4).

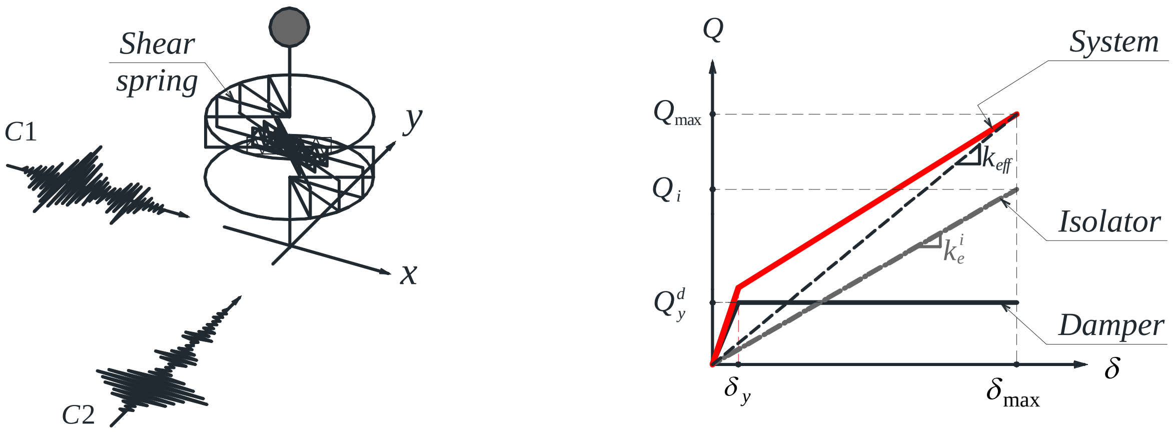

(a) MSS model (b) Restoring force characteristics

Figure II-2. Analytical model for experimental plan.

II.2.3. Preliminary analysis

To investigate the damage level induced by the original waves (when no scaling of the acceleration time-histories is applied), preliminary analysis was conducted for El Centro (EL), JMA Sendai (JS), JMA Kobe (KB) and Hachinohe (HC) ground motions.

The bidirectional displacement orbits were obtained (Fig. II-3) and, by applying rain-flow algorithm, the amplitudes of each cycle on *x* direction, respectively *y* direction were identified. The latter were further adopted to compute the bidirectional cumulative damage index of the dampers placed parallel to x axis $_XD_2$ of the bidirectional displacement history and that of the dampers parallel to y axis $_YD_2$ (Eq. (I.6)). In addition, the values of the sway-motion index J_f and contact index J_c for each displacement orbit were computed (Eq. (I.6)). The results are listed in Table II-2 and plotted against the interaction curve in Fig. II-4. It is easy to understand that the damage induced by a single ground motion when no scaling factor is applied is very small as compared to the $D_2^u - J_f$ interaction curve. The key point to this chapter is to conduct loading tests until fracture of the specimens, therefore scaling of the records is required in order to induce more damage. Furthermore, a single record is not strong enough to reach fracture, thus a loading sequence has to be established for each specimen.

Table II-2. Analytical results of preliminary analysis

No.	Ground motion		$_XD_2$ [-]	$_YD_2$ [-]	J_f [rad]	J_c [rad]
1	El Centro	EL	0.021	0.018	0.40	-0.24
2	JMA Sendai	JS	0.048	0.044	1.01	0.67
3	JMA Kobe	KB	0.033	0.030	1.21	0.63
4	Hachinohe	HC	0.024	0.029	0.51	-0.40

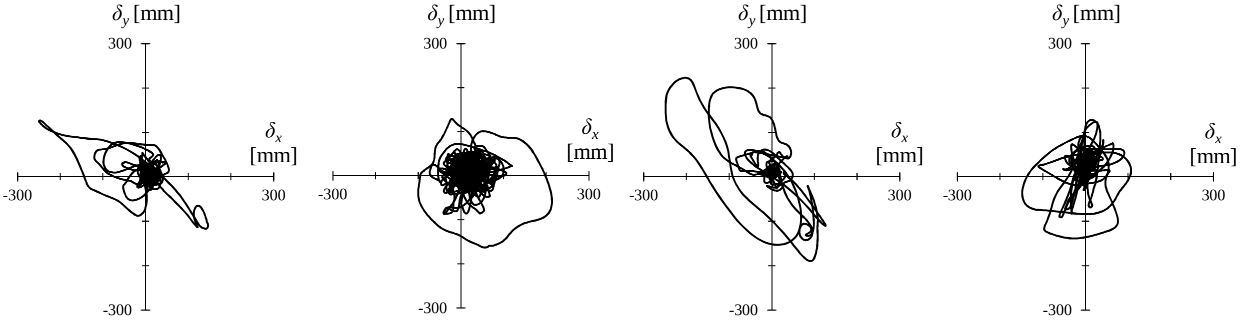

(a) El Centro (b) JMA Sendai (c) JMA Kobe (d) Hachinohe

Figure II-3. Bidirectional displacement orbits for preliminary analysis.

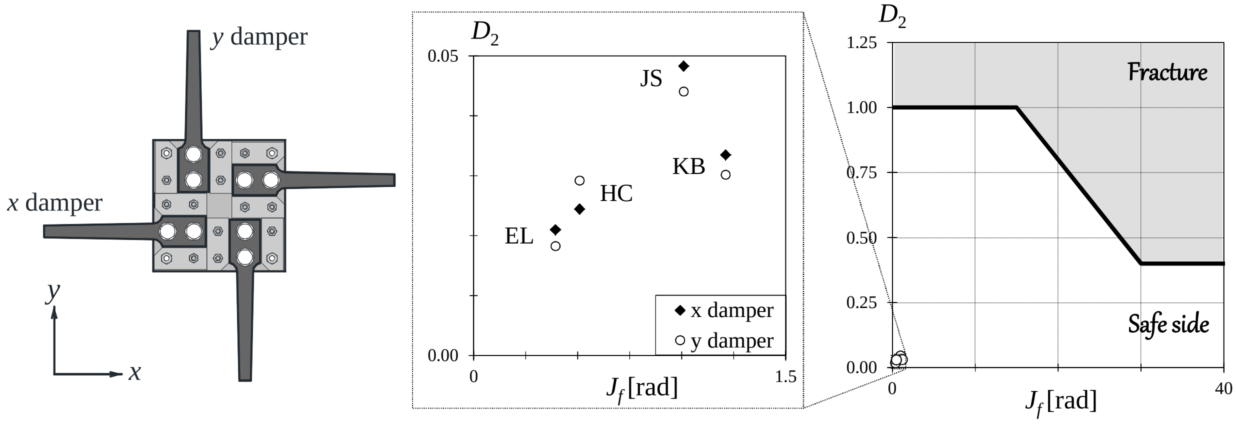

(a) Unit of 4 dampers (b) Location of (D_2, J_f) values obtained in the preliminary analysis

Figure II-4. Results of the preliminary analysis against the $D_2^u - J_f$ interaction curve.

II.2.4. Analytical results

In the previous section it was found that the damage of unscaled records is not enough to induce fracture of the specimens. Hence each ground motion was scaled such that the maximum displacement response $R_{\max}$ reaches 400(mm). The latter is defined as shown in Eq. (II.1), and the value of 400(mm) was established based on the most frequently encountered design value against seismic hazard level L2 [II.4].

$$R_{\max} = \max\left(\sqrt{\delta_x^2 + \delta_y^2}\right) \tag{II.1}$$

where δ_x, δ_y are the displacement response of the system along x, respectively y direction (Fig. II-3).

The results of the scaled ground motions are given in Table II-3, while the corresponding bidirectional displacement orbits are shown in Fig. II-5 where the dotted circle represents the limit of the maximum displacement $R_{\max}$ = 400(mm). It is worth mentioning that the Ishinomaki hospital record (Fig. II-5(e)) was not scaled up to reach 400(mm) because during the loading tests, the damage induced by the original wave was of interest.

By comparing the values of the parameters of interest listed in Table II-3, the following remarks can be made:

- The values of the bidirectional cumulative damage index D_2 are less than 0.100, which means that loading sequences consisting of several ground motions are needed to ensure that fracture of the specimen occurs.
- The largest damage index (0.100) was obtained for y damper (${}_YD_2$) subjected to Ishinomaki hospital record, in spite of the fact that this record has not been scaled up to reach the maximum displacement of 400(mm). This is explained by the fact that IH ground motion contains a high number of cycles in the plastic range, which leads to the accumulation of damage.
- The largest value of the sway-motion index J_f = 5.07(rad) was obtained for Agnews hospital record. This is explained by the complex shape of the bidirectional displacement orbit combined with many cycles of large amplitude (Fig. II-5(q)). On the opposite side of the spectrum lie the J_f values for orbits resembling a straight line (NTT Kobe – Fig. II-5(n); Port Island – Fig. II-5(k)).

For the reasons mentioned above, the seismic records that induce very little damage or have a displacement orbit similar to a straight line are excluded from the experimental plan. Hence 14 ground motions are employed to conduct the dynamic loading tests. These selected ground motions are discussed in the next section where they are grouped into loading protocols that aim at reaching fracture of the specimens.

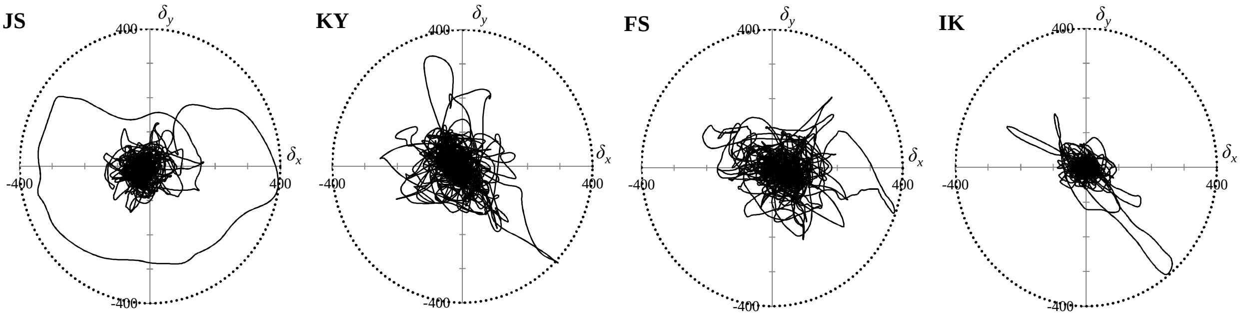

(a) JMA Sendai (b) K-net Koriyama (c) K-net Fukushima (d) K-net Iwaki

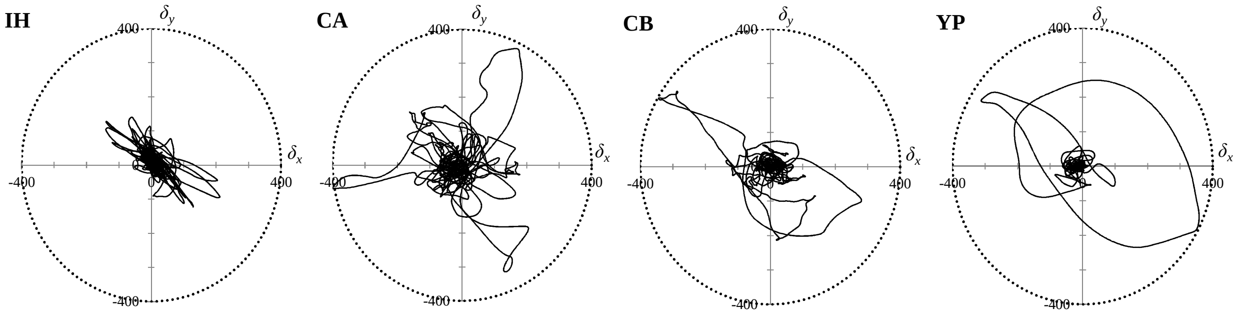

(e) Ishinomaki hos. (f) TCU078 (g) TCU129 (h) Yarimca

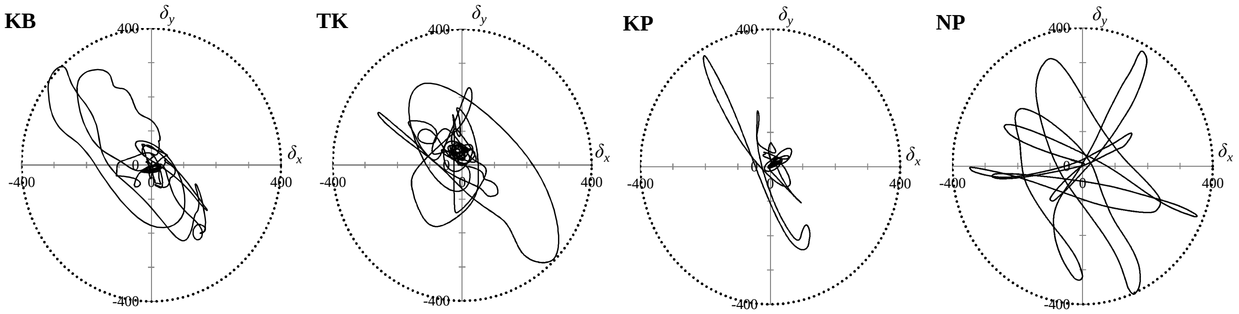

(i) JMA Kobe (j) Takatori (k) Port Island (l) Osaka NKP

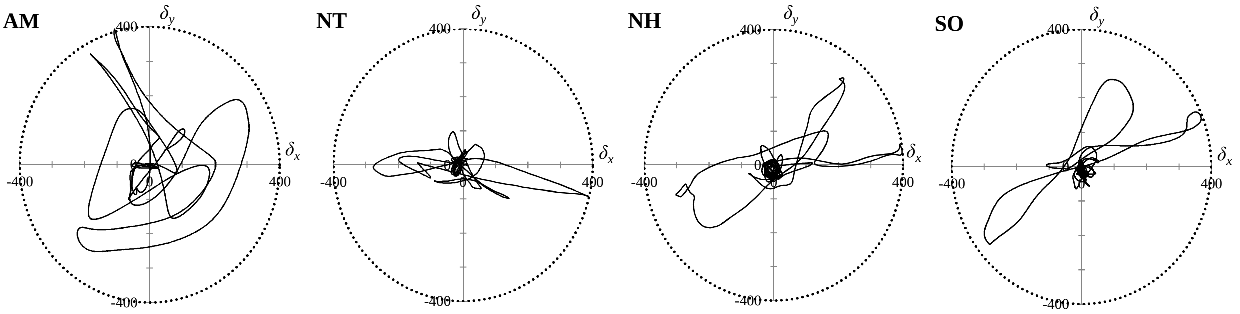

(m) Amagasaki (n) NTT Kobe (o) Newhall (p) Olive View

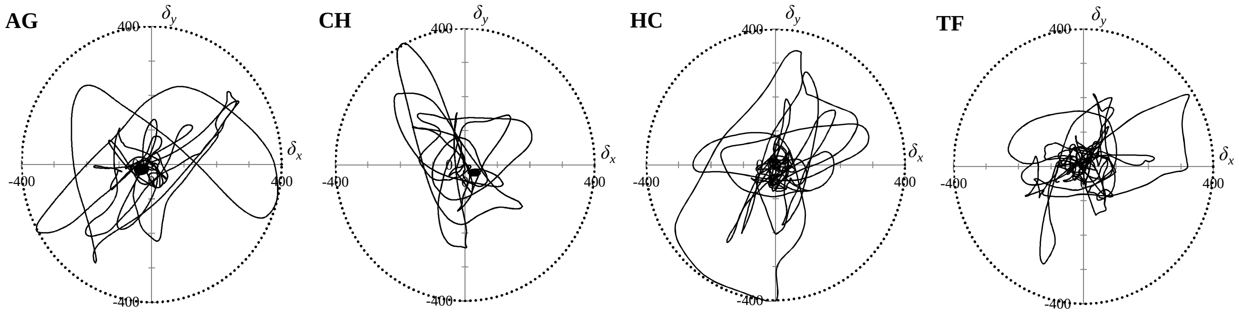

(q) Agnews hospital (r) Chihuahua (s) Hachinohe (t) Taft

Figure II-5. Bidirectional displacement orbits for experimental plan (1)

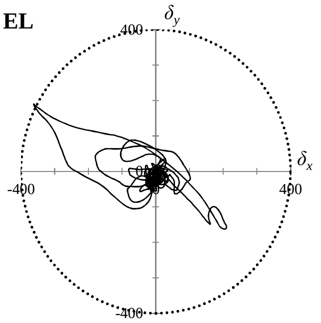

(u) El Centro

Figure II-5. Bidirectional displacement orbits for experimental plan (2).

Table II-3. Analytical results for experimental plan

No.	Ground motion		s_f	${}_XD_2^{(**)}$	${}_YD_2^{(**)}$	J_f	J_c
	Full name	Abv.	[-]	[-]	[-]	[rad]	[rad]
1	JMA Sendai	JS	1.55	0.044	0.055	4.09	− 3.78
2	K-net Koriyama	KY	3.20	0.097	0.108	2.82	− 0.47
3	K-net Fukushima	FS	3.80	0.065	0.084	3.37	− 1.02
4	K-net Iwaki	IK	1.25	0.039	0.042	0.75	+ 0.29
5	Ishinomaki hospital (*)	IH	-	0.086	0.100	1.24	− 0.65
6	TCU078	CA	2.60	0.041	0.059	2.37	+ 1.17
7	TCU129	CB	1.35	0.044	0.056	1.98	− 0.67
8	Yarimca	YP	0.57	0.037	0.042	3.36	+ 3.14
9	JMA Kobe	KB	1.23	0.048	0.044	2.45	− 1.24
10	JR Takatori	TK	0.65	0.063	0.058	2.75	− 2.12
11	Port Island	KP	0.60	0.004	0.012	0.60	− 0.23
12	Osaka Nanko-Port	NP	2.20	0.089	0.096	2.87	− 1.33
13	Amagasaki	AM	1.20	0.072	0.069	3.52	+ 1.32
14	NTT Kobe	NT	0.75	0.019	0.032	0.49	+ 0.27
15	Newhall	NH	0.85	0.029	0.036	1.31	+ 0.49
16	Olive View	SO	0.80	0.031	0.037	1.12	+ 0.33
17	Agnews hospital	AG	2.60	0.091	0.092	5.07	+ 5.07
18	Chihuahua	CH	2.39	0.056	0.064	2.26	+ 1.50
19	Hachinohe	HC	1.90	0.063	0.059	2.94	+ 2.49
20	Taft	TF	4.00	0.069	0.062	2.68	− 0.97
21	El Centro	EL	1.30	0.022	0.013	1.04	+ 0.67

(*) No scaling factor is applied.

(**) Subscripts X, Y refer to the damper for which the damage index is computed (Fig. II-4(a)).

In Fig. II-6 the obtained analytical results listed in Table II-3 are plotted against the $D_2^u - J_f$ interaction curve. As noted above, the values are still significantly smaller than the fracture limit, therefore several bidirectional displacement orbits are adopted to load a specimen, as explained in the next section. Moreover, it can be observed that most of the plots are situated inside the triangle defined by the lines $J_f / D_2 = 15$, $J_f / D_2 = 75$, respectively the interaction curve, therefore this area is targeted when establishing the loading protocols.

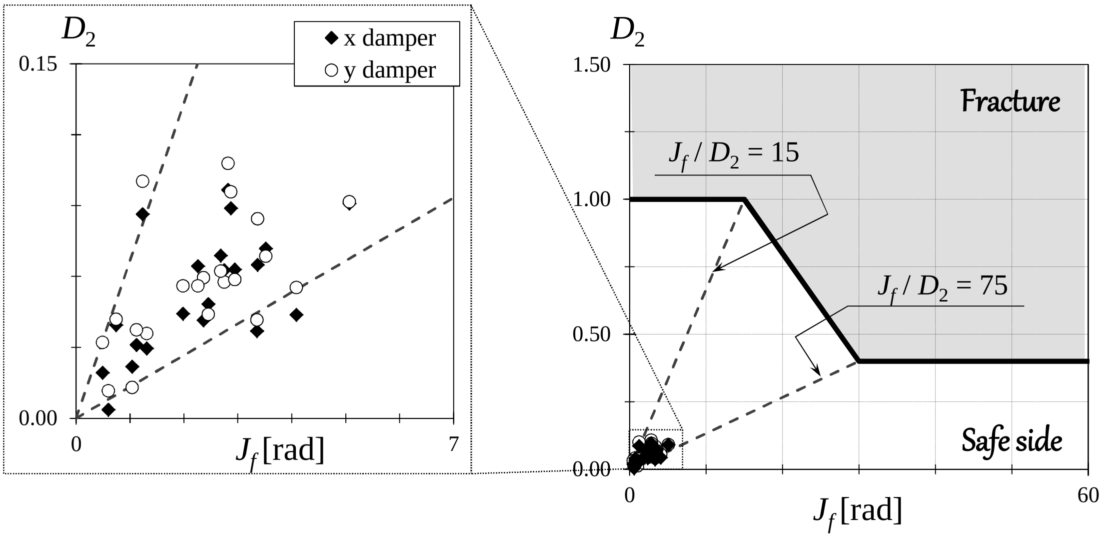

Figure II-6. Analytical results against the $D_2^u - J_f$ interaction curve.

II.2.5. Loading protocols

In establishing the loading protocols for the dynamic test, the following aspects were considered:

1. Select the ground motions with large values for D_2 and J_f.
2. Evaluate the fatigue behavior of the dampers under various seismic motions.
3. Assess whether the limit value for the contact index (J_c = 26.8(rad)) proposed by Kishiki *et al.* (2012) is valid for predicting the contact occurrence when the dampers are subjected to realistic loading histories.
4. Investigate the behavior under a loading sequence that approaches the lines $J_f / D_2 = 15$, respectively $J_f / D_2 = 75$ to verify the accuracy of the interaction curve at its discontinuity points (Fig. II-6).

14 of the investigated ground motions were selected and grouped into 4 different loading protocols, each having a specific objective, as listed in Table II-4. Note that a loading protocol approaching the line $J_f / D_2 = 15$ was found to require too many loading cycles, hence making it difficult to be carried out. For this reason, no loading sequence with this objective was proposed. Moreover, since there are 4 specimens with 4 elements, 4 corresponding loading protocols were

established. The rest of the specimens (2 units of 8 elements) were loaded using the same protocols, as discussed in Section II.3.

Considering that a specimen is subjected to n bidirectional displacement histories, the total value of the cumulative damage index D_2 for each damper is obtained by adding up those corresponding to each loading history (Eq. (II.2)). The total values of the sway-motion index J_f and contact index J_c are computed in the same way (Eq. (II.3), (II.4)):

$$D_2 = \sum_{i=1}^{n} D_{2,i} \tag{II.2}$$

$$J_f = \sum_{i=1}^{n} J_{f,i} \tag{II.3}$$

$$J_c = \sum_{i=1}^{n} J_{c,i} \tag{II.4}$$

where i is the number of the current displacement history

n is the total number of displacement histories conducted in a loading protocol

$D_{2,i}$ is the bidirectional cumulative damage index of x damper (or y damper) for i th displacement history

$J_{f,i}$, $J_{c,i}$ are the sway-motion index, respectively contact index for i th displacement history.

In addition, it is worth noting that because of the limitations of the experimental facility (maximum cumulative displacement of the loading history 8.0(m)), some of the records had to be either trimmed or divided into two parts.

Table II-4. Summary of loading protocols

Denomination	Displacement orbits	Objective
LP1	(TK→HC→MX)x3	Evaluate the fatigue behavior when subjected to repeated changes in the direction of the maximum displacement; similar amount of damage for each orbit
LP2	AGx5	Evaluate the fatigue behavior when subjected to an orbit with large values D_2 and J_f
LP3	JSx8→YPx1	Evaluate the accuracy of the limit value of J_c and the fatigue behavior at $J_f / D_2 = 75$
LP4	IH→SO→NH→CA→NP→ MX→CB→IK→FS→AG	Evaluate the fatigue behavior when subjected to various seismic records

Loading protocol LP1

The objective of loading protocol *LP1* is to assess the behavior of U-shaped steel dampers subjected to bidirectional histories where the direction of the maximum displacement changes (Fig. II-7). To this purpose, a loading sequence was established consisting of Takatori, Hachinohe and Chihuahua displacement histories taken in this specific order. These three loading histories are repeated as a set until the damage interaction curve is intersected (Fig. II-8). According to the estimated values of the cumulative damage indices for *x* and *y* dampers and to the corresponding values of the sway-motion index, the dampers are expected to fracture during the 4th loading of Takatori orbit (Set 4).

Another noticeable fact is that the damage of each damper for the three selected orbits is almost the same, which means that the lines described by the damage indices and sway-motion index for both dampers are almost straight lines.

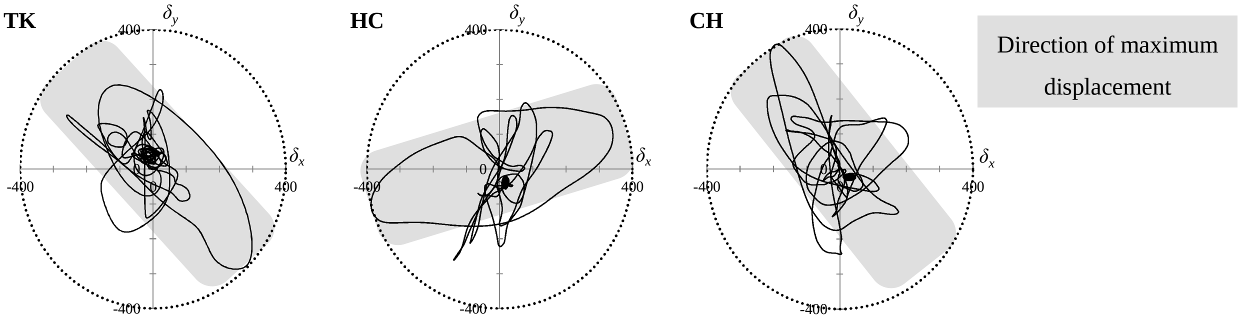

(a) Takatori (b) Hachinohe (c) Chihuahua

Figure II-7. Bidirectional displacement histories for loading protocol *LP1*.

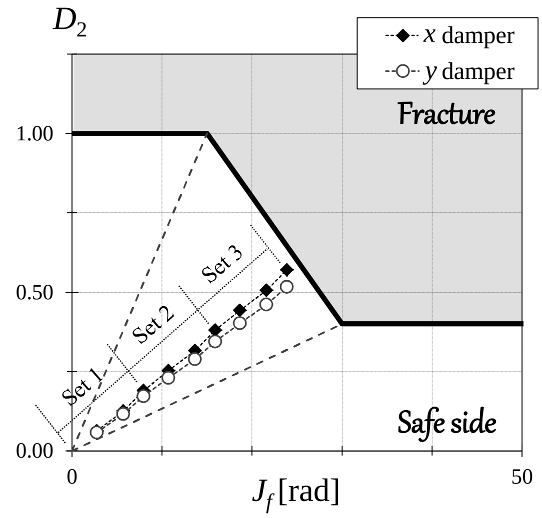

Figure II-8. (D_2, J_f) values for loading protocol *LP1* against the interaction curve.

Loading protocol LP2

Among the considered records, the displacement response of Agnews hospital (Loma Prieta earthquake) reaches the interaction curve in the least number of loadings. This is due to the fact that both D_2 and J_f have large values. Moreover, it can be noticed that due to the fact that large displacement amplitudes occur in almost every direction, the damage indices for *x* and *y* dampers are nearly the same (Fig. II-9(b)).

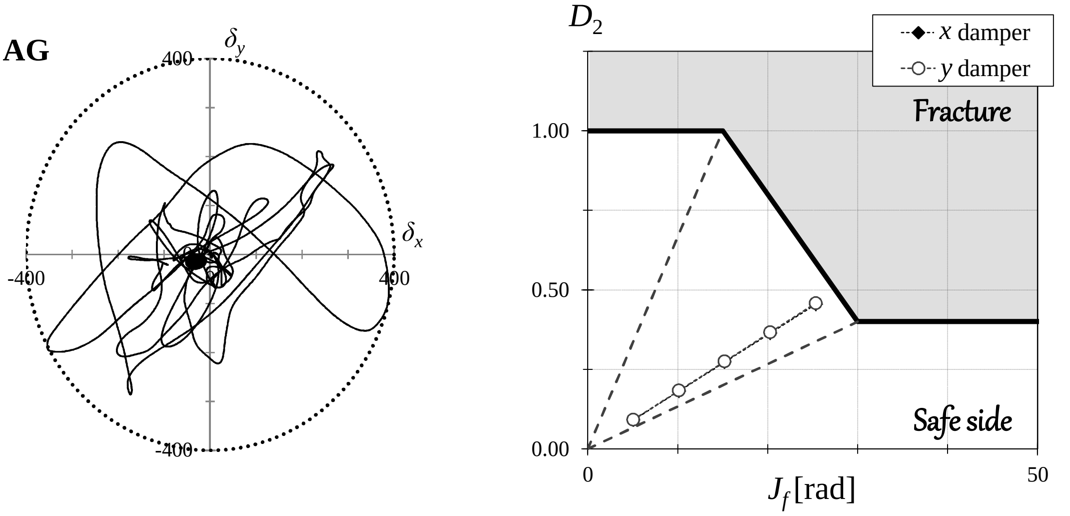

(a) Displacement history (b) (D_2, J_f) values against the interaction curve

Figure II-9. Loading protocol *LP2*.

Loading protocol LP3

Loading protocol *LP3* was established mainly to verify the accuracy of the limit value of the contact index J_c (26.8(rad)) proposed by Kishiki *el al.* (2012). The largest value of J_c index was obtained for JMA Sendai (JS) seismic record, which was, thus, engaged in this loading protocol. It was estimated that that during the 8th loading of JMA Sendai displacement orbit contact will occur. By carefully analyzing the displacement response of JMA Sendai record it was found that the maximum amplitude cycle has a single loading sense (clockwise, Fig. II-10). The second largest value of J_c was obtained for Yarimca (YP), with the noticeable exception that the largest loading cycle occurs in the counterclockwise loading sense (Fig. II-10). Hence, based on the observations made in [II.2] that the out-of-plane deformations are reversed when loading in reverse sense is conducted, Yarimca orbit will be loaded after contact occurs and until the interaction curve is intersected (Fig. II-11).

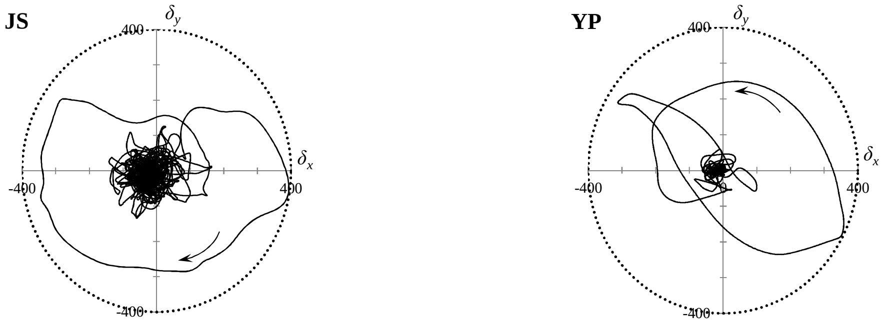

Figure II-10. Bidirectional displacement histories for loading protocol *LP3*.

Another objective of loading protocol *LP3* is to assess the validity of the interaction curve at the intersection with the straight line J_f / D_2 = 75. As it can be noticed from Fig. II-11, the latter almost coincides with the damage of *y* damper.

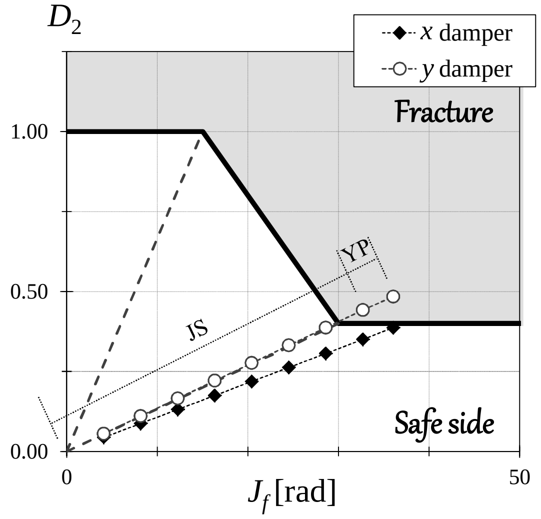

Figure II-11. (D_2, J_f) values for loading protocol *LP3* against the interaction curve.

Loading protocol LP4

The main objective of loading protocol *LP4* is to assess the behavior of U-shaped steel dampers when subjected to different seismic records. 10 displacement histories were selected (Ishinomaki hospital, Olive View, Newhall, TCU078, Osaka NP, Chihuahua, TCU129, Iwaki, Fukushima, and Agnews hospital) to this purpose and arranged in such an order that the damage line is roughly situated in the middle of the straight lines J_f / D_2 = 15, respectively J_f / D_2 = 75 (Fig. II-12). The Ishinomaki hospital and Fukushima displacements had to be divided into 2 parts because the cumulative displacement was larger than the testing facility could accommodate in a single loading (8.0(m)) as shown in Fig. II-13.

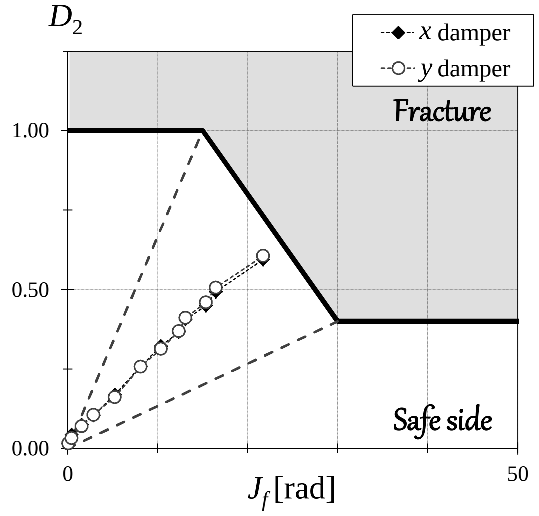

Figure II-12. (D_2, J_f) values for loading protocol *LP4* against the interaction curve.

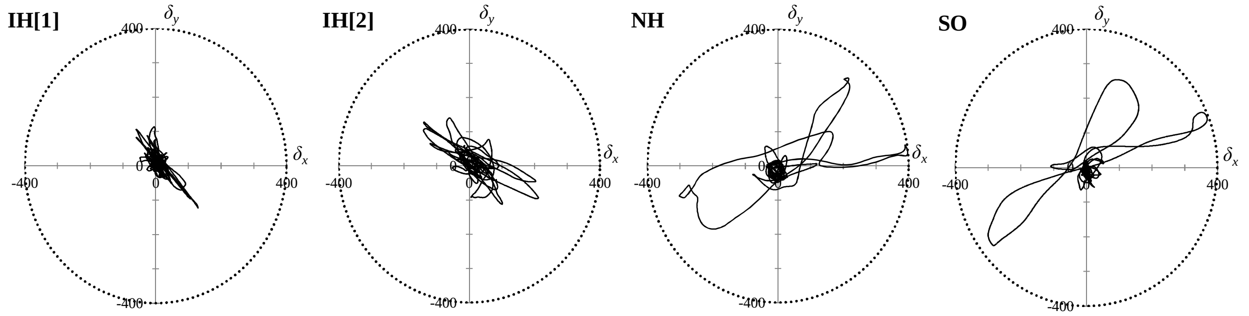

(a) Ishinomaki hospital (b) Newhall (c) Olive View

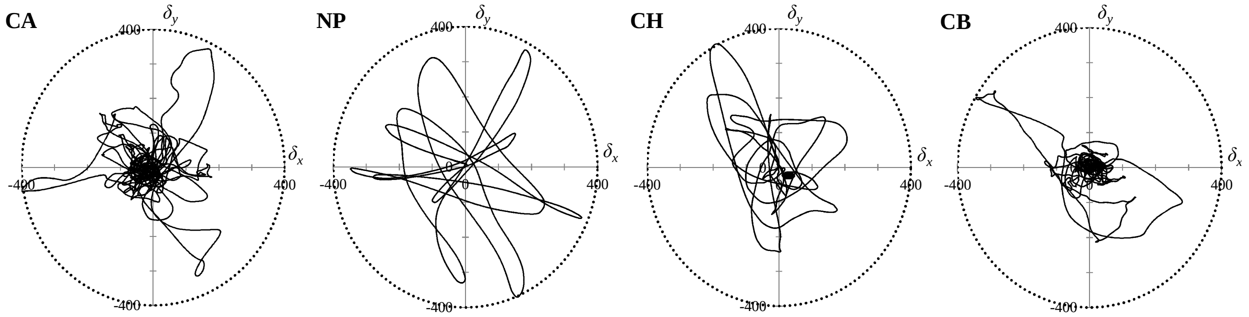

(d) TCU078 (e) Osaka NKP (f) Chihuahua (g) TCU129

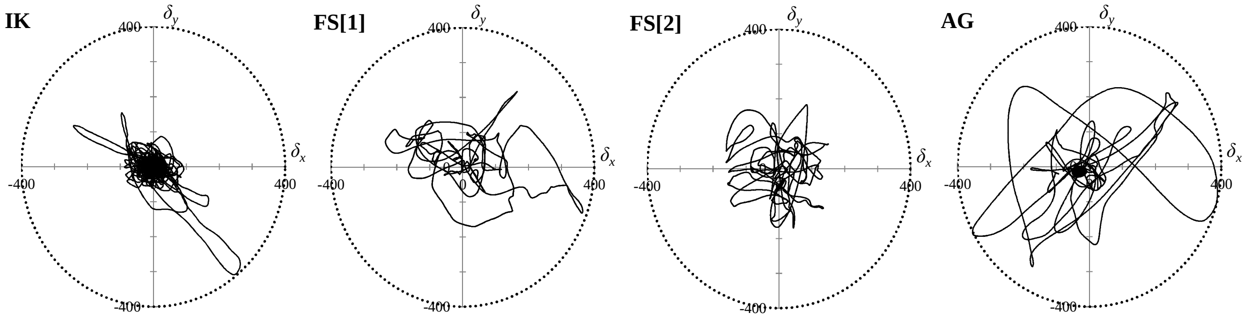

(h) Knet-Iwaki (i) K-net Fukushima (k) Agnews hospital

Figure II-13. Bidirectional displacement histories for loading protocol *LP4*.

Using the established loading protocols, dynamic loadings tests are conducted in University of California San Diego on full-scale units of 4, respectively 8 UD50 dampers.

II.3. Bidirectional dynamic loading tests

In this section details about the specimens, setup and results of the dynamic loading tests conducted at University of California San Diego (UCSD) are described. All the specimens have been loaded dynamically using the SRMD (Seismic Response Modification Device) testing facility and the loading protocols established in the previous section.

II.3.1. Specimens and loading facilities

The specimens in UCSD test consist of 4 units of 4 UD50 elements and 2 units of 8 UD50 elements (Fig. II-14) whose geometric characteristics as listed in Table II-5. Each damper element is named according to its position with respect of the displacement history (δ_x, δ_y) as shown in Fig. II-14(c). Loading is displacement-controlled, meaning that the specimen is fixed at its upper part to the steel reaction beam and at its bottom part displacement is imposed by moving the loading table (Fig. II-15).

Each unit was loaded as shown in Table II-6. All the input orbits were loaded dynamically, with the exception of the second set of (TK, HC, CH) conducted for unit U1 which was loaded quasi-statically.

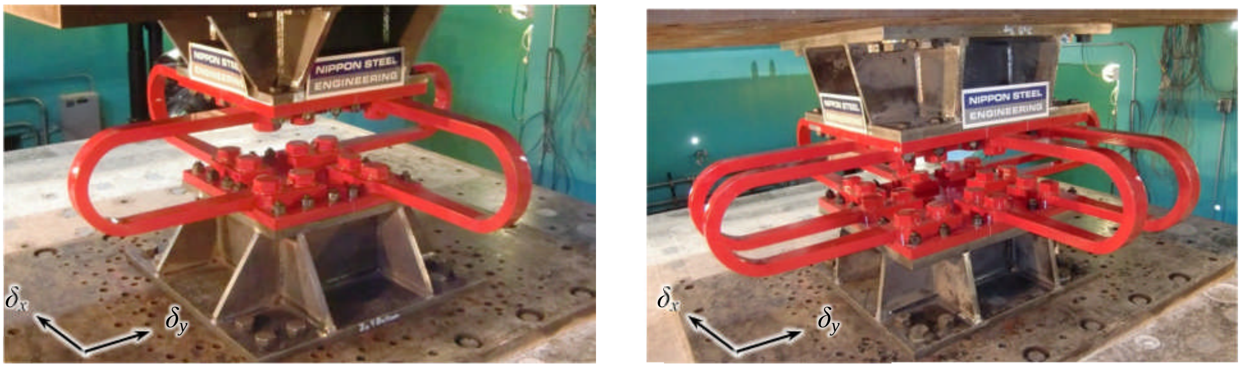

(a) Unit of 4 UD50 dampers (b) Unit of 8 UD50 dampers

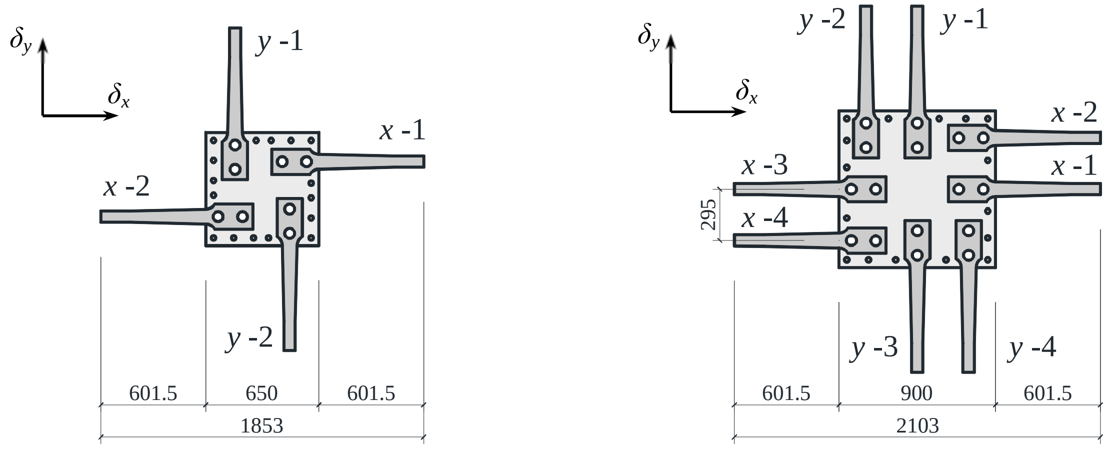

(c) Notation of damper elements with respect to the axes of the displacement histories

Figure II-14. Specimens tested in UCSD dynamic test.

Table II-5. Geometric characteristics of a UD50 damper

L_t	L_f	h	w	t
[mm]	[mm]	[mm]	[mm]	[mm]
882	602	335	87	40

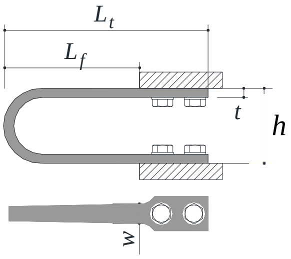

In the following paragraphs, some basic information about the SRMD testing facility and the setup of UCSD test are presented. Fig. II-15 shows the basic functioning concept of the SRMD testing facility. It consists of a prestressed concrete box and a loading table, connected by 4 horizontal actuators. The loading table slides on an oil-film over 4 vertical hydrostatic low friction hydraulic bearings and is stabilized by 4 outrigger arms which also have low friction sliding actuators at their tops. A removable steel cross beam and the prestressed concrete box form a self-reacting vertical frame, such that the 4 vertical hydrostatic bearings beneath the loading table can apply the necessary forces. The specimen is attached to the loading table and to the underside of the fixed cross beam above. Seismic motion is simulated as the 4 horizontal actuators move the loading table. The longitudinal direction represents the *x* axis, while the transversal one is the *y* axis of the input displacement.

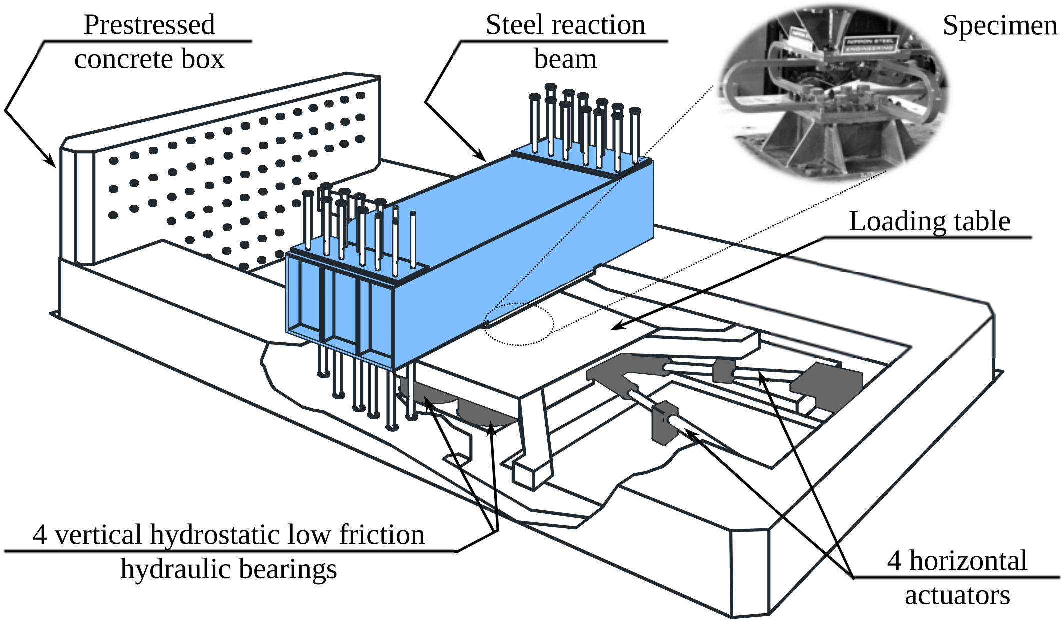

Figure II-15. SRMD testing facility (UCSD).

Each of the 4 horizontal actuators is equipped with a load cell to measure its axial force. Knowing each of these 4 forces, the net horizontal force in the loading table can be determined. However, not all of the loading table force goes into the specimen above, some goes into the inertia of the loading table (which weights 72.6 tones) and some goes into friction. The loading table inertia can be measured with accelerometers and accounted for, but the friction forces are not as straight forward and there is some question as to how well they can be predicted. This directly impacts how accurate the net force across the test bearing specimen can be measured and thus how its performance is characterized. For this reason, an independent, objective load cell is required between the upper portion of the test bearing and the fixed cross-beam. Since this load cell will be subjected to neither friction, nor inertia effects, the force it measures should be the true force across the test bearing. This is not a typical load cell, however. Whereas most load cells are subjected to a single axial force, this one experiences forces in all 6 degrees of freedom. It is extremely difficult to build a load cell that can measure each individual force without experiencing cross-coupling effects from the other five. Essentially, the load cell cannot tell which force component is the cause of which strain readings. Although there are 6 different force components (3 moments and 3 forces) on the load cell, the primary force of interest is the horizontal shear force in the horizontal direction. In fact, a load cell that measures this one force alone is acceptable. Even so, the load cell must still be strong enough to resist the other 5 (very large) components. More importantly, it must be able to distinguish those forces and read only the one of interest.

II.3.2. Test results

The purpose of the present chapter is to assess whether the damage evaluation method, as well as the interaction curve delimiting the safe zone from fracture zone proposed by Kishiki *et al.* (2012) are suitable to evaluate the damage of U-shaped steel dampers subjected to biaxial seismic excitation. Thus, the most important set of results obtained by conducting the dynamic tests are the values of the bidirectional cumulative damage index, respectively those of the sway-motion index at the time when the specimens fracture. Secondly, the contact occurrence is investigated and the fidelity of the contact index is assessed. Lastly, the characteristics of the force – deformation relations are investigated to understand whether the dampers are reliable under strong bidirectional loading.

It is important to notice that all the specimens fractured after intersecting the interaction curve, which means that they met their minimum required inelastic deformation capacity. The displacement histories conducted after meeting the interaction curve can be found in Table II-6 under the column named “Additional loading”. Moreover, the latter are differentiated from the designed loading protocols as shown in Fig. II-16.

All of the tested specimens have acquired large deformations before fracture, their initial U-shape being significantly distorted towards the end of loading. Generally, during the first (2 or 3) cycles, the plastic deformations are relatively evenly distributed along the length of the U-shaped steel dampers, after which load-concentration zones appear. Fracture is initiated later for specimens subjected to various loading histories (U4, Fig. II-16(d)) because the plastic deformations are distributed along their entire length. On the contrary, for specimens under a single loading history (U2), the plastic deformations are concentrated at certain locations, leading more rapidly to fracture (Fig. II-16(b)).

Table II-6. Displacement histories conducted during the dynamic test

Unit no.	Specimen type	Designed loading protocol		Additional loading	Observations (*)
U1	4UD50	*LP1*:	(TK→HC→CH)x3	(TK→HC→ CH)x2	*x*-1, *y*-1 fractured during CH4, *x*-2 during TK5, *y*-2 in CH5;
U2	4UD50	*LP2*:	AGx5	AGx2	*y*-1, *y*-2 fractured during AG6, *x*-1, *x*-2 during AG7;
U3	4UD50	*LP3*:	JSx8→YPx1	YPx3	Slight contact during JS8; when loading YP, deformation starts to reverse; *x*-1 fractured during YP2, *x*-2 & *y*-1 in YP3, *y*-2 in YP4;
U4	4UD50	*LP4*:	IH→SO→NH→CA →NP→MX→CB→ IK→FS→AG	(NP→AG)x4 → NP	Little damage after the designed loading protocol; *y*-1 fractured in NP4, *y*-2 in AG4, *x*-1 & *x*-2 in NP5;
U5 (**)	8UD50	*LP1*:	(TK→HC→MX)x3	TK→HC→ CH→TK	*x*-1 fractured during CH4, the rest of 7 U-dampers fractured during TK5;
U6	8UD50	*LP3*:	JSx5 (***) → YPx4	YPx8	1st contact during JS5 → switch to YP; *x*-1 fractured during YP9, *y*-1 in YP10, *y*-2 in YP11, *x*-2 in YP12; 2nd contact during YP12 → stopped loading;

(*) *x*-1, *y*-1, *x*-2, *y*-2 represent the position of the dampers with respect to the displacement history (Fig. II-14(c)).

(**) Before conducting loading protocol *LP1*, 50 cycles of circular loading with radius R = 73(mm) have been conducted (D_2 = 0.150, J_f = 3.37(rad)).

(***) Only 5 out of 8 loadings of JMA Sendai (JS) could be conducted before contact.

The problem of contact occurrence was carefully monitored during the loading tests. Specimens U3 (4 elements) and U6 (8 elements) loaded using JMA Sendai made slight contact after having acquired extreme residual out-of-plane deformations. For specimen U3, slight contact between some damper elements and the loading jigs occurred during the 8th loading (Fig. II-16), when the contact index J_c was situated between -26.16 and -29.90(rad). For specimen U6, because two elements are placed on each side, contact occurred earlier than the limit value proposed by Kishiki *et al.* (2012), at J_c between -14.95 and -18.69(rad). Moreover, when loading was switched to Yarimca orbit, contact occurred a second time (J_c between 34.54 and 37.68(rad)). The behavior of these specimens is similar to that exhibited by the specimens tested by Kishiki *et al.* (2012) using a circular pattern. This finding is explained by the following:

1. The maximum displacement amplitude cycle of JMA Sendai history (JS) has a particularly rounded shape, similar to the circular loading histories in [II.2].
2. A considerably large number of cycles are conducted until contact.

It can thus be stated that contact becomes imminent only under extreme conditions that are not likely to occur during a single seismic event. Moreover, as discussed in the next section, the force – deformation relations are not significantly affected by this phenomenon. Therefore, contact occurrence is not thought to represent a real problem for practical use, as long as the dampers are not placed on a wide foundation block that obstructs their up-and-down movement.

In addition, it is worth mentioning that after contact occurred, Yarimca (YP) displacement orbit was loaded for both specimens U3 and U6, and – because the displacement cycles with the largest amplitude have an opposite loading sense (counterclockwise) – the out-of-plane deformations were reversed to some extent.

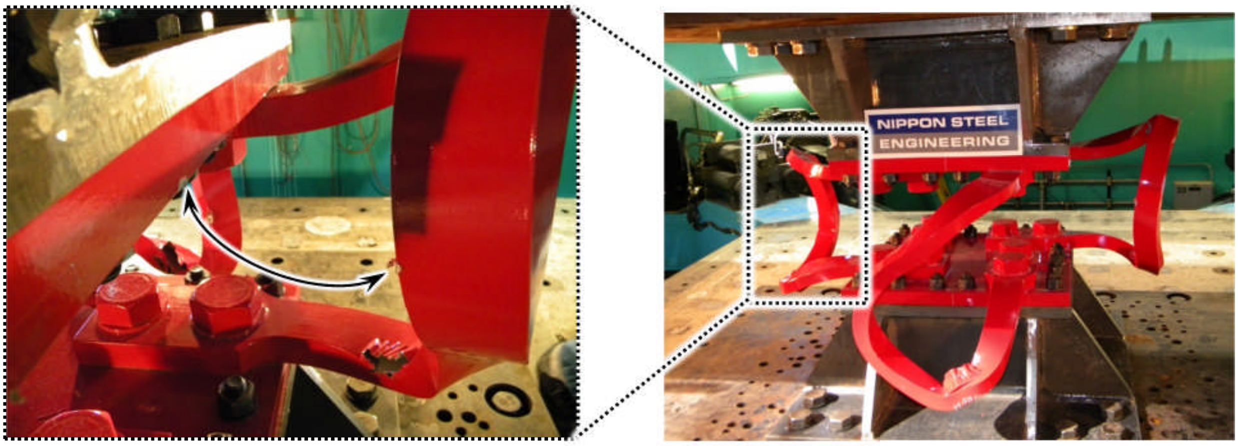

(a) Slight contact with the jigs (b) Residual out-of-plane deformations

Figure II-16. Contact occurrence for specimen U3 (during 8th loading of JMA Sendai – JS).

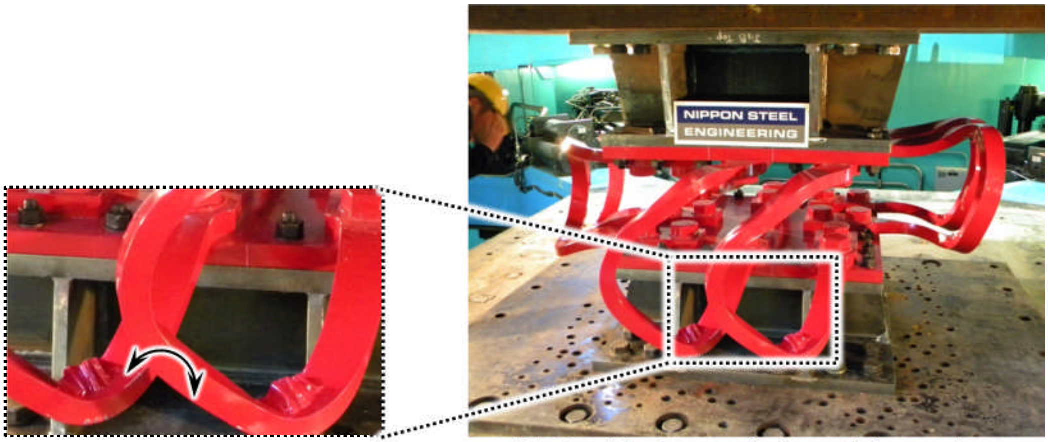

(a) Slight contact between dampers (b) Residual out-of-plane deformations

Figure II-17. Contact occurrence for specimen U6 (during 5th loading of JMA Sendai – JS).

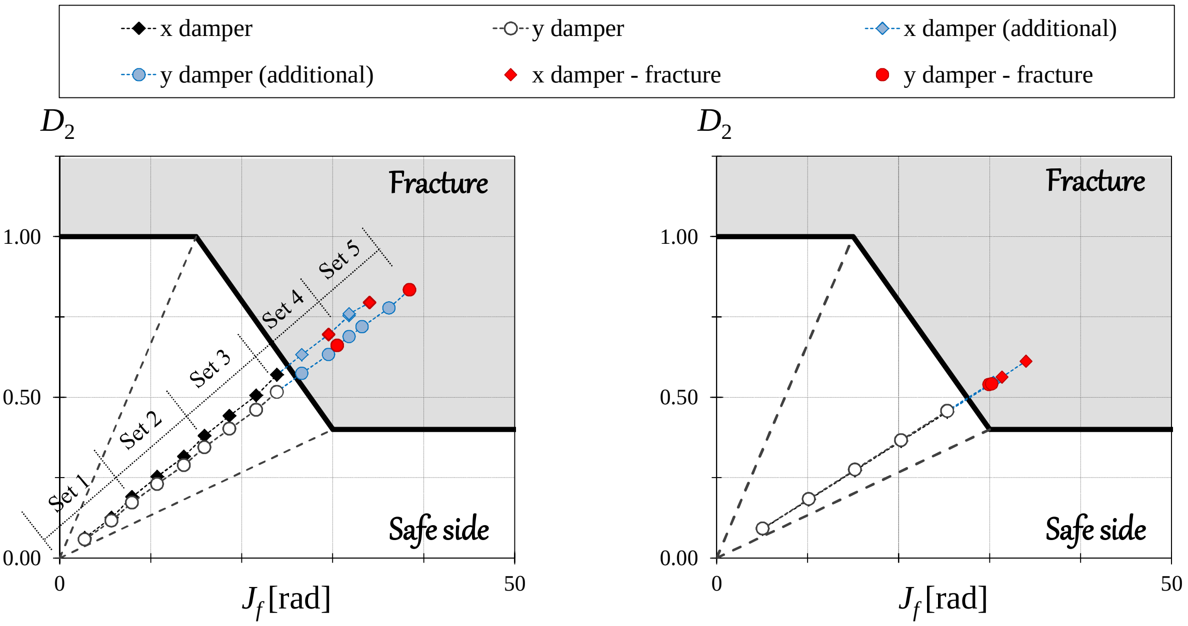

(a) Specimen U1 (*LP1*) (b) Specimen U2 (*LP2*)

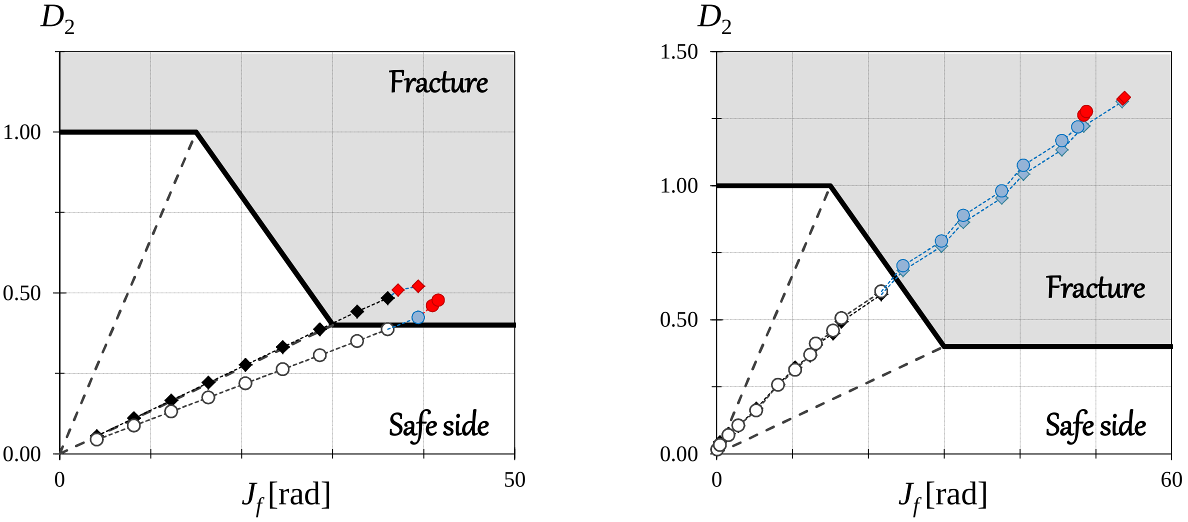

(c) Specimen U3 (*LP3*) (d) Specimen U4 (*LP4*)

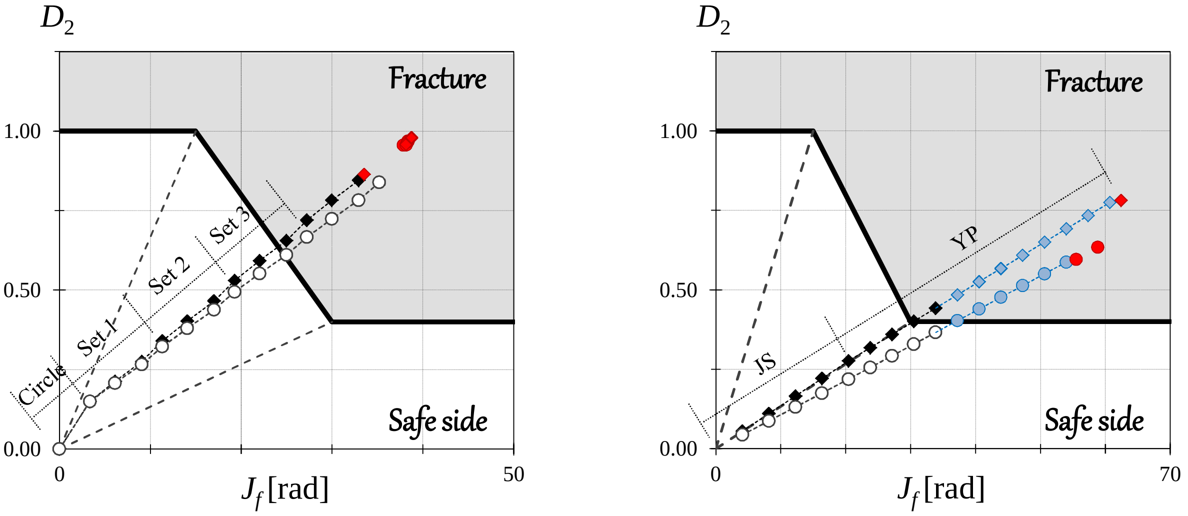

(e) Specimen U5 (*LP1*) (f) Specimen U6 (*LP3*)

Figure II-18. Values of (D_2, J_f) for the complete loading sequence of each specimen (Table II-6).

Values of D_2 and J_f at fracture

First, it is important to note that even if loaded the same, not all elements of a unit fracture simultaneously; hence, they will have slightly different values for D_2 and J_f, as listed in Table II-7.

The D_2 and J_f values at fracture for all elements are plotted in Fig. II-19 against the interaction curve. All points are situated above the interaction curve, showing that the latter can be safely adopted because it represents the upper bound of the cumulative damage a U-shaped damper under seismic excitation can suffer without reaching fracture. Moreover, as the majority of the elements fracture at D_2 values lower than 1.0 and to the right of J_f = 30(rad) —the point after which D_2^u is reduced to 0.4—it can be stated that the test results confirm the reduction of the cyclic deformation capacity caused by a complex swaying motion between the upper and the lower jig. Furthermore, J_f is found to be a suitable index to quantify and express said reduction of the low-cyclic deformation capacity when plotted against the cumulative damage index D_2.

Table II-7. Values of D_2 and J_f at fracture of specimens

Specimen	*x*-1		*x*-2		*y*-1		*y*-2	
	J_f [rad]	D_2	J_f [rad]	D_2	J_f [rad]	D_2	J_f [rad]	D_2
U1	38.47	0.52	42.94	0.59	40.75	0.44	40.75	0.44
U2	35.30	0.62	32.39	0.58	31.25	0.55	30.91	0.54
U3	34.84	0.74	32.52	0.70	40.69	0.96	31.13	0.73
U4	55.48	1.42	55.23	1.41	43.90	1.11	50.26	1.26
U5	51.86	0.65	62.42	0.78	55.52	0.60	58.84	0.63
U6	38.73	0.98	38.29	0.97	37.85	1.04	38.17	1.04
	x-3		*x*-4		*y*-3		*y*-4	
	34.26	0.89	38.13	0.96	38.34	1.05	38.35	1.05

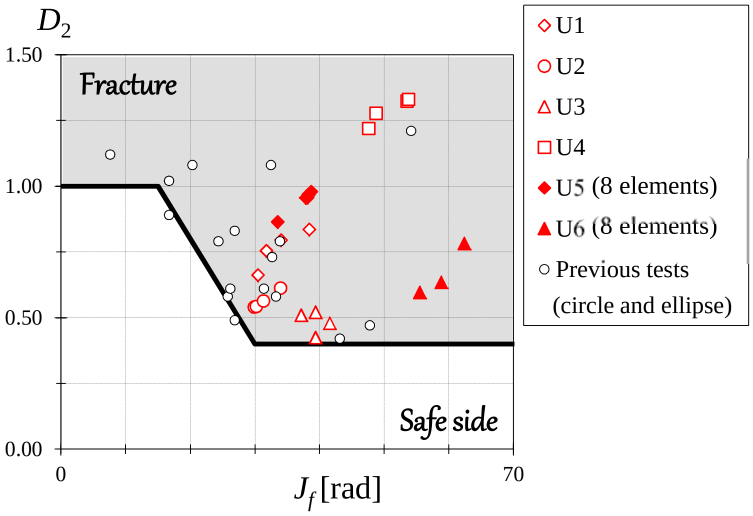

Figure II-19. Values of D_2 and J_f at fracture of specimens in the dynamic test (red) and previous test results [II.2].

Force – deformation relations

The energy dissipation capacity of U-shaped dampers and their stable hysteretic behavior under uniaxial loading have been confirmed by previous experimental studies on single elements and on sets of 2 elements placed in orthogonal directions [II.1][II.3]. However, it is essential to verify whether these statements still hold true for the case of seismic excitations when the dampers suffer complex deformations otherwise not encountered in uniaxial loading.

In Fig. II-20 the force – deformation relations for the first, third and fifth loadings of each displacement history of specimen U1 are shown. The red line corresponds to the last loading set (TK5, HC5, MX5) when the dampers fractured (starting with TK5). The fact that specimen U1 was loaded using 3 displacement histories makes it slightly more difficult to notice, but the dampers had stable behavior until the fracture of the first element. This fact is considerably easier to understand by from Fig. II-21 where the hysteretic curves of specimen U2 are plotted, due to the fact that the same displacement orbit was employed (Agnews hospital – AG). The first, third, fifth, sixth, respectively seventh loadings are shown. A slight decrease in the maximum shear force is observed going from the 1st loading to the 5th; in the 7th, the force decreases dramatically because 2 dampers fractured in the previous cycle. The shape of the hysteretic loops, however, remains almost the same until the fracture of the first element at the beginning of the 6th cycle, which confirms that U-shaped steel dampers have stable behavior even if subjected to severe seismic loading.

In addition, the effect of the contact occurrence between the damper elements and the loading jigs on the force – deformation relations is investigated next. To this purpose, the hysteresis curves of the first, fourth, seventh and eighth loading of JMA Sendai (JS), respectively the first, second and third loading of Yarimca (YP) for specimen U3 are shown in Fig. II-22. The contact occurred during the eighth loading of JS and, as it can be observed from Fig II-22(b) and (c), the hysteretic curves corresponding to JS8 are almost the same with those obtained in the previous loading (JS7). Therefore it can be stated that even if slight contact occurs between the dampers and the jigs, it will not affect the energy dissipation capacity of the former. Moreover, by comparing Fig. II-22 to Fig. II-20 and Fig. II-21 it can be observed that the forces on both directions are greater than those obtained at the approximately same values of the displacement for specimens U1 and U2.

The stable behavior of U-shaped steel dampers under various bidirectional displacement orbits is also confirmed by the results obtained for specimen U4 which was loaded with 11 different histories. To demonstrate this, only the additional cycles of Osaka Nanko-Port and Agnews hospital are shown in Fig. II- 23, while the rest of the force – deformation relations are given in Annex A. It can be observed that the shape of the hysteresis curves for Agnews hospital displacement history (Fig. II-23(b)) is similar to that obtained for specimen U2, even if specimen U4 was subjected to other 9 different loadings. However, the maximum force in each cycle is indeed smaller than the values obtained for specimen U2.

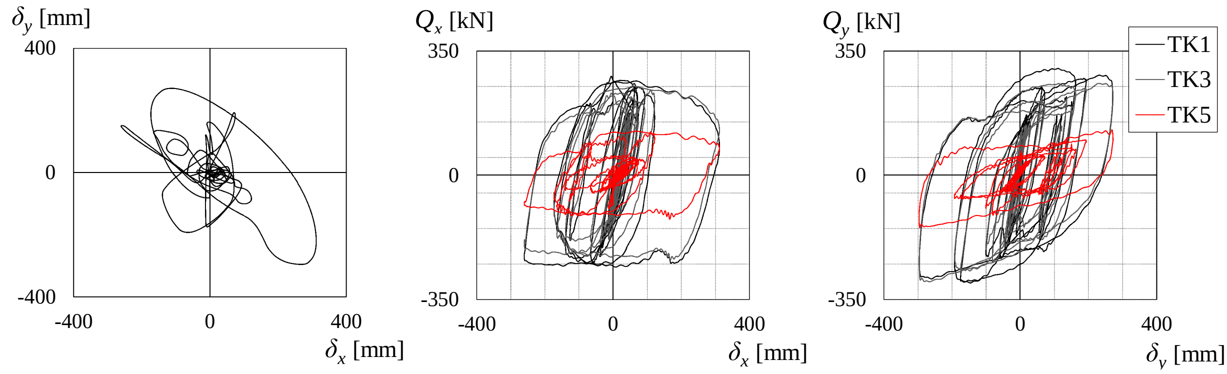

(a) Takatori orbit (b) Hysteresis curves on *x* (c) Hysteresis curves on *y*

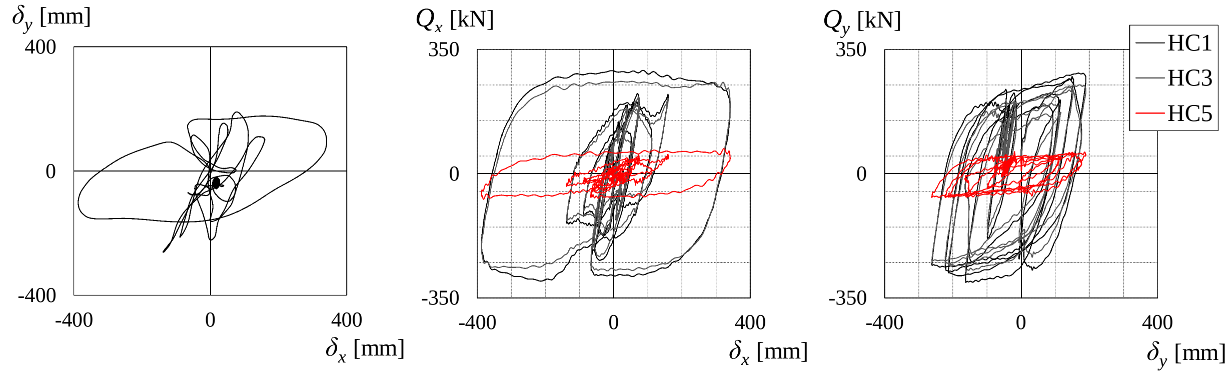

(d) Hachinohe orbit (e) Hysteresis curves on *x* (f) Hysteresis curves on *y*

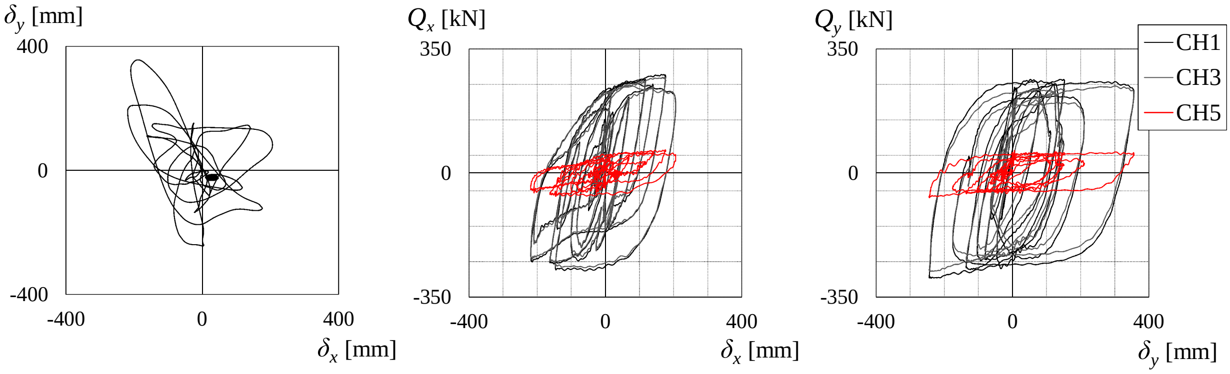

(g) Chihuahua orbit (h) Hysteresis curves on *x* (i) Hysteresis curves on *y*

Figure II-20. Examples of force – deformation relations of specimen U1 (1st, 3rd and 5th loadings of each displacement history).

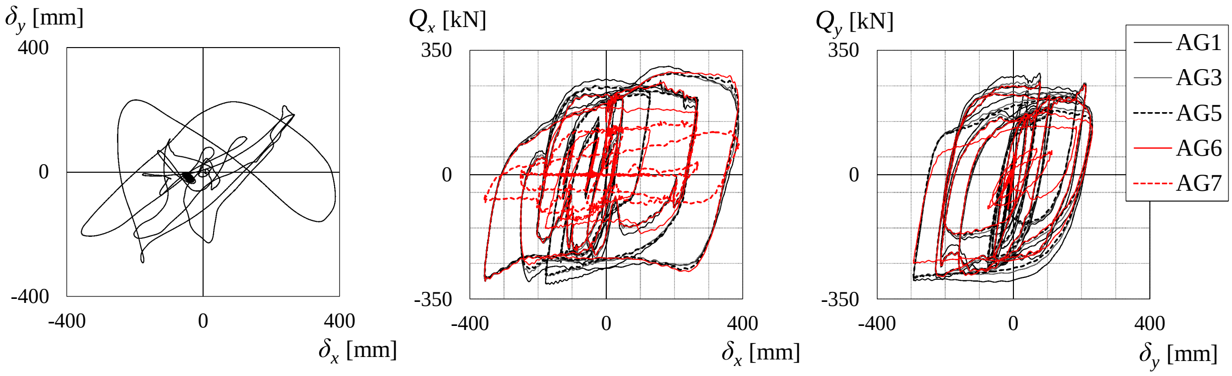

(a) Agnews hospital orbit (b) Hysteresis curves on *x* (c) Hysteresis curves on *y*

Figure II-21. Examples of force – deformation relations of specimen U2.

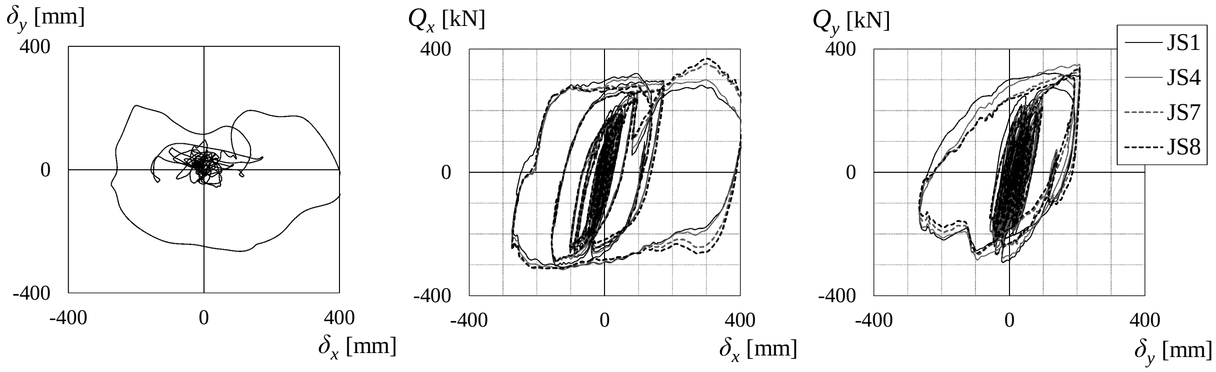

(a) JMA Sendai orbit (b) Hysteresis curves on x (c) Hysteresis curves on y

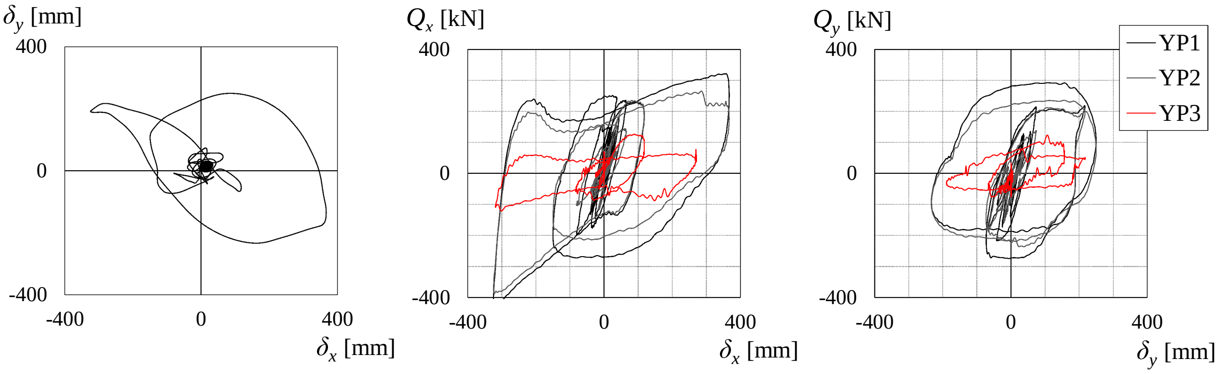

(d) Yarimca orbit (e) Hysteresis curves on x (f) Hysteresis curves on y

Figure II-22. Examples of force – deformation relations of specimen U3.

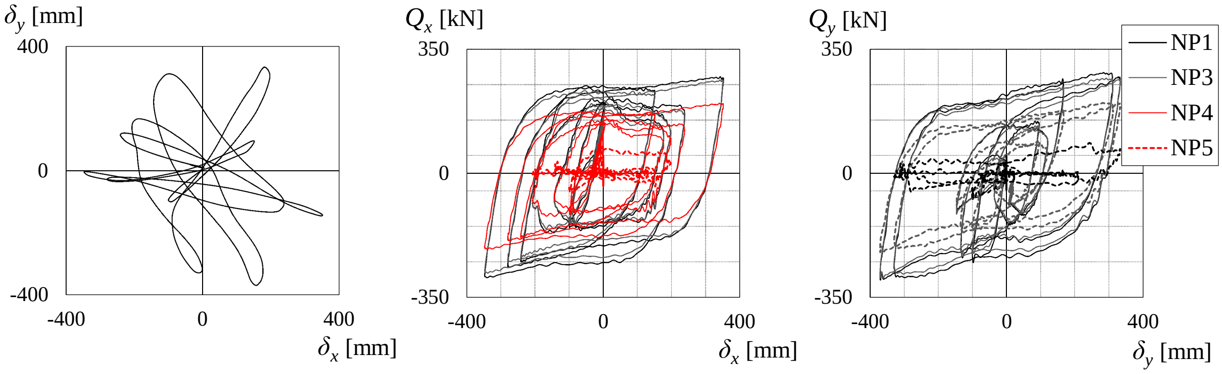

(a) Osaka NKP orbit (b) Hysteresis curves on x (c) Hysteresis curves on y

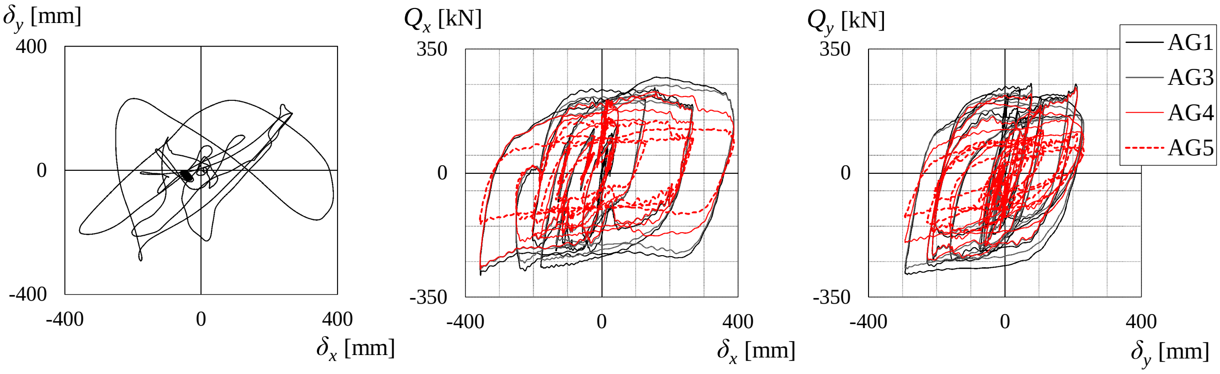

(d) Agnews hospital orbit (e) Hysteresis curves on x (f) Hysteresis curves on y

Figure II-23. Examples of force – deformation relations of additional loading for specimen U4.

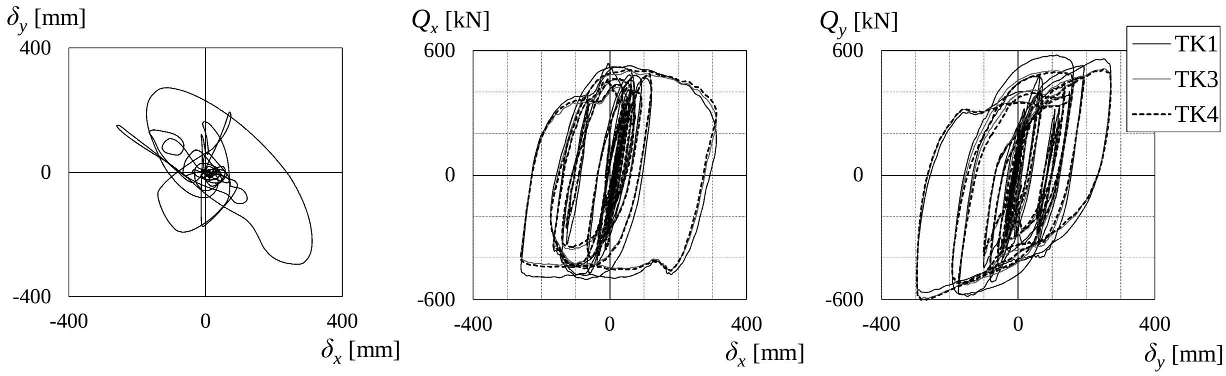

(a) Takatori orbit (b) Hysteresis curves on *x* (c) Hysteresis curves on *y*

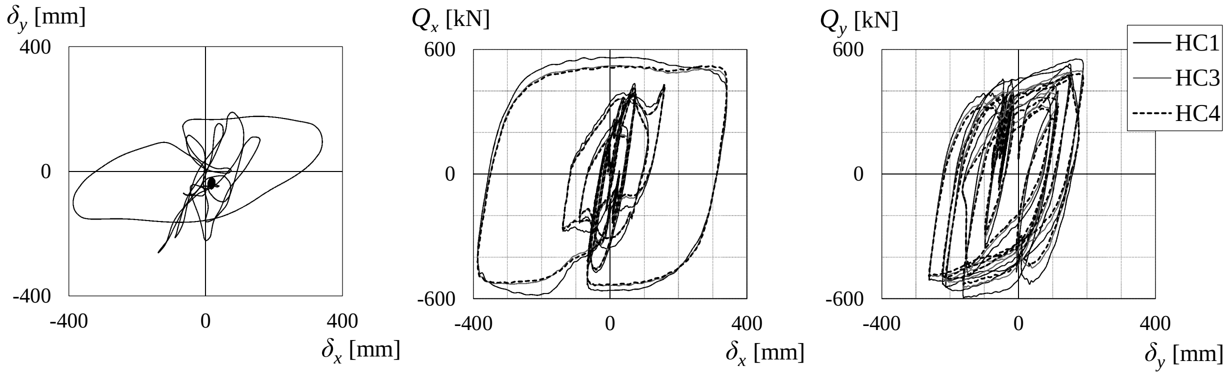

(d) Hachinohe orbit (e) Hysteresis curves on *x* (f) Hysteresis curves on *y*

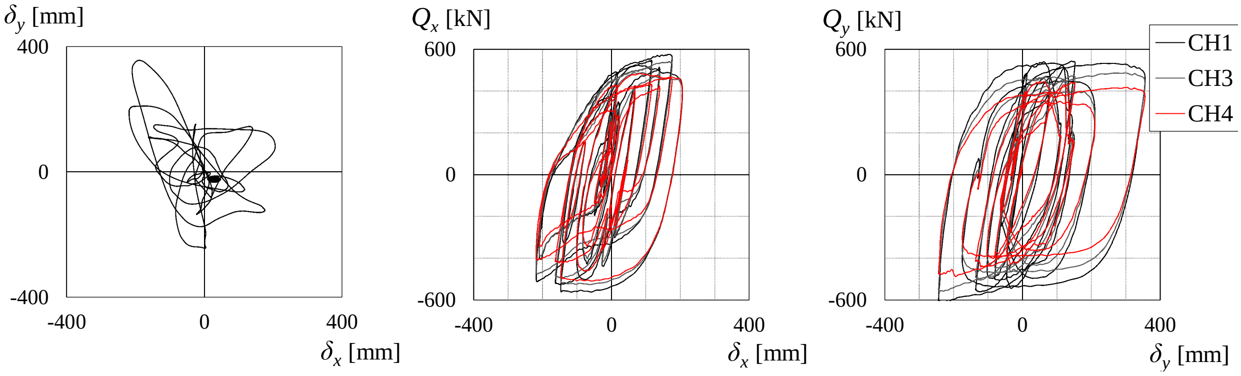

(g) Chihuahua orbit (h) Hysteresis curves on *x* (i) Hysteresis curves on *y*

Figure II-24. Examples of force – deformation relations of specimen U5 (8 elements).

For specimens U5 and U6 that have 8 damper elements, the restoring force for the same displacement histories is about twice as great than that corresponding to the specimens with 4 dampers. This can be noticed by comparing Fig. II-24 to Fig. II-20. It is worth recalling that specimen U5 was additionally loaded with a circular pattern with radius R = 73(mm), therefore part of the decrease of the maximum force (slightly less than 2 times that for specimen U1) is caused by this fact.

In addition, the specimens with 8 elements exhibit the same reliable hysteretic behavior.

II.4. Bidirectional quasi-static loading tests

The dynamic loading tests described in Section II.3 proved that $D_2^u - J_f$ interaction curve can safely be used to estimate the ultimate inelastic deformation capacity of UD50-size U-shaped steel dampers under bidirectional loading, and confirmed the efficiency of the bidirectional cumulative damage index D_2 and sway-motion index J_f. However, to prove that the interaction curve is valid regardless of the damper size (made by the same manufacturer), it is required to test at least one different damper size under realistic bidirectional loadings. This represents the main goal of the present section.

In addition to the main purpose of assessing the fidelity of the interaction curve for another damper size, the following aspects are also investigated:

1. Effect of loading speed on the energy dissipation capacity of U-shaped steel dampers under bidirectional loading.
2. Fidelity of employing the height of the damper h to account for similitude principle of force – deformation relations.

To be able to evaluate the above-mentioned aspects, the second set of bidirectional tests are conducted on 2 full-scale units of 4 UD40 elements, by using the same ground motions as employed in Section II. It should be noted that, to obtain the same amount of damage, the displacement histories are reduced by multiplying them to the ratio between the height of a UD40 element and that of a UD50. This procedure is described in detail in the following section.

II.4.1. Loading protocols

In establishing the loading protocols for the quasi-static test, the following aspects have to be considered:

- The testing facilities are not the same. For the quasi-static tests, the loading facilities in Tokyo Institute of Technology are used, for which the displacement orbits have to be manually controlled step-by-step. This is very time-consuming, therefore the same number of loading steps employed for the case of dynamic tests is not feasible. Moreover, not all the displacement orbits employed in Section II.3 can be conducted.
- The displacement orbits have to be reduced to make sure that the same amount of damage is induced to the specimens of the quasi-static test as it was for those of the dynamic test.

Thus, only loading protocols *LP1* and *LP2* are adopted here. Moreover, it is worth noting that some of the small amplitude parts of the displacement histories were neglected to facilitate the loading process. The resulting displacement histories are hereafter referred to as “simplified orbits”. Their displacement amplitudes are obtained by applying Eq. (II.5):

$$\delta_s = \frac{h_{UD40}}{h_{UD50}} \cdot \delta \tag{II.5}$$

where δ_s is the simplified displacement (either on x or y direction)
δ is the displacement adopted for the dynamic test (UCSD)
h_{UD40}, h_{UD50} are the heights of the UD40 (231(mm)), respectively UD50 (335(mm)).

The maximum displacement in the dynamic tests was set to 400(mm), which means that that of the quasi-static test is 276(mm). To get an image on the difference between the original and simplified displacement orbits, those corresponding to Agnews hospital seismic record are shown in Fig. II-25. For the simplified orbit (Fig. II-25(b)), each step is represented by a diamond plot. Each of the four resulting simplified displacement orbits have about 210 steps (Fig. II-26).

In the dynamic test, the displacement history which caused the dampers to fracture in the least number of loadings was found to be Agnews hospital. For this reason, to avoid having to load a considerable number of histories until fracture, for the first loading protocol loading AGs (Agnews hospital simplified orbit) was loaded after the first set of (TKs, HCs, CHs). The resulting loading protocols for the specimens of the quasi-static test are shown in Fig. II-27.

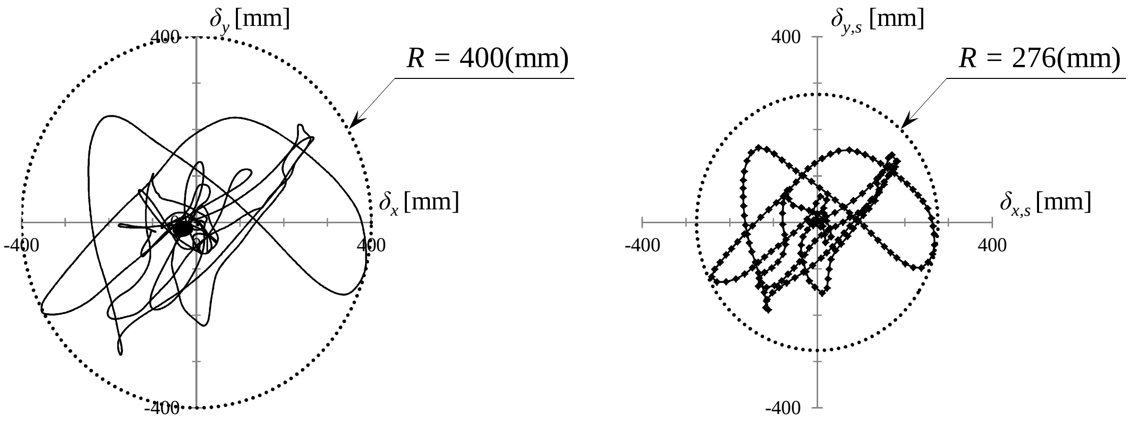

(a) Original orbit (dynamic test) (b) Simplified orbit (quasi-static test)

Figure II-25. Difference between the Agnews hospital displacement history in the dynamic and quasi-static tests.

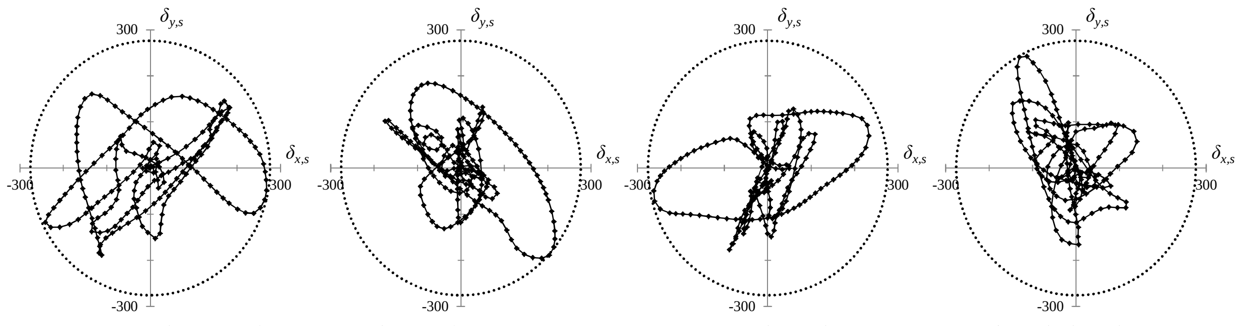

(a) Agnews hospital (b) Takatori (c) Hachinohe (d) Chihuahua

Figure II-26. Simplified displacement histories for quasi-static loading test.

The damage induced to each damper (*x* damper, *y* damper) by the simplified displacement histories is computed using the bidirectional cumulative damage index and the sway-motion index, as listed in Table II-8. It can be observed that the values of D_2 and J_f are slightly smaller than those corresponding to the original records. However, the difference is not significant (less than 14%).

Table II-8. Damage estimation for each simplified displacement history

No.	Displacement orbit		$_{X}D_2^{(*)}$ [-]	$_{Y}D_2^{(*)}$ [-]	J_f [rad]	J_c [rad]
1	Agnews hospital	AGs	0.078	0.080	4.88	4.84
2	Takatori	TKs	0.055	0.060	2.73	2.08
3	Hachinohe	HCs	0.056	0.060	2.87	–2.47
4	Chihuahua	CHs	0.054	0.063	2.22	–1.47

(*) Subscripts *X*, *Y* refer to the damper for which the damage index is computed (Fig. II-4(a)).

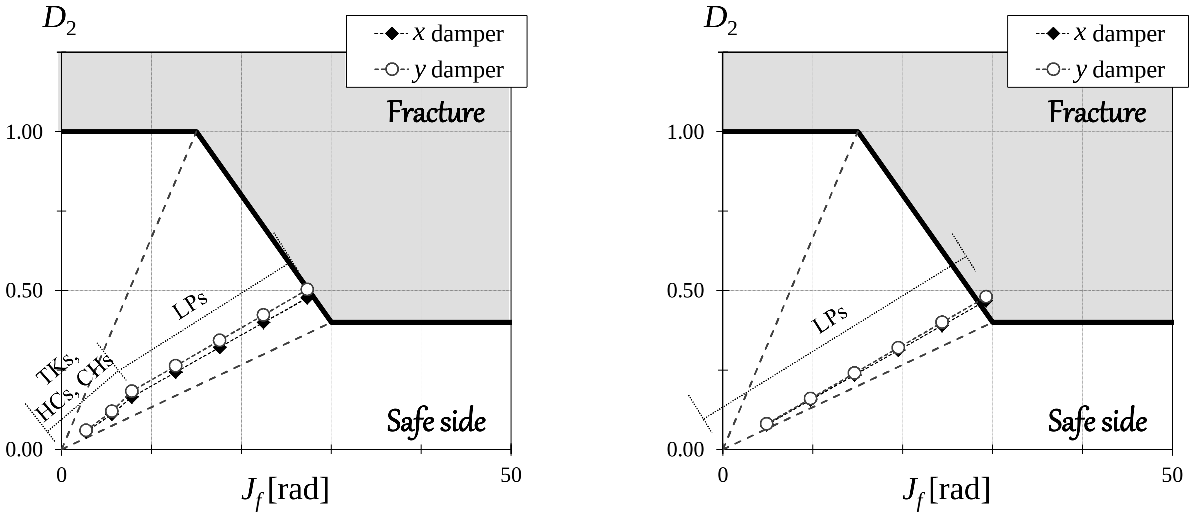

(a) Loading protocol *LP1s* (b) Loading protocol *LP2s*

Figure II-27. Loading protocols for quasi-static tests.

II.4.2. Specimens and loading facilities

The specimens considered for the quasi-static loading tests are 2 units of 4 UD40 dampers (US1, US2). The geometric characteristics of a UD40 element are given in Table II-9.

Table II-9. Geometric characteristics of a UD40 damper

L_t [mm]	L_f [mm]	h [mm]	w [mm]	t [mm]
611	416	231	60	28

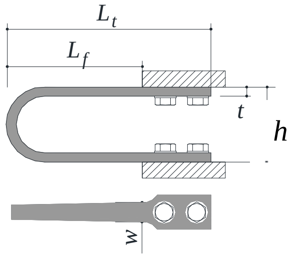

The quasi-static loading tests were conducted using the testing facilities in Tokyo Institute of Technology. The bottom part of the loading equipment, as shown in Fig. II-28, consists of 2 orthogonal horizontal oil jacks (±1000kN, ±500 mm) acting upon a loading table that moves in the *xy* plane by sliding on two biaxial perpendicular sliders. The upper part is a reaction frame whose position can be adjusted using 4 vertical oil jacks. The specimens are placed between the loading table and a cross-shaped beam connected to the upper reaction frame (Fig. II-29). The connections between the specimens and the loading table and between the specimens and the cross-shaped beam are made through 2 jigs (A and B, Fig. II-29). The connections between the jigs and the specimens are bolted connections through a steel plate. The in-plane rotation angles (θ_x, θ_y) and the vertical displacement δ_z of the reaction block are set to 0.

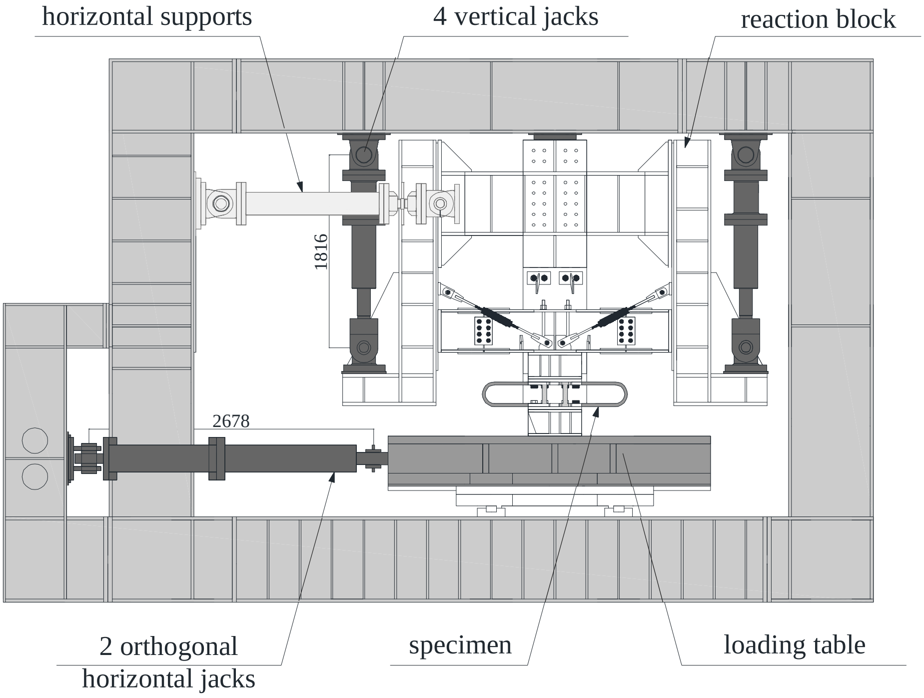

(a) Loading frame along *x* axis

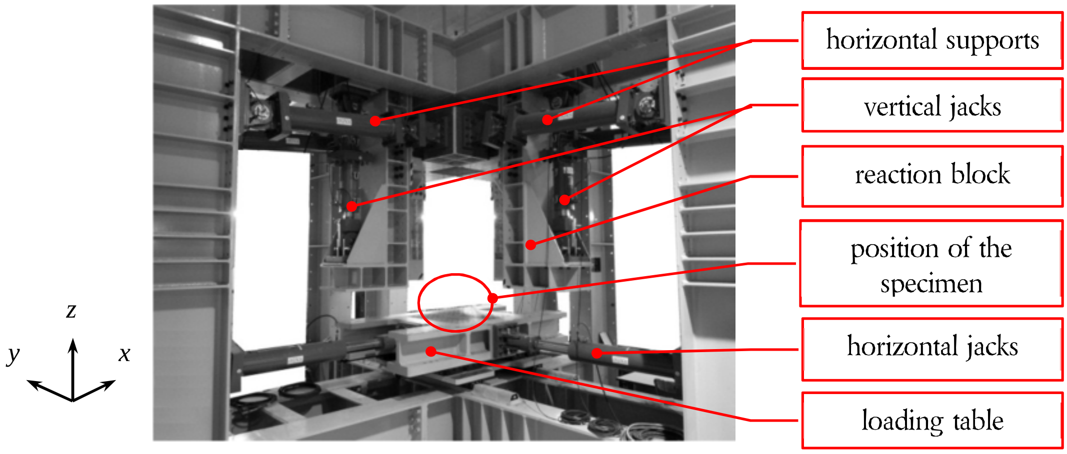

(b) Loading equipment

Figure II-28. Testing facilities for quasi-static test (Tokyo Institute of Technology).

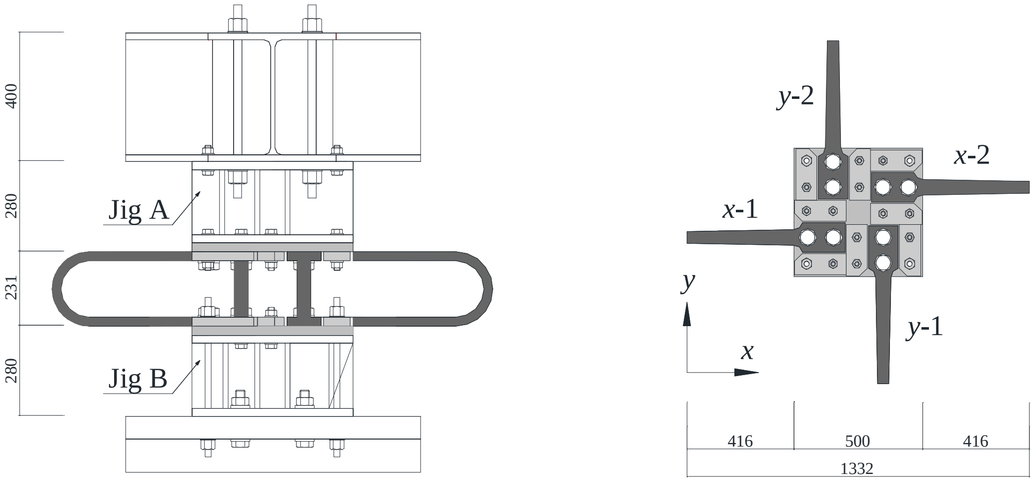

Figure II-29. Details of the connection between the specimen and the loading jigs (A and B).

In the quasi-static test, the same loading concept as that adopted in the dynamic test is applied. The specimens are fixed at their upper part, while their bottom part is subjected to displacement-control loading by operating the 2 horizontal jacks that are connected to the loading table. The restoring forces are measured by the loading cells found in the pin of each horizontal jack which are able to record the force on two orthogonal directions.

II.4.3. Test results

Similar to the dynamic test, the results of interest are the values of D_2 and J_f at the moment when the specimens fracture, respectively the force – deformation relations. In Table II-10, the loading sequences conducted for each specimen until the fracture of the first element are listed. It is worth mentioning that loading stopped after fracture was reached for the first element of each specimen. However, for specimen US2, two elements have fractures.

The values of D_2 and J_f at the moment when the specimens fractured are plotted in Fig. II-30, where those obtained in the dynamic test are also shown. The corresponding data are listed in Table II-11. It can easily be observed that the results are very close to those obtained in the dynamic test. Moreover, the fidelity of the interaction curve is also confirmed for UD40 damper size, which – adding to the results obtained in Section II.3 – points toward the conclusion that indeed the $D_2^u - J_f$ relation can be used to assess the ultimate inelastic capacity of any damper size (made by the same manufacturer).

Table II-10. Displacement histories conducted during the quasi-static test

Unit no.	Specimen type	Designed loading protocol		Additional loading	Observations (*)
US1	4UD40	*LP1s*:	TK→HC→CH →AGx4	AGx1	*x*-1 fractured during AG5
US2	4UD50	*LP2s*:	AGx6	AGx1	*x*-1 and *y*-1 fractured during AG7

(*) *x*-1, *y*-1 represent the position of the dampers with respect to the displacement history (Fig. II-29).

Table II-11. Values of D_2 and J_f at fracture of specimens in quasi-static test

Specimen	x-1		y-1	
	J_f [rad]	D_2	J_f [rad]	D_2
US1	32.23	0.557	–	–
US2	33.84	0.545	33.84	0.552

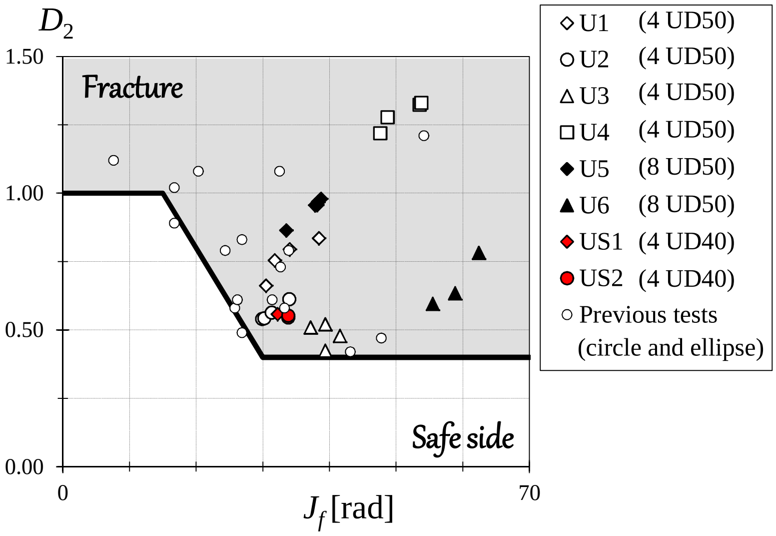

Figure II-30. Values of D_2 and J_f at fracture of the specimens in quasi-static test (red plots) and dynamic test.

The force – deformation relations are investigated next. First, the hysteresis curves for each specimen are shown in Fig. II-31 and Fig. II-32 from which one can observe that the restoring forces are smaller (generally less than half) than those obtained in the dynamic test. This is explained by the fact that different damper sizes have been adopted. However, the shape of the hysteretic curves are very similar, except in the small amplitude part which was neglected during the quasi-static test. In addition, it was found that UD40 damper elements exhibit the same stable hysteretic behavior.

II.4.3. Comparison between the dynamic and the quasi-static force – deformation relations

Further on, to investigate the effect of loading speed on the energy dissipation capacity of U-shaped steel dampers under bidirectional loading and to assess the fidelity of employing the height of the damper h to account for the similitude principle, the restoring forces measured during the quasi-static test are multiplied by $(h_{UD50} / h_{UD40})^2$ (Eq. (II.6)).

$$Q_s = \left(\frac{h_{UD50}}{h_{UD40}} \right)^2 \cdot Q \qquad \text{(II.6)}$$

where Q is the restoring force in the quasi-static test, and Q_s is the corresponding scaled-up force.

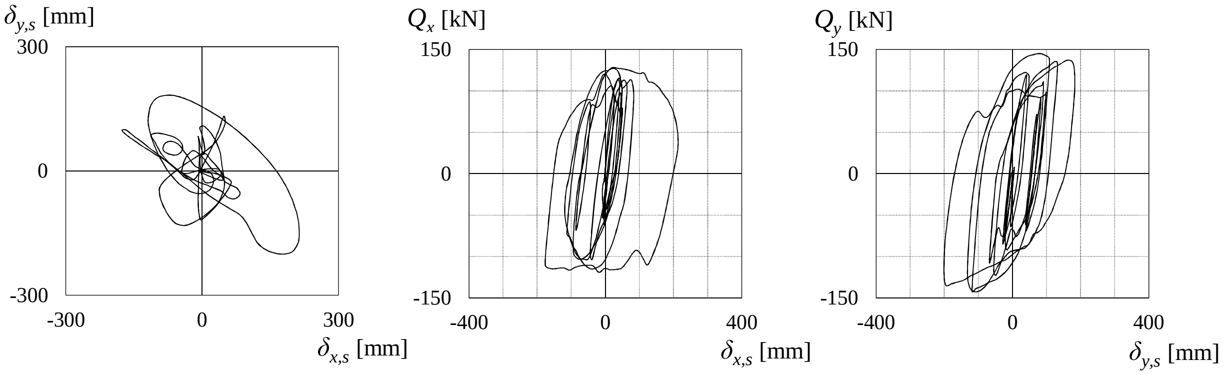

(a) Takatori (TKs) (b) Hysteresis curves on *x* (c) Hysteresis curves on *y*

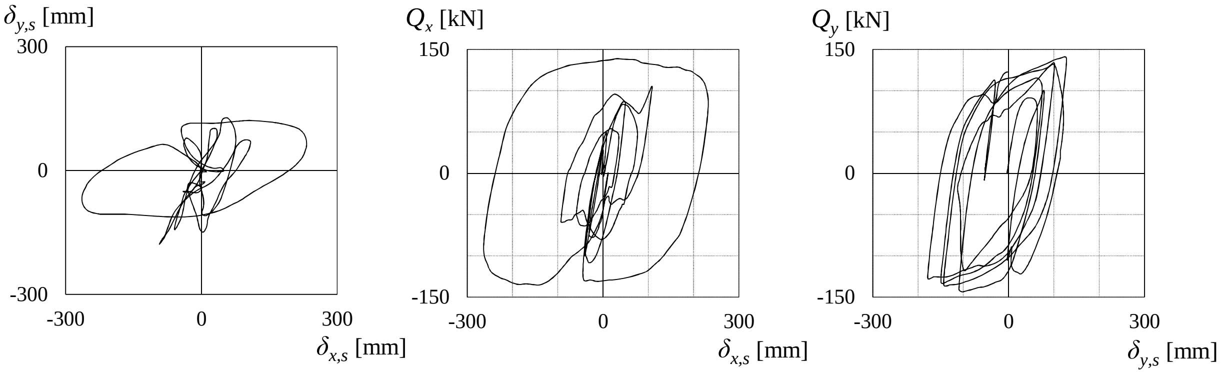

(d) Hachinohe (HCs) (e) Hysteresis curves on *x* (f) Hysteresis curves on *y*

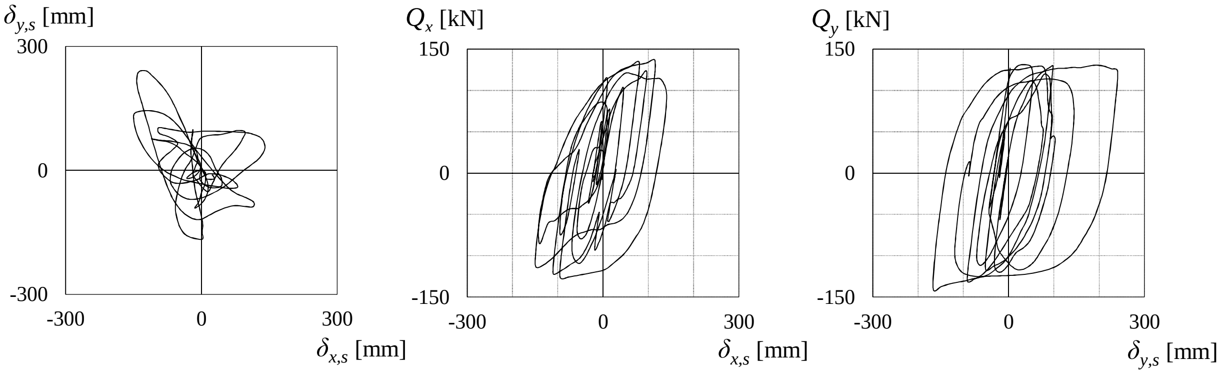

(g) Chihuahua (CHs) (h) Hysteresis curves on *x* (i) Hysteresis curves on *y*

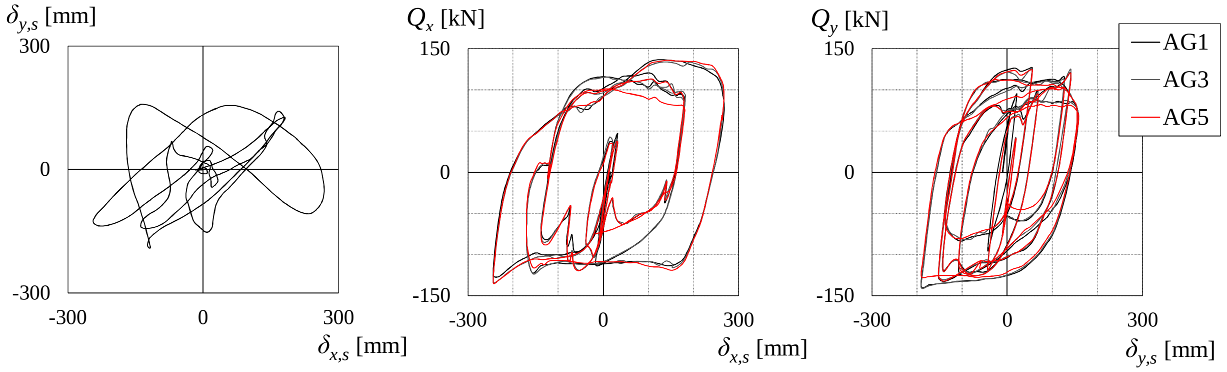

(j) Agnews hospital (AGs) (k) Hysteresis curves on *x* (l) Hysteresis curves on *y*

Figure II-31. Examples of force – deformation relations of specimen US1.

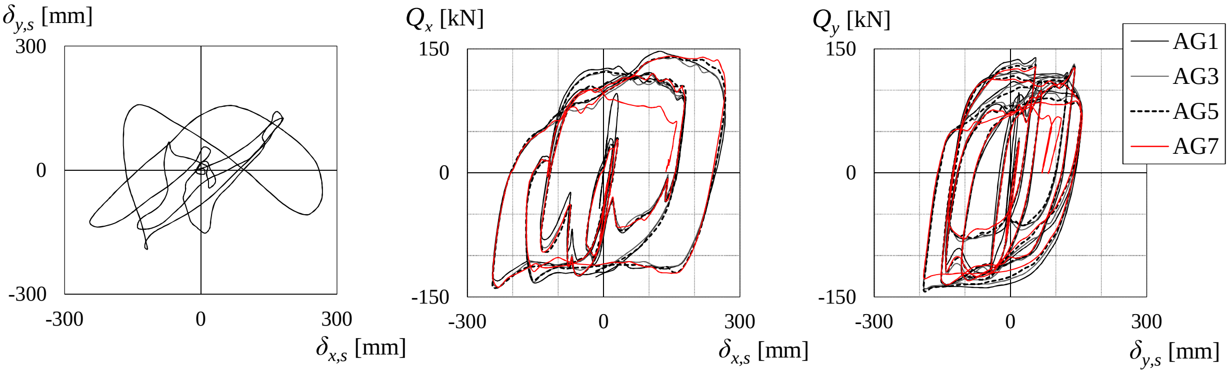

(a) Agnews hospital (AGs) (b) Hysteresis curves on *x* (c) Hysteresis curves on *y*

Figure II-32. Examples of force – deformation relations of specimen US2.

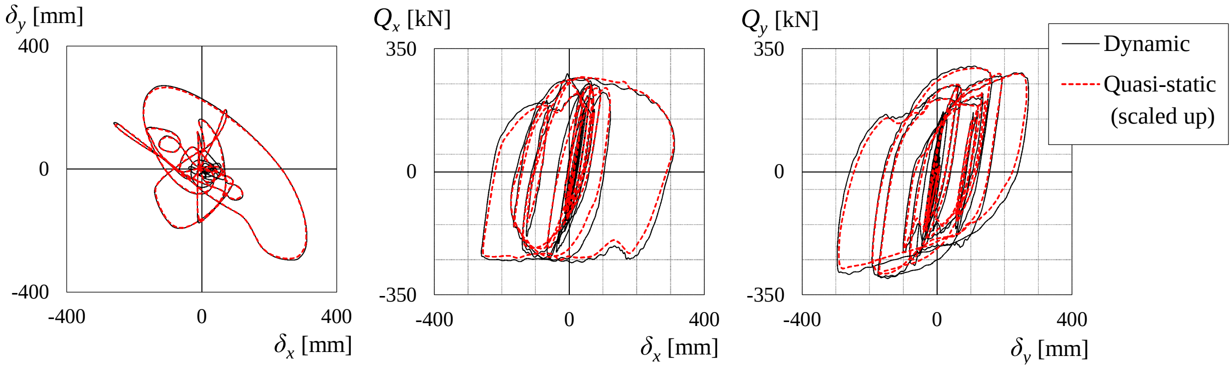

(a) Takatori (b) Hysteresis curves on *x* (c) Hysteresis curves on *y*

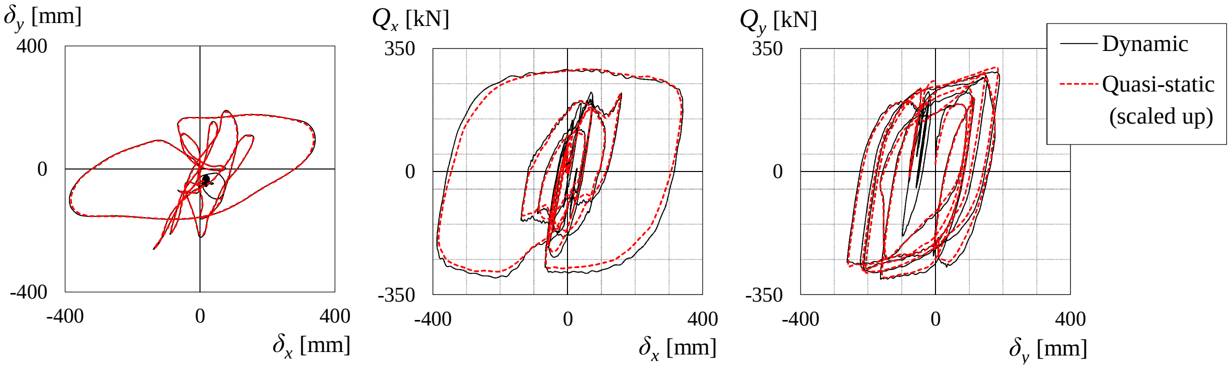

(d) Hachinohe (e) Hysteresis curves on *x* (f) Hysteresis curves on *y*

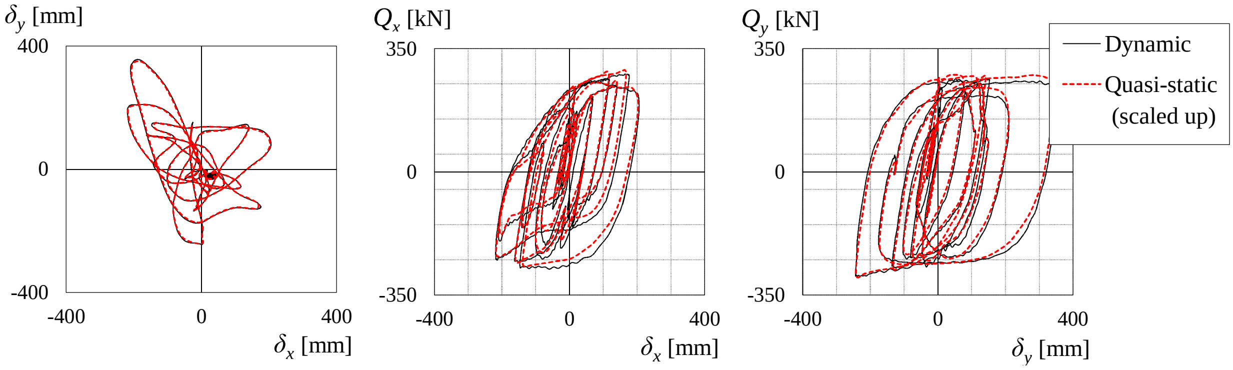

(g) Chihuahua (h) Hysteresis curves on *x* (i) Hysteresis curves on *y*

Figure II-33. Comparison between the force – deformation relations for the dynamic (U1 → black) and scaled-up quasi-static (US1 → red) tests (first three loadings).

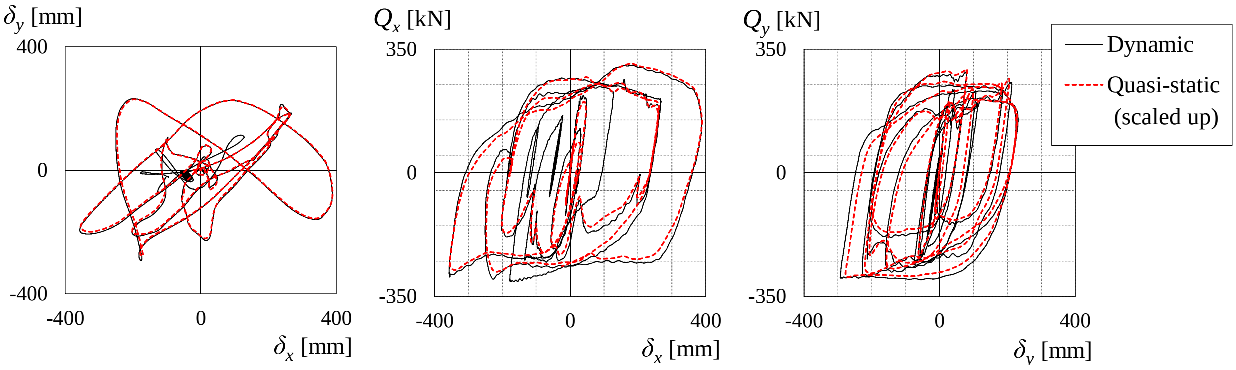

(a) Agnews hospital (b) Hysteresis curves on x (c) Hysteresis curves on y

Figure II-34. Comparison between the force – deformation relations for the dynamic (U2 → black) and scaled-up quasi-static (US2 → red) tests (first loading).

First, to compare the displacement orbits conducted in the two sets of tests, those adopted in the quasi-static test have to be reversed to their original size. To do this, the simplified orbits (Fig. II-26) are multiplied with the ratio (h_{UD50} / h_{UD40}). Using these results and the ones provided by applying Eq. (II.6), the thus obtained scaled force – deformation curves of specimens US1 and US2, are compared to those of U1 and U2 (Fig. II-33, II-34). As a general observation, one can easily note that the two sets of results agree very well, proving – thus – that the adopted equations to account for the similitude principle are suitable to derive the force – deformation relations of two different damper sizes with the purpose of comparing their behavior.

For specimens U2 and US2 loaded with Agnews hospital orbit, because of the fact that part of the displacement history with relatively large amplitudes has been neglected in the quasi-static test (Fig. II-34(a)), the corresponding part of the force – deformation relations is – obviously – missing.

Having established a method to allow comparing the two sets of results, the influence of the loading speed is investigated next. The SRMD testing facilities in University of California San Diego employed to conduct the dynamic tests are able to reproduce the velocity of real ground motions. For the considered displacement histories, the velocity of the loading table in the dynamic tests ranged between 540 and 1000(mm/s) (approximately 1.60~3.00 shear deformation angle γ per second). On the opposite side of the spectrum, the quasi-static tests were conducted at constant loading speed of 1.17(mm/s), which can be considered as static loading.

Generally, it can be observed from Figures II-33 and II-34 that the force – deformation relations of the scaled-up quasi-static tests are slightly smaller than those of the dynamic test. This implies that U-shaped steel dampers dissipate slightly more energy when subjected to dynamic loading. The difference of the maximum force, however, is not significant (±7%). These results confirm those obtained by Jiao *et al.* (2015) [II.5] that investigated the effect of the loading speed for U-shaped steel dampers subjected to one-directional loading and concluded that it can be neglected without concerns regarding their inelastic deformation capacity (and, consequently, their energy dissipation characteristics).

II.5. Summary

In this chapter, the fidelity of the D_2^u – J_f interaction curve in assessing the ultimate inelastic deformation capacity of U-shaped steel dampers under realistic bidirectional histories was confirmed by conducting dynamic and quasi-static loading tests. The main conclusions are listed below:

1. All the tested specimens fractured at values of D_2 and J_f situated above the D_2^u – J_f interaction curve, confirming it to be the lower bound of the ultimate inelastic deformation capacity of U-shaped steel dampers subjected to bidirectional loading. Two damper sizes were tested to this purpose (UD40 and UD50).
2. Specimens subjected to a larger variety of displacement histories (U4) fractured considerably later than those for which a single orbit was applied (U2). This is explained by the fact that – for the latter – load concentration zones that eventually lead to fracture appear much earlier because of cyclic loading that stresses the same parts of the specimens. On the contrary, when subjected to various histories, different parts of the specimens are stressed and plastic deformations are distributed across the entire length of the elements, avoiding stress concentration at same location.
3. U-shaped steel dampers exhibit stable behavior even when subjected to several large amplitude realistic bidirectional histories.
4. Insofar as the test results can indicate, it is highly unlikely that contact with the rest of the connection occurs during a single seismic event.
5. The influence of the loading speed on the bidirectional behavior was assessed by comparing the results obtained in the quasi-static test to those obtained in the dynamic test. In the range of the conducted experiments (maximum velocity of the loading table of 3.00 shear deformation angle γ per second), it was found that the effect of loading speed is negligible.

References

[II.1] 吉敷 祥一，大河原 勇太，山田 哲，和田 章：免震構造用U字形鋼材ダンパーの繰り返し変形性能に関する研究，日本建築学会構造系論文集　第73巻 第624号, pp.333-340, 2008.2;

[II.2] 吉敷 祥一，高山 大，山田 哲，ENE Diana，小西克尚，川村典久，寺嶋正雄：水平2方向載荷下における繰り返し変形性能に関する実験：免震構造用U字形鋼材ダンパーの水平2方向特性（その1），日本建築学会構造系論文集　第680号, pp.1579-1588, 2012.10;

[II.3] 和田章，広瀬景一：2方向地震動を受ける無限均等ラーメン構造の弾塑性応答性状，日本建築学会構造系論文報告集，第399号，pp.37-47，1989.5;

[II.4] 日本建築センター：ビルディング レター;

[II.5] Jiao, Y., Kishiki, S., Yamada, S., Ene, D., Konishi, Y., Hoashi, Y., Terashima, M., 2015. Low Cyclic Fatigue and Hysteretic Behavior of U-Shaped Steel Dampers for Seismically Isolated Buildings under Dynamic Cyclic Loadings, *Earthquake Engineering and Structural Dynamics* ***44***, pp. 1523-1538, DOI 10.1002/eqe.2533.

Chapter III

Simple Hysteretic Model for U-shaped Steel Dampers

III.1. Introduction

In general, loading tests are conducted with the purpose of verifying the performance of targeted specimens under given conditions. However, because of the fact that in reality the assumed conditions often vary due to various causes, it is common practice to define an analytical model to simulate as close as possible the behavior of the real specimen. This way, the performance under different situations can be estimated without conducting costly experimental tests.

For the case of U-shaped steel dampers, a reliable analytical model for estimating the force – displacement relations of a specimen subjected to bidirectional loading is required. Ideally, this model would also be suitable to determine the bidirectional displacement response of the isolation layer.

In the present chapter, a normal bilinear hysteretic model is proposed in Section III.3 based on the test results of specimens of 4 UD40 elements subjected to one-directional loadings as described in Section III.2. This model is used to simulate the behavior of U-shaped steel dampers under bidirectional loading, which is possible due to the fact that the characteristics (elastic and post-elastic stiffness, yield displacement and yield force) of a unit of 4 damper elements are not dependent on the investigated loading directions (x and y). The properties established for a unit of 4 UD40 are then extrapolated to the other three damper sizes (units of 4 UD45, UD50, respectively UD55). Further on, the proposed bilinear model is used in combination with an MSS element (Wada 1989) to obtain the shear forces developed in an isolation layer subjected to a given bidirectional displacement history.

The proposed analytical model is validated against the test results obtained in ***Chapter II*** for units of 4 UD50 elements dynamically loaded with realistic displacement histories (Section III.4). Quasi-static analysis is conducted to this purpose, and the correspondence between the test data and analytical data is verified by computing the coefficient of correlation ρ.

III.2. One-directional loading tests

To propose a hysteretic model for U-shaped steel dampers that accurately describes their behavior under bidirectional loading, it is necessary to first determine their basic properties under such conditions (elastic and post-elastic stiffness, yield displacement and yield force). However, as shown as an example in Fig. III-1 where data from previous research is plotted [III.1], these properties cannot be determined by using bidirectional loading histories, because the force – displacement relations are dependent on the type of loading pattern. For this reason, two sets of one-directional quasi-static loading tests were conducted using full-scale units of 4UD40 elements and the testing facilities at Tokyo Institute of Technology.

The difference between the two loading sets consists of the displacement loading history, which aims at verifying the behavior of the dampers under different conditions. Hence, for the first set, the considered loading protocol was designed in such a way that allows checking whether the values of the basic properties are the same when loading along *x*, respectively *y* direction is applied (Fig. III-2). The second set adopts a loading protocol with varying displacement amplitude that simulates a random loading history; in addition, cyclic loading is conducted until fracture, which allows verifying if the decrease in the maximum force is significant.

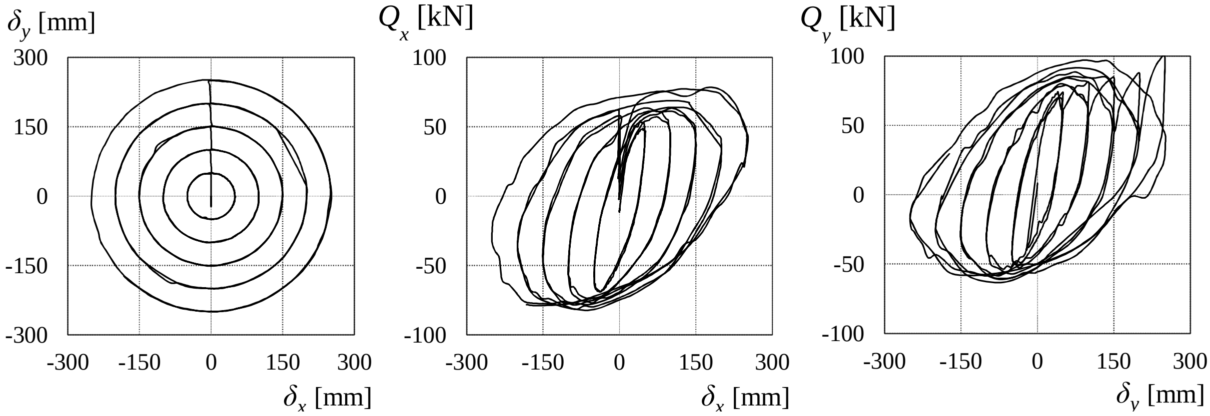

(a) Loading history (b) Hysteresis curves on *x* (c) Hysteresis curves on *y*

Figure III-1. Previous test results for a unit of 2 UD40 elements loaded using circular (bidirectional) displacement histories [III.1].

III.2.1. Evaluation of behavior along x and y directions (Loading set 1)

For loading set 1, a single specimen was used (denoted with 1D-U1), which is first loaded along *x* direction, then along *y* direction at increasing displacement amplitudes of 100, 200, 300 and 400(mm). The loading directions and loading displacement histories are shown in Fig. III-2. For each displacement amplitude, two loading cycles were conducted, and, after having completed all 16 cycles (8 for each direction), loading at constant displacement amplitude ±400(mm) is conducted for another 4 fully-reversed cycles. It is worth mentioning that none of the damper elements have fractured because the damage was relatively small (according to the manufacturer, UD40 dampers are guaranteed to resist 20 fully reversed cycles at 400(mm)).

Figures III-3 and III-4 show the displacement history and the resulting force – deformation relations for *x* and *y* directions. The following observations are made:

- When the dampers are loaded for the first time beyond their elastic range (first loading cycle at 100(mm) amplitude), due to the effect of strain hardening, the corresponding force is less than that of the following cycles, even for those having the same amplitude (Fig. III-3(c)). When switching to loading along *y* direction, it can be observed that the force in the first cycle at 100(mm) is comparable to that of the subsequent cycles. This is because the dampers have been subjected to large inelastic deformations on the orthogonal direction and strain hardening already took place.
- Except for the effect of strain hardening explained above, similar behavior was observed for both loading directions. This confirms the results obtained by Kishiki *et al.* (2012) who found that a unit of 2 UD40 elements has negligible dependency with the loading direction [III.1]. Therefore the observations listed below are valid for both directions.
- When the dampers return from the maximum displacement of a given cycle towards $\delta = 0$(mm) and after the unloading part, the post-elastic stiffness decreases, and for the 400(mm) cycles the slope becomes negative. Moreover, the value of the post-elastic stiffness is sensitive to the displacement amplitude. Thus it is expected that in these regions (both positive and negative displacement ranges), the behavior of the dampers cannot be modeled accurately using a single value for the post-elastic stiffness.
- The hysteresis curves suggest that the behavior of the dampers can be modeled using a bilinear model, although this may lead to underestimating the force in the regions mentioned in the previous observation. This is discussed in Section III.3.

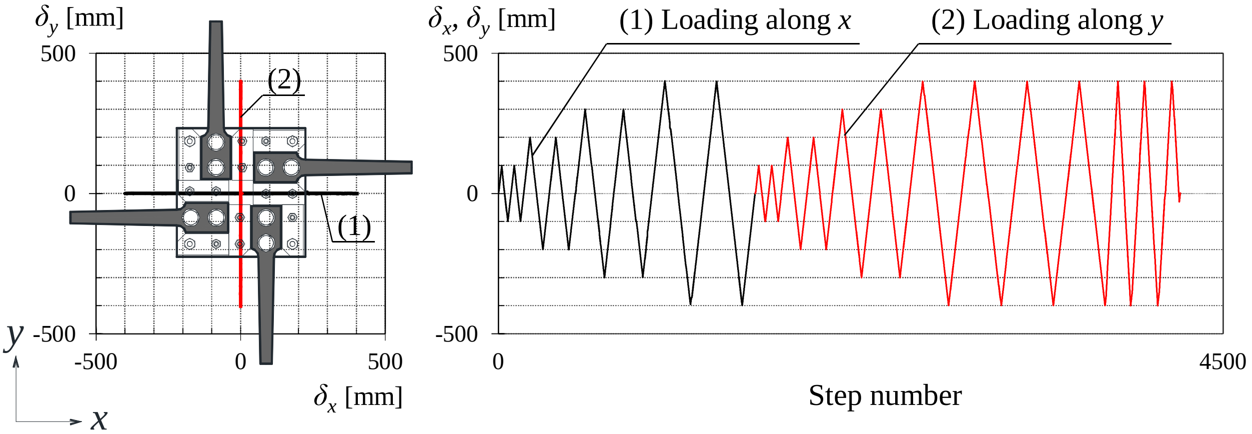

(a) Loading directions (b) Displacement loading history

Figure III-2. Loading protocol for first set (specimen 1D-U1).

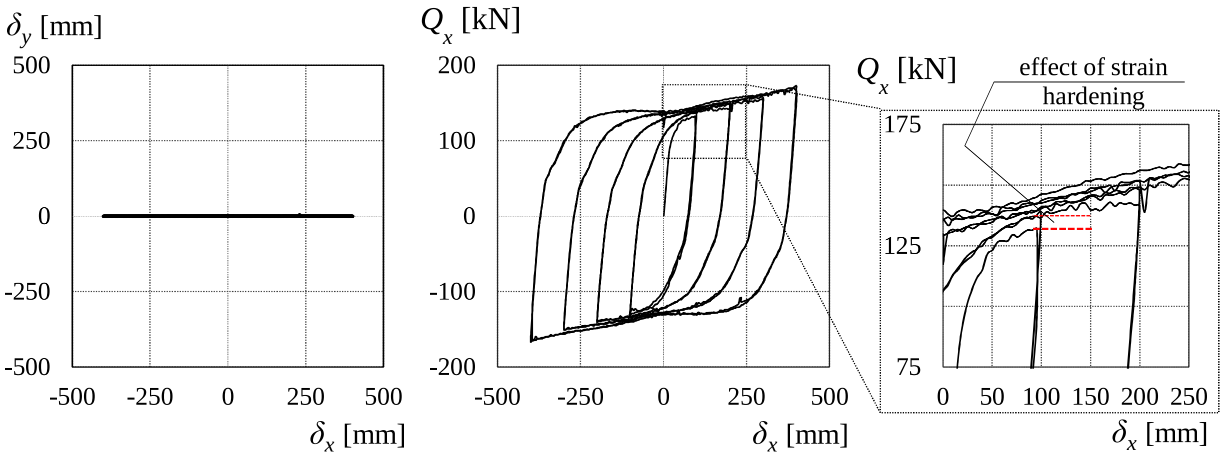

(a) Loading history (b) Hysteresis curves on *x* (c) Effect of strain hardening

Figure III-3. Force – deformation relation of specimen 1D-U1 along *x* direction.

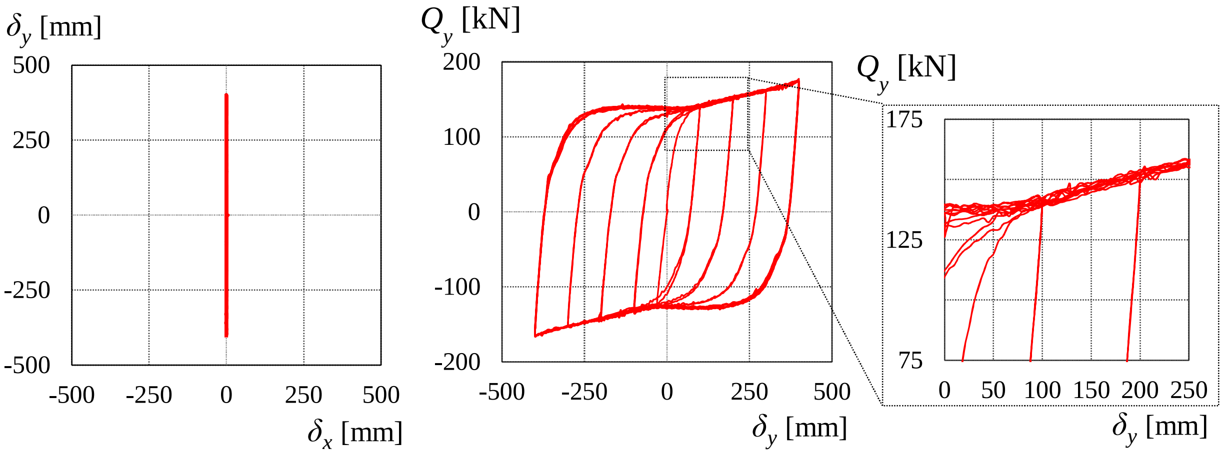

(a) Loading history (*y* direction) (b) Hysteresis curves on *y* (c) Effect of strain hardening

Figure III-4. Force – deformation relation of specimen 1D-U1 along *y* direction.

III.2.2. Evaluation of behavior under incremental and monotonic loading (Loading set 2)

The second loading set is conducted on two specimens (4UD40) denoted with 1D-U2, respectively 1D-U3. The loading sequence adopted is the one given by the US design code ASCE/SEI 7-10 (“Minimum design loads for buildings and other structures”) for verifying the behavior of seismic isolation devices.

Loading sequence

This standard loading protocol was established to determine the deformation characteristics and damping values of the isolation system to be used for design of seismically isolated structures.

The amplitudes of the displacement history are established function of the design displacement D_D and the maximum displacement D_M of the isolation layer as follows:

1. ***Set I***: 20 fully reversed cycles at a lateral force corresponding to the wind design force

2. ***Set II***: 3 fully reversed cycles at each of the following increments of the total design displacement D_D: 0.25 D_D, 0.50 D_D, 1.00 D_D and 1.00 D_M
3. ***Set III***: 3 fully reversed cycles at the total maximum displacement 1.10 D_M
4. ***Set IV***: $30S_{D1}/S_{DS}B_D$ but not less than 10 fully reversed cycles at the total design displacement 1.10 D_D.

   Here, S_{DS}, S_{D1} are the design earthquake response accelerations for short periods, respectively for 1.0(sec) period, while B_D is a numerical coefficient defined based on the effective damping. To define the loading sequence, the maximum values of the design earthquake response accelerations given in ASCE/SEI 7-10 are considered. In addition, for U-shaped steel dampers, the coefficient B_D is equal to 0.80. It results that the minimum number of cycles that the specimens have to be verified to is 28. The loading sequence for the general case of seismic isolation devices is shown in Fig. III-5.

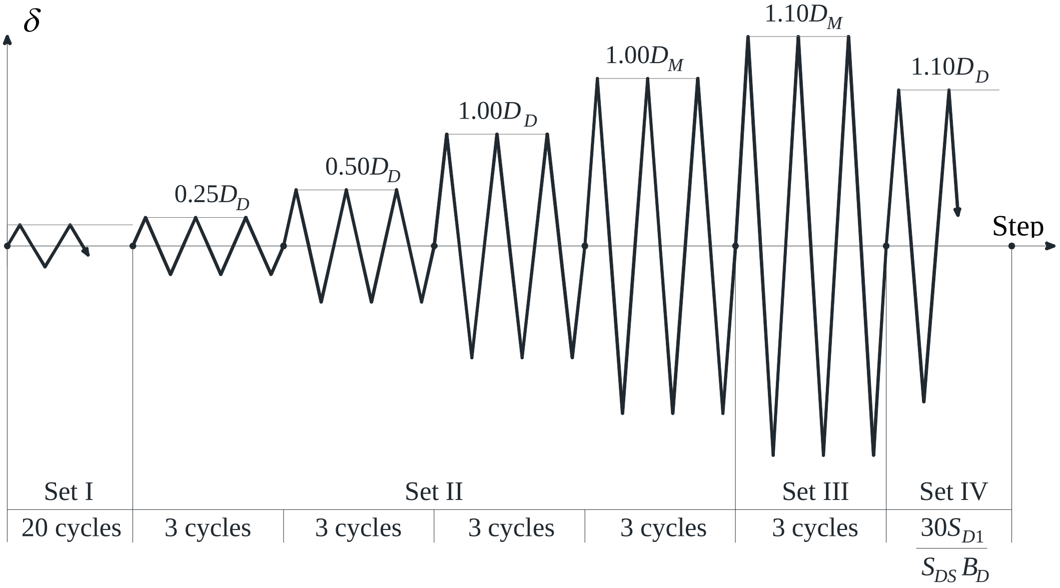

Figure III-5. Loading sequence – general case (ASCE/SEI 7-10).

The design displacement D_D is defined in ASCE/SEI 7-10 as "*the design earthquake lateral displacement, excluding additional lateral displacement due to actual and accidental torsion*". The maximum displacement D_M is to be established in the most critical direction of the horizontal response of the isolation system. For the present study, as the damage of the U-shaped steel dampers depends on the displacement amplitude and on the damper size, a unit of 4UD50 elements is considered as reference to establish the values of D_D and D_M. The maximum displacement is set at 80% of the displacement at which 20 fully reversed cycles are completed before fracture occurs:

$$ {}_{UD50}D_M = 0.80 \cdot 500(\mathrm{mm}) \quad \Rightarrow \quad {}_{UD50}D_M = 400(\mathrm{mm}) \tag{III.1}$$

where ${}_{UD50}D_M$ is the maximum displacement of the reference damper size (a unit of 4UD50). The design displacement of the reference damper unit ${}_{UD50}D_D$ is set to 2/3 of ${}_{UD50}D_M$ (Eq. (III.2)):

$$ {}_{UD50}D_D = \frac{2}{3} \cdot {}_{UD50}D_M \quad \Rightarrow \quad {}_{UD50}D_D = 267(\text{mm}) \tag{III.2}$$

The specimens of the second loading set are units of 4 UD40 elements, therefore similarity principle has to be applied in order to ensure that the same amount of damage is induced. This is done by multiplying the values of ${}_{UD50}D_D$ and ${}_{UD50}D_M$ to the ratio between the heights of the two damper sizes h_{UD40}/h_{UD50} (Eq. (III.3)). The resulting amplitudes for each required set are shown in Fig. III-6. It is worth noting that the shear forces produced in the isolation layer because of the wind load are considered to be within the elastic range of U-shaped steel dampers. For this reason, the loading cycles required at point (1) above are not conducted.

$$D_D = \frac{h_{UD40}}{h_{UD50}} \cdot {}_{UD50}D_D \quad \Rightarrow \quad D_D = 184(\text{mm}) \tag{III.3a}$$

$$D_M = \frac{h_{UD40}}{h_{UD50}} \cdot {}_{UD50}D_M \quad \Rightarrow \quad D_M = 202(\text{mm}) \tag{III.3b}$$

where D_D and D_M are the design, respectively the maximum displacements for a unit of 4UD40. The last set of the loading sequence (***Set IV***), contains 28 fully reversed cycles. However, loading was conducted until fracture of the specimens. This presents the opportunity to evaluate the decrease of the maximum force when the dampers are subjected to cyclic loading.

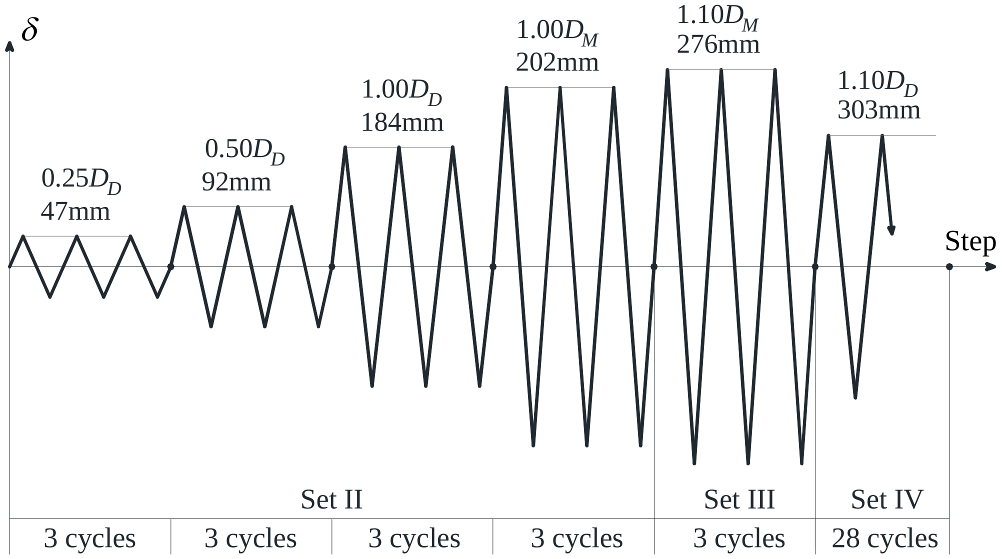

Figure III-6. Loading sequence for a unit of 4 UD40 elements (ASCE/SEI 7-10).

Test results

The loading cycles for each specimen are listed in Table III-1, together with the corresponding damage indices for the dampers placed along x direction ($D_{0°}$) and those placed on y direction ($D_{90°}$). The loading sequence is the same, the only exception being that the second specimen lasted half a cycle longer than the first one before fracture occurred. In addition, it can be observed that the damage indices for the dampers that reached fracture are barely above the fracture limit for one-directional loading (D = 1.00), meaning that they have fulfilled the minimum required inelastic deformation capacity without any considerable surplus.

The obtained test results are analyzed considering the following two main aspects: (a) force – deformation relations, and (b) effective stiffness k_{eff}.

(a) The *force – deformation relations* for each specimen are shown in Fig. III-7, respectively in Fig. III-8. The following observations can be made:

- Compared to the results obtained for the first loading set, due to the fact that the displacement amplitudes are smaller this time, the change of the post-elastic stiffness is less evident.
- For both specimens it can be observed that the maximum force of the cycles in ***Set IV*** decreases gradually until fracture occurs. For specimen 1D-U2, there is a 12% decrease, while for specimen 1D-U3 – 14%. This behavior is difficult to simulate, especially if the dampers are subjected to random displacement amplitudes, as is the case when they are subjected to seismic excitation. This aspect is evaluated in detail at point (b) by computing the effective stiffness k_{eff} of each cycle.

Table III-1. Test results for loading set 2 (specimens 1D-U2, 1D-U3)

Loading Set No.	Displacement amplitude (mm)		No. of cycles	$D_{0°}$	$D_{90°}$
II	± 0.25 D_D	± 46 (mm)	3	0.006	0.002
	± 0.50 D_D	± 92 (mm)	3	0.018	0.006
	± 1.00 D_D	± 184 (mm)	3	0.050	0.020
	± 1.00 D_M	± 276 (mm)	3	0.093	0.041
III	± 1.10 D_M	± 303 (mm)	3	0.107	0.053
IV	± 1.10 D_D	± 202 (mm)	37.0 (1D-U2)	0.714	0.287
			37.5 (1D-U3)	0.724	0.291
Total			52.0 (1D-U2)	***1.017*** (*)	0.419
			52.5 (1D-U3)	***1.018*** (*)	0.420

(*) One damper of each specimen placed parallel to the loading direction has reached fracture.

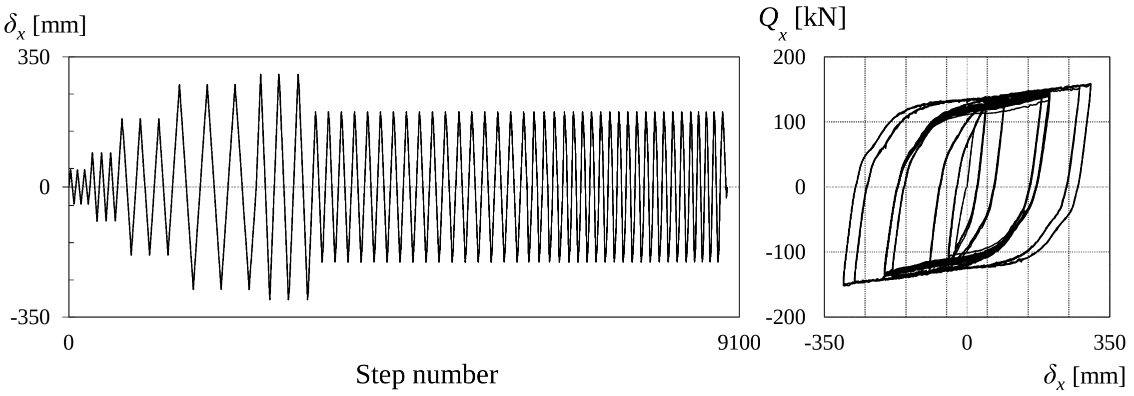

(a) Loading history (b) Hysteresis curve

Figure III-7. Force – deformation relation of specimen 1D-U2.

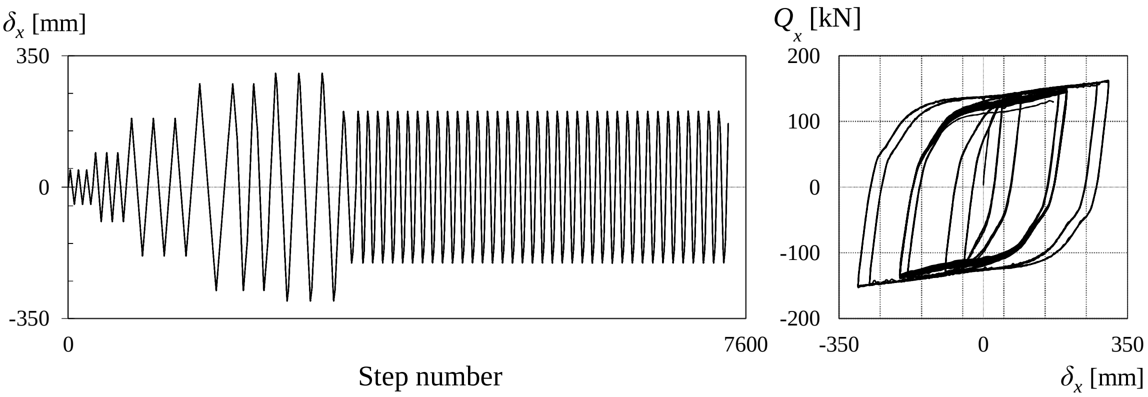

(a) Loading history (b) Hysteresis curve

Figure III-8. Force – deformation relation of specimen 1D-U3.

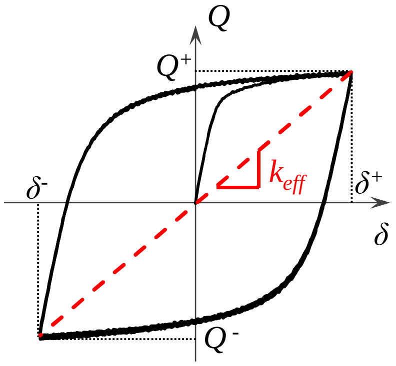

Figure III-9. Definition of effective stiffness k_{eff}.

(b) The *effective stiffness* k_{eff} is defined as shown in Fig. III-9 and given in Eq. (III.4):

$$k_{eff} = \frac{|Q^{+}| + |Q^{-}|}{|\delta^{+}| + |\delta^{-}|} \tag{III.4}$$

where δ^+,δ^- are the maximum displacements of each cycle (Fig. III-9)

Q^+,Q^- are the shear forces at the maximum displacements of each cycle

The value of k_{eff} decreases with the increase of the displacement amplitude. This can be observed in Fig. III-10, where the effective stiffness for each cycle is shown against the corresponding cycle number. The red lines show the average values of k_{eff}. The difference between the average value and the value computed for each cycle is obtained and shown in Fig. III-10. It can be observed that its value is less than 4% for both specimens. Moreover, for the last loading set (***Set IV***), the difference between the maximum and minimum values was also computed and the results were less than 6%. These facts imply that the amount with which the force decreases because of cyclic loading does not significantly affect the effective stiffness.

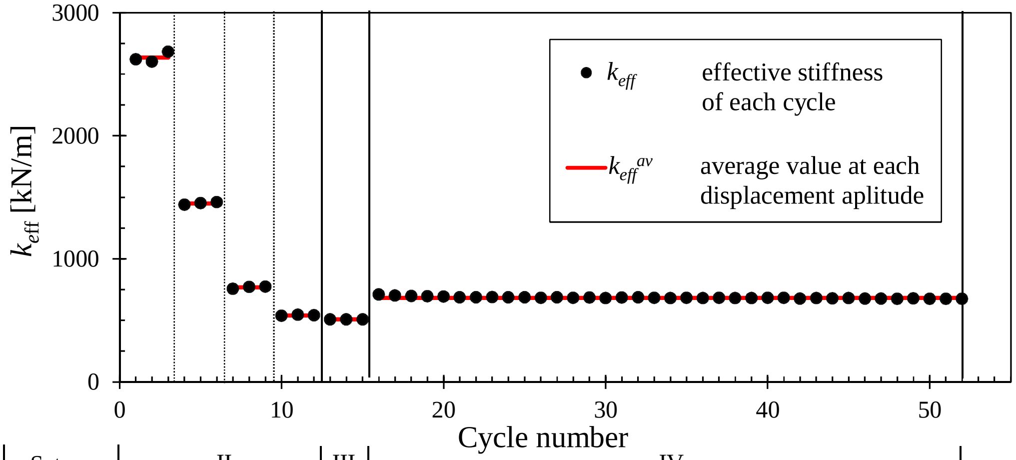

Set no.		II			III	IV
$\lvert k_{eff}- k_{eff}^{av}\rvert$ (%)	2.0	1.0	1.5	1.0	0.5	4.0

(a) Specimen 1D-U2

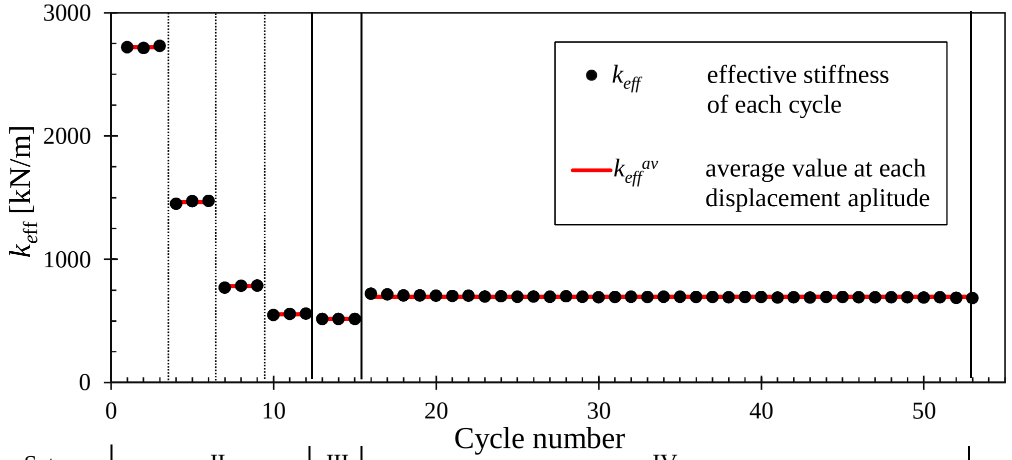

Set no.		II			III	IV
$\lvert k_{eff}- k_{eff}^{av}\rvert$ (%)	0.5	1.0	1.5	1.5	0.5	3.5

(b) Specimen 1D-U3

Figure III-10. Variation of the effective stiffness k_{eff} with the number of cycles.

III.2.3. Remarks

In the present section, the following important findings are to be noted:

- Based on the obtained force – deformation relations, the behavior of a unit of 4UD40 under one-directional loading can be approximated using a bilinear model. However, it may be difficult to model the parts where the deformation returns from its maximum value using a single value of the post-elastic stiffness.
- The maximum force decreased with 12~14% when cyclic loading at the same displacement amplitude was applied. This fact does not significantly affect the effective stiffness.

III.3. Establishing the analytical model

In the previous section, two sets of one-directional quasi-static loading tests using full-scale units of 4UD40 damper elements were conducted. The first objective of the present section is to propose a hysteretic model for units of 4UD40 and investigate a way to extrapolate the results for the other three damper sizes. In addition, the proposed constitutive law for the U-shaped steel dampers has to be employed in a given analytical framework. This represents the second objective of this section. The analytical model as a whole (hysteretic model + analytical framework) is validated in the next section against the test results obtained in Section III.2 and ***Chapter II***.

Based on the force – deformation relations obtained in the previous section it was concluded that U-shaped steel dampers can be modeled as having a bilinear hysteretic model. Therefore, the following parameters have to be established based on the experimental data:

- Elastic stiffness k_e
- Post-elastic stiffness k_p
- Yield force Q_y

It is worth noting that the yield force Q_y (Fig. III-11) is defined at the intersection between the lines given by the elastic stiffness k_e and the post-elastic stiffness k_p, where the latter is fitted through the test data. Further on, the yield displacement δ_y is defined by Eq. (III.5):

$$\delta_y = \frac{Q_y}{k_e} \tag{III.5}$$

where Q_y is the yield force defined at the intersection between the lines given by the elastic stiffness k_e and the post-elastic stiffness k_p (Fig. III-11).

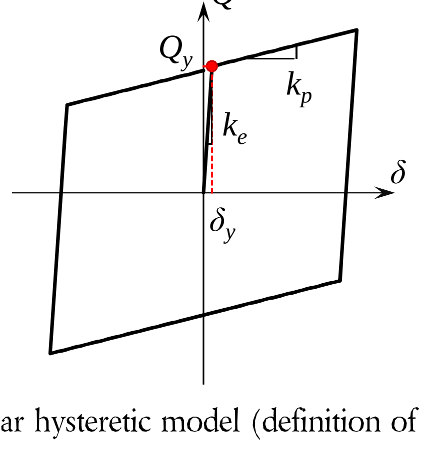

Figure III-11. Bilinear hysteretic model (definition of k_e, k_p, δ_y and Q_y).

III.3.1. Elastic stiffness k_e

To find an adequate value for the elastic stiffness, first the experimental elastic stiffness ${}_ek_e$ is obtained based on the unloading part of the first cycle of each specimen considered in Section III.2 (Fig. III-12). The results are listed in Table III-2 and are compared to the catalog values given by the manufacturer (Table III-3). It is worth noting that the average value is very close to the catalog value ($0.98 \cdot {}_ck_e$), therefore for the bilinear hysteretic model investigated here it is proposed that the value of the elastic stiffness k_e is set to be equal to the catalog value.

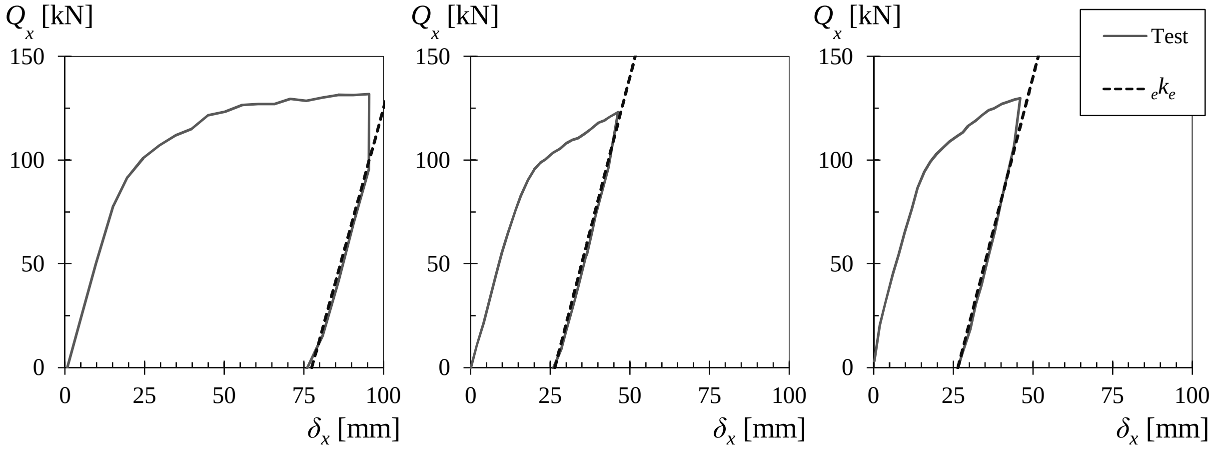

(a) 1D-U1 (b) 1D-U2 (c) 1D-U3

Figure III-12. Determining the experimental elastic stiffness ${}_ek_e$ of the specimens (Section III.2) based on the unloading stiffness of the first loading cycle.

III.3.2. Post-elastic stiffness k_p

The post-elastic stiffness ${}_ek_p$ of each specimen tested in Section III.2 is determined by fitting a straight line through the plastic range of the hysteresis curves in the region where both the force and the displacement are positive as shown in Fig. III-13. The dashed line represents the slope given by ${}_ek_p$ equal to the catalog value, namely 100(kN/m) (Tables III-2, III-3).

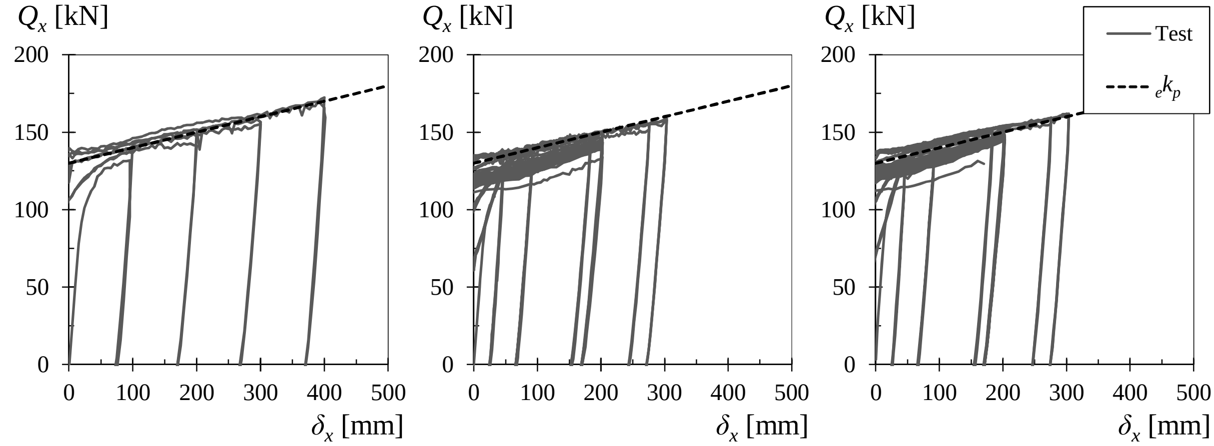

(a) 1D-U1 (b) 1D-U2 (c) 1D-U3

Figure III-13. Determining the experimental post-elastic stiffness ${}_ek_p$ (Table III-3).

In Fig. III-13(b) and III-13(c) it can be noted that for the last set of cyclic loading, because the maximum force decreased with the number of cycles, the post-elastic stiffness is situated at a lower force. This suggests that, by using a bilinear hysteretic model that does not account for the decrease of the maximum force due to cyclic loading, the accuracy of the obtained results may drop as the number of cycles in the inelastic range increases. This aspect is investigated in the next section.

The catalog value of the post-elastic stiffness agrees well with the experimental data in the regions where both the force and the displacement are positive or negative. The fidelity in the rest of the regions is considered to be satisfactory for a conventional bilinear model (Fig. III-14). This is demonstrated in Section III.4.

The value of the post-elastic stiffness k_p of the proposed hysteretic model is – thus – the catalog value, as shown in Table III-4.

III.3.3. Yield force Q_y

As explained above, in the present study, the yield force is defined to be the force at the point of intersection between the slopes of the elastic and post-elastic stiffnesses. The experimental values ${}_eQ_y$ computed for each specimen are shown in Table III-2, from which it can be observed that they are almost the same. Moreover, by comparing the average value of ${}_eQ_y$ (132.3(kN)) to the catalog value ${}_cQ_y$ (112.0(kN), Table III-3), their ratio is 1.18. For this reason, the value of the yield force Q_y of a unit of 4UD40 for the proposed bilinear model is set to 1.18 times the catalog value, as listed in Table III-4.

Table III-2. Experimental values of ${}_ek_e$, ${}_ek_p$ and ${}_eQ_y$ (4UD40)

Specimen	${}_ek_e$ (kN/m)	${}_ek_p$ (kN/m)	${}_eQ_y$ (kN)
1D-U1	5550	100	132.4
1D-U2	5956	100	132.2
1D-U3	5958	100	132.2
Average	5821	100	132.3

Table III-3. Catalog values of ${}_ck_e$, ${}_ck_p$ and ${}_cQ_y$ (4UD40, 4UD45, 4UD50, 4UD55)

Damper size	${}_ck_e$ (kN/m)	${}_ck_p$ (kN/m)	${}_cQ_y$ (kN)
4UD40	5920	100	112
4UD45	7600	128	184
4UD50	8320	144	232
4UD55	9600	160	304

III.3.4. Bilinear hysteretic model

The values of the characteristics necessary to describe a bilinear hysteretic model for a unit of 4 UD40 U-shaped steel dampers were established as described above. However, the force – deformation relations of the dampers are dependent on their size. To account for this fact, the values established based on the one-directional loading tests on units 4UD40 are extrapolated to the other damper sizes by referring them to the catalog values (${}_ck_e$, ${}_ck_p$ and ${}_cQ_y$ in Table III-3). For the elastic and post-elastic stiffness, the catalog values are used, while for the yield force 1.18 times the catalog value is employed. The results are given in Table III-4.

Table III-4. Values of k_e, k_p and Q_y for the bilinear hysteretic model (4UD40, 4UD45, 4UD50, 4UD55)

Damper size	k_e (*) (kN/m)	k_p (*) (kN/m)	Q_y (**) (kN)
4UD40	5920	100	132
4UD45	7600	128	217
4UD50	8320	144	274
4UD55	9600	160	359

(*) Catalog values

(**) Values equal to 1.18 times the catalog ones.

In Fig. III-14 the hysteretic curves of each specimen are plotted on the same graphics as the proposed bilinear hysteretic model design to fit the largest loop. It is observed that for the regions in which the force and deformation have different signs, the proposed model does not accurately follow the experimental data. Therefore particular attention on this subject is required when the accuracy of the analytical data is verified against the experimental data in the next section.

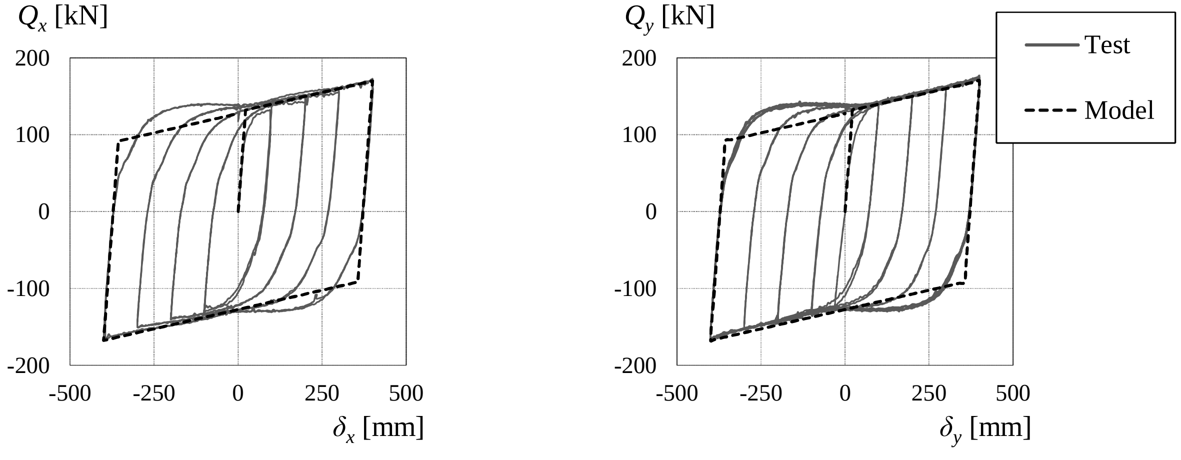

(a) 1D-U1 (*x* direction)

(b) 1D-U1 (*y* direction)

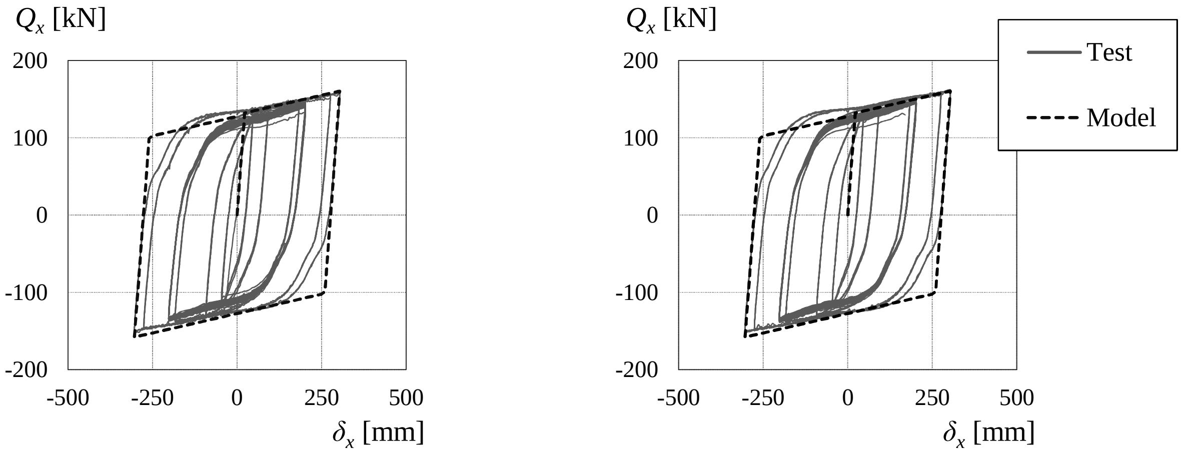

(c) 1D-U2 (d) 1D-U3

Figure III-14. Hysteresis curves for specimens 1D-U1, 1D-U2 and 1D-U3 against the proposed hysteretic bilinear model.

III.3.5. Analytical model

The hysteretic bilinear model established above requires an analytical framework to be able to simulate the force – displacement relations along two orthogonal directions. For this purpose, the multiple shear spring (MSS) model proposed by Wada is employed [III.3]. Further on, quasi-static analysis is conducted using as input data a bidirectional displacement history, while the output data consists of the force – displacement relations along the main directions.

Basics of multiple shear spring (MSS) model

The MSS model was proposed by Wada as an elegant solution to simultaneously account for the nonlinear restoring force and for the effect of interaction between the horizontal displacement components. The model consists of a number N_s of shear springs evenly distributed in a circular configuration (Fig. III-15). Although the characteristics of each spring (stiffness and yield force) can be set independently, for the purpose of the present study all the spring elements have been assigned the same characteristics to eventually meet the overall bilinear behavior of the system. The number of springs considered, $N_s = 16$, was selected by carefully optimizing the accuracy of the results and the time required to run the analysis.

By assuming that the system has the same behavior in every direction, and denoting its rigidity with K and its yield force with Q_y, the corresponding characteristics of a spring element are obtained as follows:

$$k_{s,i} = K \bigg/ \sum_{i=1}^{N_s} \cos^2\theta_i \qquad \text{(III.6a)}$$

$$q_{s,i} = Q_y \bigg/ \sum_{i=1}^{N_s} \left|\cos\theta_i\right| \qquad \text{(III.6b)}$$

where K is the stiffness (k_e, k_p in Table III-4) of the system (a unit of 4 damper elements)

Q_y is the yield force of the system (Q_y in Table III-4)

$k_{s,i}$ is the stiffness of a spring element i

$q_{s,i}$ is the yield force of spring element i

N_s is the number of spring elements

θ_i is the angle between spring element i and x axis (Fig. III-15).

The angle θ_i each spring element forms with x axis is obtained as shown in Fig. 15c, using Eq. (III.7):

$$\theta_i = \frac{\pi}{N_s}(i-1) \quad i = \overline{1, N_s} \tag{III.7}$$

The restoring force of the system at time step j is obtained by adding the incremental contributions of all the spring elements to the restoring force at the previous time step (Eq. (III.8)).

$$\begin{bmatrix} \Delta Q_x \\ \Delta Q_y \end{bmatrix} = \sum_{i=1}^{N_s} k_{s,i} \begin{bmatrix} \cos^2\theta_i & \cos\theta_i \cdot \sin\theta_i \\ \cos\theta_i \cdot \sin\theta_i & \sin^2\theta_i \end{bmatrix} \cdot \begin{bmatrix} \Delta\delta_x \\ \Delta\delta_y \end{bmatrix} \tag{III.8}$$

where $\Delta Q_x, \Delta Q_y$ are the increments of the restoring force of the system on x and y directions

$\Delta\delta_x, \Delta\delta_y$ are the displacement increments of the system on x and y directions.

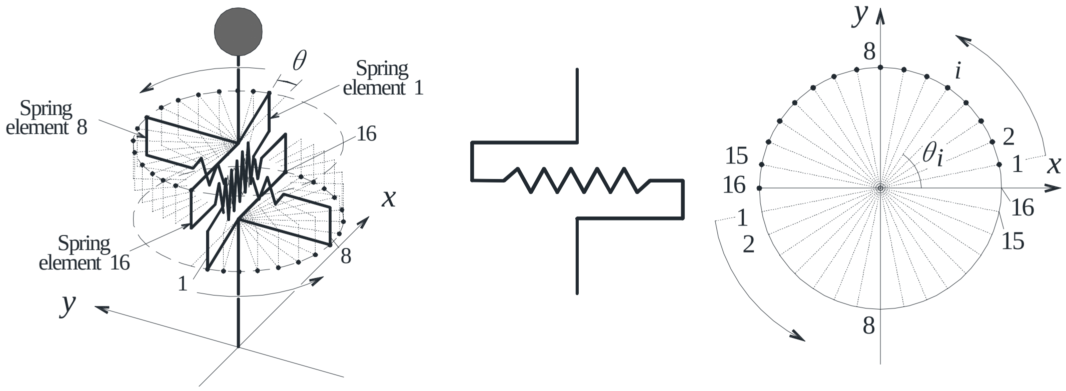

(a) Overall configuration (b) Spring element (c) In-plane configuration

Figure III-15. Multiple Shear Spring (MSS) model.

The difference between the targeted bilinear hysteretic model proposed in this section and the characteristics of a single spring element are illustrated in Fig. III-16. In the left hand side the displacement yield surfaces normalized against the yield displacement of the bilinear hysteretic model δ_y are shown. For the considered number of springs, the yield displacement of a single spring, obtained by dividing Eq. (III.6b) by Eq. (III.6a), is approximately 0.79 times δ_y. In the right hand side of Fig. III-16, the normalized restoring forces of the bilinear model, respectively of a single spring are shown against the normalized displacement. In addition, the hysteretic model which results by applying MSS is also depicted. It is worth noticing that the theoretically defined yield point considered by the bilinear model becomes a smooth transition from the elastic to the plastic range, simulating in a much more realistic way the behavior of U-shaped steel dampers.

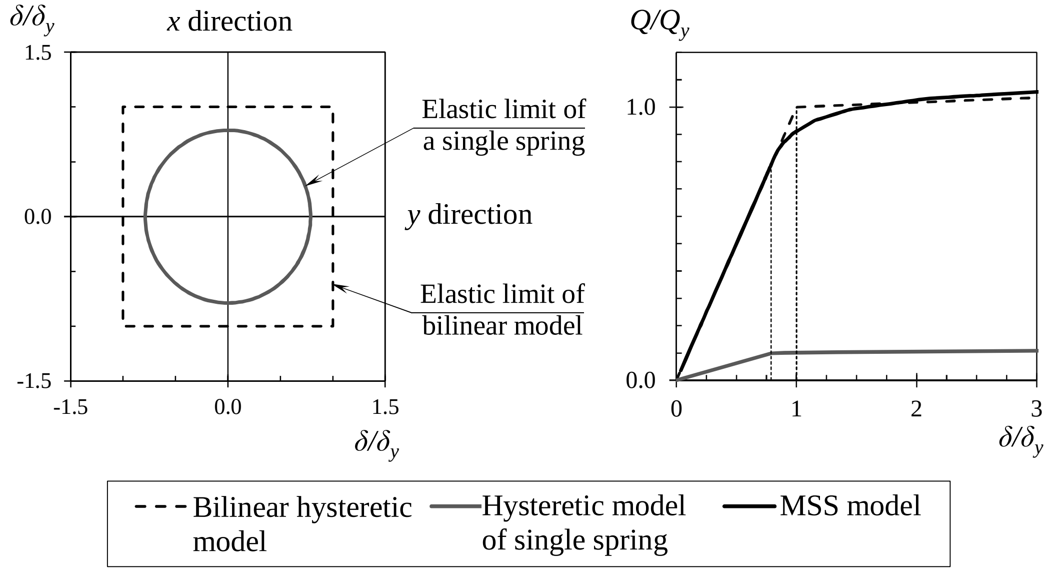

Figure III-16. Difference between the targeted bilinear hysteretic model (dashed line) and characteristics of a single spring (gray line).

III.4. Validation of the model against test results

In this section, the proposed analytical model described in Section III.3 is validated against the test data, namely the force – displacement relations. For this purpose, the analytical hysteresis curves on x, respectively on y direction are compared to the experimental ones and their difference is evaluated by using a statistical indicator, namely the correlation coefficient ρ [III.4].

The correlation coefficient ρ is a statistical indicator that determines whether there is a linear relation between two random variables, X and Y (Eq. (III.9)). Its values are situated in the interval [-1, 1], where $\rho = +1.0$ means that X linearly increases with Y, and $\rho = -1.0$ means that X linearly decreases as Y increases. Values of the correlation coefficient approaching -1.0 or 1.0 indicate the existence of a linear relation between the considered random variables (Fig. III-17).

$$\rho = \frac{Cov(X,Y)}{\sigma_X \cdot \sigma_Y} \tag{III.9}$$

$$Cov(X,Y) = E[(X - E(X))(Y - E(Y))] \tag{III.10}$$

where ρ is the correlation coefficient

X, Y are the random variables whose coefficient of correlation is computed

$Cov(X,Y)$ is the covariance of the 2 random variables (Eq. (III.10))

σ_X, σ_Y are the standard deviations

operator $E(A)$ is the mean of random variable A.

In the present study, the random variables X and Y are the force obtained analytically and the force measured during the loading tests. Hence, to evaluate the validity of the proposed analytical model, the correlation coefficient between the two sets of data is determined. It should be noted that, due to the fact that the same displacement histories are used for both cases, the values of the correlation coefficient should theoretically be equal to 1.0. In addition, it is necessary to mention that the correspondence of both hysteresis curves on x direction and those on y direction is assessed, therefore, a given displacement history, two correlation coefficients are obtained: one for the force on x direction ρ_x, the other for that on y direction ρ_y.

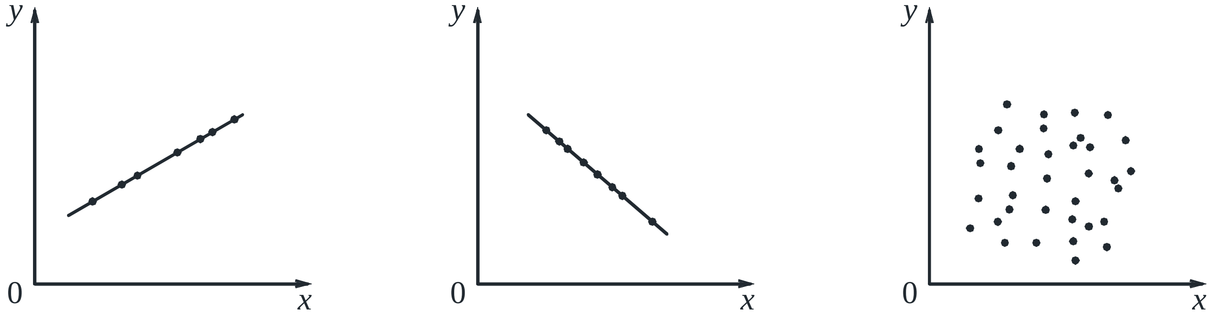

(a) $\rho = +1.0$ (b) $\rho = -1.0$ (c) $\rho = 0$

Figure III-17. Significance of correlation coefficient ρ.

The validation of the model is conducted in two steps: (1) first, the accuracy against the one-directional quasi-static loading tests described in Section III.2 is assessed, and second (2) the accuracy against the dynamic tests with realistic bidirectional displacement orbits (***Chapter II***) is evaluated to determine whether extrapolating the characteristics found for units of 4UD40 elements to units of 4UD50 size has any impact on the prediction of the force – displacement relations.

III.4.1. Validation against the one-directional quasi-static test results

The force – deformation relations obtained in the first and second one-directional loading sets are compared to those obtained analytically. To get a general image on how well the two sets of data match, they are plotted on the same graphic in Fig. III-18 for each specimen. Further on, the correspondent correlation coefficients are computed and shown in Fig. III-19, where the analytical values of the restoring force are plotted against the experimental ones. It is observed that for specimen 1D-U1, the correlation coefficient on both loading directions are greater than 0.992. For the other 2 specimens, due to the fact that the analytical model does not account for the decrease of the maximum force, ρ slightly decreases (0.988 for 1D-U2).

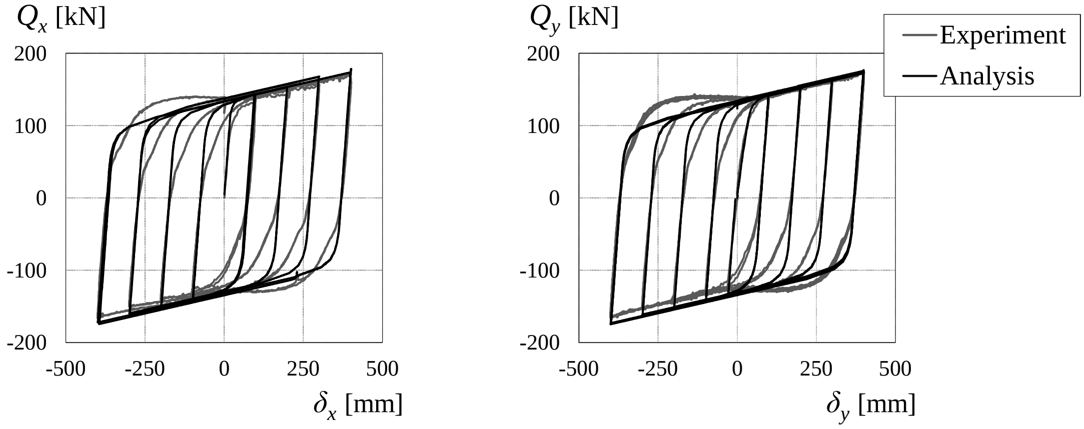

(a) Specimen 1D-U1

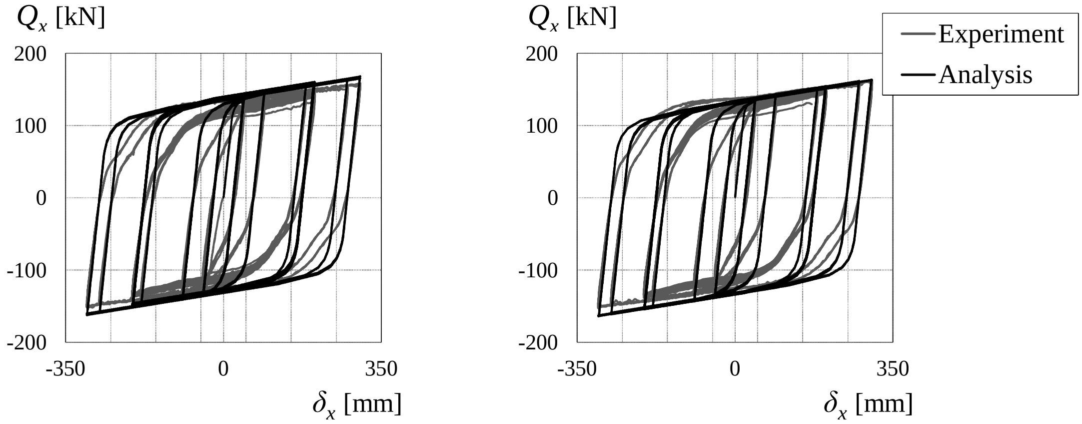

(b) 1D-U2 (c) 1D-U3

Figure III-18. Experimental (gray) vs. analytical (black) results for 1D-U1, 1D-U2 and 1D-U3.

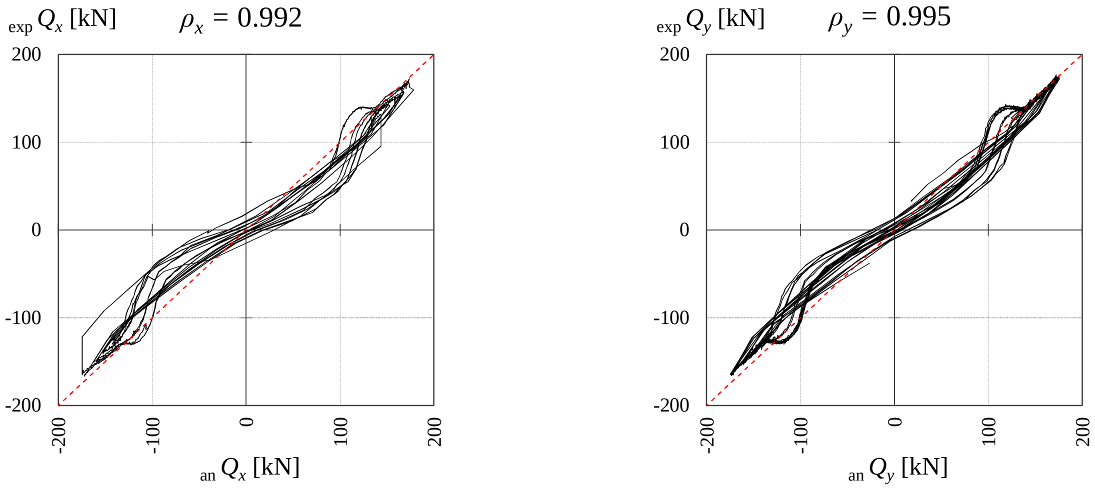

(a) 1D-U1 (*x* direction) (b) 1D-U1 (*y* direction)

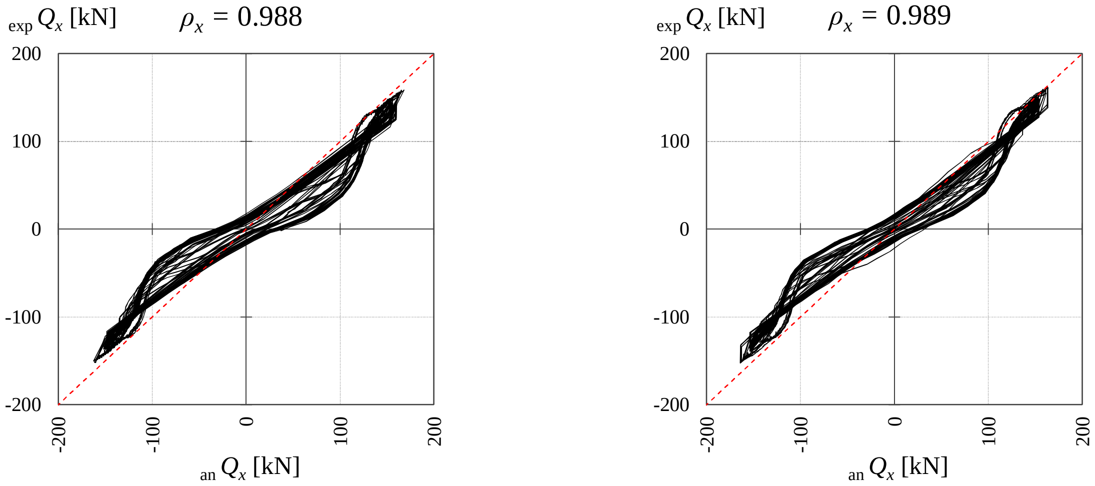

(a) 1D-U2 (b) 1D-U3

Figure III-19. Experimental (ordinate) vs. analytical (abscissa) results for 1D-U1, 1D-U2 and 1D-U3 and corresponding correlation factors ρ.

Table III-5. Correlation coefficients ρ

Specimen	Loading direction	ρ
1D-U1	*x*	0.992
	y	0.995
1D-U2	*x*	0.988
1D-U3	*x*	0.989

The obtained values of the correlation coefficients are all greater than 0.985 (Table III-5), which means that there is almost a linear relationship between the experimental and analytical restoring forces. This proves that the proposed analytical model is able to simulate with very good accuracy the behavior of U-shaped steel dampers under one-directional loading.

III.4.2. Validation against the bidirectional dynamic loading tests

The experimental data gathered in ***Chapter II*** are used here to verify the validity of the proposed analytical model for the case of realistic bidirectional loading. The specimens tested were units of 4UD50, therefore the corresponding bilinear hysteretic model given in Table III-4 is employed. To investigate the accuracy of the analytical model in predicting the force – deformation relations after a specimen was loaded several times, the correlation coefficients of x and y directions ρ_x and ρ_y are computed for the first 3 loadings of each specimen (U1, U2, U3 and U4). The relations between the experimental and analytical sets of data on each direction are plotted in Figures III-21 to III-23. The values of ρ_x, respectively ρ_y are also shown and are summarized in Table III-6.

Specimen U4 was loaded first with accelerograms recorded during Tohoku 2011 earthquake in a monitored hospital building (Ishinomaki hospital). One can recall from previous chapter that these recordings were not applied a scale factor to reach the maximum displacement of 400(mm), therefore the corresponding deformations are mainly in the elastic range, only leading to short excursions in the plastic range. For this reason, the following three displacement orbits loaded after Ishinomaki hospital ones are also investigated.

Based on the obtained results, the following remarks can be drawn:

- All the values of the correlation coefficients are larger than 0.935, with the exception of Sylmar – Olive View on x direction, which is 0.895. However, when compared to the values of the correlation coefficients obtained for the specimens under one-directional loading (Table III-5), the values are slightly smaller, even for the first loading cycles.
- The correlation coefficients for the first loading cycle of each specimen are slightly greater than those for the following cycles, which means that the proposed analytical model works best when employed to simulate the behavior of U-shaped steel dampers that are not subjected to extensive inelastic deformations until fracture. However, the correlation between experimental and analytical data is still well inside the acceptable range.

The experimental and analytical force – deformation relations for the considered loading histories are shown in Annex A.

Table III-6. Correlation coefficients ρ for dynamic loading tests

Specimen	Ground motion	Loading cycle	ρ_x	ρ_y
U1	Takatori	(1)	0.965	0.982
	Hachinohe	(2)	0.959	0.981
	Chihuahua	(3)	0.959	0.951
U2	Agnews Hospital	(1)	0.978	0.974
	Agnews Hospital	(2)	0.942	0.971
	Agnews Hospital	(3)	0.944	0.972
U3	JMA Sendai	(1)	0.956	0.976
	JMA Sendai	(2)	0.947	0.965
	JMA Sendai	(3)	0.948	0.963
U4	Ishinomaki hospital I	(1)	0.985	0.982
	Ishinomaki hospital II	(2)	0.981	0.974
	Sylmar – Olive View	(3)	0.895	0.957
	Newhall	(4)	0.968	0.935
	TCU078	(5)	0.961	0.939

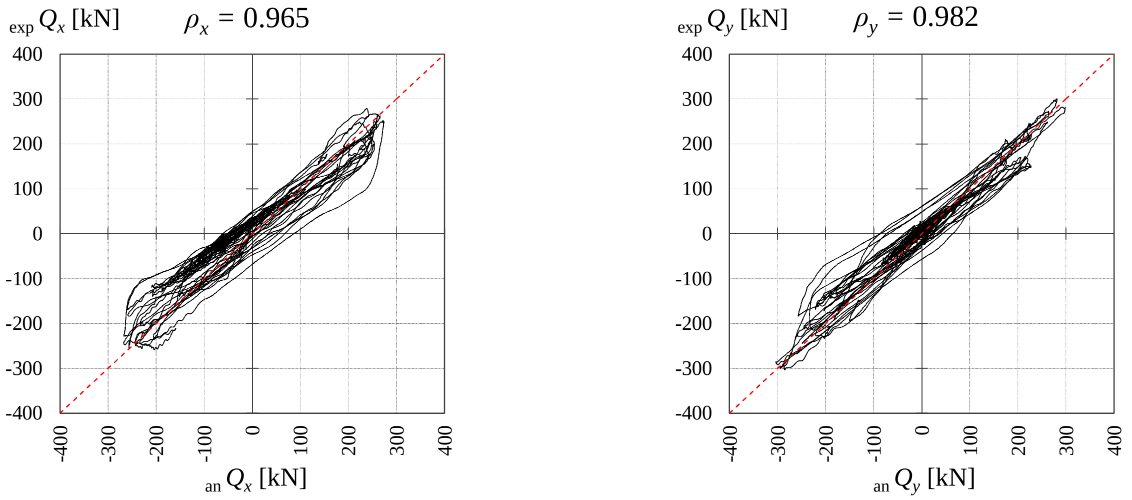

(a) Takatori (1st)

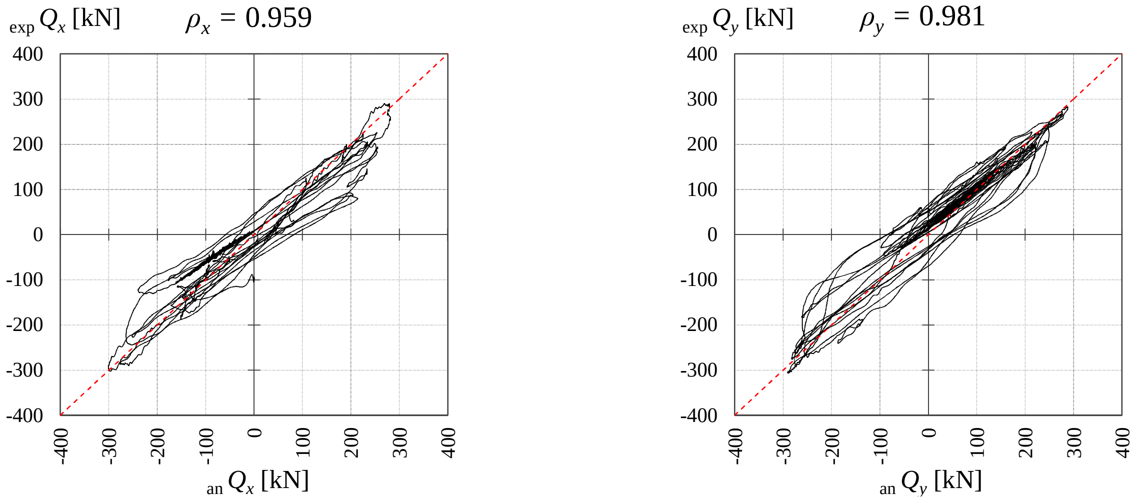

(b) Hachinohe (2nd)

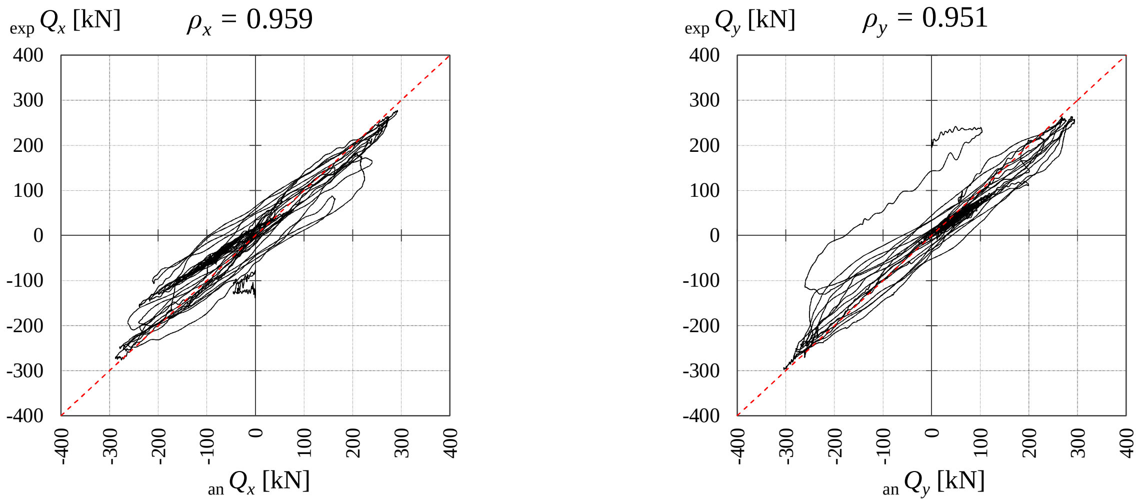

(c) Chihuahua (3rd)

Figure III-20. Correlation coefficient ρ between analytical results (on the abscissa) and test results (on the ordinate) for the first 3 loading histories of specimen U1. Graphics on the left: force on *x* direction; graphics on the right: force on *y* direction.

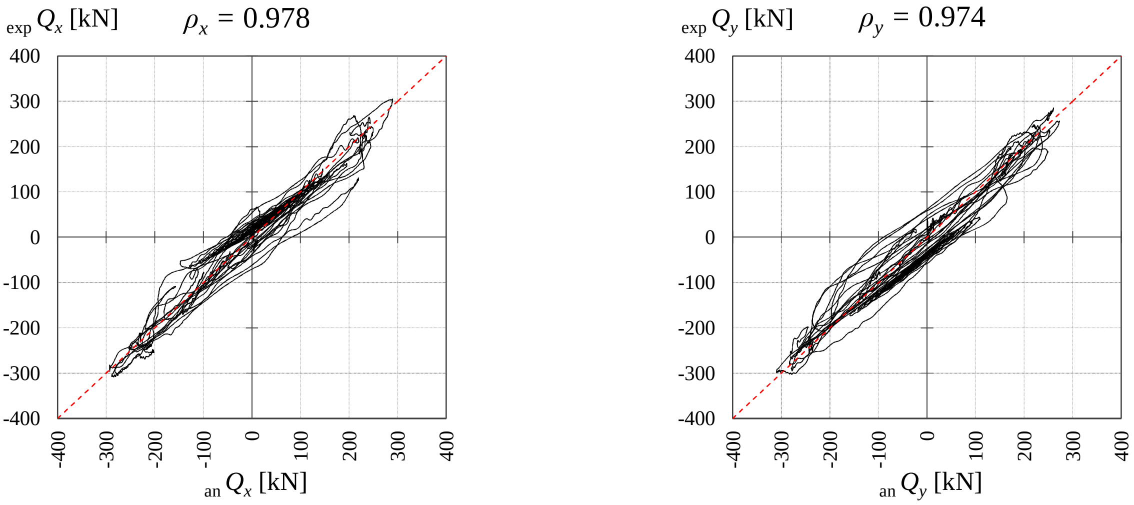

(a) Agnews Hospital (1st)

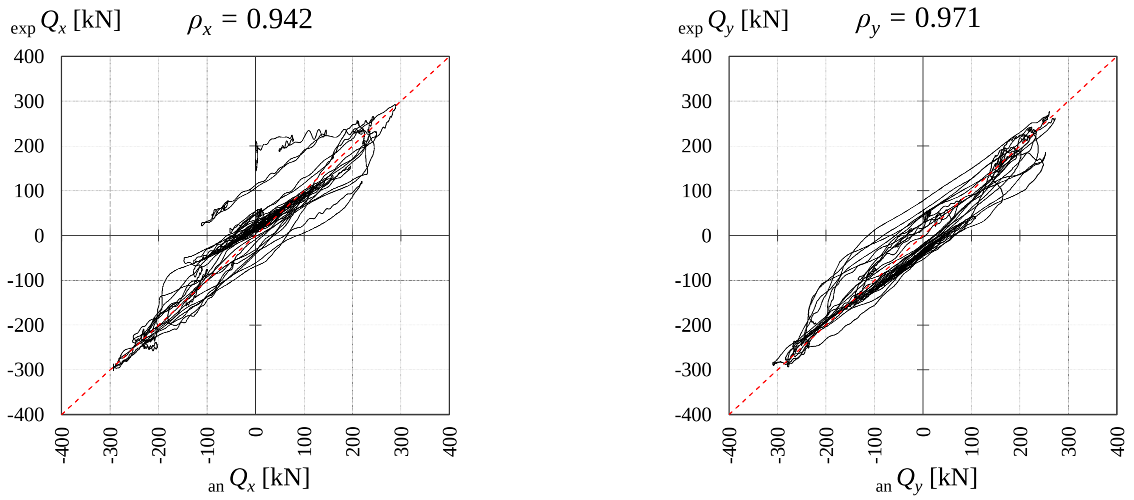

(b) Agnews Hospital (2nd)

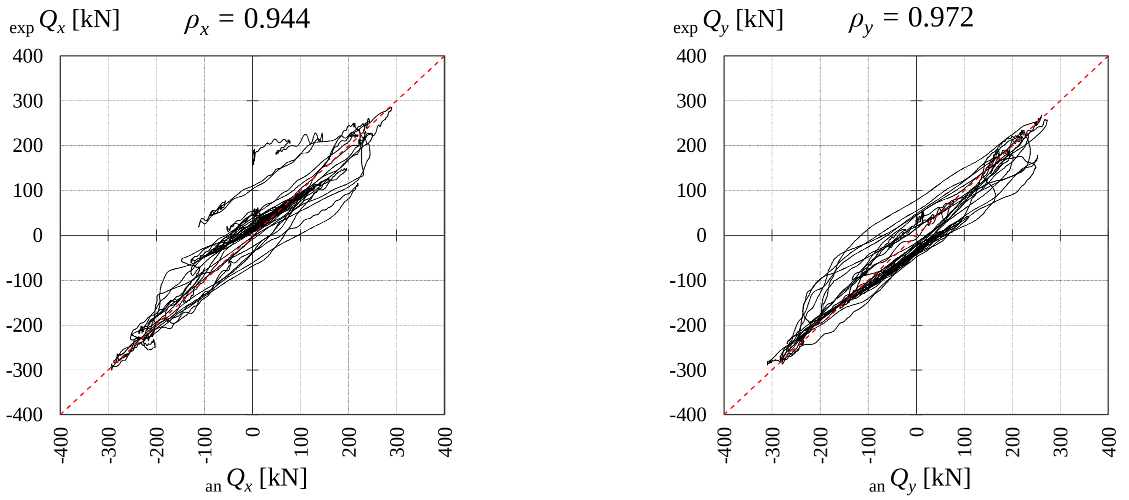

(c) Agnews Hospital (3rd)

Figure III-21. Correlation coefficient ρ between analytical results (on the abscissa) and test results (on the ordinate) for the first three loadings of specimen U2 (Agnews Hospital).

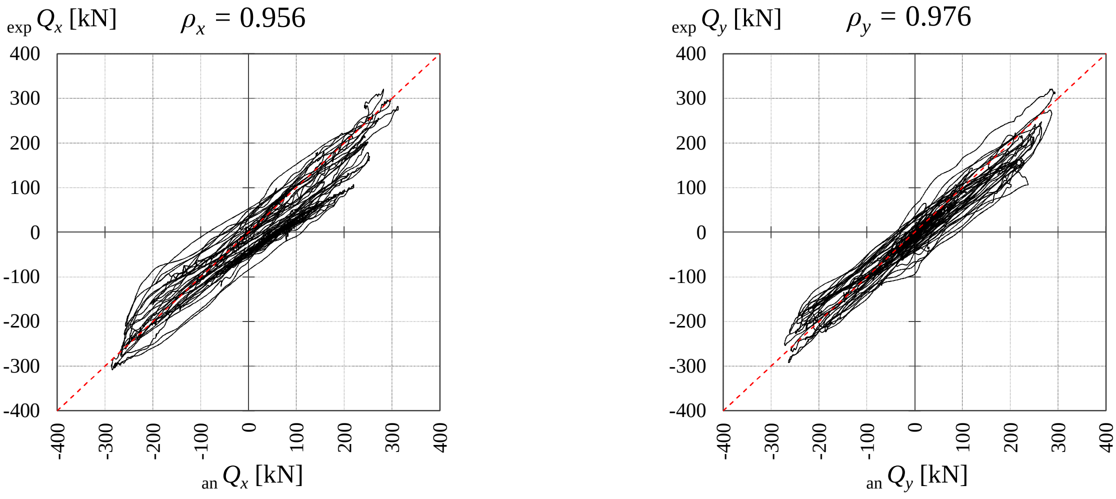

(a) JMA Sendai (1st)

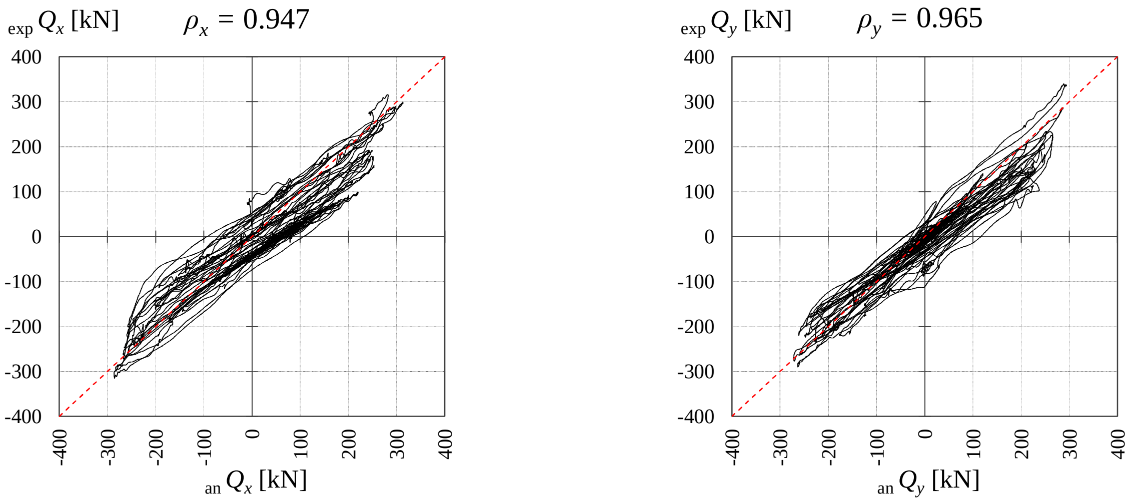

(b) JMA Sendai (2nd)

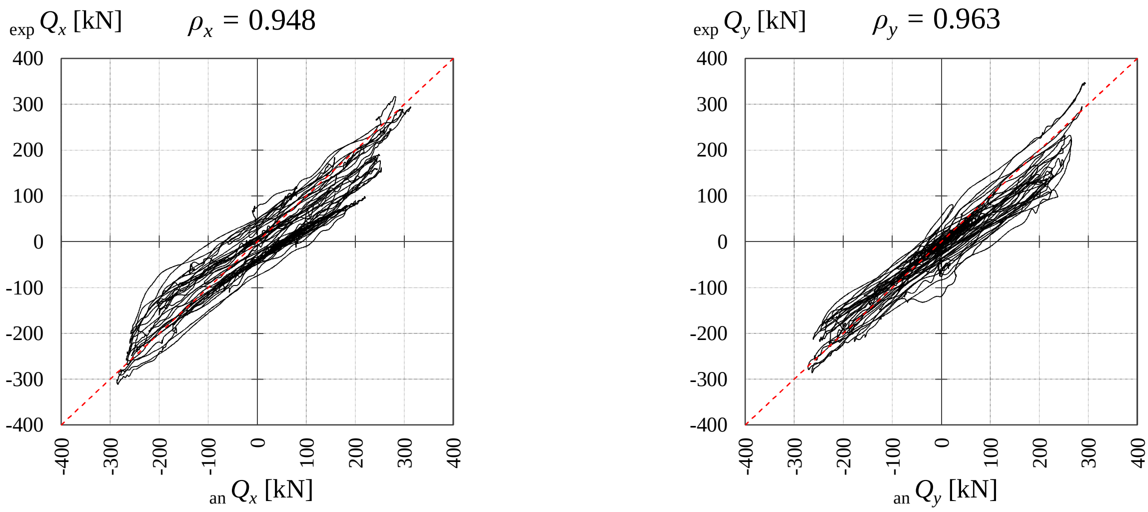

(c) JMA Sendai (3rd)

Figure III-22. Correlation coefficient ρ between analytical results (on the abscissa) and test results (on the ordinate) for the first three loadings of specimen U3 (JMA Sendai).

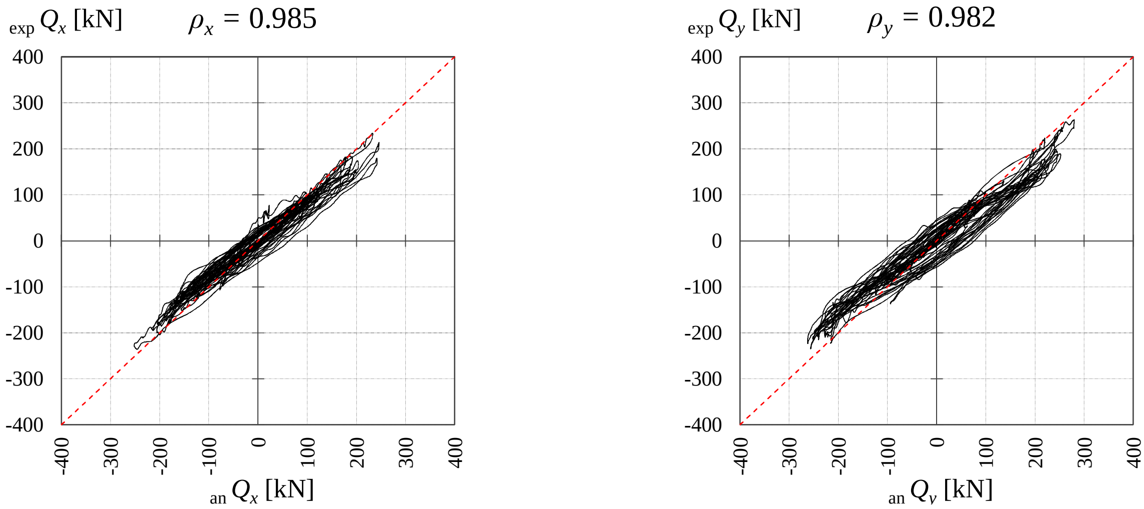

(a) Ishinomaki hospital part I (1st)

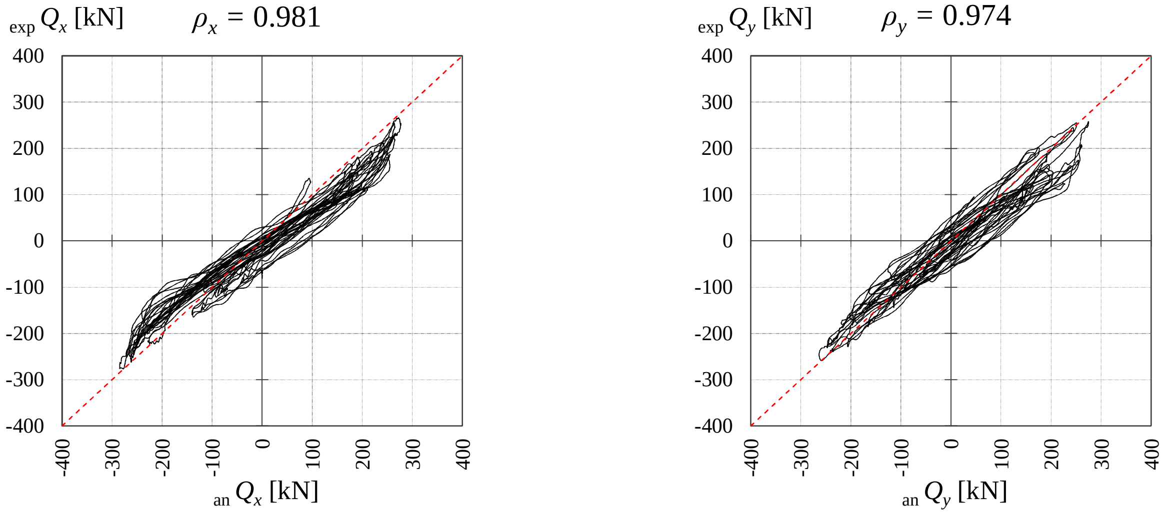

(b) Ishinomaki hospital part II (2nd)

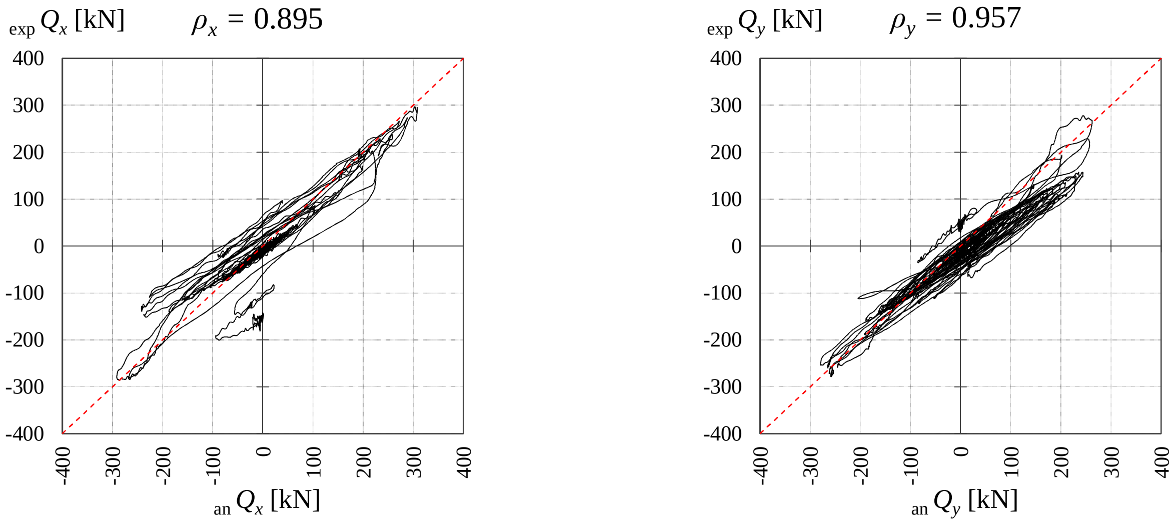

(c) Olive View (3rd)

Figure III-23. Correlation coefficient ρ between analytical results (on the abscissa) and test results (on the ordinate) for the first 5 loadings of specimen U4 (continued on next page).

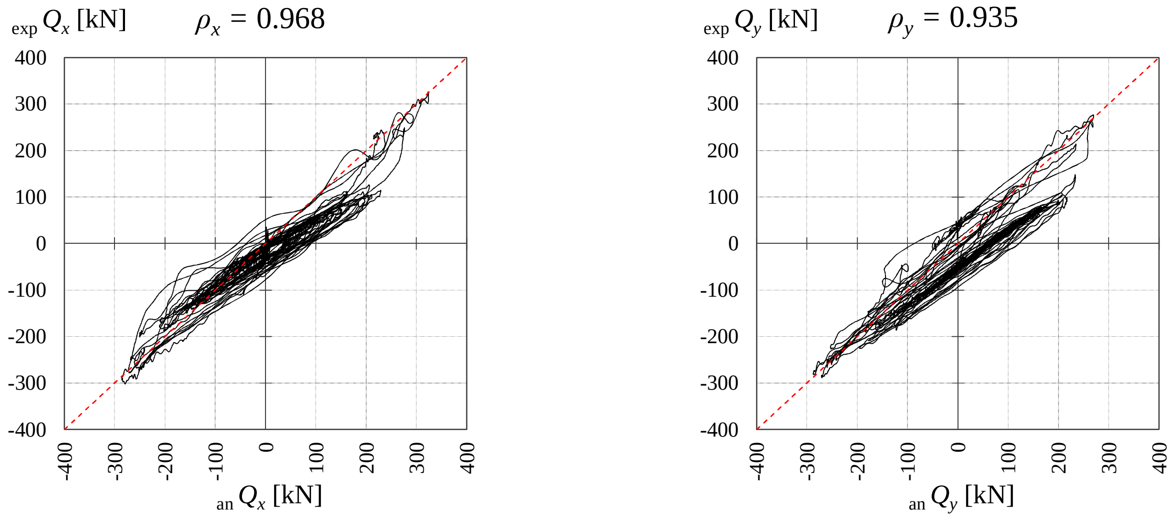

(d) Newhall (4th)

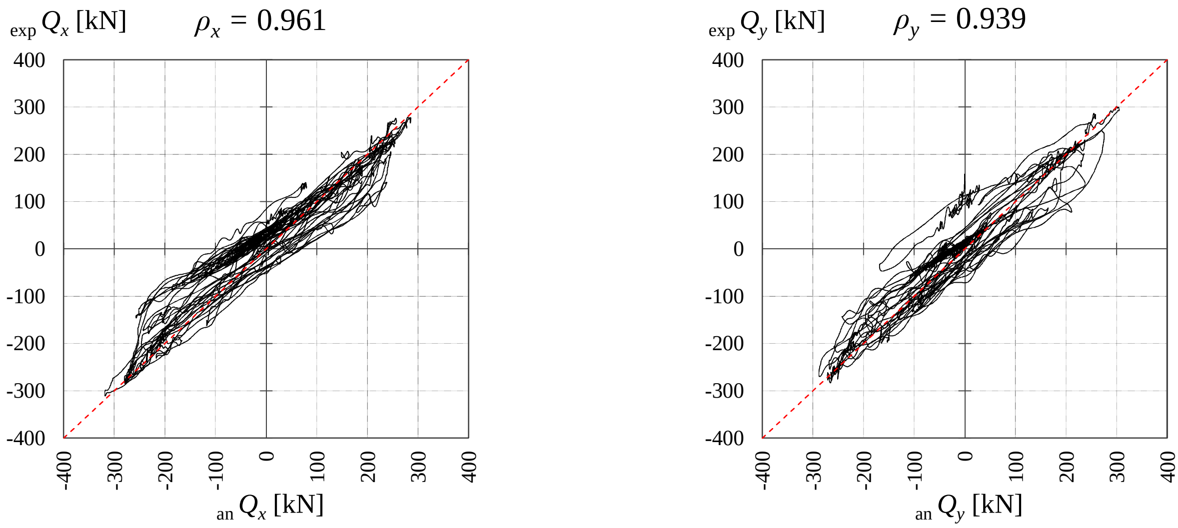

(e) TCU078 (5th)

Figure III-23. Correlation coefficient ρ between analytical results (on the abscissa) and test results (on the ordinate) for the first four loadings of specimen U4 (continued).

III.5. Summary

The main conclusions of this chapter are:

1. Two sets of one-directional loading tests were conducted to obtain the basic properties of units of 4UD40. Based on the obtained results, a normal bilinear hysteretic model was proposed and extrapolated to rest of the commonly used damper sizes.
2. An analytical model consisting of a combination between the bilinear hysteretic model and an MSS element was proposed to simulate the behavior of the dampers under bidirectional loading. Quasi-static analysis is conducted and the results consist of the force – deformation relations on x and y directions.
3. The proposed analytical model was validated against the experimental data. The correlation between the analytical and experimental force – deformation relations for the specimens subjected to one-directional loading was slightly higher (0.988~0.995) than that for the specimens under bidirectional loading (0.895~0.985). However, the difference is not significant and it can be stated that the proposed analytical model is able to simulate with good accuracy the force – deformation relations of U-shaped steel dampers subjected to bidirectional seismic excitation.
4. If several bidirectional displacement orbits are loaded upon the same specimen, the results obtained for the subsequent loading histories are not as accurate as for the first one. This is because of the fact that the model does not simulate the stiffness degradation of the specimen. Therefore the proposed model may not be as accurate if a loading history starting from initial post-elastic excursions and going all the way to fracture of the specimen is analyzed.

References

[III.1] 吉敷 祥一，高山 大，山田 哲，ENE Diana，小西克尚，川村典久，寺嶋正雄：水平2方向載荷下における繰り返し変形性能に関する実験 ：免震構造用U字形鋼材ダンパーの水平2方向特性（その1），日本建築学会構造系論文集　第680号, pp.1579-1588, 2012.10;

[III.2] American Society of Civil Engineers, Structural Engineering Institute, 2011. Minimum design loads for buildings and other structures – ASCE/SEI 7-10;

[III.3] 和田章，広瀬景一：2方向地震動を受ける無限均等ラーメン構造の弾塑性応答性状，日本建築学会構造系論文報告集，第399号，pp.37-47，1989.5;

[III.4] Ang, A.H-S., Tang, W.H., 2007 – Probability concepts in engineering. Emphasis on applications in civil & environmental engineering. 2nd edition, John Willey & Sons, Inc., USA, pp. 138-141.

Chapter IV

Reliability of U-shaped Steel Dampers as Seismic Isolation Devices for Base-Isolated Structures Subjected to Biaxial Excitation

IV.7.4. Normalized IDA curves

IV.8. Fragility curves

IV.9. Summary

IV.1. Introduction

Performance-based design is a modern framework for probabilistic assessment that relates seismic hazard to structural response, resulting damage, and economic loss, enabling owners to make informed decisions regarding the level of seismic risk. The correlation and interdependence of these four aspects require a logical process that is able to approach in a consistent manner various situations encountered in typical design. Several attempts have been made to address this issue, among which the one made by Vamvatsikos *et al.* was adopted in the present study [IV.1] - [IV.3]. In this methodology – named "Incremental Dynamic Analysis" (IDA) – individual ground motions are scaled to increasing intensities (Intensity Measure – *IM*) until the structure reaches a collapse point. Performance levels are defined in terms of one or more analytical parameters evaluating the structural damage (Damage Measure - *DM*), and their corresponding probabilities of exceedance are computed across the considered population of ground motions.

The objectives of this chapter are: (1) evaluate the performance of U-shaped steel dampers subjected to different levels of two-dimensional seismic excitation, (2) construct relations between the damage of U-shaped steel dampers and seismic intensity, and (3) derive fragility curves for considered limit states.

To meet these objectives with a satisfying degree of reliability, this would require an extensive database with ground motions of various intensities, ranging from "frequent" to "rare" and "very rare" events. Building such a database requires tremendous effort and is beyond the scope of the present study, fact which renders IDA approach as a more practical solution, since it allows filling the gaps between different seismic intensities by increasingly scaling the considered ground motions.

In this chapter, a set of seismic records suitable for base-isolated structures is selected (Section IV.2) and employed to conduct IDA. The cumulative damage index D_2 and sway-motion index J_f – whose fidelity for the case of seismic motions was confirmed in ***Chapter II*** – are adopted to evaluate the damage of U-shaped steel dampers subjected to bidirectional realistic loadings. The analytical model differs from that described in ***Chapter II*** in that that the restoring force characteristics of the dampers are bilinear (as proposed in ***Chapter III***). In addition, the yield base shear coefficient α_s of the dampers is introduced as a parameter to investigate how the amount of dampers introduced in the isolation layer affects its displacement response and what is the optimum value of α_s at which the dampers are used most efficiently. Further on, IDA curves are drawn in terms of geometric mean horizontal component of the peak ground velocity PGV_{gm} (*IM*) and bidirectional cumulative damage index D_2 (*DM*) as described in Section IV.7. Both these indices were carefully selected to faithfully express the bidirectional characteristics of the input ground motions and of the damage taken by the dampers. Based on the resulting data, fragility curves were constructed for a set of limit states and performance levels defined in Section IV.8.

IV.2. Ground motion set

In the process of assessing the performance of a structure under different levels of seismic hazard, selecting a suitable ground motion set is a critical step that can significantly influence the accuracy of the obtained results (*e.g.* fragility curves, mean annual frequency of exceedance etc). Current practices favor the use of empirical recordings of ground motions over artificial accelerograms because they present reliable characteristics (amplitude, frequency and energy content, duration and phase characteristics) and don't require additional computational efforts. This comes with the disadvantage that – as it usually is the case for most site locations – the number of the available time-histories may be too small to form a database necessary for a probabilistic assessment of the performance of a structure. One of the state-of-art methods to overcome this obstacle is incremental dynamic analysis (IDA) proposed by Vamvatsikos and Cornell (2002) [IV.1], which scales the ground motions to cover the entire intensity range from frequent to very rare events. This method was adopted in the present study due to the fact that it offers the possibility to construct a continuous relation between the bidirectional damage of a U-shaped steel damper and a suitable intensity measure. The record-to-record variability is captured by using several ground motions.

In the selection of the ground motion set, the following main aspects were considered:

- ***Very strong motions*** are required since one of the most important objectives is to assess the seismic demand that causes the dampers to reach their ultimate limit state.
- ***Far-field records*** are adopted here because there is a considerable amount of unresolved issues concerning the characterization of near-fault hazards and ground motion effects. In addition, as it was observed by Somerville (2002) and confirmed by Mavroeidis (2002), in the long period range, the acceleration response spectra for near-fault records of moderate-to-large earthquakes are weaker than those for far-field records of large events [IV.4][IV.5].
- Reliable ***long period content*** is necessary because the isolation period has, by definition, large values (usually above 2(sec)) as to reduce the response of the upper-structure.

The minimum required number of ground motions necessary to obtain an unbiased estimation of the seismic demand remains a controversial subject. For comprehensive multi-objective performance assessments, the number of ground motions can go as high as several hundreds. On the contrary, in design practices such as the US standard ASCE/SEI 7-10 [IV.6] and Eurocode 8 [IV.7], the number of ground motions may be as low as 3, if the maximum structural response is considered, or 7, if the average response is targeted.

FEMA P695 [IV.8] provides guidelines for the estimation of collapse capacity of a structure via nonlinear time-history analyses obtained with IDA. The ground motions considered here are divided into 2 sets to account for the effect of site-to-source distance: near-fault set and far-field set. The present study considers the far-field set for which the selection criteria developed by Haselton and Deierlein (2008) were applied to obtain strong motions that may cause structural collapse of modern buildings [IV.9]:

- Magnitude > 6.5
- Peak ground acceleration > 0.2g ***and*** peak ground velocity > 15(cm/s)
- Site-to-source distance > 10(km)
- Limit of 2 records from a single seismic event
- Lowest usable frequency < 0.125(Hz)
- Records labeled in the PEER-NGA database as "free field"
- Soil shear wave velocity in the upper 30(m) of soil > 180(m/s) (stiff soils)

It is worth noting that in FEMA P695, the lowest frequency is set to 0.25(Hz). This value is not suitable for base-isolated structures, where records having reliable long period contents are required. A more appropriate value is 0.125(Hz), which is consistent with the structural model and was, therefore, considered here. Due to this fact, some of the records listed in the far-field set given in FEMA P695 had to be excluded. In addition, two acceleration time-histories recorded during the Tohoku 2011 strong motion event were included (JMA Sendai and K-net Koriyama). These 2 records were selected because the buildings located in the nearby area presented significant structural damage (Fig. IV-1).

The resulting number of considered stations is 17 (Table IV-1), which means a total of 34 acceleration time-histories, since both horizontal components were adopted. All the ground motions except for those corresponding to Tohoku 2011 earthquake were selected from the next-generation attenuation (NGA) strong motion database developed by the Pacific Earthquake Engineering Research Center. The quantities PGA_{gm} and PGV_{gm} listed in Table IV-1 are the geometric means of the peak ground acceleration, respectively peak ground velocity computed by considering different sensor orientation [IV.10].

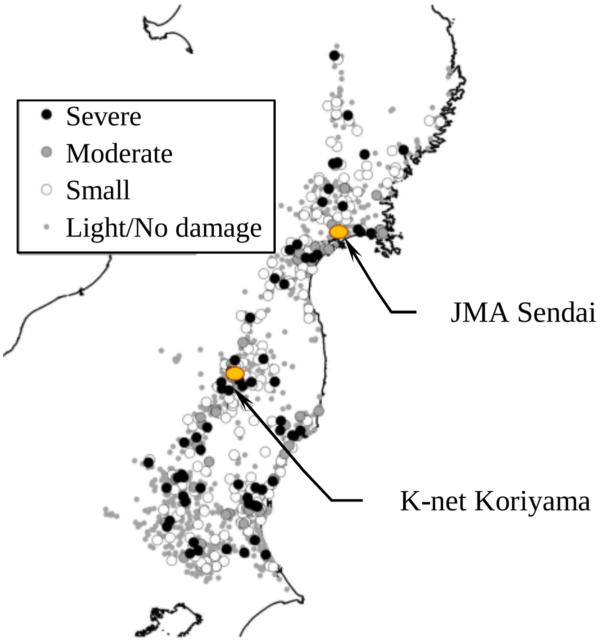

Figure IV-1. Damage to steel structures (school buildings) after Tohoku 2011 and location of JMA Sendai and K-net Koriyama stations [IV.11].

Table IV-1. Ground motion set

Earthquake				Station		PGA_{gm} (*)	PGV_{gm} (*)
No.	M	Year	Name	Full name	Abv.	[g]	[cm/s]
1	9.0	2011	Tohoku	JMA Sendai	TSD	0.419	51.80
2				K-net Koriyama	TKY	1.118	52.40
3	7.4	1990	Manjil	Abbar	MAB	0.505	43.78
4	7.3	1999	Chi-Chi	TCU045	TC0	0.473	38.89
5				TCU129	TC1	0.788	47.34
6	7.3	1992	Landers	Yermo Fire Station	LYF	0.223	36.89
7				Coolwater	LCW	0.373	34.64
8	7.2	1995	Kobe	Nishi-Akashi	KNA	0.486	35.73
9				Shin-Osaka	KSO	0.229	32.82
10	7.1	1999	Hector Mine	Hector	HMN	0.306	34.21
11	7.1	1999	Duzce	Bolu	DBL	0.766	59.68
12	7.0	1992	Cape Mendocino	Rio Dell Overpass	CMR	0.424	47.95
13	6.9	1989	Loma Prieta	Gilroy Array #3	LPG	0.462	43.11
14	6.7	1994	Northridge	Canyon Country - WLC	NCC	0.436	43.33
15	6.5	1987	Superstition Hills	El Centro Imp. Co.	SHE	0.293	45.16
16	6.5	1979	Imperial Valley	Delta	IVD	0.285	29.75
17	6.5	1976	Friuli	Tolmezzo	FTZ	0.346	25.06

(*) Except for Tohoku earthquake (No. 1 and 2) all the values for PGA_{gm} and PGV_{gm} are those listed in the PEER-NGA strong motion database obtained as the geometric mean considering different sensor orientation. For Tohoku, the vector sum of the 2 horizontal components is used.

It is worth noting that the largest PGA_{gm} is 1.118(gal) (Tohoku, Koriyama), while the smallest one is 0.223(gal) (Landers, Yermo fire station), which reflects in a fairly large coefficient of variance, $\delta_{PGA_{gm}} = 0.494$. Regarding PGV_{gm}, the largest value is 59.68(cm/s) (Duzce, Bolu), while the smallest is 25.06(cm/s) (Fruili, Tolmezzo), resulting in a reasonably small coefficient of variation, $\delta_{PGV_{gm}} = 0.218$. This fact suggests that among the 2 quantities, PGV_{gm} is the most suitable to be selected as intensity measure. This aspect is discussed in detail in Section IV.5.

The acceleration time-histories for all records are shown in Fig. IV-2, from which it can be observed that no pulse-like excitations are employed. JMA Sendai, K-net Koriyama (Tohoku), Abbar (Manjil) and Delta (Imperial Valley) have a large number of zero-acceleration crossings corresponding to relatively large acceleration amplitudes. It is, thus, expected that the amount of induced damage upon U-shaped steel dampers will be significant for these particular records.

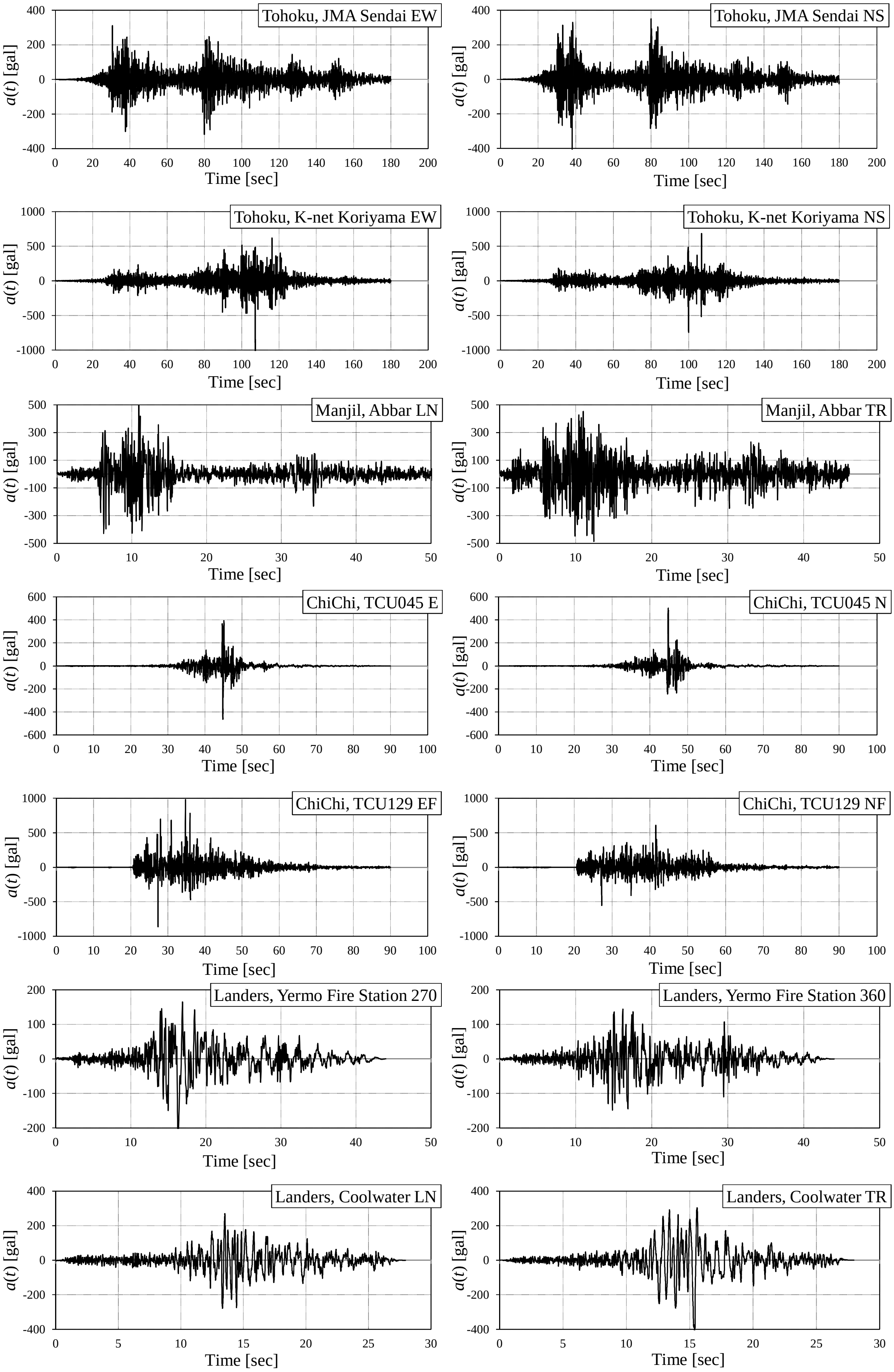

Figure IV-2. Acceleration time-histories (1)

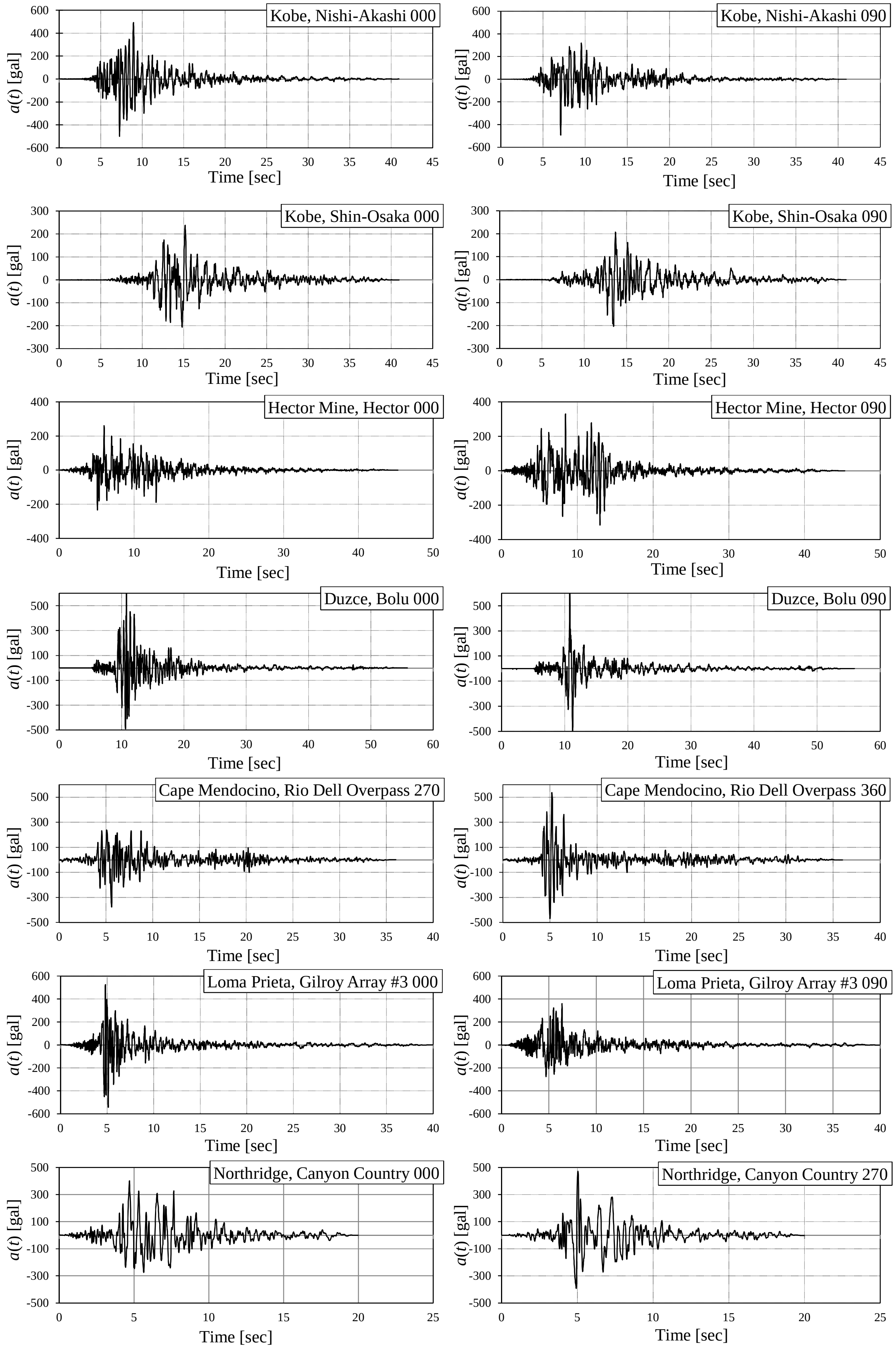

Figure IV-2. Acceleration time-histories (2)

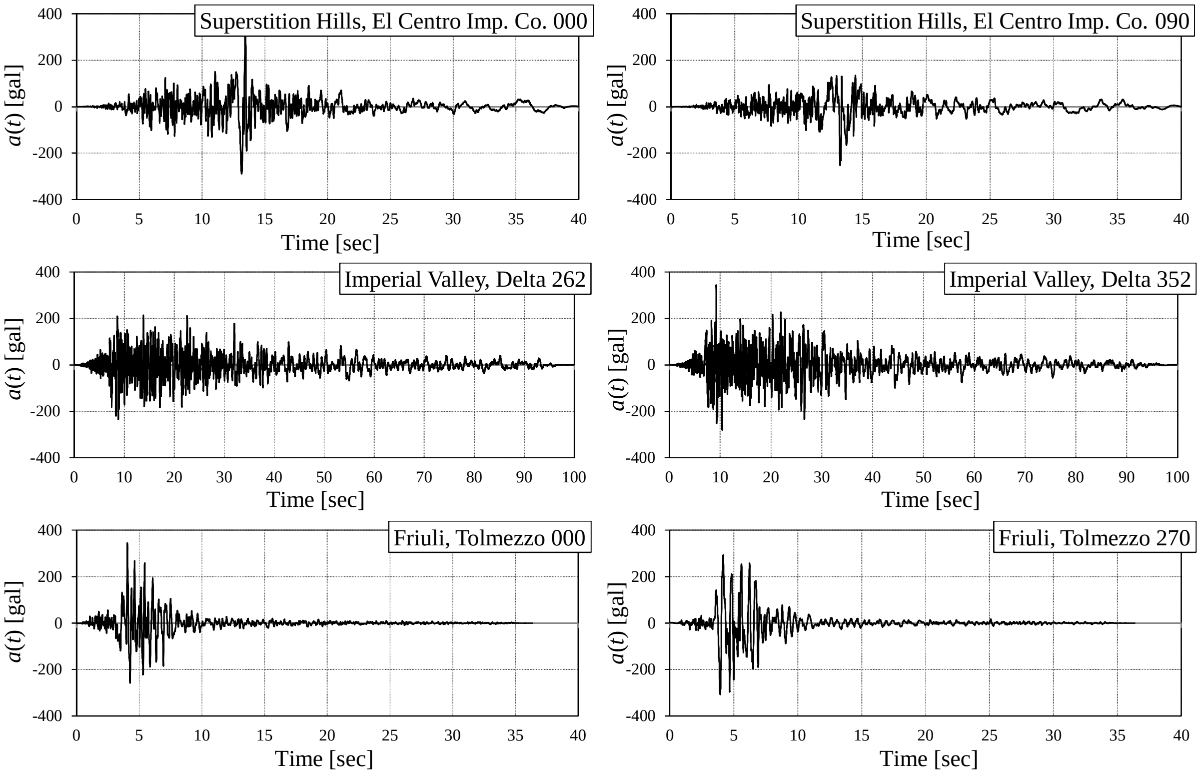

Figure IV-2. Acceleration time-histories (3).

The acceleration spectra of each ground motion at 2% of the critical damping are plotted in Fig. IV-3. At the considered effective period, T_{eff} = 4.0(sec), the smallest values for S_a(4(sec), 2%) are obtained for Cape Mendocino (Rio Del Overpass) and Friuli (Tolmezzo), while the largest ones for ChiChi (TCU045) and Manjil (Abbar).

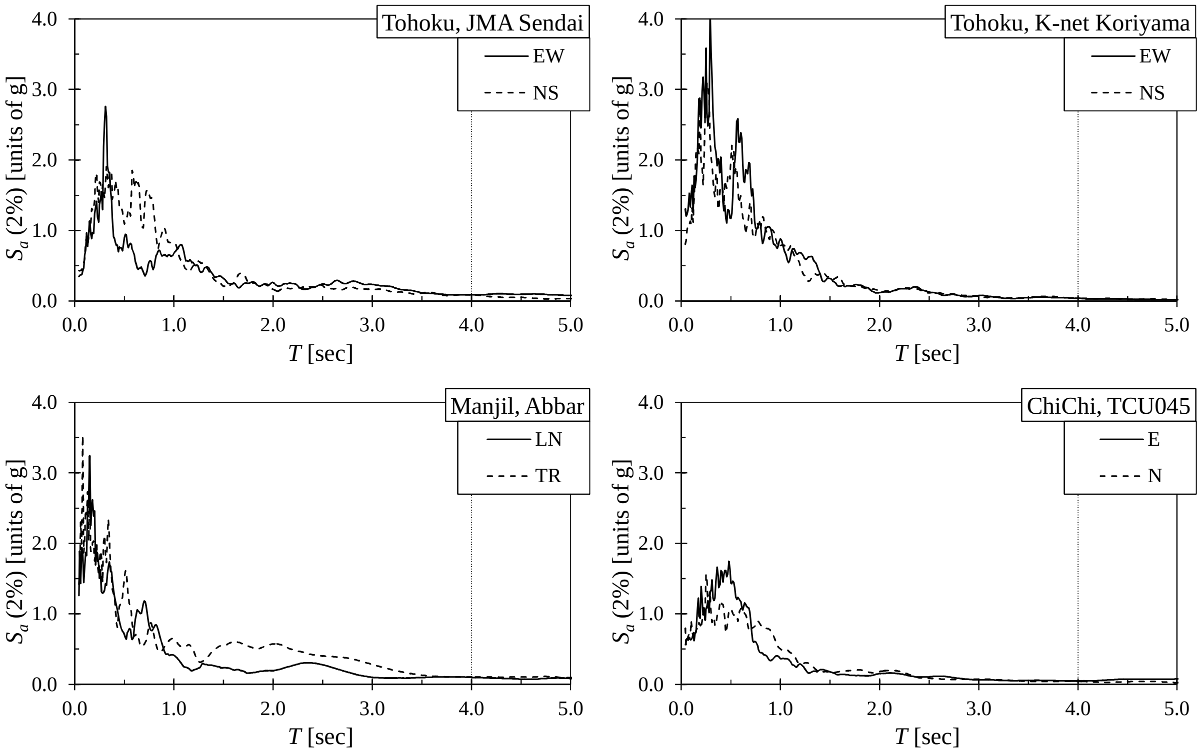

Figure IV-3. Acceleration spectra for 2% damping ratio (1)

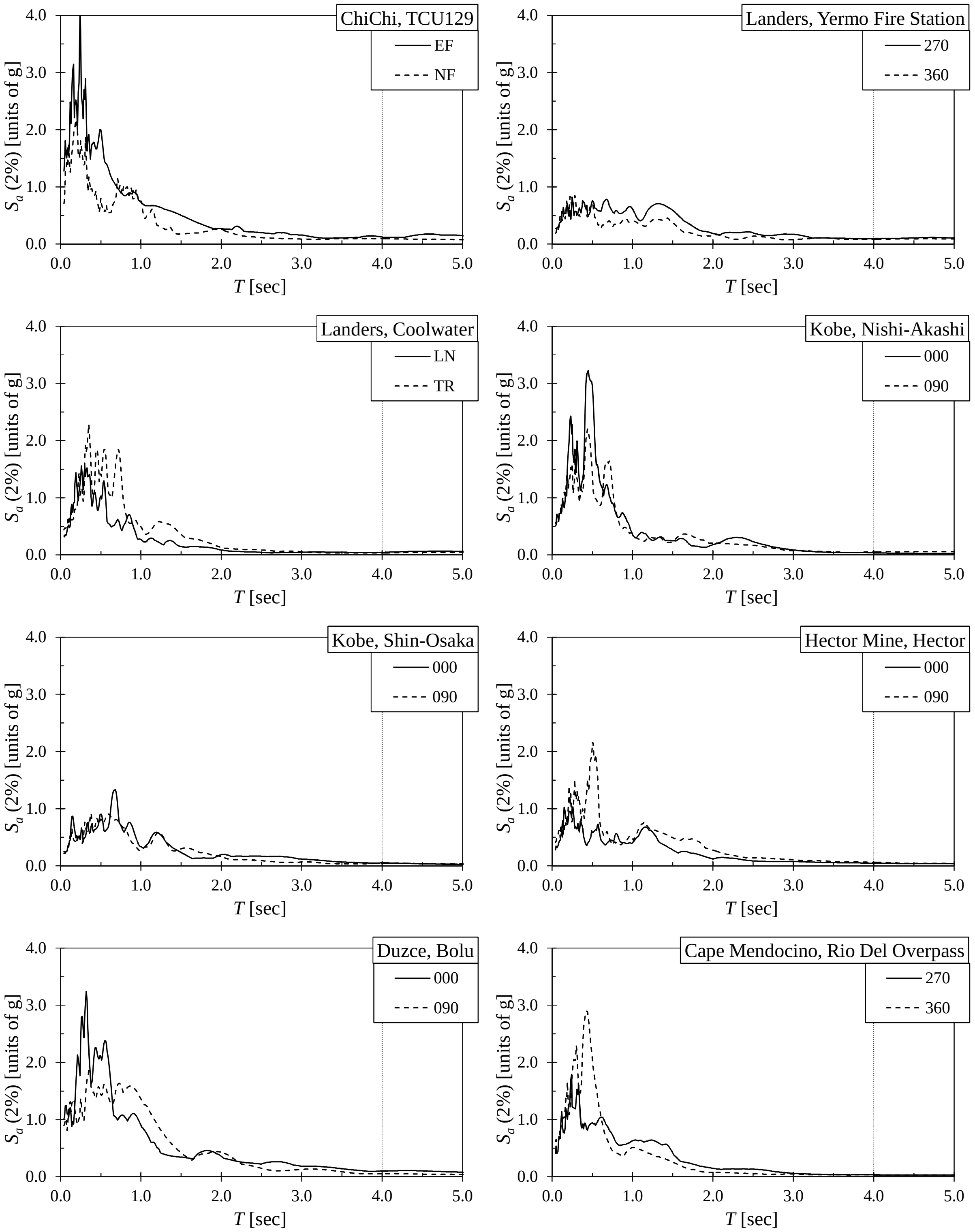

Figure IV-3. Acceleration spectra for 2% damping ratio (2)

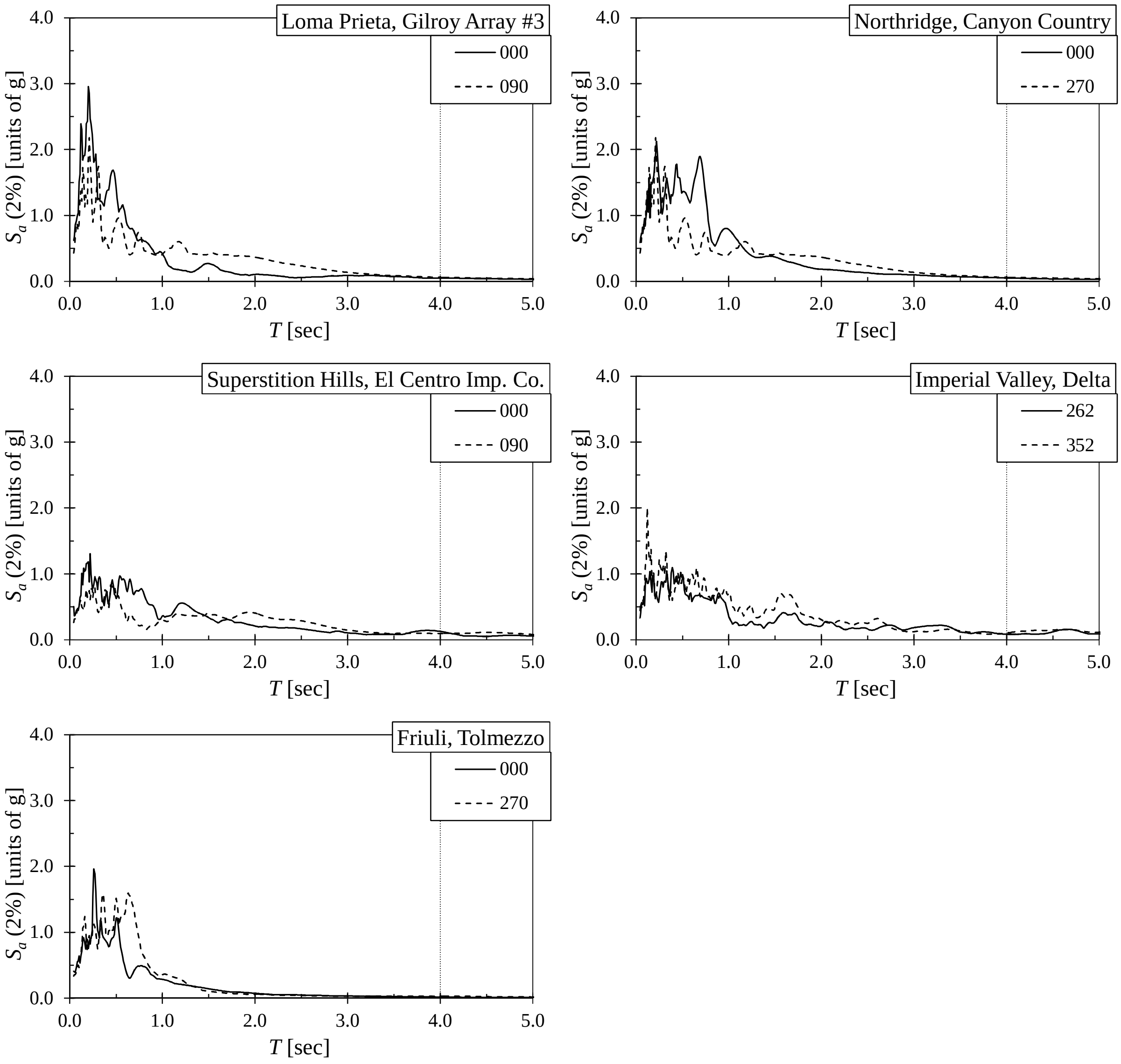

Figure IV-3. Acceleration spectra for 2% damping ratio (3).

The velocity spectra of each ground motion at 2% of the critical damping are plotted in Fig. IV-4. At the considered effective period, T_{eff} = 4.0(sec), the smallest values for S_v(4(sec), 2%) are obtained for Friuli (Tolmezzo), while the largest ones for Superstition Hills (El Centro Imp. Co.) (Annex B).

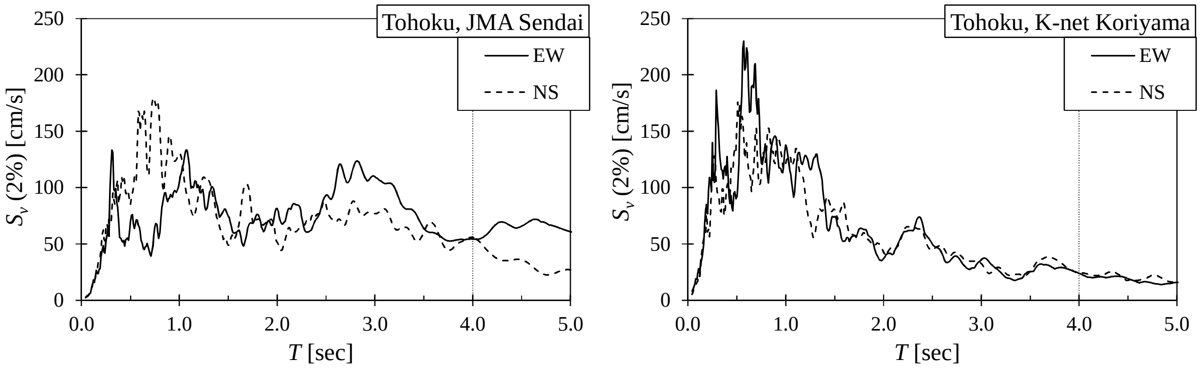

Figure IV-4. Velocity spectra for 2% damping ratio (1).

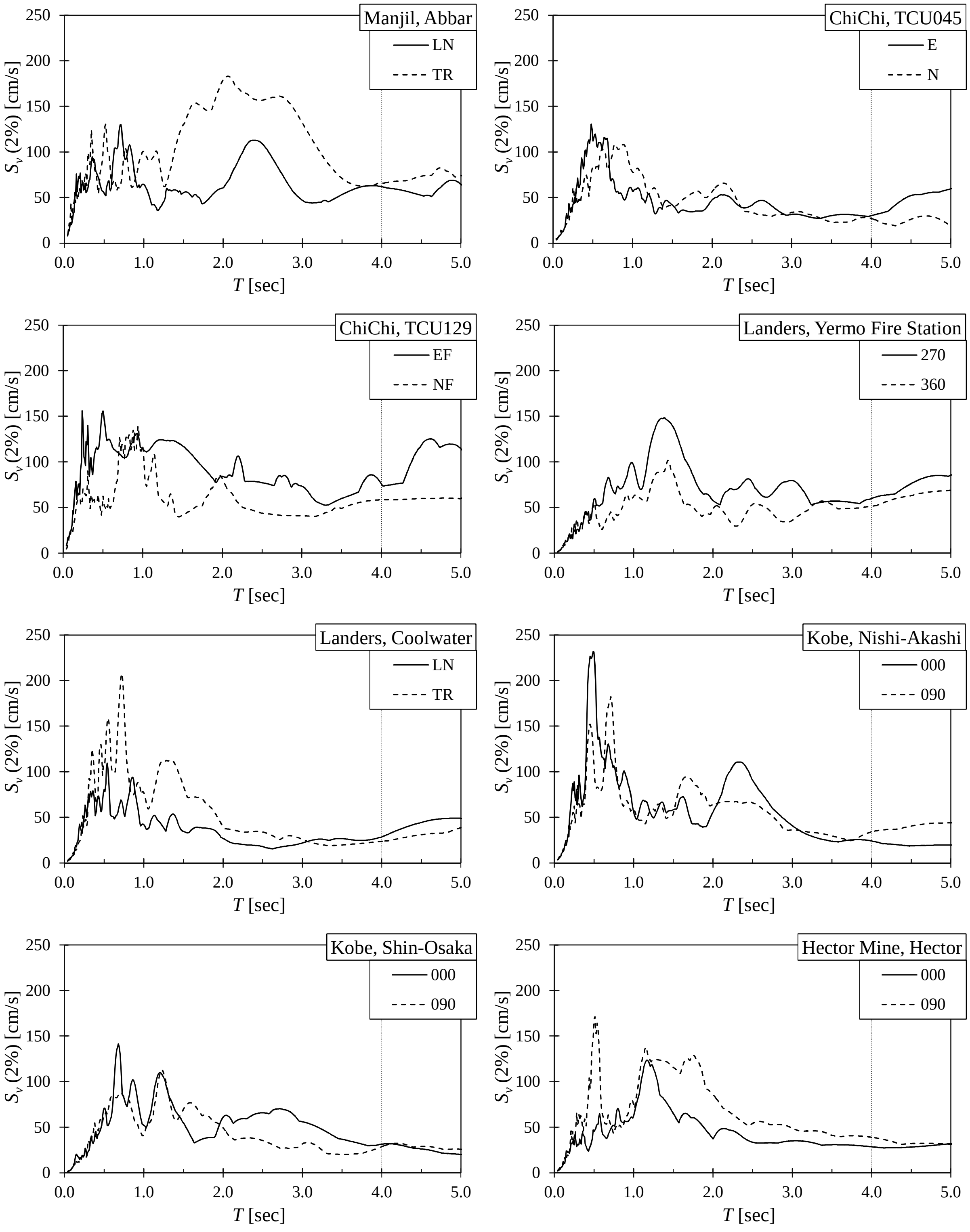

Figure IV-4. Velocity spectra for 2% damping ratio (2).

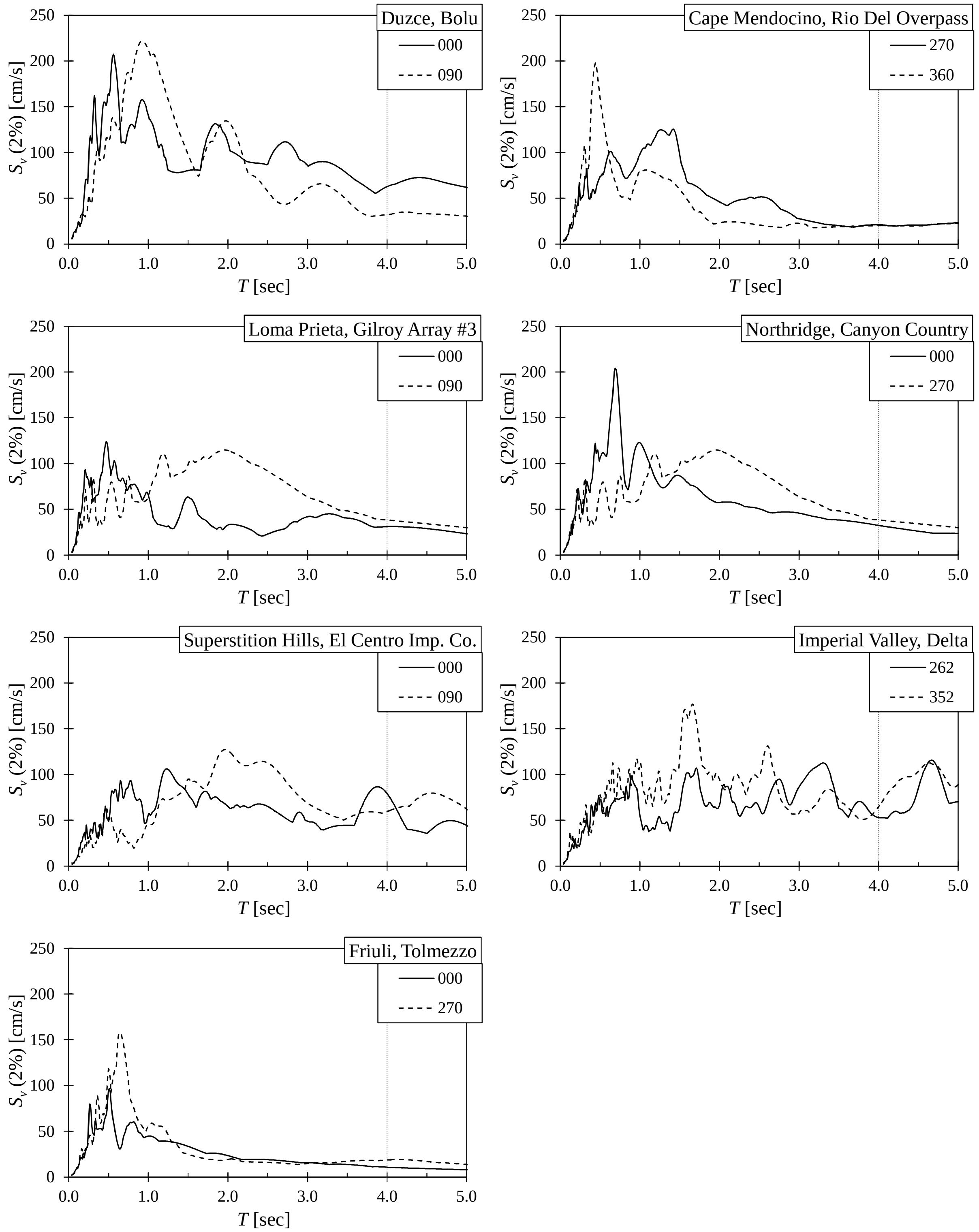

Figure IV-4. Velocity spectra for 2% damping ratio (3).

IV.3. Analytical parameters

There is a significant number of parameters that influence the behavior of an isolation system consisting of rubber bearings and U-shaped steel dampers. Among these, the most important are listed below:

1. Effective period of the isolated structure T_{eff}
2. Base shear coefficient α_1 – the ratio between the shear strength of the system and the total weight of the upper-structure
3. Clearance (isolation gap) $d_{\max}$
4. Size and characteristics of the U-shaped dampers
5. Size and characteristics of the rubber bearings
6. Dynamic properties of the upper-structure (particularly, the fundamental vibration period considering a fixed base T_f)

The analytical model employed in this chapter to simulate the bidirectional response of the isolation layer within a base-isolated structure is a single mass system having a bilinear behavior as described in detail in ***Chapter II***. Therefore, the upper-structure is modeled as a rigid body, and the effect of its higher vibration modes is not investigated in the present study. The rest of the above-mentioned parameters are discussed below.

IV.2.1. Effective period of the isolated structure T_{eff}

It is common knowledge that the fundamental vibration period of a structural system depends on its stiffness (Eq. (IV.1)). The isolation systems are generally nonlinear systems, meaning that stiffness changes with the displacement. Consequently the vibration period also becomes a function of the displacement amplitude. Therefore, in order to compare the properties of different systems, it is required to define a consistent method to evaluate the vibration period. This is achieved by considering the effective stiffness k_{eff} at the maximum displacement under certain levels of seismic hazard (L1 or L2). The resulting period is called "effective period" and is obtained by replacing the stiffness k in Eq. (VI.1) with the effective stiffness k_{eff} defined as the ratio between the maximum force $Q_{\max}$ and the maximum displacement $\delta_{\max}$.

$$T = 2\pi\sqrt{\frac{m}{k}} \tag{IV.1}$$

The maximum displacement of base-isolated structures subjected to level L2 excitations varies from one system to the other, depending on its dynamic characteristics. The Building Center of Japan [IV.13] provides an extensive database on the properties of seismically isolated structures, offering the valuable opportunity to select values for the maximum displacement and the effective period that are pertinent to those of real buildings. Nakazawa (2010) has analyzed the database (up to year 2009), by dividing it into 4 periods based on historic events that have influenced the design practices (publication of the first edition of the Design Recommendations for Base-Isolated Structures in 1989, Kobe 1995 earthquake, revision of Building Standard law) [IV.14]. The most frequent value of the effective period T_{eff} for modern buildings (completed after 2000) was found to be (Fig. IV-5):

$$T_{eff} = 4.0(\text{sec}) \tag{IV.2}$$

The maximum displacement under level L2 excitations $\delta_{\max,L2}$ is reported in the same database. Structures completed between 2005 and 2010 are considered here, and the most frequent value of $\delta_{\max,L2}$ is (Fig. VI-6):

$$\delta_{\max,L2} = 400(\text{mm}) \tag{IV.3}$$

($\delta_{\max,L2}$ is hereafter denoted δ_{400} for simplicity). In the following sections, δ_{400} is adopted as reference value to define the values of the rest of the analytical parameters.

IV.2.2. Base shear coefficient α_1

The two main characteristics that made seismic isolated structures attractive, resulting in a significant increase of their number after the occurrence of Kobe 1995 earthquake, are: (1) elastic design of the upper-structure, and (2) smaller seismic demand which may prove to be more economical than the conventional fixed-base solution. The seismic demand is quantified by the base shear coefficient α_1 which is computed as the ratio between the shear strength of the isolation layer and the total weight of the upper-structure.

$$\alpha_1 = \frac{Q_{400}}{W_s} \tag{IV.4}$$

where Q_{400} is the shear strength of the isolation layer (at displacement $\delta_{400} = 400\,(\text{mm})$);

W_s is the total weight of the upper-structure.

The typical value of the base shear coefficient α_1 for conventional earthquake-resistant structures with fixed base is about 0.30. This value can be reduced to as low as 0.10 for the case of isolated structures. Referring again to the database for isolated structures [IV.13] according to which the most frequent value of α_1 is between 0.09 and 0.11 (Fig. IV-7), the base shear coefficient in the present analysis is set to:

$$\alpha_1 = 0.10 \tag{IV.5}$$

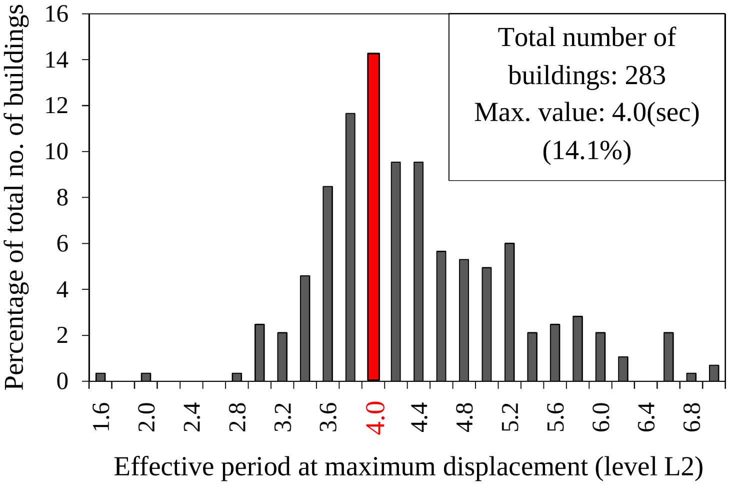

Figure IV-5. Histogram of the effective period T_{eff} at maximum displacement (level L2).

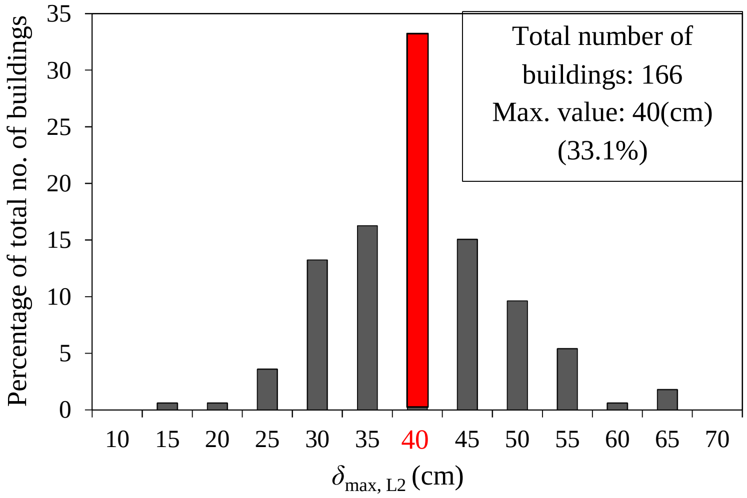

Figure IV-6. Histogram of the maximum displacement $\delta_{\max,L2}$ (level L2).

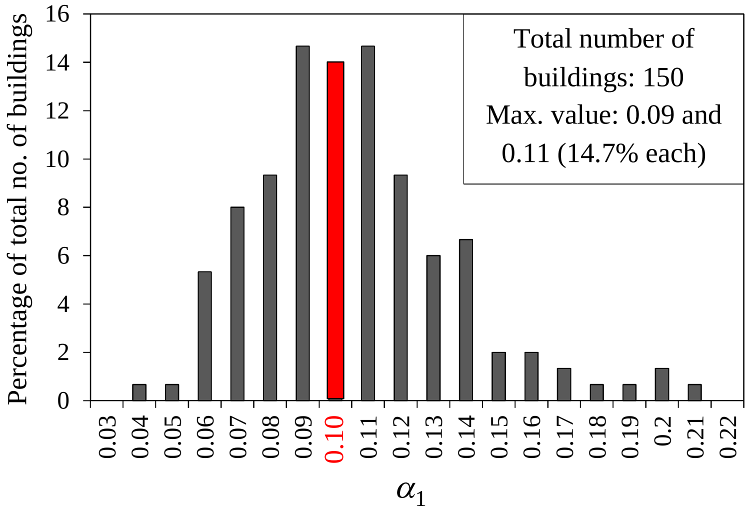

Figure IV-7. Histogram of the base shear coefficient α_1 (level L2).

IV.2.3. Clearance $d_{\max}$

The clearance $d_{\max}$ – also known as isolation gap (Fig. IV-8) – is a safety distance provided to accommodate the relative displacement between upper-structure and foundation in order to avoid pounding.

The influence of pounding on the performance of isolated structures has raised much interest in the last decade, because it may eliminate the major benefits of seismic isolation or even cause more damage to the upper-structure than the damage to similar fixed-based buildings (see, for example [IV.15]). Polycarpou *et al.* (2009) have concluded that pounding with adjacent fixed-base buildings is more likely to occur than pounding at the isolation layer [IV.17]. Qu *et al.* have conducted extensive nonlinear analyses to investigate the influence of clearance on the collapse performance of base-isolated structures. The value required to ensure that no pounding occurs was obtained for a wide array of structural systems. For the analytical model considered in the current analysis, this value was found to be 500(mm) [IV.18].

In the present study the clearance $d_{\max}$ was selected to be:

$$d_{\max} = 800(\text{mm}) \tag{IV.6}$$

Eq. (IV.6) considers a significantly larger value than the most frequent one which was found to be 600(mm) (with a frequency of 42% for buildings completed between 2000 and 2009 [IV.14]). Although the percentage of buildings with a clearance equal to or greater than 800(mm) is only 5%, it is worth noting that the considered value ($d_{\max} = 800(\text{mm})$) is not a pure theoretical one. By adopting this value, it becomes reasonable to assume that pounding does not occur, therefore its effects on the reliability of U-shaped steel dampers are not investigated here. However, this aspect should be investigated in future research as part of the performance of the dampers under near-fault ground motions, where pounding is more likely to occur due to the pulse-like characteristics of such excitations.

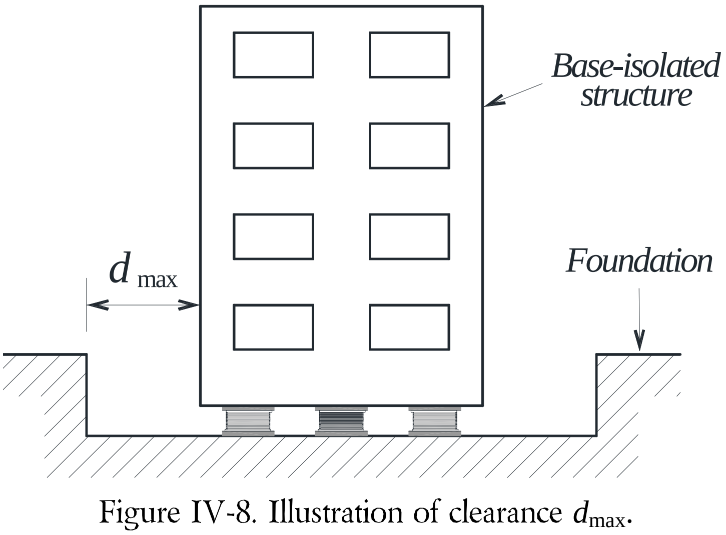

Figure IV-8. Illustration of clearance $d_{\max}$.

IV.2.4. Size and characteristics of U-shaped steel dampers

A unit of 4 UD50-size elements is considered in the analysis, because it is the combination most commonly adopted for real buildings. The bilinear restoring force characteristics – established in ***Chapter III*** by extrapolating the test results obtained for 2 units of 4UD40 elements – are shown again in Table IV-2 for convenience.

The effective stiffness T_{eff} was defined at displacement δ_{400} = 400(mm), therefore the value of dampers' shear strength at the same displacement Q_{400}^{d} is of interest (Fig. IV-9):

$$Q_{400}^{d} = Q_{y}^{d} + k_{p}^{d}\left(\delta_{400} - \delta_{y}\right) \tag{IV.7}$$

where $Q_{y}^{d}, \delta_{y}, k_{p}^{d}$ are the yield strength, yield displacement, respectively post-elastic stiffness of a unit of 4UD50 elements (Table IV-2)

δ_{400} is the maximum displacement under level L2 seismic hazard (Eq. (IV.3)).

The resulting value of Q_{400}^{d} is listed in Table IV-3.

Table IV-2. Restoring force characteristics of a unit of 4UD50

Q_{y}^{d} (*) [kN]	k_{e}^{d} (**) [kN/m]	k_{p}^{d} (**) [kN/m]
274	8320	144

(*) 1.18 times the catalog value

(**) catalog value

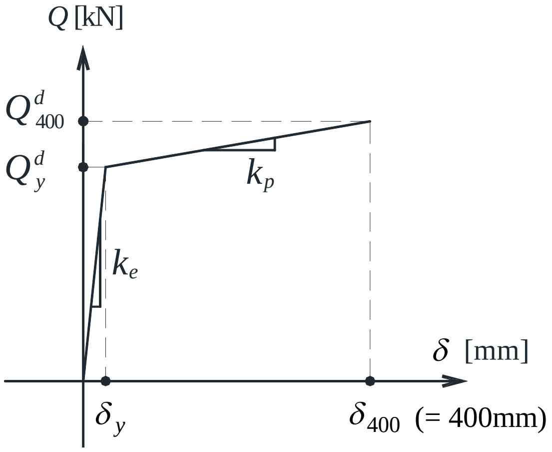

Figure IV-9. Restoring force characteristics of a unit of 4UD50 elements.

In practical design, the structural engineer selects based on experience an appropriate value for the yield base shear coefficient of the dampers α_s. This coefficient is defined as:

$$\alpha_s = \frac{Q_y^d}{W_s} \tag{IV.8}$$

where Q_y^d is the yield strength of the dampers

W_s is the total weight of the upper-structure

For hysteretic steel dampers, the values of α_s are usually situated between 0.01 and 0.06 [IV.14]. For a given structure, where the total weight of the upper-structure is fixed, a greater value for α_s means: (a) an increased number of dampers, or (b) dampers with greater yield strength. In the present study, the size of the dampers is fixed, which means that so is the yield strength, therefore the value of α_s can be adjusted only by varying the weight of the upper-structure W_s. To investigate how the amount of dampers introduced in the isolation layer affects its displacement response and what is the value of α_s at which the dampers are used most efficiently, three different values were considered:

$$\alpha_s = 0.010, 0.025, 0.040 \tag{IV.9}$$

Among these values, $\alpha_s = 0.025$ is the most encountered one in practice, and is consequently set as reference value.

IV.2.5. Size and characteristics of rubber bearings

U-shaped steel dampers are generally used together with elastomeric rubber bearings. This type of bearings don't dissipate earthquake energy, and have an essentially elastic behavior (Fig. IV-10) up to large values of shear strain (about 400%).

The values of the base shear coefficient α_1 (Eq. (IV.5)), the effective period T_{eff} (Eq. (IV.2)) at displacement δ_{400} = 400(mm) and the properties of the dampers were set as described above. Moreover, the overall behavior of the isolation layer is given by superimposing the characteristics of the dampers with those of the isolators, therefore the properties of the latter (shear force Q_{400}^i at δ_{400}, elastic stiffness k_e^i) are derived from the established parameters as described in Section IV.3. It should be noted that, the ratio between the shear force resisted by the isolator Q_{400}^i and that resisted by the dampers Q_y^d decreases as the yield base shear coefficient α_s increases. This means that there is a tradeoff between the contribution of the dampers and that of the isolators which occurs because the same effective period is targeted.

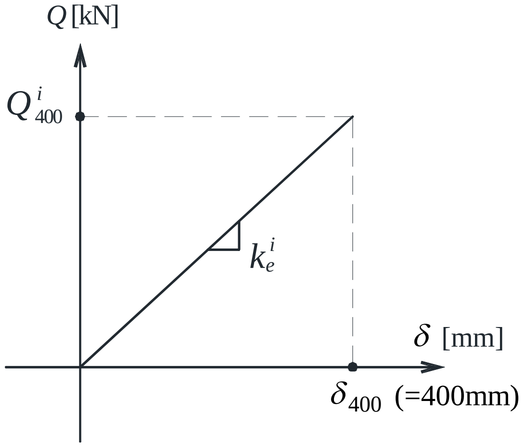

Figure IV-10. Restoring force characteristics of rubber bearings.

Table IV-3. Summary of analytical parameters

No.	Parameter		Value	
1.	Maximum displacement at level L2	δ_{400}	400	(mm)
2.	Effective period at δ_{400}	T_{eff}	4.0	(sec)
3.	Base shear coefficient	α_1	0.10	(-)
4.	Clearance	$d_{\max}$	800	(mm)
	Characteristics of dampers			
5.	Yield strength	Q^d_y	271	(kN)
	Elastic stiffness	k^d_e	8320	(kN/m)
	Postelastic stiffness	k^d_p	144	(kN/m)
	Shear strength at δ_{400}	Q^d_{400}	314.6	(kN)
	Yield base shear coefficient	α_s	0.010 0.025 0.040	(-)
	Characteristics of rubber bearings			
6.	Shear strength at δ_{400}	Q^i_{400}	(*)	
	Elastic stiffness	k^i_e	(*)	

(*) Values vary with α_s. See Table IV-4.

IV.4. Analytical model

The concept of the analytical model was introduced in ***Chapter II***, where nonlinear response analysis was conducted to establish the experimental plan. The model adopted in ***Chapter IV*** is similar – a single mass system with a bilinear behavior and two degrees of freedom conferred by MSS model –, with the important exception that the characteristics of the dampers are updated to comply with the bilinear hysteretic model proposed in ***Chapter III***.

The yield base shear coefficient of the dampers α_s is introduced as an additional parameter (Section IV.2.4.) to investigate the effect of different amounts of dampers. To this purpose, the effective period T_{eff}, the base shear coefficient α_1 and the properties of the dampers are kept constant (Table IV-3). From Eq. (IV.8) it results that the total weight of the upper-structure W_s is obtained as:

$$W_s = \frac{Q_y^d}{\alpha_s} \tag{IV.10}$$

Further on, by substituting Eq. (IV.10) into the definition of the base shear coefficient α_1 (Eq. (IV.5)), the maximum shear strength Q_{400} of the isolation layer at displacement δ_{400} = 400(mm) is obtained as follows:

$$Q_{400} = \frac{\alpha_1}{\alpha_s} Q_y^d \tag{IV.11}$$

In the next step, the required shear strength of the isolators at the same displacement is computed as:

$$Q_{400}^i = Q_{400} - Q_{400}^d \tag{IV.12}$$

where Q_{400}^d is given by Eq. (IV.7) and Table IV-3.

It is worth noting that, since the value of Q_{400}^d depends on that of the yield base shear coefficient α_s, it results that the properties of the isolators will also be a function of α_s. These results are shown in Table IV-4.

The values listed in Table IV-4, obtained as described above, have to satisfy Eq. (IV.2), namely the effective period at δ_{400} = 400(mm) should be 4.0(sec). This is verified to be true, with a negligible error of +0.01(sec).

The proportion between the shear strength of the dampers and that of the isolators at displacement δ_{400} = 400(mm) is shown in Table IV-5. It can be observed that the contribution of the dampers increases as the yield base shear coefficient α_s increases. The restoring force characteristics of both the dampers and the rubber bearings are shown in Fig. IV-11.

Table IV-4. Restoring force characteristics of rubber bearings

α_s	0.010	0.025	0.040
W_s (kN)	26120	10448	6530
Q_{400}^{i} (kN)	2297.4	730.2	338.4
k_e^{i} (kN/m)	5743.4	1825.4	845.9

Table IV-5. Proportion between the shear strength of dampers and that of rubber bearings at displacement δ_{400} = 400(mm)

α_s	0.010	0.025	0.040
$Q_{400}^{d} : Q_{400}^{i}$	3 : 22	3 : 7	1 : 1

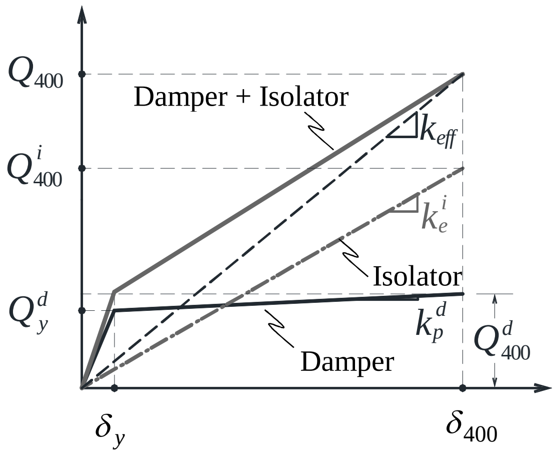

Figure IV-11. Restoring force characteristics of the isolation layer.

IV.5. Intensity measure IM and damage measure DM

To construct an IDA curve, it is required to select an intensity measure *IM* and a damage measure *DM*. Generally, the selection process is strongly related to the type of structure or system to be analyzed and has to be carefully considered. Seismic isolated structures represent a particularly challenging system because of their characteristics (large displacements in the isolation layer, targeted performance of the upper-structure is elastic range).

The damage measure *DM* adopted in the present study is the bidirectional cumulative damage index D_2, which expresses the damage of a U-shaped steel damper subjected to a random bidirectional loading history. This means that, in order to draw the IDA curves, a corresponding *IM* suitable to express the characteristics of both horizontal components of a ground motion is required. This issue is discussed in the present section, which also describes how the maximum D_2 index is obtained for each displacement orbit.

IV.5.1. Intensity measure IM: geometric mean horizontal component of the peak ground velocity PGV_{gm}

The quantities typically adopted as IMs for conventional earthquake-resistant structures (such as the 5% damped spectral acceleration at the structure's first mode period) are usually not very conclusive for seismically isolated buildings because of their long period of vibration. The studies conducted so far on this topic have adopted different approaches. Qu *et al.* (2013) evaluated the collapse performance of a base-isolated structure by adopting as *IM* the energy-equivalent velocity V_E [IV.18]. V_E represents the velocity at which the kinematic energy of a system with mass m and natural vibration period T equals the earthquake input energy E_i (Eq. (IV.13)) and it is widely used in Japan.

$$V_E = \sqrt{\frac{2E_i}{m}} \tag{IV.13}$$

where V_E is the energy-equivalent velocity

m is the mass of the system

E_i is the earthquake input energy

Bakhshi and Mostafavi (2014) have developed a set of fragility curves for base-isolated RC structures by using the cumulative absolute velocity (*CAV*), which is the integral of the absolute value of an acceleration series (Eq. (IV.14)) [IV.19]. This parameter has generated a great deal of interest ever since its introduction in 1988 because it has the capacity of including the cumulative effects of ground motion duration [IV.20].

$$CAV = \int_0^{t_{\max}} |a(t)|dt \tag{IV.14}$$

where CAV is the cumulative absolute velocity

$t_{\max}$ is the maximum duration of the seismic record (in seconds)

$a(t)$ is the acceleration series

An extensive study on the efficiency of a significant number of *IM*s in predicting the response of base-isolated structures was conducted by Mollaioli *et al.* (2013) who classified the *IM*s into: (1) structure-specific *IM*s obtained from response spectra of ground motion time histories depending on the period of the structure, and (2) non-structure-specific *IM*s calculated directly from the ground motion time histories [IV.22]. The structure-specific *IM*s were further grouped into three categories: (i) acceleration-related (*e.g.* *PGA*, Arias intensity, *CAV* etc), (ii) velocity-related (*e.g.* *PGV*, incremental velocity etc), (iii) displacement-related (*e.g.* *PGD*, incremental displacement etc). The prediction capability of the considered *IM*s with respect to various engineering demand parameters (or damage measures) was investigated. The results showed that the peak ground velocity *PGV* is one of the most efficient *IM*s, having in addition a stable behavior with the variation of the isolation properties.

However, all the above-mentioned studies – along with the great majority of the rest of the technical literature – require only a single horizontal component of the seismic record in order to run the analysis. For the case of two-dimensional analysis (adopted in the present study), this raises the problem of finding an *IM* able to express the characteristics of both horizontal components of a ground motion. Campbell and Bozorgnia (2008) have developed a new empirical ground motion model for the geometric mean horizontal component of *PGA*, *PGV* and *PGD*. This model considers different sensor orientations and was applied throughout the PEER NGA strong motion database [IV.21]. Considering the fact that the present study has mainly adopted seismic records given in PEER database, and given the results published by Mollaioli *et al.* who confirmed *PGV* to be one of the most efficient *IM*s for seismic isolated structures, the considered *IM* in the present study is the geometric mean horizontal component of the peak ground velocity, PGV_{gm}.

IV.5.2. Damage measure DM: bidirectional cumulative damage index D_2

In the present study, the damage of a U-shaped steel damper is evaluated using the bidirectional cumulative damage index D_2. Its value is directly related to both the values of the displacement amplitude and to the direction they are applied to the damper. For this reason, given a displacement orbit with a fixed orientation, the value of D_2 varies function of the angle θ made by the damper's axis with the horizontal axis of the orbit (Fig. IV-12). The considered analytical model adopted to compute the bidirectional displacement response in the isolation layer uses an MSS element which offers the great advantage that it presents no directionality with respect to the input acceleration time histories. In other words, to obtain the maximum displacement response it is required to run the analysis only once. This fact allows the computation of the maximum possible cumulative damage index of a given orbit by simply varying angle θ between 0 and 180°:

$$D_2 = \max_{0 \le \theta \le \pi} ({}_{\theta}D_2) \tag{IV.15}$$

where ${}_{\theta}D_2$ is the bidirectional cumulative damage index of a damper placed at angle θ with respect to x axis (Fig. IV-13).

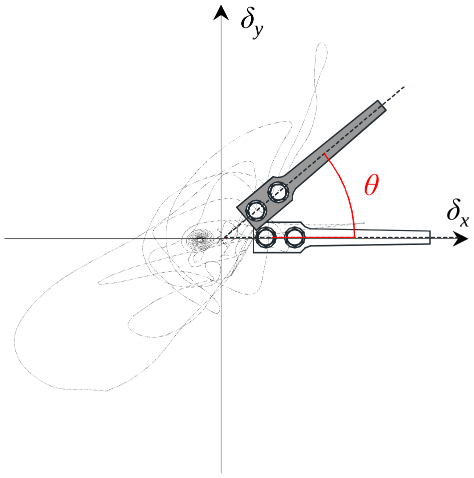

Figure IV-12. Definition of rotation angle θ (position of damper with respect to the considered displacement history).

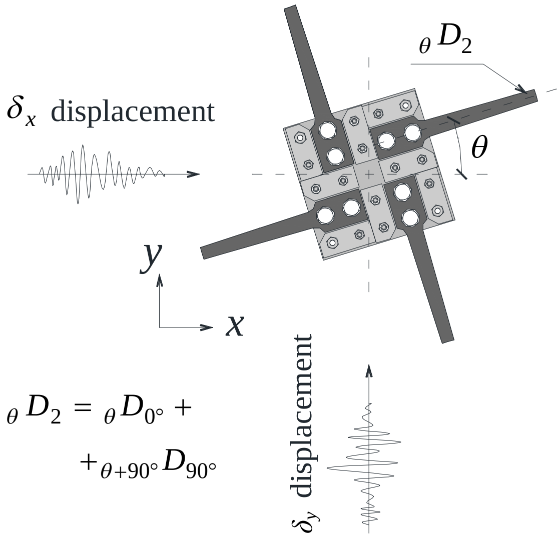

Figure IV-13. Definition of the bidirectional cumulative damage index ${}_{\theta}D_2$ of a damper situated at angle θ with respect to the positive sense of x axis of the displacement history.

IV.6. Performance levels and limit states

To evaluate the reliability of U-shaped steel dampers subjected to bidirectional excitation, it is required to defined a set of performance levels and limit states. In general, performance levels of a certain structural archetype or of a structural member are defined based on observations made during post-earthquake reconnaissance reports and loadings tests or on engineering judgment. These levels quantify the structural (and/or nonstructural) damage based on appropriate engineering demand parameters (e.g. interstory drift ratio).

The performance of U-shaped steel dampers is dependent on the characteristics of the displacement history, as it was shown in ***Chapter II***. Although for experienced professionals the deformed shape of the dampers may offer some insight on their damage extent, it is extremely difficult to clearly relate the highly random character of the displacement orbit to an appropriate engineering parameter (damage measure). For this reason, in the present study limit states were defined with respect to D_2^u - J_f interaction curve as follows:

1) Limit state LS1: 10% from D_2^u - J_f interaction curve (Eq. (IV.16a));
2) Limit state LS2: 30% from D_2^u - J_f interaction curve (Eq. (IV.16b));
3) Limit state LS3: 60% from D_2^u - J_f interaction curve (Eq. (IV.16c));
4) Limit state LS4: the D_2^u - J_f interaction curve itself (Eq. (I.8)).

Fig. IV-14 shows each limit state, while Fig. IV-15 shows corresponding examples of the deformed shape of the dampers.

$$D_2^{LS1} = \left| \begin{array}{ll} 0.1 & (0 \le J_f \le 1.5) \\ 0.16 - 0.04 \cdot J_f & (1.5 < J_f \le 3.0) \\ 0.04 & (J_f > 3.0) \end{array} \right. \tag{IV.16a}$$

$$D_2^{LS2} = \left| \begin{array}{ll} 1/3 & (0 \le J_f \le 5.0) \\ \dfrac{1.6}{3} - 0.04 \cdot J_f & (5.0 < J_f \le 10.0) \\ 0.4/3 & (J_f > 10.0) \end{array} \right. \tag{IV.16b}$$

$$D_2^{LS3} = \left| \begin{array}{ll} 0.6 & (0 \le J_f \le 9.0) \\ 0.96 - 0.04 \cdot J_f & (9.0 < J_f \le 18.0) \\ 0.04 & (J_f > 18.0) \end{array} \right. \tag{IV.16c}$$

Performance levels are defined between two consecutive limit states in terms of the remaining inelastic deformation capacity (Fig. IV-16):

1) ***PL1***: Negligible or no damage (100 ~ 90% remaining inelastic deformation

capacity);

2) ***PL2***: Minor damage (90 ~ 70% remaining inelastic deformation capacity);
3) ***PL3***: Moderate damage (70 ~ 40% remaining inelastic deformation capacity);
4) ***PL4***: Severe damage (40 ~ 0% remaining inelastic deformation capacity);
5) ***PL5***: Fracture (no remaining inelastic deformation capacity).

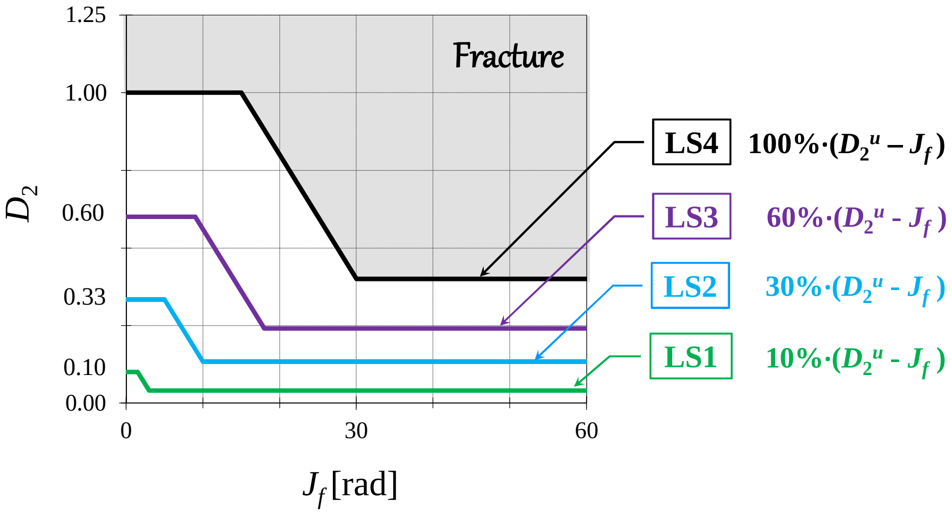

Figure IV-14. Definition of limit states.

(a) LS1 (b) LS2 (c) LS3 (d) LS4

Figure IV-15. Illustration of damage of the dampers at each limit state (examples).

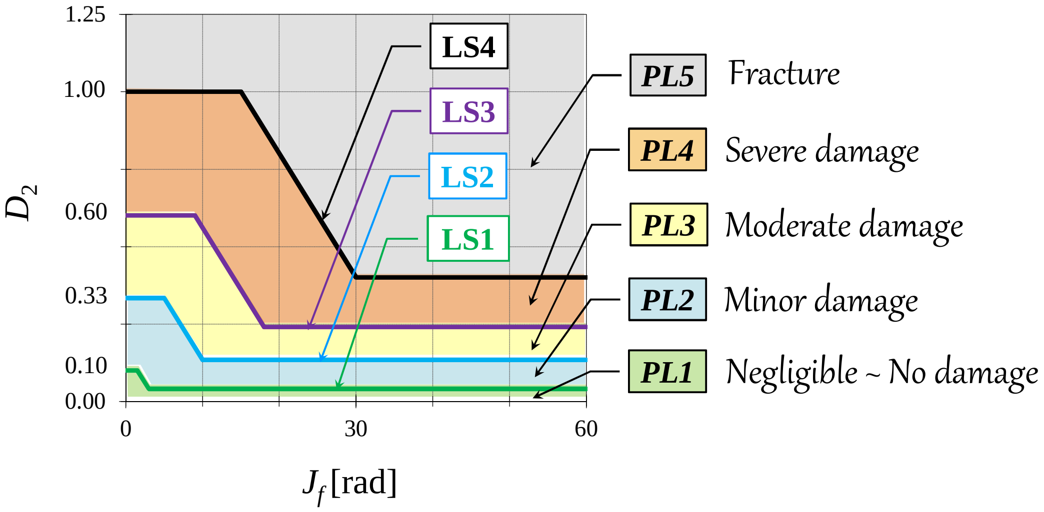

Figure IV-16. Definition of performance levels.

IV.7. IDA curves

An IDA curve is obtained by running the analysis several times, at increasing scale factors, and fitting a curve through the obtained discrete points plotted on the same graphic. In the present study, second order cubic spline functions are adopted to derive a continuous function of the damage measure *DM* given the intensity measure *IM*. This procedure is also applied to obtain the values of different quantities of interest such as sway-motion index J_f, maximum peak-to-peak shear deformation angle $\gamma_{t,\max}$ etc.

To make sure that consistent results are obtained, a systematic methodology is required, as outlined in the next section.

IV.7.1. Analytical methodology

Fig. IV-18 shows the analysis flowchart for a given ground motion. First, the value of the scale factor s_f is selected and applied to both horizontal components of the considered record by simply multiplying the values of the acceleration time histories. The scaled acceleration time histories thus obtained are used as input data to conduct nonlinear elasto-plastic dynamic analysis employing the analytical model described in Section IV.4. The response of interest is the displacement one, characterized by its maximum value, $R_{\max}$ (Fig. IV-17, Eq. (IV.17)). In the next step, the displacement response is adopted to evaluate the damage of U-shaped steel dampers in terms of the cumulative damage index D_2 and sway-motion index J_f. This process is repeated for gradually increasing values of the scale factor until the ultimate limit state is reached. The conditions considered in this study for the ultimate limit state are discussed in the next section.

$$R_{\max} = \max_{0 \le t \le t_f}\left(\sqrt{\delta_x^2 + \delta_y^2}\right) \tag{IV.17}$$

where $R_{\max}$ is the maximum bidirectional displacement

t is the time step

t_f is the last time step

δ_x and δ_y are the displacement responses on x, respectively y directions obtained by decomposing the bidirectional orbit along the two directions.

The value of the scale factor s_f is decided as the minimum between 0.50 and the value at which the maximum displacement $R_{\max}$ increases with 100(mm) with respect to the previous point. For each ground motion, the analysis is run at least 10 times following the flow-chart shown in Fig. IV-18.

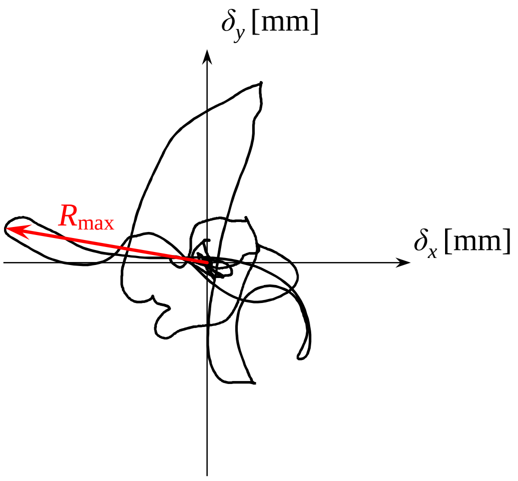

Figure IV-17. Definition of maximum displacement of the isolation layer $R_{\max}$ for a bidirectional displacement history.

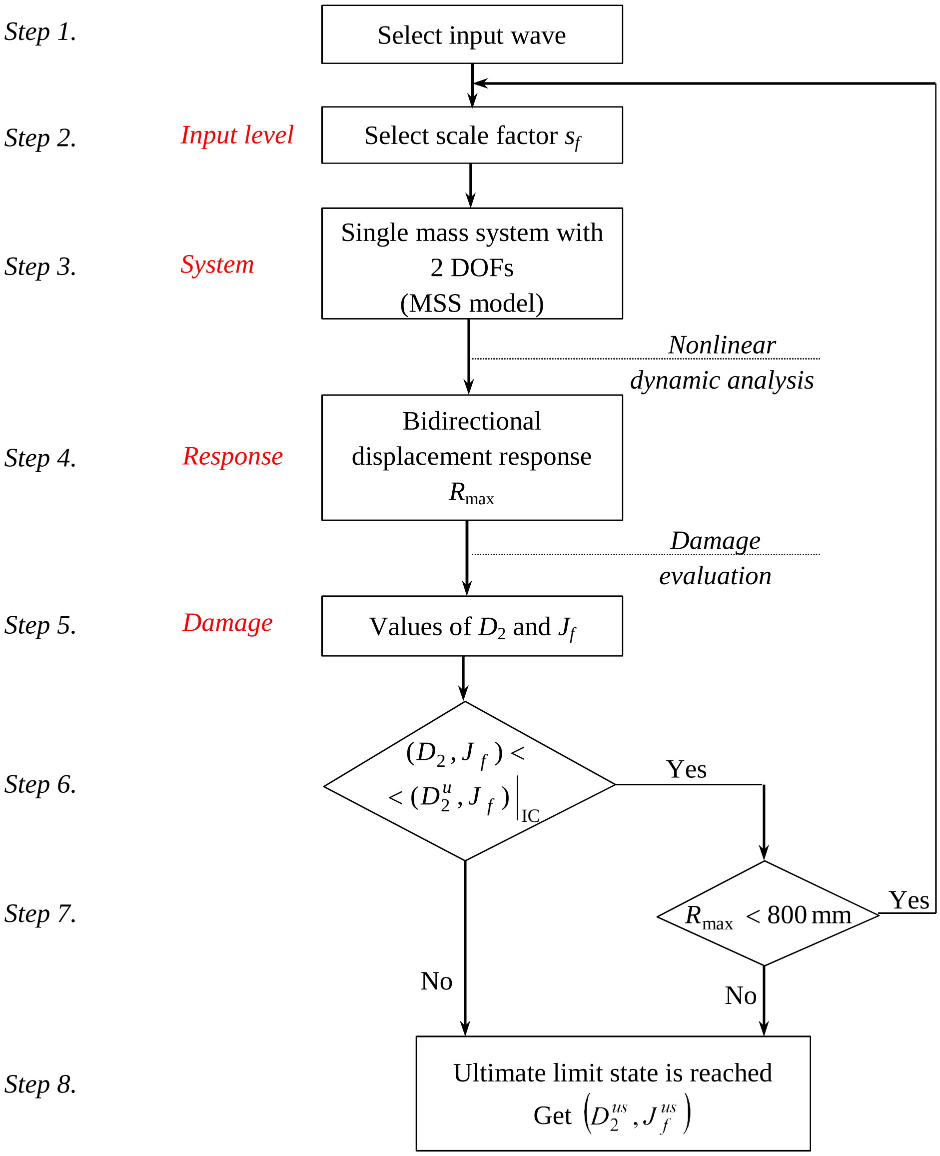

Figure IV-18. Analysis flowchart for a single ground motion.

IV.7.2. Ultimate limit state

IDA analysis is generally conducted until one of the following conditions occur: (1) the IDA curve becomes unstable (sudden and repeated changes of the slope), or (2) the system has reached a collapse mechanism, (IDA curves flattens). Flattening of the IDA curve as the *DM* almost goes to infinity is the main premise of the IDA approach indicating the dynamic instability of the system. However, one should bear in mind that this can only be achieved for systems with significant non-linear behavior, for which it is relatively easy to select a convergent *DM*.

In the present study, ultimate limit state is reached when: (1) the damper fractures, or (2) extremely large displacements occur. The criteria are discussed below.

1. Fracture of the damper (intersection with interaction curve)

   Fracture occurs when the damper has reached its ultimate inelastic deformation capacity. This happens when the analytic values of the cumulative damage index D_2 and sway-motion index J_f are situated on the interaction curve. In Fig. IV-19 this concept is illustrated for Imperial Valley earthquake (Delta station). Fig. IV-19(a) shows the bidirectional displacement response, while Fig. IV-19(b) depicts the analytical values of D_2 and J_f against the interaction curve. The intersection point between the curve described by the analytical values of D_2 and J_f at increasing scale factor s_f and the interaction curve is shown with red. This point is the point where the analysis is stopped (ultimate limit state is reached), because the damper is considered fractured.

2. Extremely large displacements ($R_{\max}$ = 800(mm))

   Under extreme displacements (peak-to-peak shear deformation angle $\gamma_t \geq 500\%$), the following problems arise: (a) U-shaped steel dampers straighten in tension, which places their connection to the upper-structure and foundation under severe strain, (b) the value of cumulative bidirectional damage index D_2 cannot be evaluated because the fatigue curves are limited to $\gamma_t \leq 500\%$, and (c) the maximum displacement $R_{\max}$ becomes larger than the considered clearance ($d_{\max}$ = 800(mm)), which means that pounding would occur.

   For the considered damper size (UD50), the aspect presented at point (b) limits $R_{\max}$ at 838(mm) (Eq. (IV.18)), which is larger than the considered clearance. This means that, in order to comply with the assumption that pounding does not occur, the maximum allowable displacement ${}_{all}R_{\max}$ has to be limited to 800(mm) (Eq. (IV.19)).

$$\gamma_t = \frac{2R_{\max}}{h} = 500\% \quad \Leftrightarrow \quad R_{\max} = 838\text{mm} \quad \text{(UD50)} \qquad \text{(IV.18)}$$

where $R_{\max}$ is the maximum displacement amplitude (Fig. IV-17)

γ_t is the peak-to-peak shear deformation angle

h is the height of a UD50 damper element (335(mm))

$$ {}_{all}R_{\max} = 800\,(\text{mm}) \tag{IV.19} $$

where ${}_{all}R_{\max}$ is the maximum allowable displacement amplitude.

Fig. IV-20 shows as an example the displacement orbit of Loma Prieta earthquake (Gilroy Array #3 station) at a scale factor that causes the maximum displacement $R_{\max}$ to reach the value of 800(mm). In this case, the analysis is stopped before the dampers reach fracture, therefore the values of D_2 and J_f do not reach the interaction curve (Fig. IV-20(b)).

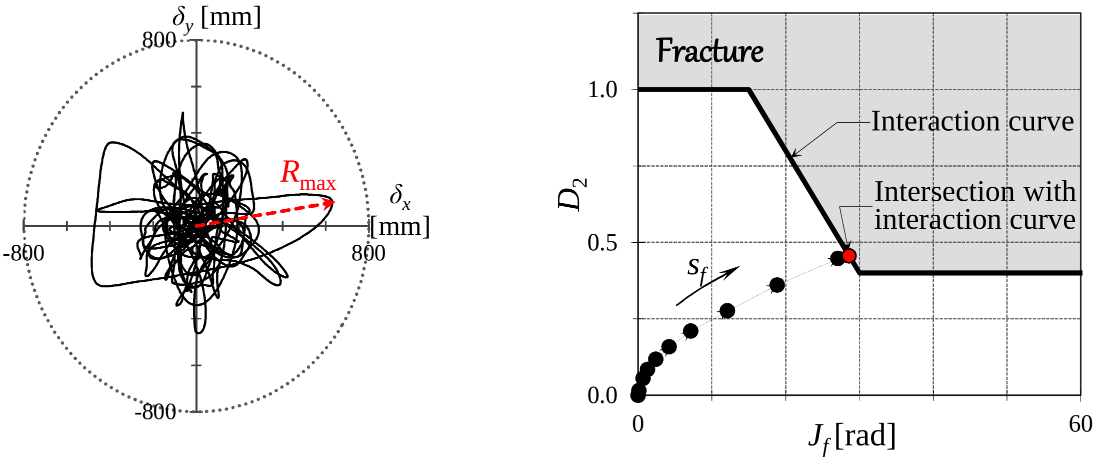

(a) Displacement orbit at intersection point ($R_{\max}$ < 800(mm))

(b) Analytical values of D_2 and J_f

Figure IV-19. Ultimate limit state – criterion (1): fracture of the damper (Imperial Valley earthquake, Delta station, scale factor s_f = 2.72, $\alpha_s = 0.025$).

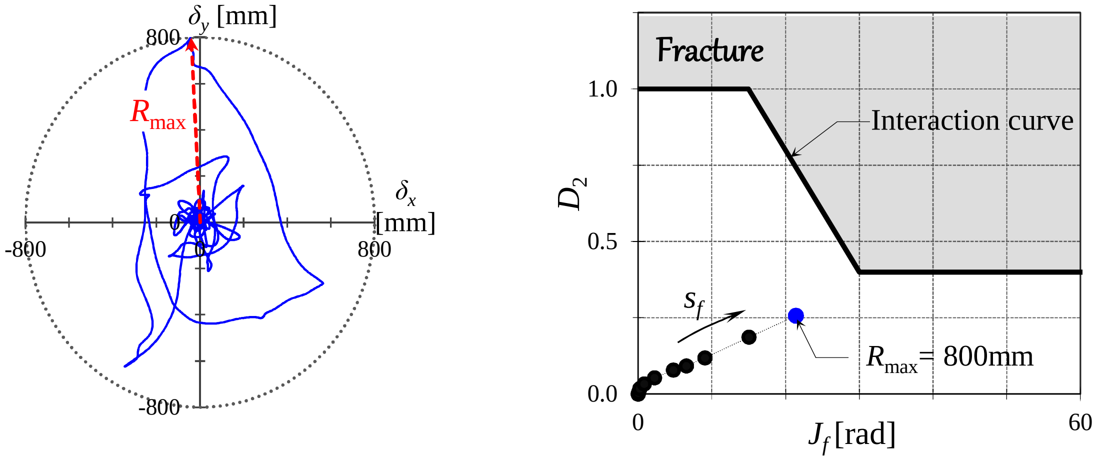

(a) Displacement orbit ($R_{\max}$ = 800(mm))

(b) Analytical values of D_2 and J_f

Figure IV-20. Ultimate limit state – criterion (2): extremely large displacements ($R_{\max}$=800(mm)) (Loma Prieta – Gilroy #3 station, s_f = 3.86, $\alpha_s = 0.025$).

IV.7.3. Conventional IDA curves

In this section the results obtained by following the analytical methodology described above are discussed. The IDA curves of all the considered ground motions, relating the bidirectional cumulative damage index D_2 to the geometric mean horizontal component PGV_{gm}, are plotted for each value of the yield base shear coefficient α_s in Fig. IV-21.

The following observations are made:

- The largest record-to-record variability of the intensity measure PGV_{gm} is obtained for $\alpha_s = 0.010$.
- The ground motion causing the most severe damage is Imperial Valley, Delta station (IVD).
- The criterion governing the ultimate limit state is influenced by the value of the yield base shear coefficient α_s as follows (Table IV-6): only 2 ground motions cause the dampers to fracture for $\alpha_s = 0.040$, while for $\alpha_s = 0.010$ 9 ground motions cause fracture; the rest of the ground motions reached the ultimate limit state by fulfilling the second criterion ($R_{\max}$ = 800(mm)). Therefore it can be stated that by increasing the contribution of the dampers they will perform better, exhibiting a smaller risk of fracture before being subjected to extremely large deformations.
- The IDA curves do not reach a flat line because the bidirectional cumulative displacement damage index D_2 has finite and stable values ensured by the criteria imposed for the ultimate limit state. This fact represents an obstacle for the computation of the median, respectively median +/- one standard deviation of the obtained IDA curves, which are important indicators that relate the capacity of the U-shaped steel dampers to the seismic demand. To address this issue, the IDA curves were normalized with respect to the value of D_2 at ultimate limit state of each ground motion as described in the next section.

Table IV-6. Criterion governing the ultimate limit state

Criterion	Number of ground motions		
	$\alpha_s = 0.010$	$\alpha_s = 0.025$	$\alpha_s = 0.040$
(1) Fracture of damper	9	4	2
(2) Extremely large displacements	8	13	15
Total	17	17	17

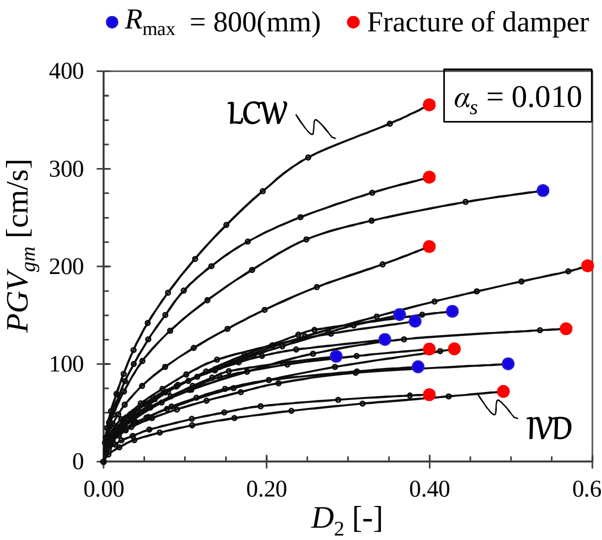

(a) IDA curves for $\alpha_s = 0.010$

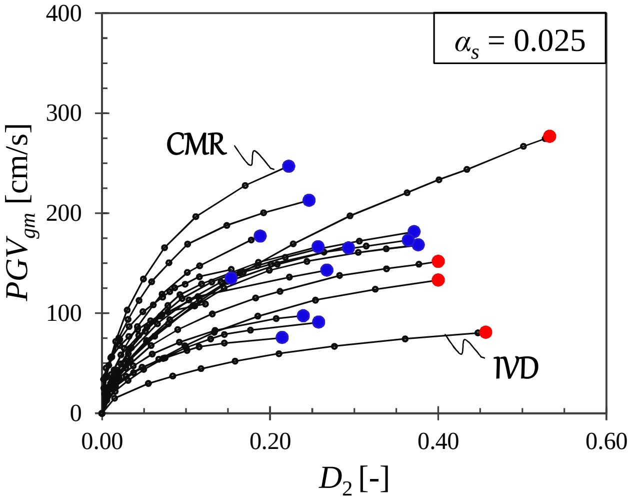

(b) IDA curves for $\alpha_s = 0.025$

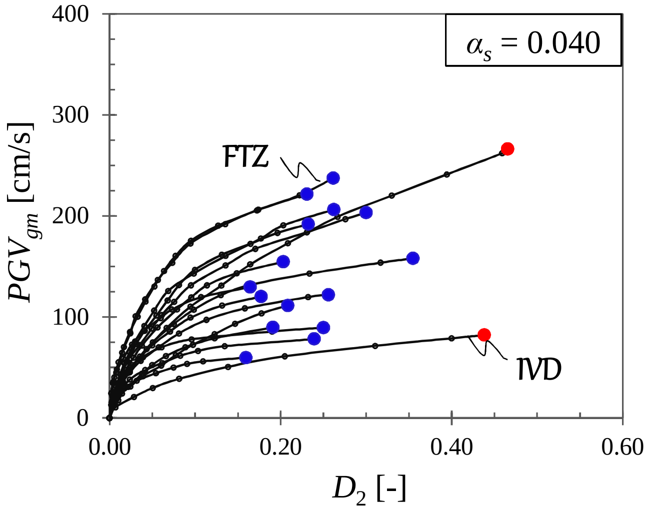

(c) IDA curves for $\alpha_s = 0.040$

Figure IV-21. IDA curves and criteria at ultimate limit state (blue dots: R_{max} = 800(mm); red dots: fracture of the damper).

IV.7.4. Normalized IDA curves

The goal of a set of IDA curves is to predict the capacity of a system under different seismic intensity levels. To this purpose, the median of the *DM* with respect to the *IM* is computed across the set of IDA curves. In the present study, the values of the bidirectional cumulative damage index at ultimate limit state D_2^{us} differ from record to record (IDA curves do not reach a flat line), fact which does not allow computing the median value of the set at each value of *DM*. To address this issue, the IDA curves were normalized with respect to D_2^{us} (Eq. (IV.20)). The normalized IDA curves – shown in Fig. IV-23 – relate the PGV_{gm} to the percentage of maximum damage a damper can withstand before reaching its ultimate limit state. Their median, respectively median +/- one standard deviation are important indicators that offer information about the reliability of U-shaped steel dampers under different seismic intensity levels.

$$DP_{ij} = \frac{D_{2,ij}}{D_{2,j}^{us}} \cdot 100 \qquad \text{(IV.20)}$$

where i denotes the step number (related to the applied scale factor s_f)

j the number of the ground motion

DP_{ij} is the damage percentage

$D_{2,ij}$ is the cumulative damage index at step i

$D_{2,j}^{us}$ is the cumulative damage index at the ultimate state of j^{th} ground motion (Fig. IV-22).

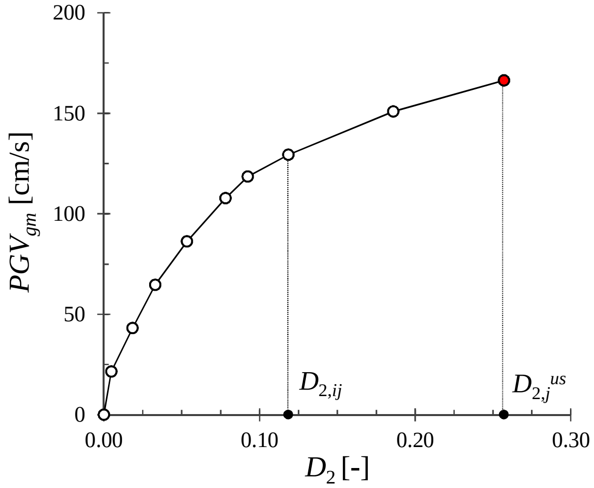

Figure IV-22. Definition of $D_{2,j}^{us}$ and $D_{2,ij}$ (IDA curve for Loma Prieta – Gilroy #3).

In Japan, the basic concept of performance-based design is applied for seismic isolated structures by adopting three levels of seismic hazard (L1, L2 and L3) and corresponding target performance levels (Table IV-7). To check the performance of a building, nonlinear dynamic time-history analyses are conducted using historic records scaled to reach each hazard level. The scaling is done using the peak ground velocity *PGV* such that it reaches the values listed in Table IV-7.

The median damage percentage *DP* at PGV_{gm} corresponding to each design seismic hazard level is listed in Table IV-8. It can be observed that:

- For levels L1 and L2, the median damage percentage *DP* does not vary significantly with the value of the yield base shear coefficient α_s (less than 3 for L1, approximately 10% for level L2);
- For level L3, the median damage percentage *DP* corresponding to $\alpha_s = 0.025$ is significantly smaller than that corresponding to $\alpha_s = 0.010$ (less than half) only slightly smaller than that for $\alpha_s = 0.040$. This means that the optimum value for α_s is 0.025 and a further increase of the contribution of the dampers will not results in a better performance.

The second observation is confirmed by Fig. IV-24 where the median IDA curves for each considered value of α_s are plotted. For PGV_{gm} greater than 48.0(cm/s), the case with $\alpha_s = 0.025$ has less damage.

Table IV-7. Design seismic hazard levels and targeted performance of base-isolated structures

Level	*PGV* (cm/s)	Frequency	Targeted performance
L1	25.0	Rare earthquakes that can occur more than one time during the life cycle of a building	Upper-structure in elastic range
L2	50.0	Very rare earthquakes (return period of approximately 50 years)	Accidental initiation of yielding of the structural elements may occur; development of full plastic mechanism must be prevented
L3	75.0	Extremely rare earthquakes (maximum credible earthquake)	Check safety margin against collapse

Table IV-8. Median damage percentage *DP* at each design seismic hazard level

Level	PGV_{gm} (cm/s)	Median *DP* (%)		
		$\alpha_s = 0.010$	$\alpha_s = 0.025$	$\alpha_s = 0.040$
L1	25.0	2.40	2.76	2.74
L2	50.0	9.47	9.30	10.22
L3	75.0	46.27	19.57	21.87

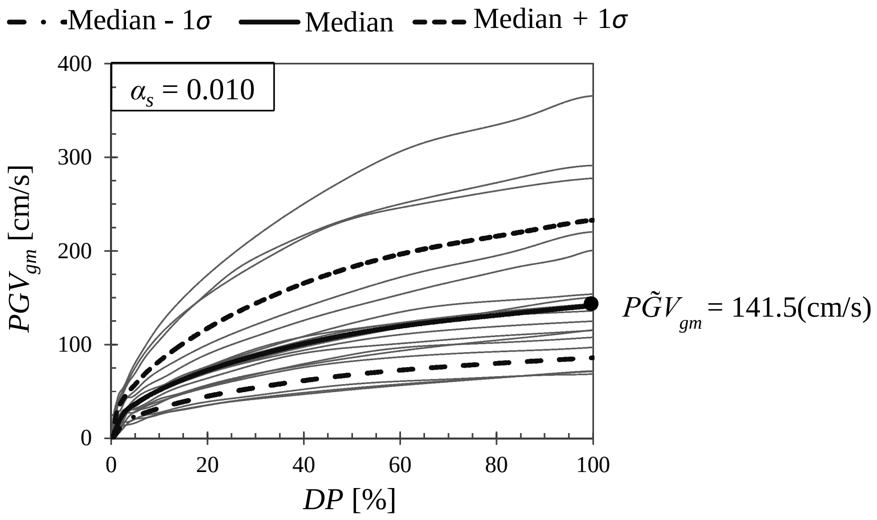

(a) Normalized IDA curves for $\alpha_s = 0.010$

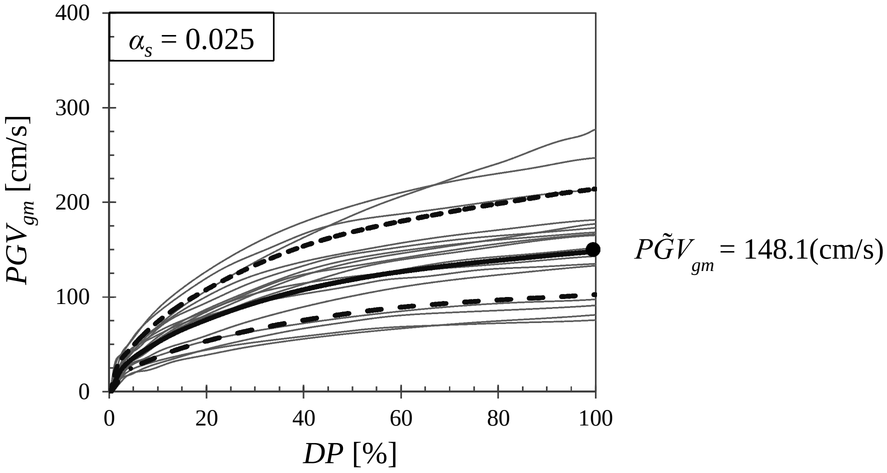

(b) Normalized IDA curves for $\alpha_s = 0.025$

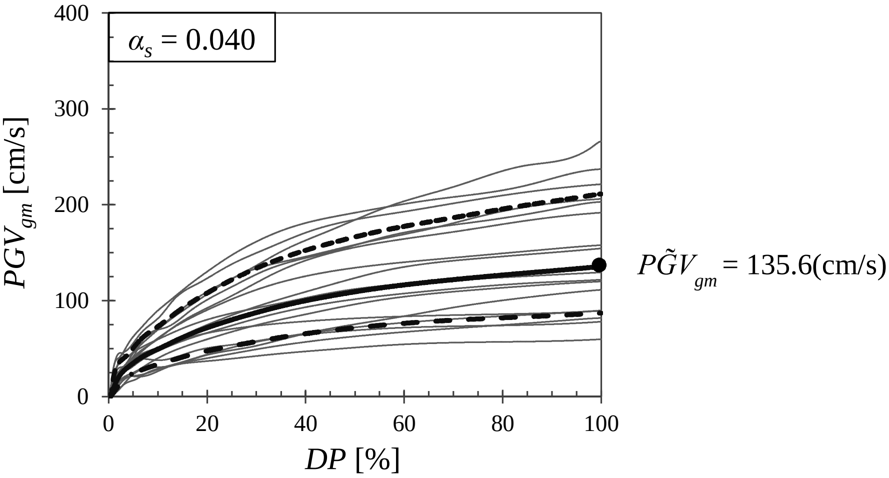

(c) Normalized IDA curves for $\alpha_s = 0.040$

Figure IV-23. Normalized IDA curves (with respect to damage at ultimate limit state D_2^{us}).

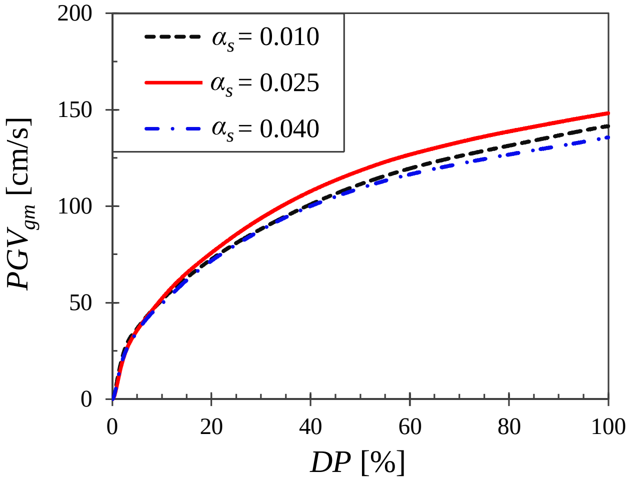

Figure IV-24. Median normalized IDA curves.

IV.8. Fragility curves

The performance of U-shaped steel dampers under bidirectional seismic excitation was investigated in the previous section where the IDA curves were obtained. In this section, these results are processed and fragility curves are drawn to estimate what is the probability that a damper reaches a certain performance level at a given seismic intensity level (PGV_{gm}). To this purpose, two sets of fragility curves are drawn:

1. Fragility curves for each limit state
2. Fragility curves for reference values of the maximum displacement $R_{\max}$ (200, 400, 600 and 800(mm))

A fragility curve for a certain limit state is obtained by first finding the points where the limit state is reached. Figures IV-25, IV-26 and IV-27 show the intersection points with limit states LS1, LS2, respectively LS3 for the reference case with yield base shear coefficient $\alpha_s = 0.025$, their resulting lognormal probability density functions (PDF) and corresponding cumulative distribution functions. The latter are better known as "fragility curves". As expected, the median value of PGV_{gm} increases from limit state LS1 (79.8(cm/s)) to limit state LS3 (147.1(cm/s)). For the case with $\alpha_s = 0.025$, limit state LS4 was reached only by 4 ground motions (Fig. IV-19(b)), therefore a fragility curve could not be obtained.

The fragility curves for the other 2 values of α_s are obtained in a similar way and are shown in Fig. IV-28. It is worth mentioning that the only case for which the fragility curves for all four limit states could be derived is that corresponding to $\alpha_s = 0.010$. On the contrary, for $\alpha_s = 0.040$, only the fragility curves for the first 2 limit states could be drawn because there are not enough points intersecting LS3, respectively LS4. For this reason, since the ultimate limit state is reached when $R_{\max}$ = 800(mm), the corresponding fragility curve was derived and shown in Fig. IV-28(c) with red line. Fragility curves define the limits between the performance levels described in Section IV.6. The case with $\alpha_s = 0.010$ is the only one for which enough ground motions have reached limit state LS3, therefore the corresponding fragility curve could be drawn (Fig. IV-28(a)).

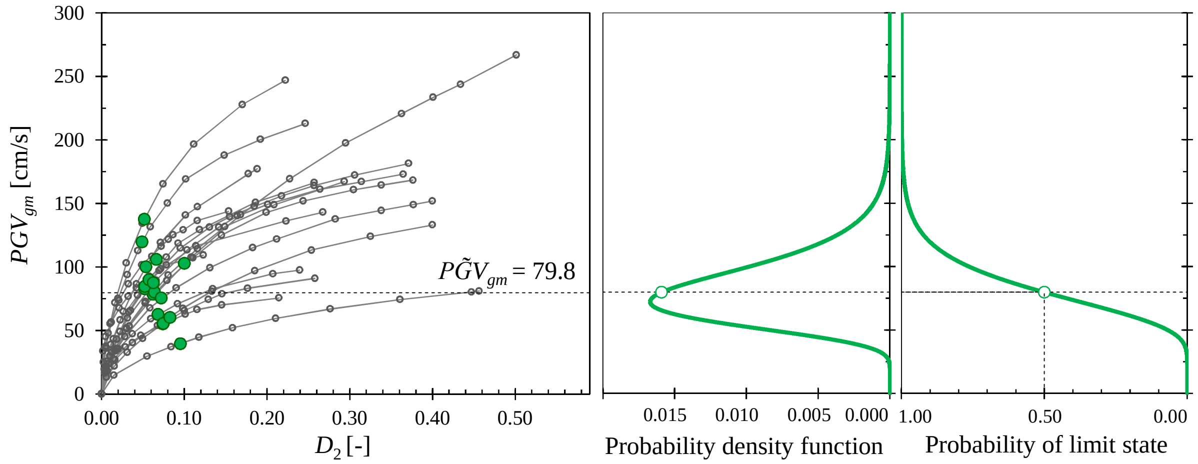

(a) Position of intersection points with LS1 (b) PDF (c) Fragility curve

Figure IV-25. Position of intersection points with limit state LS1 ($\alpha_s = 0.025$).

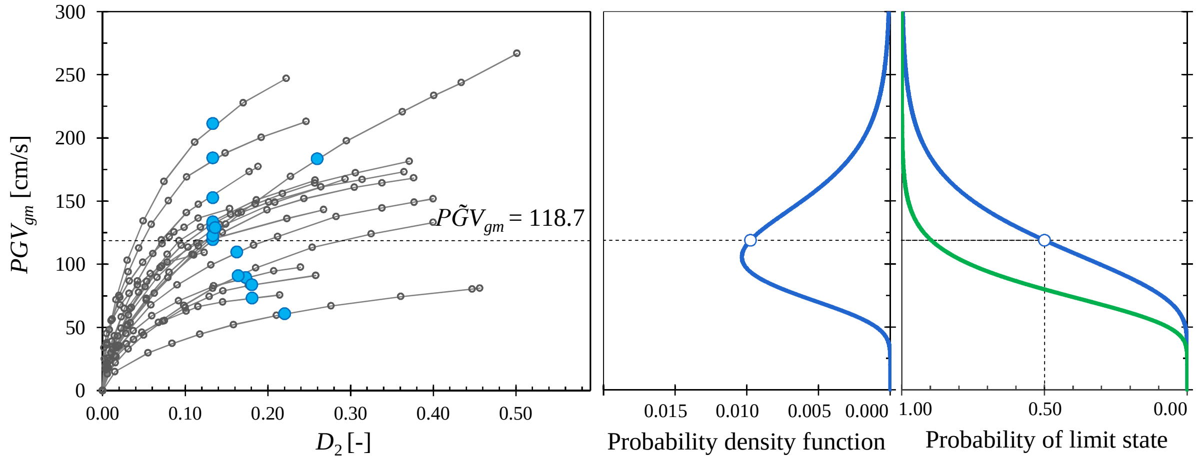

(a) Position of intersection points with LS2 (b) PDF (c) Fragility curve

Figure IV-26. Position of intersection points with limit state LS2 ($\alpha_s = 0.025$).

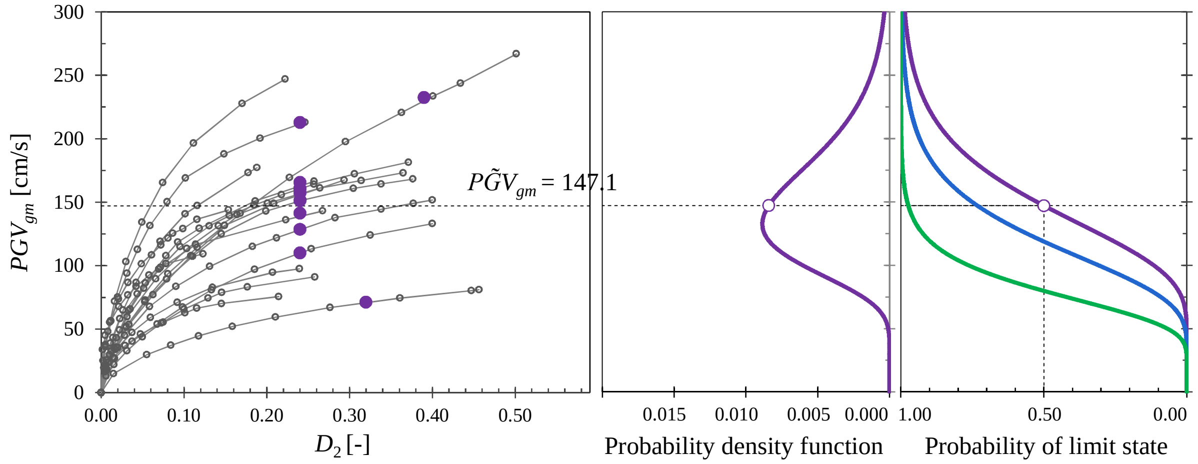

(a) Position of intersection points with LS3 (b) PDF (c) Fragility curve

Figure IV-27. Position of intersection points with limit state LS3 ($\alpha_s = 0.025$).

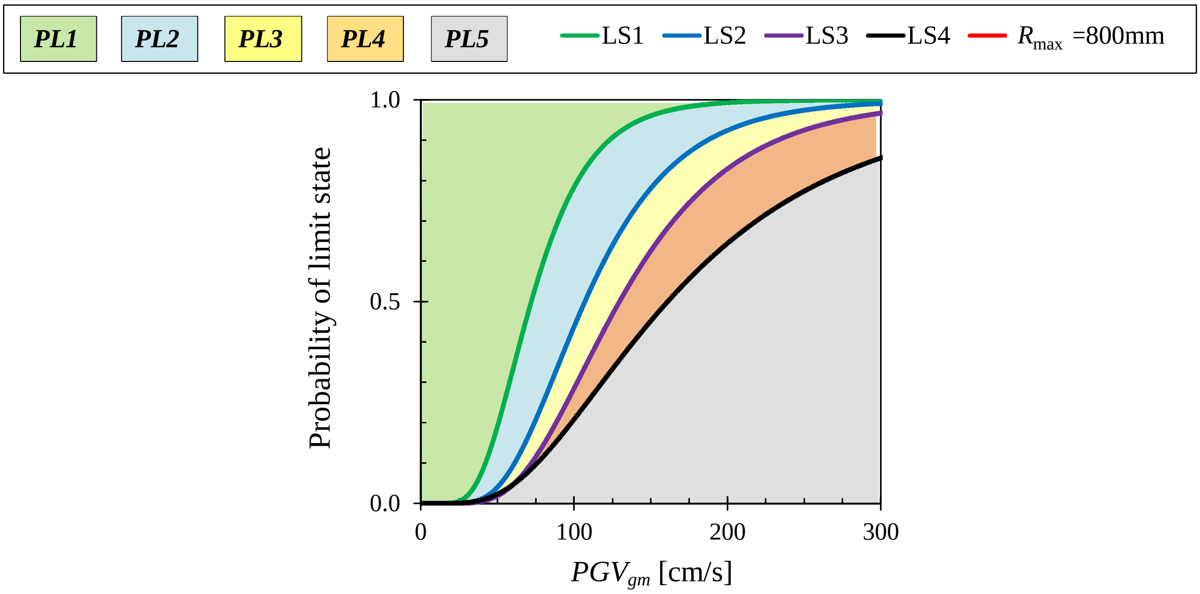

(a) $\alpha_s = 0.010$

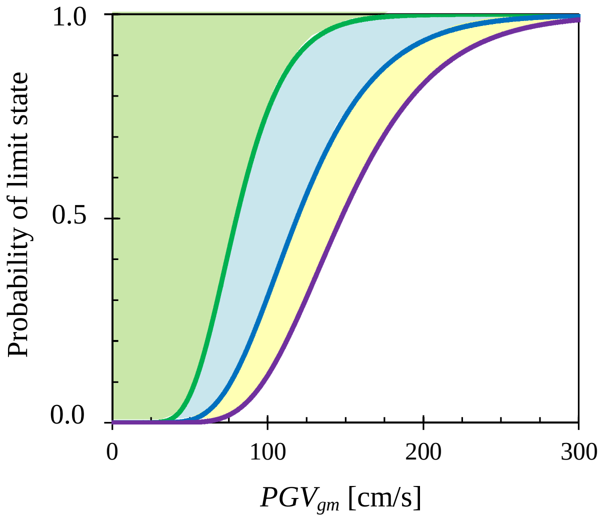

(b) $\alpha_s = 0.025$

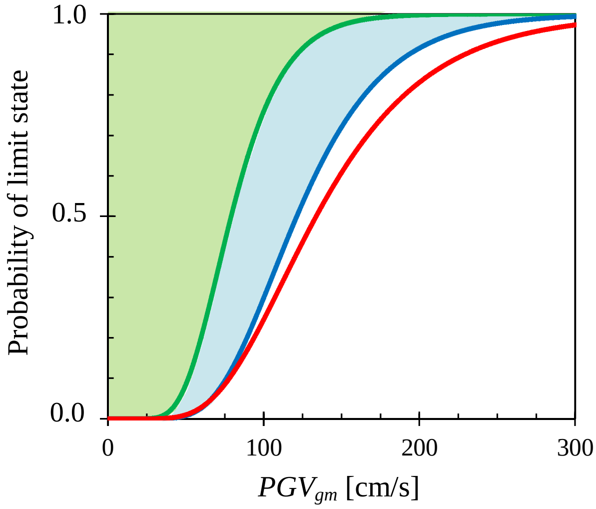

(c) $\alpha_s = 0.040$

Figure IV-28. Fragility curves for intersection with limit states.

In Table IV-9 are listed the probabilities for each performance level at seismic hazard levels L2 (PGV_{gm} = 50(cm/s)) and L3 (PGV_{gm} = 75(cm/s)). The probabilities for level L1 are not given here since they are negligible (≈ 10^{-3}(%)). The results are plotted in Fig. IV-29 from which it can be understood that under very rare earthquakes (level L2), the dampers have over 80% probability that they have a remaining plastic deformation capacity of 90% (performance level ***PL1***). This fact confirms the studies made by Konishi *et al.* who have extracted several U-shaped steel dampers from the isolation layer of a hospital in Ishinomaki subjected to Tohoku 2011 earthquake and conducted loading tests until fracture. The peak ground velocity of a nearby site was a little over 50(cm/s), corresponding, thus, to a level L2 hazard. The results have shown that residual plastic deformation capacity was about 90% [IV.23], which confirms again the high reliability of the dampers even under severe motions.

For seismic hazard level L3, the probability that the dampers are situated inside performance level ***PL1*** drops to 46% for the case with $\alpha_s = 0.040$, and to about 58% for $\alpha_s = 0.025$. On the other hand, the probability that the dampers are situated inside ***PL2*** increases to approximately 33%.

Table IV-9. Probability of each performance level at seismic hazard levels L2 and L3

Level	PGV_{gm} (cm/s)	Performance level	Probability (%)		
			$\alpha_s = 0.010$	$\alpha_s = 0.025$	$\alpha_s = 0.040$
L2	50.0	*P*(***PL1***)	***80.93***	***93.12***	***91.60***
		P(***PL2***)	15.03	6.27	7.66
		P(***PL3***)	2.19	0.56	0.74 (*)
		P(***PL4*** ∪ ***PL5***)	1.85	0.05	
L3	75.0	*P*(***PL1***)	***46.14***	***57.78***	***56.40***
		P(***PL2***)	33.12	33.09	34.27
		P(***PL3***)	9.18	7.28	9.33 (*)
		P(***PL4***)	1.92	1.85 (**)	
		P(***PL5***)	9.64		

(*) Probability for ***PL3*** ∪ ***PL4*** ∪ ***PL5***; (**) Probability for ***PL4*** ∪ ***PL5***.

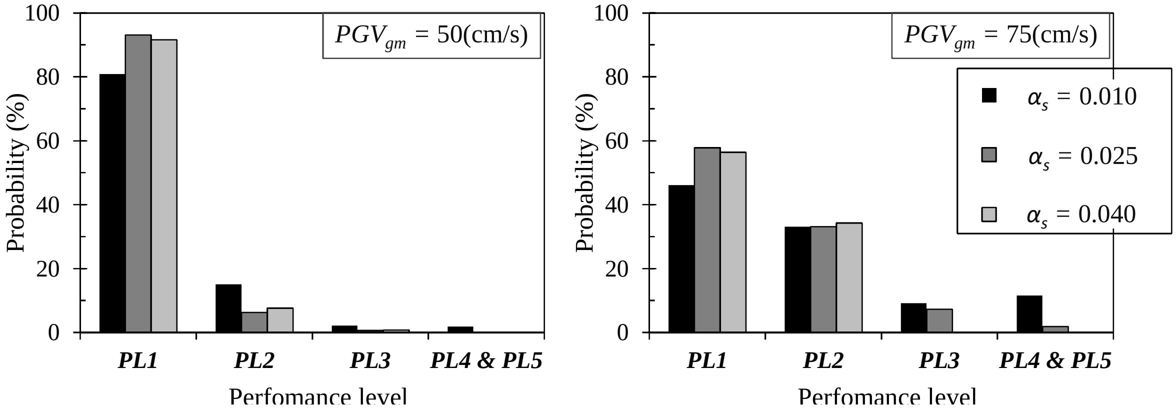

Figure IV-29. Probabilities of each performance level for seismic hazard L2 and L3.

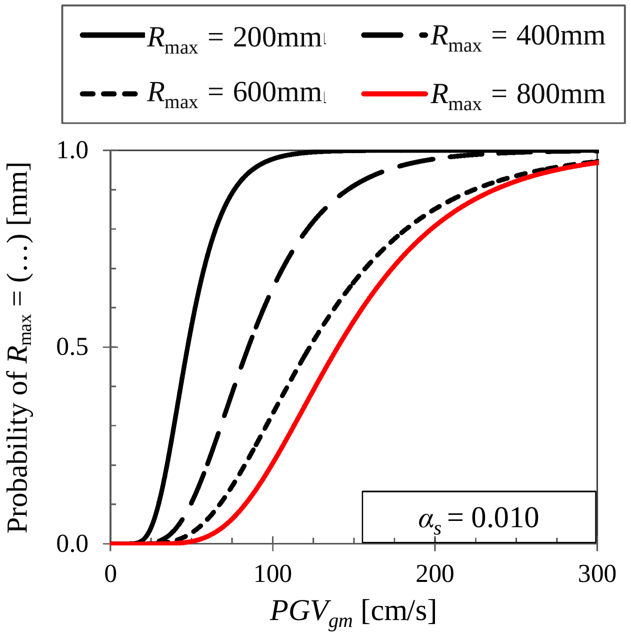

(a) $\alpha_s = 0.010$

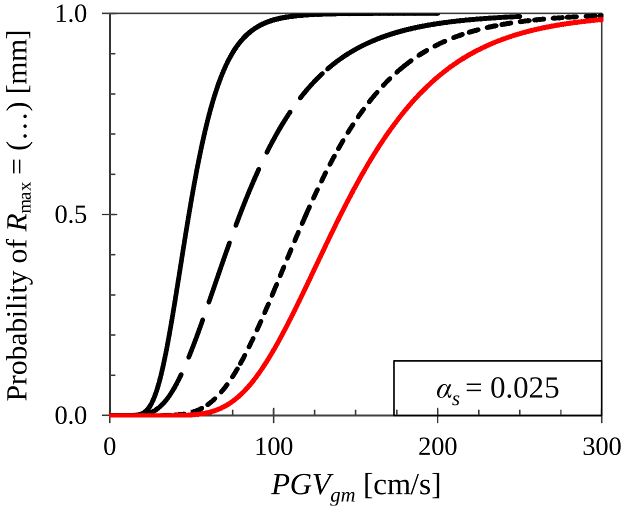

(b) $\alpha_s = 0.025$

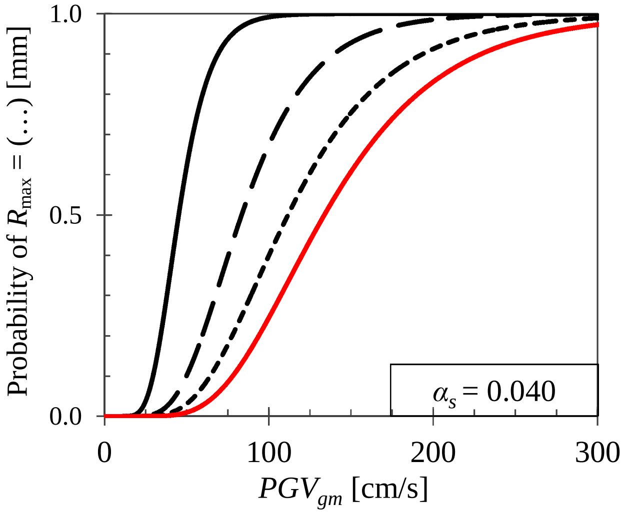

(c) $\alpha_s = 0.040$

Figure IV-30. Fragility curves for maximum displacement R_{max} = 200, 400, 600, 800(mm).

In the design process, the maximum displacement of the isolation layer is one of the most important parameters since it is used to decide the required clearance or the optimal flexibility of the isolation layer. For this reason, fragility curves for different values of $R_{\max}$ are derived (Fig. IV-30). Table IV-10 summarizes the probabilities that the maximum displacement $R_{\max}$ is situated in the intervals (0, 200], (200, 400], (400, 600], (600, 800] or greater than 800(mm), for each design seismic hazard level L1, L2 and L3. The maximum values are shown in bold. It can be observed that for level L1, regardless of the value of α_s, the probability that the isolation layer has a maximum displacement $R_{\max}$ less or equal to 200(mm) is over 96%.

For level L2, the highest probability for the case with $\alpha_s = 0.025$ is obtained for $R_{\max} \leq$ 200(mm) (≈46%). For the other 2 cases, it was found to be most probable that the isolation layer has a maximum displacement $R_{\max}$ situated between 200(mm) and 400(mm). However, the probability that $R_{\max} \leq$ 200(mm) still occupies an important percentage (greater than 38%). This finding is in accordance with the reconnaissance report published by the National Institute for Land and Infrastructure Management after Tohoku 2011 earthquake, in which it was stated that in most cases, the maximum displacement was estimated to be around 200(mm) [IV.24]. The JMA seismic intensity for the investigated buildings was mainly VI (lower or upper) which roughly corresponds to seismic hazard level L2 [IV.25].

For level L3, the highest probability is obtained for $R_{\max} \in (200, 400]$ (mm).

Table IV-10. Probability of maximum displacement $R_{\max}$ (mm) at seismic levels L1, L2, L3

Level	PGV_{gm} (cm/s)	Performance level	Probability (%)		
			$\alpha_s = 0.010$	$\alpha_s = 0.025$	$\alpha_s = 0.040$
L1	25.0	$P(R_{\max} \leq 200)$	***99.96***	***97.42***	***96.30***
		$P(200 < R_{\max} \leq 400)$	0.04	1.87	3.57
		$P(400 < R_{\max} \leq 600)$	0.00	0.71	0.11
		$P(600 < R_{\max} \leq 800)$	0.00	0.00	0.02
		$P(R_{\max} > 800)$	0.00	0.00	0.00
L2	50.0	$P(R_{\max} \leq 200)$	44.57	***46.09***	38.04
		$P(200 < R_{\max} \leq 400)$	***44.94***	37.63	***51.86***
		$P(400 < R_{\max} \leq 600)$	7.72	15.51	7.01
		$P(600 < R_{\max} \leq 800)$	2.18	0.62	2.12
		$P(R_{\max} > 800)$	0.59	0.15	0.96
L3	75.0	$P(R_{\max} \leq 200)$	10.82	9.78	6.31
		$P(200 < R_{\max} \leq 400)$	***50.80***	***45.13***	***54.17***
		$P(400 < R_{\max} \leq 600)$	23.72	35.39	21.77
		$P(600 < R_{\max} \leq 800)$	8.33	6.20	9.30
		$P(R_{\max} > 800)$	6.33	3.50	8.45

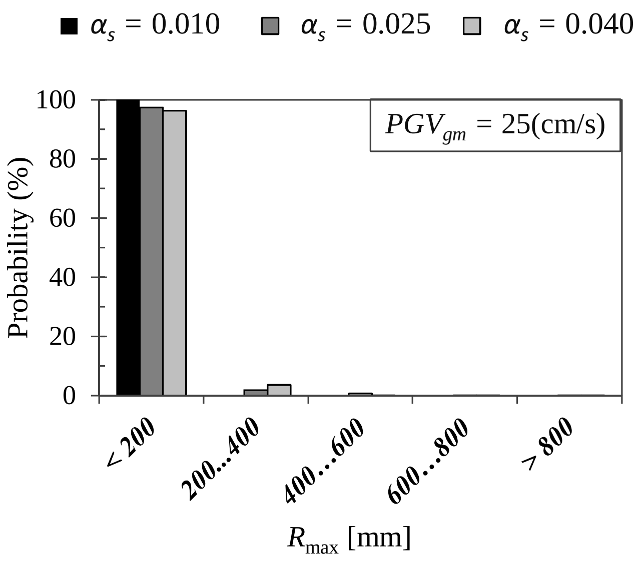

(a) Level L1: PGV_{gm} = 25(cm/s)

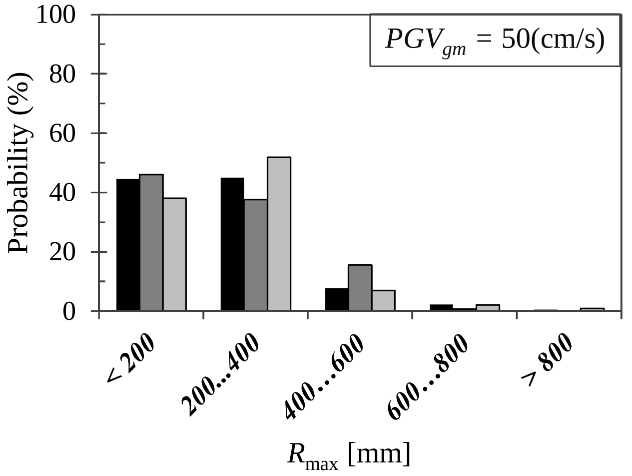

(b) Level L2: PGV_{gm} = 50(cm/s)

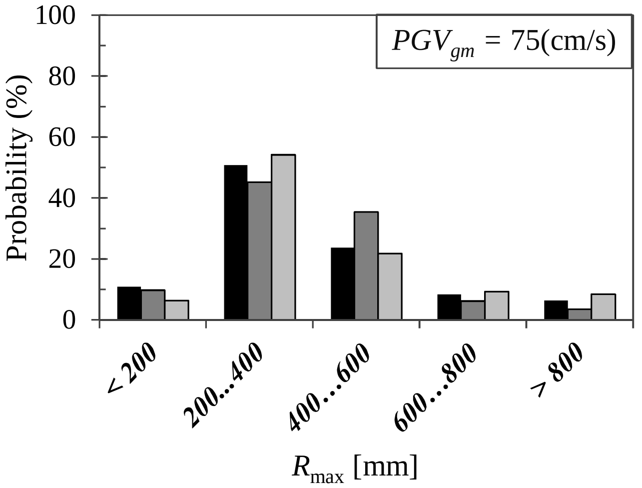

(c) Level L3: PGV_{gm} = 75(cm/s)

Figure IV-31. Probabilities of maximum displacement $R_{\max}$ for seismic hazard levels L1, L2 and L3.

In Table IV-11 are listed the probabilities of reaching the ultimate limit state (hereafter denoted with P_{ULS}) under seismic hazard levels L1, L2, respectively L3. For level L1, the probability of reaching the ultimate limit state P_{ULS} is virtually 0, while it can go as high as 2.12% for level L2 and as high as 9.08% for level L3. It is worth noting that among the considered values for the yield base shear coefficient α_s, 0.025 is the one for which the smallest probability of failure is obtained (P_{ULS} = 3.23% for level L3). To confirm this finding, the fragility curves of the last points of each IDA curve are constructed and shown in Fig. IV-32. For PGV_{gm} values less than 163(cm/s), indeed the smallest probability of reaching the ultimate limit state is obtained for $\alpha_s = 0.025$. For extremely severe ground motions with PGV_{gm} greater than 163(cm/s), the smallest P_{ULS} is obtained for $\alpha_s = 0.010$. However, given the fact that during the useful life of U-shaped steel dampers the probability of an event with a PGV_{gm} greater than 163(cm/s) is extremely small, it is the author's opinion that the best solution in design of an isolation system is to set α_s at 0.025 provided that the site is not located near an active fault (for which further studies are required).

Table IV-11. Probabilities of reaching the ultimate limit state (ULS)

Level	PGV_{gm} (cm/s)	Probability of reaching ULS (%)		
		$\alpha_s = 0.010$	$\alpha_s = 0.025$	$\alpha_s = 0.040$
L1	25.0	0.01	0.00	0.00
L2	50.0	2.12	0.16	1.22
L3	75.0	8.44	3.23	9.08

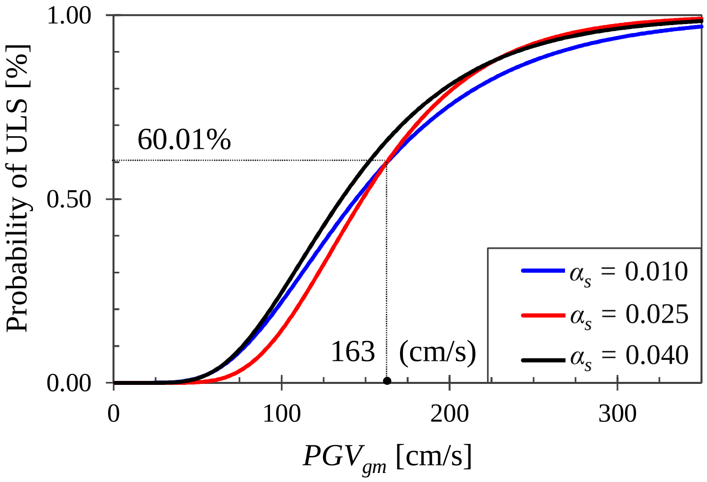

Figure IV-32. Probability of reaching ultimate limit state (ULS).

IV.9. Summary

The main conclusions of this chapter are:

1. The damage of U-shaped steel dampers has a significant record-to-record variability, therefore a probabilistic approach such as the one adopted in this chapter is of paramount importance.
2. U-shaped dampers are reliable under extremely severe ground motions (median value of the geometric mean horizontal component of the peak ground velocity PGV_{gm} at ultimate limit state is greater than 135(cm/s) regardless of the value of α_s).
3. Within the considered parameters, U-shaped steel dampers are most efficiently used if the value of yield base shear force coefficient α_s is set to 0.025.
4. In the seismic intensity range for which U-shaped steel dampers are designed, (hazard levels L1, L2, L3) the following observations were made:
    - For level L1, the probability that U-shaped steel dampers are situated in either performance level ***PL1*** (no damage or slight damage) or ***PL2*** (moderate damage) is almost 100%.
    - For level L2, this probability is greater than 95%.
    - For level L3, the probability that U-shaped steel dampers are situated in either performance level ***PL1*** or ***PL2*** decreases to 79%, but still represents a significant percentage of the total.
    - The probability that a damper reaches its ultimate limit state P_{ULS} under a bidirectional seismic excitation depends on the value of α_s. The smallest P_{ULS} (3.23%) is obtained for $\alpha_s = 0.025$ for values of PGV_{gm} less than 163(cm/s).

References:

[IV.1] Vamvatsikos, D., Cornell, C. A. 2001: Incremental dynamic analysis, *Earthquake Engineering and Structural Dynamics* ***31***, pp. 491-514;

[IV.2] Vamvatsikos, D., Cornell, C. A. 2004: Applied incremental dynamic analysis, *Earthquake Spectra* ***20***, No. 2, pp. 523-553;

[IV.3] Moehle, J., Deierlein, G.G. 2004: A framework methodology for performance-based earthquake engineering, *Proceedings of 13th World Conference on Earthquake Engineering*, Vancouver, Canada, paper no. 679;

[IV.4] Somerville, P. 2000. New developments in seismic hazard estimation, *Proceedings of the Sixth International Conference on Seismic Zonation (6ICSZ)*, 12–15 November 2000, California: Palm Springs;

[IV.5] Mavroeidis, G. P., Papageorgiou, A. S. 2002. Near-source strong ground motion: characteristics and design issues, *Proceedings of the Seventh U.S. National Conference on Earthquake Engineering (7NCEE)*, 21–25 July 2002, Massachusetts: Boston.

[IV.6] American Society of Civil Engineerings, Structural Engineering Institute 2011. *Minimum design loads for buildings and other structures (ASCE/SEI 7-10)*;

[IV.7] CEN, European Committee for Standardisation TC250/SC8/ 2003. Eurocode 8: *Design Provisions for Earthquake Resistance of Structures, Part 1.1: General rules, seismic actions and rules for buildings*, PrEN1998-1;

[IV.8] Applied Technology Council 2009. *Quantification of building seismic performance factors*: *Federal Emergency Management Agency P695*;

[IV.9] Haselton, C.B., Deierlein, G.G. 2008. Assessing seismic collapse safety of modern reinforced-concrete moment-frame buildings, PEER Report 2007/08, February 2008;

[IV.10] Campbell, K. W., Bozorgnia, Y. 2008: NGA Ground Motion Model for the Geometric Mean Horizontal Component of PGA, PGV, PGD and 5 Damped Linear Elastic Response Spectra for Periods Ranging from 0.01 to 10 s, *Earthquake Spectra* ***24***, No. 1, pp. 139–171;

[IV.11] 山田 哲, 伊山 潤, 島田 侑子, 松本, 由香, 長谷川 隆, 清家 剛, 中野, 達也, 吉敷 祥一. 東北地方太平洋沖地震および余震による学校体育館の構造被害, 日本建築学会技術報告集, 第20巻第44号，121-126，2014年2月;

[IV.12] Pan, P., Zamfirescu, D., Nakashima, M., Nariaki, N., Hisatoshi, K. 2005. Base-isolation design practice in Japan: Introduction to the post-Kobe approach, Journal of Earthquake Engineering 9(1), pp. 147-171;

[IV.13] 日本建築センター：ビルディング レター;

[IV.14] 中澤俊幸 2010. 過大入力下の動的挙動の統計的考察に基ずく免震構造物の耐震性向上に関する研究, 東京工業大学博士論文, 2010.2;

[IV.15] Pant, D.R., Wijeyewickrema, A.C. 2012. Structural performance of a base-isolated reinforced concrete building subjected to seismic pounding, *Earthquake Engineering and Structural Dynamics* ***41***, pp. 1709-1716;

[IV.16] Tsai, H.C. 1997. Dynamic analysis of base-isolated shear beams bumping against stops. *Earthquake Engineering and Structural Dynamics* ***26***, pp. 515–528;

[IV.17] Polycarpou, P.C., Komodromos, P. 2010. On poundings of a seismically isolated building with adjacent structures during strong earthquakes, *Earthquake Engineering and Structural Dynamics* ***39***, pp. 933–940;

[IV.18] Qu, Z., Kishiki, S., Nakazawa, T. 2013. Influence of isolation gap size on collapse performance of seismically isolated buildings, *Earthquake Spectra* ***29***(4), pp. 1477-1494;

[IV.19] Bakhshi, A., Mostafavi, S.A. 2014. Development of fragility curves for base isolated structures, *Proceedings of the 9th International Conference on Structural Dynamics*, EURODYN 2014, Porto, Portugal, June 30th – July 2nd 2014;

[IV.20] Campbell, K. W., Bozorgnia, Y. 2010: Analysis of cumulative absolute velocity (CAV) and JMA instrumental seismic intensity (IJMA) using the PEER-NGA strong motion database, Pacific Earthquake Engineering Research Center, PEER 2010/102;

[IV.21] Campbell, K. W., Bozorgnia, Y. 2008: NGA Ground Motion Model for the Geometric Mean Horizontal Component of PGA, PGV, PGD and 5% Damped Linear Elastic Response Spectra for Periods Ranging from 0.01 to 10 s, *Earthquake Spectra,* Volume 24, No. 1, pp. 139–171;

[IV.22] Mollaioli, F., Lucchini, A., Cheng, Y., Monti, G. 2013. Intensity measures for the seismic response prediction of base-isolated buildings, *Bulletin of Earthquake Engineering* ***11***, pp. 1841-1866;

[IV.23] Konishi, Y., Kawamura, N., Terashima, M., Kishiki, S., Yamada, S., Aiken, I. and Black, C. 2012. Evaluation of the fatigue life and behavior characteristics of U-shaped steel dampers after extreme earthquake loading, *Proceedings of 15th World Conference on Earthquake Engineering*, Lisbon;

[IV.24] National Institute for Land and Infrastructure Management (NILIM) and Building Research Institute (BRI), 2011. Summary of the Field Survey and Research on "The 2011 off the Pacific coast of Tohoku Earthquake" (the Great East Japan Earthquake), Response of seismically isolated buildings (accessed on December 6th 2013) http://www.kenken.go.jp/english/contents/topics/20110311/0311summaryreport.html;

[IV.25] 日本建築構造技術者協会編：JSCA 応答制御構造設計法－付.免震・建築雑誌(JABS), Vol. 127, No. 1637, pp. 29-30, 2012.10.

Chapter V

Comparison between One-Directional and Bidirectional Damage Evaluation Approaches

V.1. Introduction

As part of the isolation layer of base-isolated structures, U-shaped steel dampers are subjected to random loadings with a large range of displacement amplitudes, from frequent small amplitudes caused by low-intensity seismic events or strong winds, to large amplitudes (several tens of centimeters) caused by strong shaking. In addition, in the light of the lessons learnt after Tohoku 2011 earthquake, when a significant number of U-shaped lead dampers were reported to exhibit advanced cracks, more and more researchers and structural designers become concerned with the behavior of seismic isolation devices under bidirectional loading [V.1].

In ***Chapter IV*** an overall bidirectional approach was adopted to assess the performance of the dampers subjected to biaxial excitations with different characteristics and intensities. It was found that the dampers are highly reliable even under extremely severe shakings (median PGV_{gm} at ultimate limit state is greater than 135(cm/s)). However, as reported by Kishiki *et al.* [V.2] and confirmed by the results obtained in ***Chapter III***, the ultimate inelastic capacity of U-shaped steel dampers subjected to bidirectional loadings is reduced because of the effect of torsion stresses occurring in the steel bars. This finding pointed out the importance of properly evaluating the behavior under bidirectional displacement to avoid the possibility of early fracture of the dampers. However, typical design practices for seismic isolated structures adopt an in-plane frame analysis (Fig. V-1(b)), and only the response of special buildings is simulated using realistic 3D models to compute the bidirectional response of the isolation layer (Fig. V-1(a)). Moreover, the current *Design Recommendations for Base-Isolated Structures* [V.4] in Japan generally provides a one-directional approach for the damage estimation of seismic isolation devices to comply with the current design procedures. For the case of U-shaped steel dampers it was proved that a one-directional approach will most likely lead to unsafe design, because the damage is underestimated. However, it is not clear whether this issue has a strong impact in the range in which the dampers are designed to function. Moreover, it is necessary to estimate with satisfactory accuracy the safety margin against extremely severe earthquakes and decide whether this safety margin remains more or less within the same limits when a one-directional approach is employed.

The main objective of this chapter is to compare the damage estimated using the bidirectional approach adopted in this study (***Chapter IV***) to the damage obtained by applying the design recommendations for base-isolated structures (Fig. V-1). For this purpose, the following aspects are considered:

1. IDA was conducted using the same ground motions as in previous chapter – with the notable exception that this time they are applied independently – then estimate the damage index D of the dampers according to the provisions given in the design recommendations for base-isolated structures.

2. The difference between the bidirectional cumulative damage index D_2 computed using the bidirectional approach presented in ***Chapters II*** and ***IV*** and the cumulative damage index D obtained by applying the one-directional approach is quantitatively assessed.
3. The safety margin against fracture for the two damage evaluation methods (one-directional and bidirectional) is compared.

There are two main aspects that influence the difference between the two sets of results: (1) the damage evaluation method (D_2 versus D), and (2) the analytical model (bidirectional versus one-directional displacement response). These aspects are discussed in detail in the next sections. The results offer valuable information that help the structural designer to select the most suitable design scenario for each building.

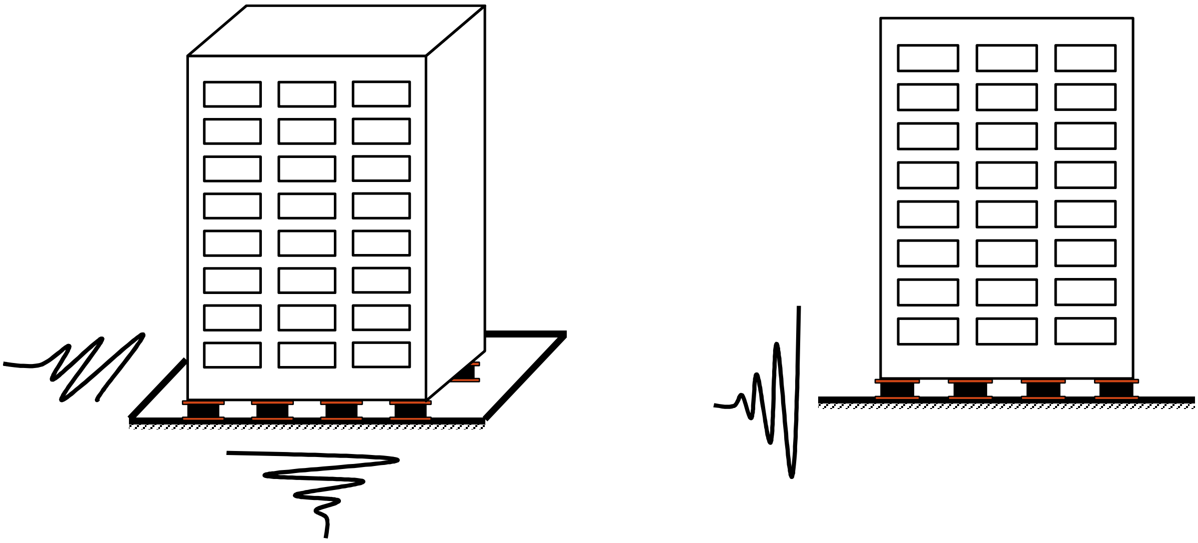

(a) Bidirectional analysis (2D approach) (b) In-plane analysis (1D approach)

Figure V-1. Bidirectional approach (2 horizontal components) and typical design practices in Japan (in-plane frame analysis with a single horizontal component).

V.2. Typical design requirements for seismic isolated structures and U-shaped steel dampers in Japan

In Japan, pioneer work on seismic isolated structures was conducted by several researchers. Kozo Kawai outlined the concept of seismic isolation in 1889; Kenzaburo Kito received the patent in 1920s for an aseismic device similar to modern friction pendulums. Toshio Otsuki proposed in 1951 a device to mitigate the transmitted force by using rollers provided in the foundation which were operable to intersect at right angles. Hideyuki Tada and Shoichi Yamaguchi designed the first seismic isolation building in Japan to employ rubber bearings [V.5].

In January 1987 the subcommittee of base-isolated structures was established within the Committee of the Architectural Institute of Japan. The first publication of the *Design Recommendations for Base-Isolated Structures* was released in March 1989 and included the following aspects: (1) evaluation of input earthquake motion, (2) dynamic response and structural design, (3) general design problems, (4) design examples, and (5) mechanical properties of isolators and dampers. The second edition – published in 1993 – added specifications about the durability and performance of seismic isolation devices under large displacements and about the basic characteristics of base-isolated structures, which contributed to their development throughout Japan.

In 2001, after the occurrence of Kobe 1995 earthquake that confirmed the efficiency of seismic isolation, a third edition was published which allowed for the first time the construction of base-isolated buildings taller than 100(m). The fourth edition – currently in use nowadays – was published in 2013, after the occurrence of Tokachi-oki 2003, Niigata 2004 and Fukuoka 2005 strong motion events. Additional sections providing recommendations about the selection of ground motions and of appropriate seismic isolation devices were included. Moreover, the 2013 edition aims at ensuring a proper performance of the isolation layer as well as providing guidance towards the selection of an adequate isolation gap (clearance) in order to avoid pounding with the retaining walls.

The current edition of the *Design Recommendations for Base-Isolated Structures* [V.4] includes a section about U-shaped steel dampers whose damage is estimated based on the two fatigue evaluation curves described in ***Chapter I***, and by further employing Miner's rule. The performance of the damper is then evaluated by comparing the damage index D with 1.0, where it is assumed that fracture occurs. Since for the case of U-shaped steel dampers there are two low-cycle fatigue evaluation curves, two damage indices D_{0° and D_{90° are computed independently by assuming that the specimen is loaded at 0° direction or at 90° direction respectively with the same horizontal component of the seismic motion. In design, the larger of the two damage indices is employed to verify whether the damper is in the safe range (Eq. (V.1)). Therefore, in practical design, only the one-directional fatigue behavior of the damper is considered, disregarding the effect of the bidirectional character of the relative displacement between the upper-structure and its foundation. Hence, by using this approach, the reduction of the plastic deformation capacity cannot be taken into consideration, leading to potentially dangerous situations in which the dampers fracture and lose their energy dissipation properties.

Considering the above, there are two possible approaches for estimating the damage of a U-shaped steel damper:

1. ***One-directional approach: 1D*** (hereafter referred to as ***1D approach***) in which both the damage evaluation method and the displacement response of the considered system are one-directional, and
2. ***Bidirectional approach: 2D*** (hereafter referred to as ***2D approach***) in which both the displacement response and the damage evaluation method are bidirectional. This methodology was the one adopted so far throughout the present study (***Chapters II, III and IV***).

The following sections describe the characteristics for each approach by comparing the damage evaluation methods and the analytical models. The main differences and similarities are summed up at the end of this section, in Table V-1.

V.2.1. Analytical models

Typical practices in Japan adopt an in-plane frame analysis (Fig. V-2(a)) for the design of seismic isolation devices, while for special buildings more realistic 3D models are employed to simulate the bidirectional response of the isolation layer (Fig. V-2(b)). In both cases, by modeling the upper-structure, the contribution of higher vibration modes can be taken into account. Although this is a very important aspect without which sizing the structural members of the upper-structure cannot be conducted, its effect on the displacement response of the isolation layer is small (provided that the upper-structure is not particularly tall). Therefore, for the purpose of the present study – where the displacement response of the isolation layer is of main concern – the upper-structure is modeled as a rigid body having a single mass. The in-plane frame analysis procedure typically adopted in design becomes, thus, a simple single degree of freedom system for which only the response to a single seismic excitation at a time can be obtained (Fig. V-2). This model is hereafter referred to as "1D model". Furthermore – based on the same observation –, the 3D model is simplified to a single mass system with two degrees of freedom (bidirectional displacement) as shown in Fig. V-3 conferred by using a multiple shear spring (MSS) element (Wada 1989, [V.6]). In the MSS model, the yield surface is almost circular which allows capturing the maximum response of the system without having to change the direction of the input wave. This aspect represents a great advantage over the basic SDOF model, and it is expected to be one of the causes why the one-directional damage index D will be underestimated with respect to the bidirectional damage index D_2.

It is worth noting that normally for the 1D approach, the structural designer uses as input wave only a single horizontal component, usually the one having the largest peak ground velocity.

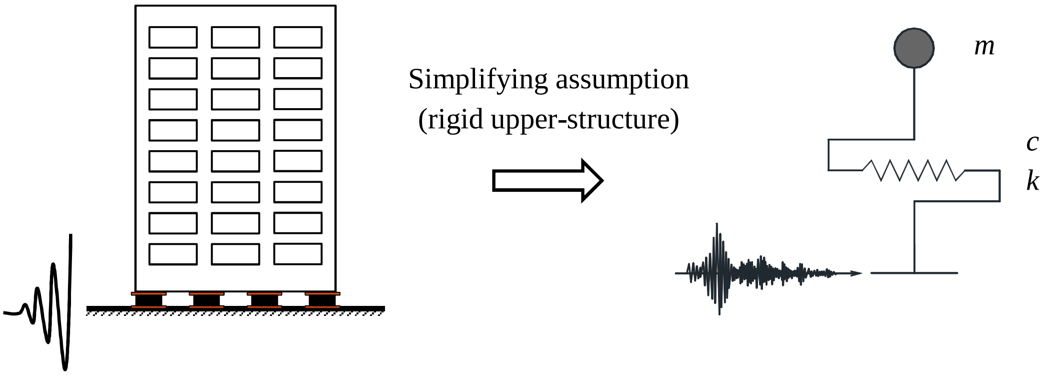

(a) In-plane frame analysis (typically used in design)
(b) SDOF system (considered for 1D approach)

Figure V-2. Simplification of the analytical model for 1D approach.

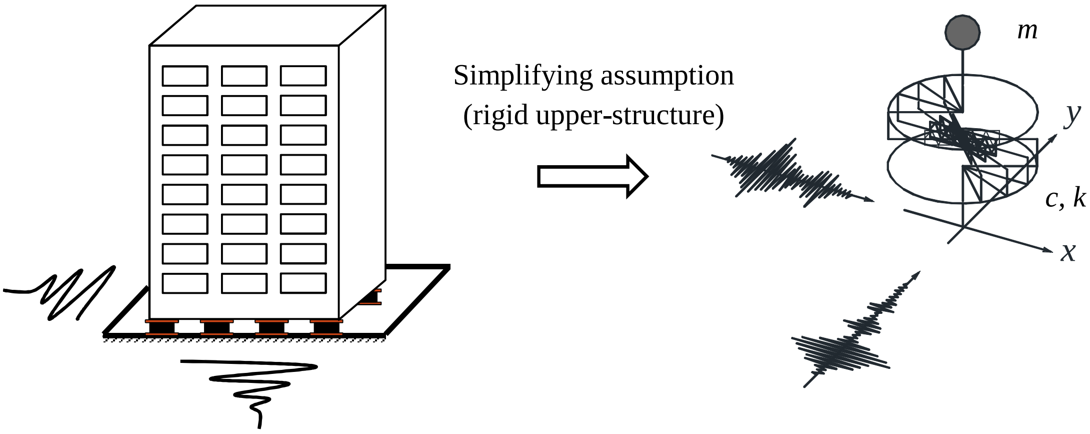

(a) 3D frame analysis (typically used in design)
(b) Single mass system with 2DOF (considered for 2D approach)

Figure V-3. Simplification of the analytical model for 2D approach.

Another essential difference between 1D and 2D analytical models is that the latter allows to compute the sway-motion index J_f. This is an especially important aspect because by employing this index the reduction of the inelastic deformation capacity can be evaluated, further allowing a realistic estimation of the safety margin against fracture of the dampers.

V.2.2. Damage evaluation methods

There are two methods to estimate the damage suffered by a U-shaped steel damper. The first one is directly based on the low-cycles fatigue evaluation curves and Miner's rule as described in Section I.3, while the second one considers in addition the effect of the displacement applied perpendicular to the longitudinal axis of the specimen (Section I.4). The difference between the two methods is graphically illustrated in Fig. V-4 for a better understanding. The black line shown in the right side is the D_2^u - J_f interaction curve (Eq. (I.8)). D is the one-directional damage index computed using the procedure given in the design recommendations, while D_2 is the bidirectional damage index obtained by simultaneously considering the in-plane and out-of-plane damage of a damper ([V.2], Eq. (I.6)). The value of D_2 is clearly larger than that of D since in design practices the latter is defined as the maximum of the terms summed in Eq. (V.1). This leads to the difference denoted with d_1 which is directly related to the damage evaluation procedure. Difference d_2 is related to the analytical model since for the 2D approach it allows the computation of the sway-motion index J_f which accounts for the effect of torsional stresses induced by a bidirectional displacement orbit.

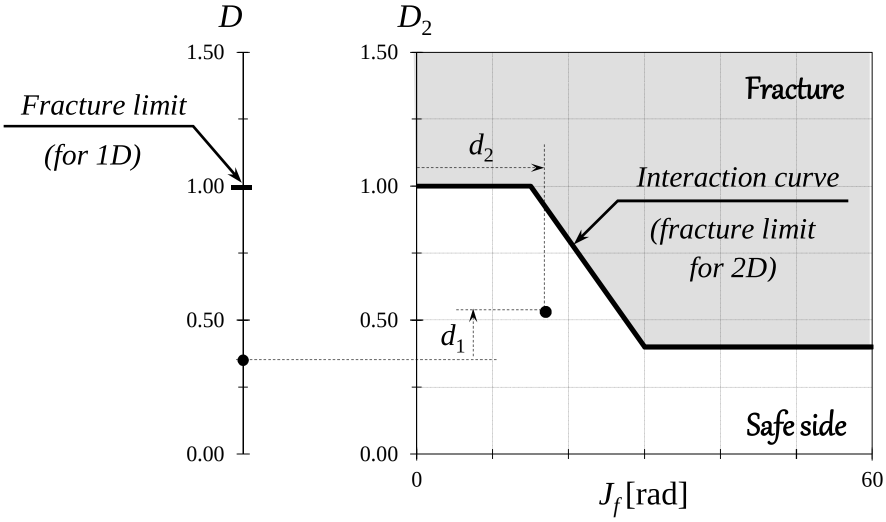

(a) 1D method (b) 2D method

Figure V-4. Difference between the damage evaluation method adopted in the design recommendations for base-isolated structures – 1D method (Eq. (V.1)) and the bidirectional damage evaluation – 2D method (Eq. (I.6)). d_1 results by considering the damage on the orthogonal direction, while d_2 evaluates the reduction of the ultimate inelastic deformation capacity under 2D loading.

One-directional damage evaluation method D

The low-cycle fatigue behavior of U-shaped steel dampers was found to be influenced by the loading direction. Therefore one-directional Manson-Coffin type low-cycle fatigue evaluation curves for 0° and 90° directions were developed, and are currently adopted by the design recommendations for base-isolated structures in Japan to estimate the damage of U-shaped steel dampers. These curves relate the displacement amplitude of a constant amplitude cyclic loading test to the number of cycles until fracture of the specimen.

The damage induced by an irregular displacement history is estimated by applying Miner's rule using a cycle-counting algorithm. In the present study, rain-flow counting algorithm with full cycles has been employed [V.3]. The result is the cumulative damage index D. The performance of the damper is evaluated by comparing this damage index D with 1.0, where it is assumed that fracture occurs. Since for the case of U-shaped steel dampers there are two low-cycle fatigue evaluation curves, two damage indices D_{0° and D_{90°, are computed independently by assuming that the specimen is loaded at 0° direction or at 90° direction respectively, with the same loading history (Fig. V-5). In design, the larger of the two damage indices is employed to verify whether the damper is in the safe range (Eq. (V.1)).

Therefore, in practical design only the one-directional fatigue behavior of the damper is considered.

$$D = \max\left(D_{0^\circ}, D_{90^\circ}\right) \tag{V.1}$$

where D is the one-directional cumulative damage index for 1D approach

D_{0° is the cumulative damage index when the damper is loaded along its longitudinal axis (Fig. V-5(a), (b))

D_{90° is the cumulative damage index when the damper is loaded perpendicular to its longitudinal axis (Fig. V-5(a), (c))

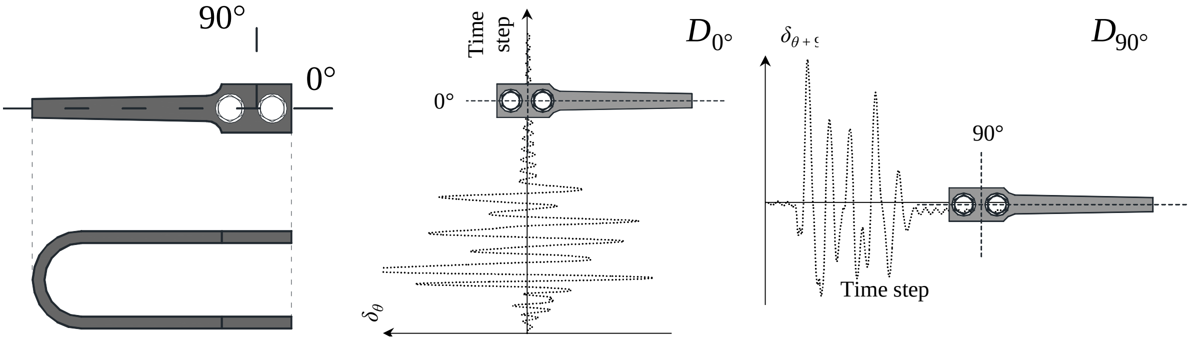

(a) Local axes of a damper (b) Loading at 0° (c) Loading at 90°

Figure V-5. Illustration of one-directional cumulative damage index D obtained by using the one-directional displacement response δ for a single seismic component.

In addition, it is important to recall that in order to compare the results for the one-directional approach to those obtained in ***Chapter IV***, it is necessary to compute the damage indices D_{0° and D_{90° for each horizontal component. Therefore, if we denote the horizontal acceleration time-histories with "x component" and "y component", the maximum one-directional damage evaluation index D is obtained using Eq. (V.2):

$$D = \max\left({}_{x}D_{0^\circ}{}', {}_{x}D_{90^\circ}{}', {}_{y}D_{0^\circ}{}', {}_{y}D_{90^\circ}{}' \right) \tag{V.2}$$

where the dash is used to make the distinction between the bidirectional displacement response (δ_x, δ_y) obtained in ***Chapter IV*** and the one-directional response computed using the same input waves, but a different analytical model that does not take into consideration the interaction between the displacement components (δ_x', δ_y').

<u>*Bidirectional damage evaluation method*</u> D_2

The bidirectional cumulative damage index D_2 adopted in this chapter is the same as that described in Section IV.4.2. It is obtained by decomposing the bidirectional displacement orbit into two orthogonal components (*e.g.* δ_θ, $\delta_{\theta+90^\circ}$) and adding the corresponding damage indices (${}_{\theta}D_{0^\circ}$ and ${}_{\theta+90^\circ}D_{90^\circ}$). The maximum value of the damage index D_2 is obtained by considering different orientations of the damper with respect to the bidirectional displacement orbit as given in Eq. (V.3) (vary angle θ as described in Figures V-6).

$$D_2 = \max_{0\le\theta\le\pi}\left({}_{\theta}D_{0^\circ} + {}_{\theta+90^\circ}D_{0^\circ}\right) \tag{V.3}$$

where D_2 is the bidirectional cumulative damage index for 2D approach

${}_{\theta}D_{0^\circ}$ is the cumulative damage index when the damper is loaded with displacement δ_θ parallel to its longitudinal axis (Fig. V-6(b))

${}_{\theta+90^\circ}D_{90^\circ}$: cumulative damage index when the damper is loaded with displacement $\delta_{\theta+90^\circ}$ perpendicular to its longitudinal axis (Fig. V-6(c))

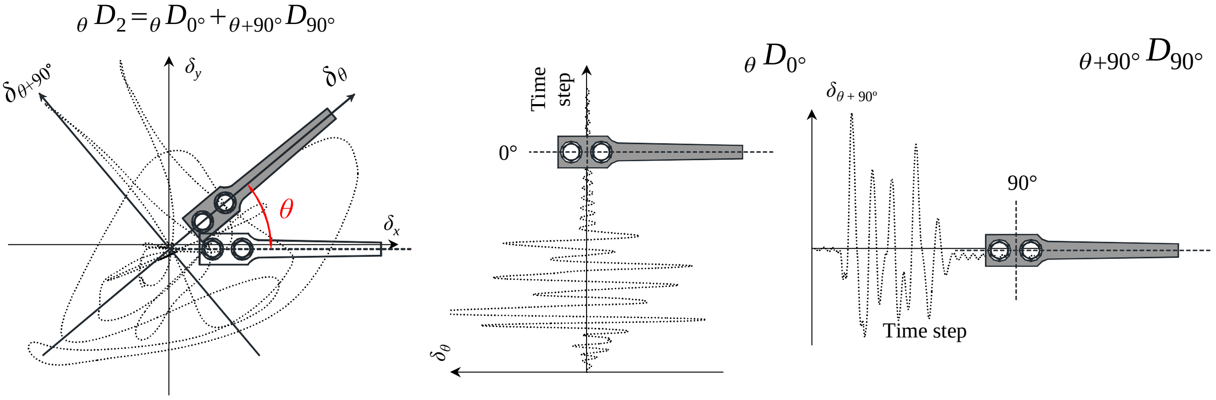

(a) Bidirectional displacement history and variation of θ
(b) Displacement at θ → damage index ${}_{\theta}D_{0^\circ}$
c) Displacement at θ + 90° → damage index ${}_{\theta+90^\circ}D_{90^\circ}$

Figure V-6. Computation of bidirectional cumulative damage index D_2.

Table V-1. Similarities and differences between one-directional (1D) and bidirectional (2D) approaches

Method	Analytical model	Damage evaluation	Observations
1D	SDOF (in-plane analysis)	$D = \max(D_{0^\circ}, D_{90^\circ})$ Fracture when D = 1.0	• Typical design method • Input wave: only one horizontal component of the seismic motion • Damage is expected to be underestimated
2D	Single mass system with 2DOFs (MSS model)	$D_2 = {}_{\theta}D_{0^\circ} + {}_{\theta+90^\circ}D_{90^\circ}$ Fracture when $D_2 - J_f$ interaction curve is reached	• Assumed to be the correct analytical method • Results are assumed to be accurate

V.2.3. Summary of comparison methodology

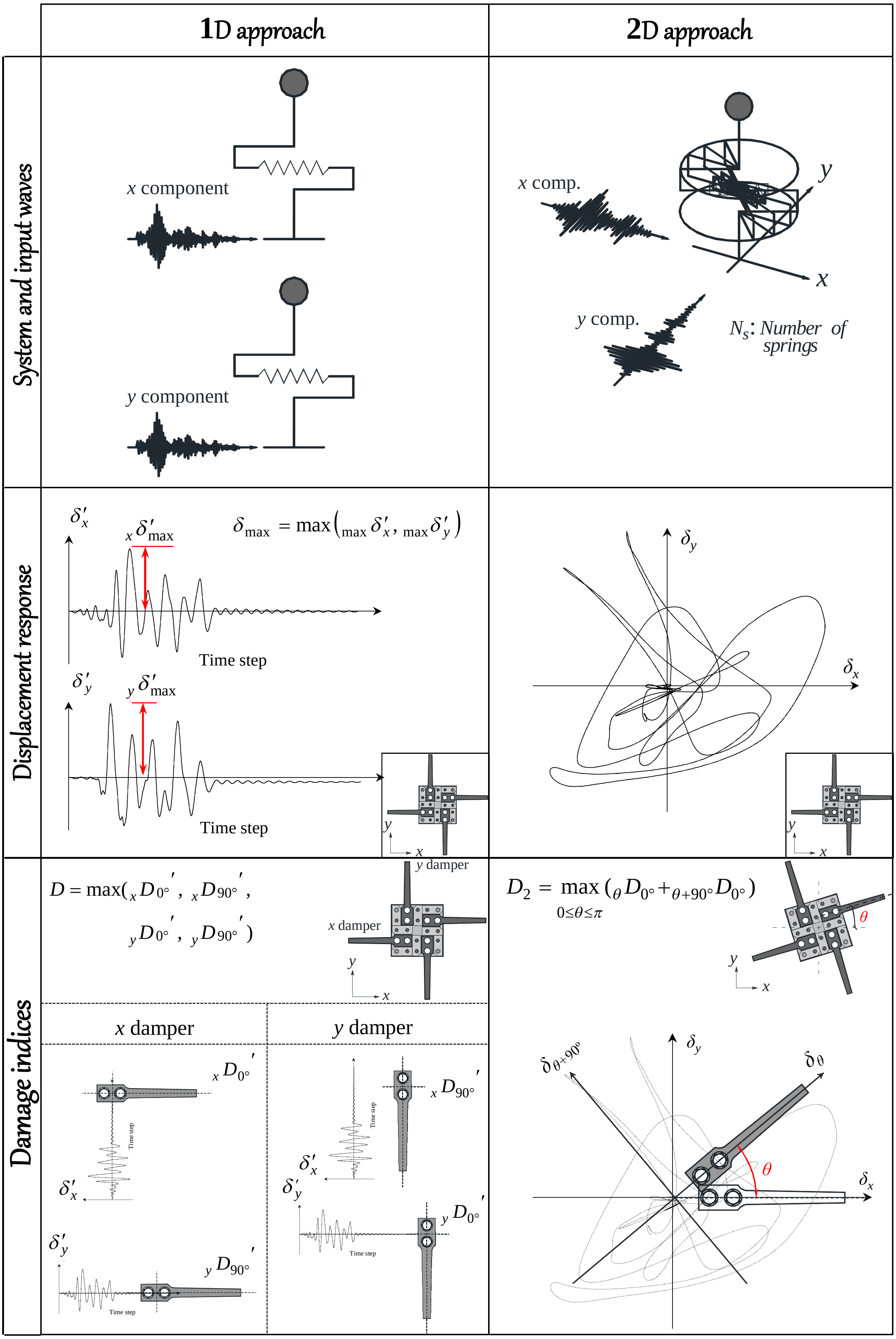

V.3. Preliminary comparison between one- and bidirectional approaches with focus on design seismic hazard levels in Japan

The main differences between de two approaches for damage evaluation of U-shaped steel dampers were described in the previous section. The present section aims at conducting a preliminary comparison between these approaches, focusing on ground motions recorded in Japan or typically used in the design of seismic isolated structures in Japan. The employed ground motions are listed in Table V-2.

Employing the analytical models described in Section V.2, and setting the value of the yield base shear coefficient to 0.025 – as typically used in design –, the difference between the results obtained for the 1D and 2D approaches is evaluated at the seismic intensities corresponding to the design seismic hazard levels L1, L2 and L3. The design seismic hazard levels are associated to values of the peak ground velocity *PGV* of 25, 50, respectively 75(cm/s) (Table IV-7). In addition, the results obtained for *PGV* of 100(cm/s) are also investigated to assess the difference under extremely large seismic events.

Table V-2. Ground motions for preliminary comparison between 1D and 2D approaches

No.	Earthquake	Site		*PGV* [cm/s] (*)	
				PGV_x	PGV_y
1	Imperial Valley 1940	El Centro	EL	***48.8***	38.1
2	Kern Kounty 1952	Taft	TF	17.5	***18.2***
3	Tokachi-oki 1968	Hachinohe	HC	***37.0***	34.2
4	Loma Prieta 1989	Angnews Hospital	AG	***25.9***	17.6
5	Cape Mendocino 1992	Rio Dell Overpass	CM	***43.8***	41.9
6	Northridge 1994	Olive View	SO	78.0	***129.2***
7	Kobe 1995	Amagasaki	AM	***85.9***	49.5
8	Kobe 1995	Nishi-Akashi	KN	***37.3***	36.6
9	Chi-Chi 1999	TCU129	TC	***55.4***	51.0
10	Tohoku 2011	JMA Sendai	JS	53.3	***54.5***

(*) Values shown in bold correspond to the dominant component *C1*, the ones in gray to the second component C2.

In typical design, the horizontal component with the largest *PGV* (dominant component, hereafter denoted with *C1*) is selected to conduct time-history analysis (Eq. (V.4)), therefore in the present chapter only the *PGV* of the dominant component *C1* was considered. In the next step, time-history analyses were conducted for both components of each ground motion, both for the 1D approach and for the 2D approach. Except for the analytical model, the difference between the two approaches is that the input waves are applied simultaneously for 2D method, while for 1D method, they are applied independently. The *PGV* values for the dominant component *C1* are listed in Table V-2 with bold, while those corresponding to the second component *C2* are shown with gray.

$$PGV = \max\left(PGV_x, PGV_y\right) \tag{V.4}$$

where PGV is the peak ground acceleration of the dominant horizontal component *C1*

PGV_x, PGV_y are the peak ground accelerations of the horizontal component along x direction, respectively along y direction.

The scale factors s_f were computed such that the *PGV* of the dominant component *C1* reaches the targeted values. The obtained values of s_f were also applied to the second horizontal component. It is worth noting that the same scale factors are used for both 1D and 2D approaches to ensure that comparing the two sets of results is appropriate.

The obtained analytical results for each approach are listed in Table V-3, where the minimum and maximum values are also shown. In the next pages, the two sets of results are compared and discussed in detail considering the following aspects:

- Maximum displacement of the isolation layer
- Cumulative damage indices
- Safety margin against fracture

Table V-3. Analytical results (preliminary analysis) for 1D and 2D approaches (*)

PGV [cm/s]	GM	1D approach		2D approach			
		δ_{max} [mm]	*D* [-]	R_{max} [mm]	D_2 [-]	J_f [rad]	*DR* [%]
25	EL	80	0.0066	106	0.0072	0.06	0.7
	TF	108	0.0111	134	0.0112	0.09	1.1
	HC	114	0.0149	116	0.0219	0.25	2.2
	AG	116	0.0189	137	0.0209	0.17	2.1
	CM	65	0.0026	70	0.0033	0.02	0.3
	SO	104	0.0056	112	0.0054	0.03	0.5
	AM	87	0.0094	100	0.0088	0.07	0.9
	KN	109	0.0090	102	0.0101	0.08	1.0
	TC	94	0.0101	98	0.0075	0.10	0.8
	JS	65	0.0135	74	0.0112	0.14	1.1
Min. val.		65	0.0026	64	0.0033	0.02	0.3
Max. val.		116	0.0189	137	0.0219	0.25	2.2

(*) The table is continued on the next page

Table V-3. Analytical results (preliminary analysis) for 1D and 2D approaches (c-ted)

PGV [cm/s]	GM	1D approach		2D approach			
		$\delta_{\max}$ [mm]	D [-]	$R_{\max}$ [mm]	D_2 [-]	J_f [rad]	DR [%]
50	EL	268	0.0237	314	0.0274	0.54	3.1
	TF	236	0.0319	276	0.0408	0.73	4.4
	HC	244	0.0476	242	0.0623	1.48	7.6
	AG	259	0.0537	302	0.0687	1.88	9.0
	CM	122	0.0096	114	0.0101	0.13	1.0
	SO	183	0.0113	203	0.0148	0.15	1.5
	AM	170	0.0189	188	0.0212	0.28	2.1
	KN	182	0.0219	171	0.0284	0.49	3.0
	TC	203	0.0260	241	0.0305	0.55	3.3
	JS	179	0.0548	196	0.0577	0.86	5.8
Min. val.		122	0.0096	114	0.0101	0.13	1.0
Max. val.		268	0.0548	314	0.0687	1.88	9.0
75	EL	440	0.0465	516	0.0606	2.29	9.5
	TF	337	0.0628	403	0.1017	3.44	15.0
	HC	362	0.0897	380	0.1199	5.59	21.5
	AG	461	0.0965	486	0.1495	9.93	34.2
	CM	193	0.0163	187	0.0202	0.48	2.5
	SO	260	0.0212	298	0.0284	0.59	3.2
	AM	274	0.0327	296	0.0474	1.41	6.5
	KN	277	0.0401	246	0.0532	1.79	7.8
	TC	344	0.0568	445	0.0712	2.48	10.6
	JS	289	0.1019	357	0.1148	4.27	17.9
Min. val.		193	0.0163	187	0.0202	0.48	2.5
Max. val.		461	0.1019	516	0.1495	9.93	34.2
100	EL	618	0.0817	710	0.1224	6.09	22.9
	TF	432	0.1125	530	0.1898	11.18	39.8
	HC	465	0.1369	535	0.1930	14.71	48.3
	AG	651	0.1794	673	0.3176	30.45	79.4
	CM	251	0.0261	265	0.0335	1.25	5.2
	SO	342	0.0326	400	0.0449	1.45	6.4
	AM	388	0.0546	407	0.0867	4.21	15.9
	KN	356	0.0609	368	0.0903	5.06	18.3
	TC	528	0.1088	675	0.1424	7.74	28.3
	JS	489	0.1563	519	0.1932	12.66	43.7
Min. val.		251	0.0261	265	0.0335	1.25	5.2
Max. val.		651	0.1794	710	0.3176	30.45	79.4

V.3.1. Comparison of the maximum displacement of the isolation layer ($\delta_{\max}$ and $R_{\max}$)

As discussed in Section V.2.1, the displacement response for the two approaches is obtained differently, by engaging two different analytical models. For the 1D approach, the maximum displacement – denoted with $\delta_{\max}$ – is obtained by computing the independent displacement response of the system subjected to each horizontal component and taking their maximum value (Eq. (V.5a)).

$$\delta_{\max} = \max\left({}_{\max}\delta'_x,\ {}_{\max}\delta'_y\right) \tag{V.5a}$$

$${}_{\max}\delta'_x = \max_{0\le t\le t_f}\left(\delta'_x\right);\quad {}_{\max}\delta'_y = \max_{0\le t\le t_f}\left(\delta'_y\right) \tag{V.5b}$$

where $\delta_{\max}$ is the maximum displacement for the 1D approach, considering the response of each horizontal component

${}_{\max}\delta'_x$, ${}_{\max}\delta'_y$ are the maximum one-directional displacements for each horizontal component (x, respectively y, as shown in Section V.2.3)

t is the time step

t_f is the last time step

For the 2D approach, the maximum displacement $R_{\max}$ was defined in ***Chapter IV*** (Eq. (IV.16)) as the maximum displacement measured from the origin of the bidirectional displacement orbit (Fig. IV-17).

To assess the influence of the analytical model, first the two sets of maximum displacements of the isolation layer ($\delta_{\max}$ and $R_{\max}$) are compared as shown in Fig. V-7. The results corresponding to each considered value of *PGV* are plotted using different colors. It can be observed that the scatter of the data is not significant, regardless of the value of the *PGV*. Moreover, the results show that $R_{\max}$ is about 10% larger than $\delta_{\max}$, which can be used to express the calculated value ${}_cR_{\max}$ as given in Eq. (V.6).

$${}_cR_{\max} = 1.10\cdot\delta_{\max} \tag{V.6}$$

where $\delta_{\max} \in [65, 700](\mathrm{mm})$.

For level L2, at which the base-isolated buildings are checked against collapse, the maximum displacements were found to be between 114 and 314(mm), with an average of about 100(mm). In addition, as the seismic intensity increases, it can be observed that the record-to-record variability for each value of the peak ground velocity also increases.

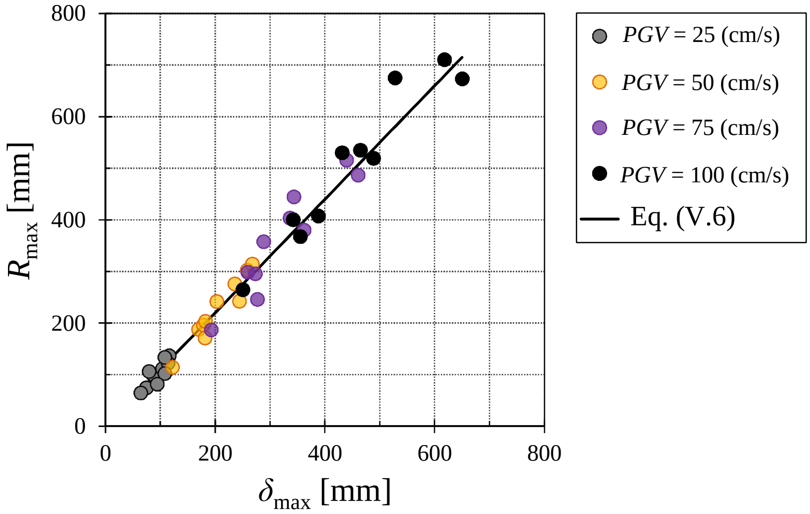

Figure V-7. Relation between the maximum displacement of the isolation layer obtained using 1D approach (δ_{max}) and that obtained using 2D approach (R_{max}).

V.3.2. Comparison of damage indices and safety margin against fracture

The direct comparison of the damage indices D and D_2 offers a general idea about the contribution of the damage on the orthogonal direction as well as the effect of considering different orientations of the damper with respect to the bidirectional displacement orbit. From Fig. V-8, in which the damage indices for each *PGV* level are plotted, it can be understood that as the seismic intensity increases, so does the difference between D and D_2. This is explained by the fact that the damage index on the orthogonal direction increases more rapidly at large displacement amplitudes (due to the characteristics of the fatigue evaluation curve for 90° direction). Another important observation in Fig. V-8 is that for the seismic hazard level L2 (*PGV* = 50(cm/s)) or less – for which the typical base-isolated structures are designed to prevent collapse – the damage indices for either approach are less than 0.100.

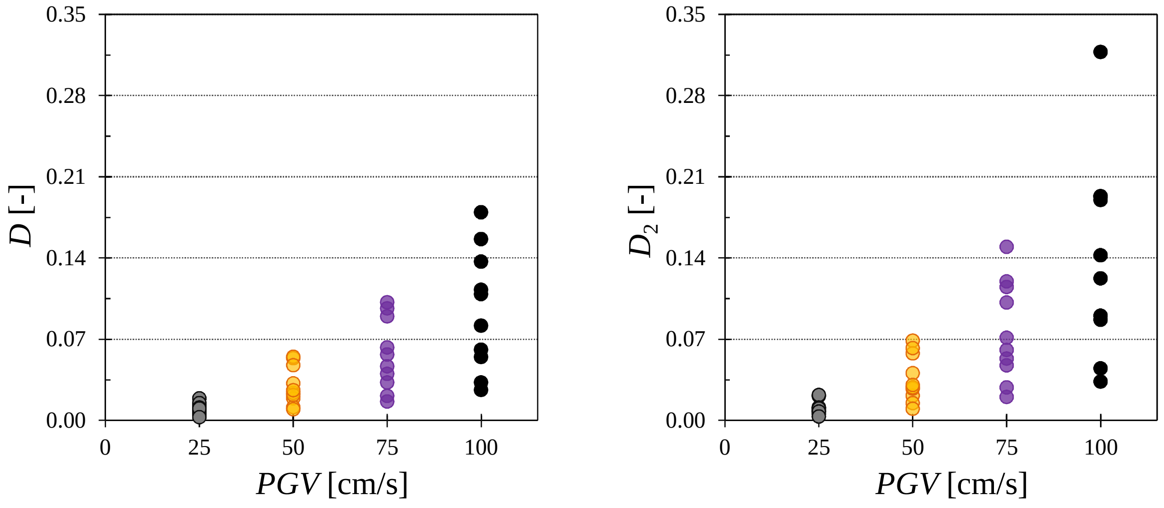

(a) 1D approach (b) 2D approach

Figure V-8. Difference between the one-directional and bidirectional cumulative damage indices with respect to the *PGV* of the dominant component *C1*.

To further investigate the difference between D and D_2, their ratio is plotted against the considered values of the PGV (Fig. V-9). Contrary to the results obtained for the maximum displacement of the isolation layer, the largest record-to-record variability is observed for PGV = 25(cm/s), which is also the only case where some of the values of the damage ratio D/D_2 are greater than 100(%). For the rest of the cases, the damage ratio D/D_2 drops as the PGV decreases to as low as 56(%) for Loma Prieta earthquake under PGV = 100(cm/s). These observations point toward the conclusion that for low seismic intensities (PGV = 25(cm/s)), the 1D approach can safely be employed to estimate the damage of U-shaped steel dampers. For level L2, the D/D_2 ratio is roughly between 80~100(%), while for PGV = 100(cm/s) – between 60~80(%), therefore for these cases by using the 1D approach the damage is underestimated.

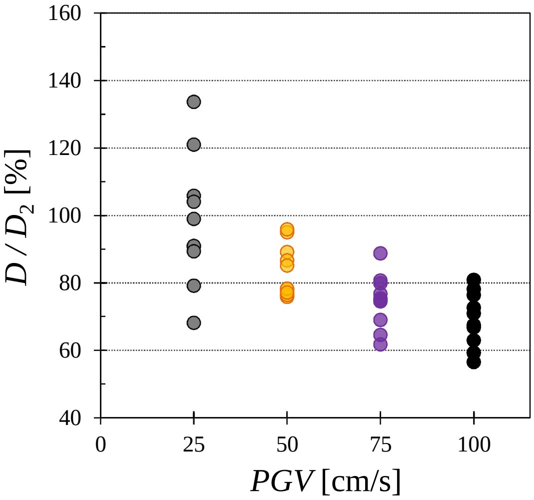

Figure V-9. Damage ratio D/D_2 (%) against the PGV of the dominant component $C1$.

Definition of safety margin and damage ratio DR

The safety margin against fracture is the residual inelastic deformation capacity of a U-shaped steel damper after the occurrence of a seismic event. Generally, the greater is the earthquake-induced damage, the smaller the corresponding safety margin. In the following paragraphs an indicator to assess the safety margin is proposed and computed for the obtained analytical results.

Although by directly comparing the values of the damage indices D and D_2 one could understand that the contribution of the damage on the orthogonal direction increases with the seismic intensity, because of the fact that fracture is defined differently for the two approaches (Fig. V-4), the safety margin cannot be assessed in a consistent manner using a direct comparison. Therefore, to this purpose, it is necessary to find an indicator that is independent on the adopted approach. This indicator must be able to follow the effect of the torsional deformations induced by the sway-motion for the case of bidirectional displacement orbits as shown in Fig. V-10. One very important observation that can be drawn from Fig. V-10 is that, according to the 2D approach, even if the largest value of D_2 is less than 0.350, because of the influence of the sway-motion index J_f, this value comes very close to the interaction curve. This means that the safety margin is significantly smaller than that computed using the 1D approach in which the damage index is compared to 1.0. In conclusion, the desired indicator must be expressed with respect to the fracture limit of each method.

For 1D approach, the computations are straight forward, because the fracture limit is constant ($D = 1.0$), therefore the safety margin can be expressed by subtracting from 1.0 the ratio between the one-directional cumulative damage index D and the fracture limit value, which obviously means that the safety margin is equal to $(1 - D)$. For 2D approach, the safety margin has to be defined with respect to the interaction curve. For this purpose, the damage ratio DR between the bidirectional cumulative damage index D_2 and the damage index found at the intersection with the interaction curve $D_{2,\,int}$ as shown in Fig. V-11(a) and given in Eq. (V.7) is employed. Therefore the safety margin for 2D approach is defined as $(1 - DR)$, which is consistent to that for 1D approach.

$$DR = \frac{D_2}{D_{2,\mathrm{int}}} \tag{V.7}$$

where DR is the safety margin indicator for 2D approach
$D_{2,\,int}$ is defined as shown in Fig. V-11(a) and given in Eq. (V.8).

It is worth noting that if we consider a fixed value for D_2, the corresponding value of DR varies with that of the sway-motion index J_f. Furthermore, the value of $D_{2,int}$ can be obtained by applying Eq. (V.8). The corresponding value of $J_{f,int}$ is computed in a similar manner by simply deriving the abscissa of the intersection point, knowing the value of $D_{2,int}$ and the slope of the line uniting the origin with point (D_2, J_f) as shown in Fig. V-11(a).

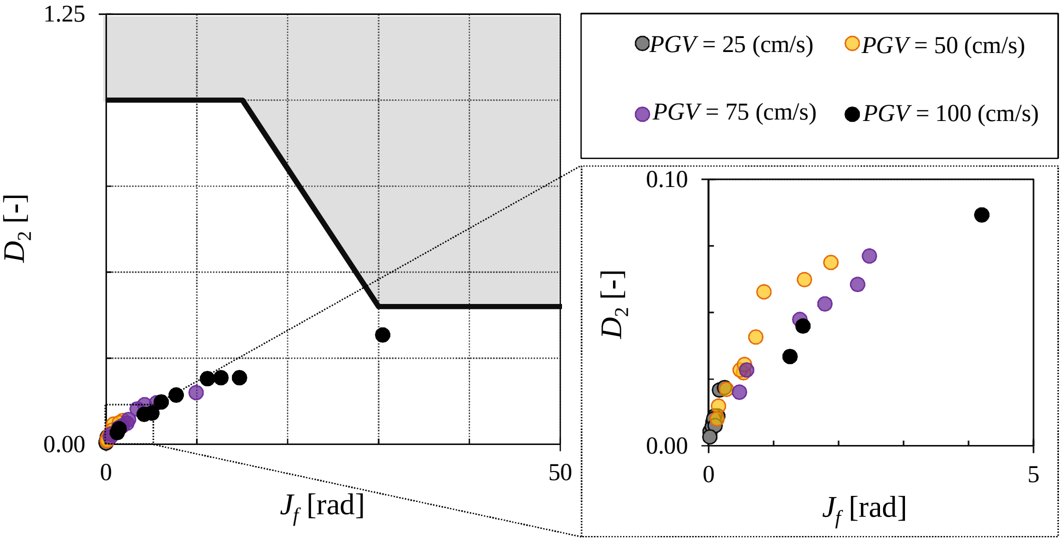

Figure V-10. Bidirectional cumulative damage index D_2 and sway-motion index J_f for PGV = 25, 50, 75 and 100(cm/s) plotted against the interaction curve.

$$D_{2,int} = \begin{vmatrix} 1.0 & \left(0 \le J_f / D_2 < 15\right) \\ 1.6 - 0.04 \cdot J_f & \left(15 \le J_f / D_2 < 75\right) \\ 0.4 & \left(J_f / D_2 \ge 75\right) \end{vmatrix} \tag{V.8}$$

where $D_{2,int}$ is the value of the bidirectional damage index D_2 at the assumed intersection with the interaction curve

D_2 and J_f are the bidirectional damage index, respectively the sway-motion index of a damper subjected to a given bidirectional displacement history; the limit values of their ratio are shown in Fig V-11(b).

In conclusion, to compare the safety margin obtained using the two approaches, one has to compare the values of the one-directional cumulative damage index *D* to those of the damage ratio *DR*. The results are listed in Table V-3.

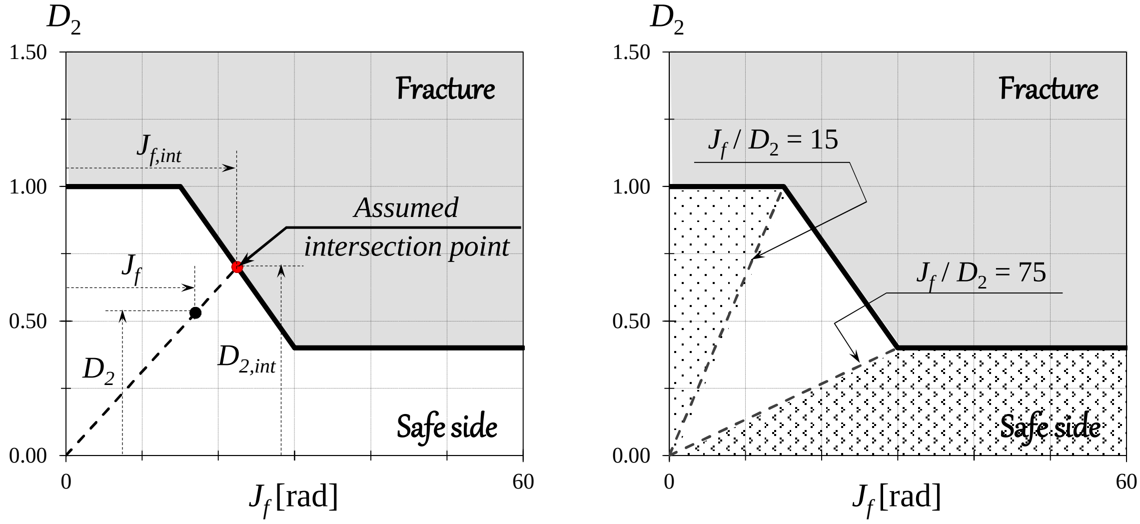

(a) Assumed intersection point (b) Limit values of J_f / D_2 ratio

Figure V-11. Definition of the safety margin indicator *DR* for 2D approach.

Comparison of one-directional cumulative damage index D and damage ratio DR

As explained above, to evaluate the safety margin of each method, the one-directional cumulative damage index *D* and the damage ratio *DR* are compared. The safety margin is conversely proportional to *D*, respectively *DR*, therefore the larger the values of *D* and *DR*, the smaller is the safety margin against fracture. In the next pages, based on the analytical results listed in Table V-3 an equation is proposed to obtain the damage ratio *DR* using the one-directional cumulative damage index *D*.

In Fig. V-12, the ratio between *DR* and *D* was computed and plotted against the damage index *D* for each value of *PGV*. These graphics express how much does the damage of a U-shaped steel damper subjected to a seismic biaxial excitation increases when compared to the damage induced by a single seismic component, all reported with respect to the fracture limit of each approach. The following observations can be made:

- As the seismic intensity increases, so does the ratio between *DR* and *D*. This is consistent with the fact observed in Fig. V-10 that as the input level increases, the plots approach the interaction curve. Therefore it can be stated that the proposed damage ratio *DR* is able to express the decrease of the safety margin for the case of 2D approach.
- For (D_2, J_f) pairs with J_f/D_2 less than 15, the value of the bidirectional damage index at intersection with the interaction curve $D_{2,int}$ is 1.0, same with the fracture limit for 1D approach. Therefore, in such cases, the values of *DR* are not significantly different than those of damage index *D*. This is proven by the fact that the average value of *DR* / *D* for *PGV* = 25(cm/s) is 1.05, while for *PGV* = 50(cm/s) is 1.30. In addition, for these cases, the damage indices are small (less than 0.100), therefore it can be stated that for seismic levels L1 and L2 it is safe to use the 1D approach.
- For (D_2, J_f) pairs with J_f/D_2 between 15 and 75, the ratio *DR* / *D* increases, having an average of 2.10 for *PGV* = 75(cm/s), respectively 2.80 for *PGV* = 100(cm/s). It should be noted that for Loma Prieta earthquake, the point corresponding to *PGV* = 100(cm/s) was excluded when computing the average because the value of J_f/D_2 ratio was greater than 75.
- A single point was found to have J_f/D_2 ratio greater than 75. As mentioned above, this point corresponds to Loma Prieta earthquake normalized to reach *PGV* = 100(cm/s) and has the largest *DR* value (0.794), because it is very close to the interaction curve.

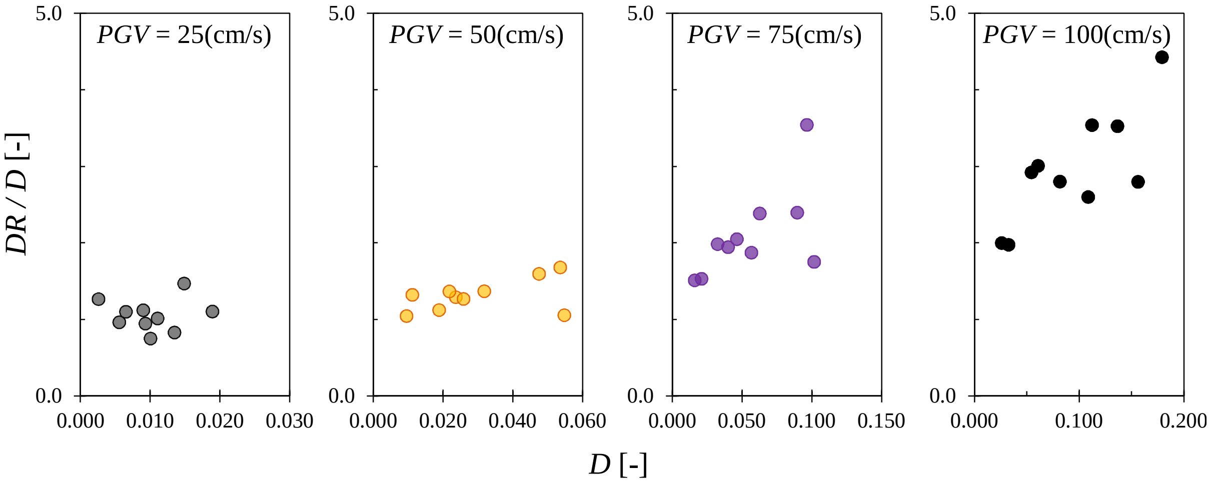

Figure V-12. Relation between damage index *D* (1D approach) and ratio *DR* / *D*.

To investigate the relation between the damage ratio *DR* and damage index *D* regardless of the seismic intensity level, their analytic values are plotted against each other in Fig. V-13. It can be noted that the scatter of the data is not significant, therefore Eq. (V.9) was proposed to find an equivalent value for the damage ratio *DR* using the one-directional cumulative damage index *D*. This equation is plotted on the same graphic with the obtained analytical data (Fig. V-13).

$$DR_c = 7 \cdot D^{1.4} \tag{V.9}$$

where DR_c is the calculated bidirectional damage ratio using the one-directional damage index *D* with $D \in [0.003, 0.179]$.

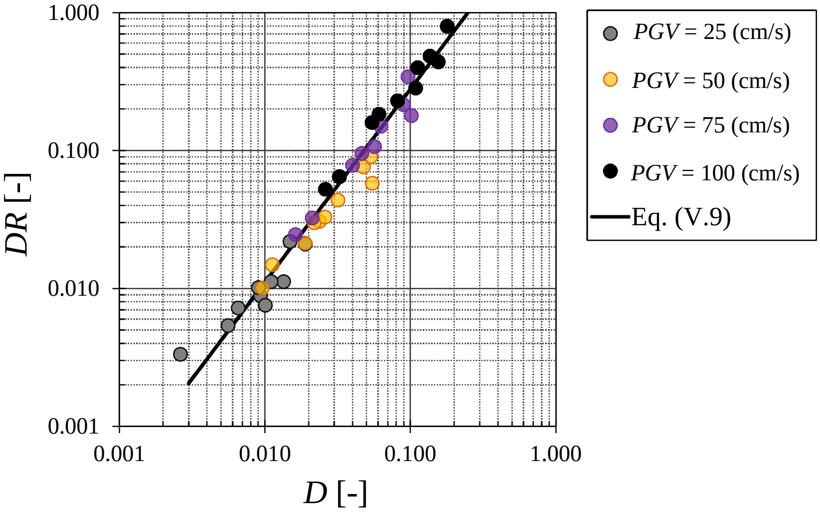

Figure V-13. Analytical results of the one-directional cumulative damage index *D* (1D approach) versus the damage ratio *DR* (2D approach) and their proposed relation (Eq. (V.9)).

V.3.3. Alternative method for bidirectional damage evaluation using one-directional displacement response

In the previous section, the one-directional displacement response was obtained independently for each horizontal component of the ground motion (*C1*, *C2*), and the maximum one-directional damage index *D* was derived. The present section investigates an alternative method based on the assumption that the previously obtained independent displacement responses can be regarded as the orthogonal components of an equivalent bidirectional orbit (Fig. V-14). The aim of this method is to assess whether better agreement with the results provided by the 2D approach can be obtained.

This approach is possible because both the duration *t* and the time increment Δt of the two seismic components of a ground motion are the same, which enables plotting the one-directional displacement responses against each other to obtain an equivalent bidirectional orbit as shown in Fig. V-14. Further on, the damage of U-shaped steel dampers is estimated by following the same procedure as for the 2D approach, as given in Eqs. (I.6) and (I.7). The results are described by the equivalent values of the bidirectional cumulative damage index D_2’, the sway-motion index J_f’ and the damage ratio *DR*’.

The steps required to apply alternative method are described below:

- Use the one-directional displacement response obtained for the dominant seismic horizontal component *C1* δ'_{C1} and that for the second seismic horizontal component *C2* δ'_{C2} , as described in Section V.2.3, and plot an equivalent bidirectional orbit. (Consider that the one-directional response of the dominant component is applied along *x* direction, while that of the second component along *y* direction.)
- Based on the equivalent orbit, compute the equivalent values for the sway-motion index $J_f{}'$, the bidirectional cumulative damage index $D_2{}'$ (Eq. (V.10)), the maximum displacement $R_{\max}{}'$ and the damage ratio DR' .

$$D_2{}' = \max\left({}_{C1}D_{0^\circ}{}' + {}_{C2}D_{90^\circ}{}' \,,\, {}_{C1}D_{90^\circ}{}' + {}_{C2}D_{0^\circ}{}' \right) \qquad \text{(V.10)}$$

where ${}_{C1}D_{0^\circ}{}' + {}_{C2}D_{90^\circ}{}'$ is the damage index of the damper placed parallel to the direction of dominant seismic component *C1* (Fig. V-14)

${}_{C2}D_{0^\circ}{}' + {}_{C1}D_{90^\circ}{}'$ is the damage index of the damper placed parallel to direction of second seismic component *C2* (Fig. V-14)

${}_{C1}D_{0^\circ}{}'$, ${}_{C1}D_{90^\circ}{}'$, ${}_{C2}D_{0^\circ}{}'$, ${}_{C2}D_{90^\circ}{}'$ are the damage indices produced by each one-directional displacements δ'_{C1} and δ'_{C2} shown in Fig. V-14.

- Compare the equivalent bidirectional indices to the bidirectional indices obtained using the 2D approach.

In addition, a comparison with the values computed by employing Eqs. (V.6) and (V.9) is also conducted to determine which of the two proposed methods (Sections V.3.2 and V.3.3) provides the best estimate of the bidirectional damage using one-directional indicators.

First, the values of D_2 and J_f indices obtained using the 2D approach are compared to the equivalent ones given by employing the one-directional displacement responses for each seismic component – $D_2{}'$ and $J_f{}'$. The results – plotted in Fig. V-15 – show that for small seismic intensity levels the two sets of results agree well, both for the bidirectional cumulative damage index and for the sway-motion index. However, for both indices, the values obtained using the alternative approach were situated mostly towards the unconservative side for *PGV* = 75, 100(cm/s).

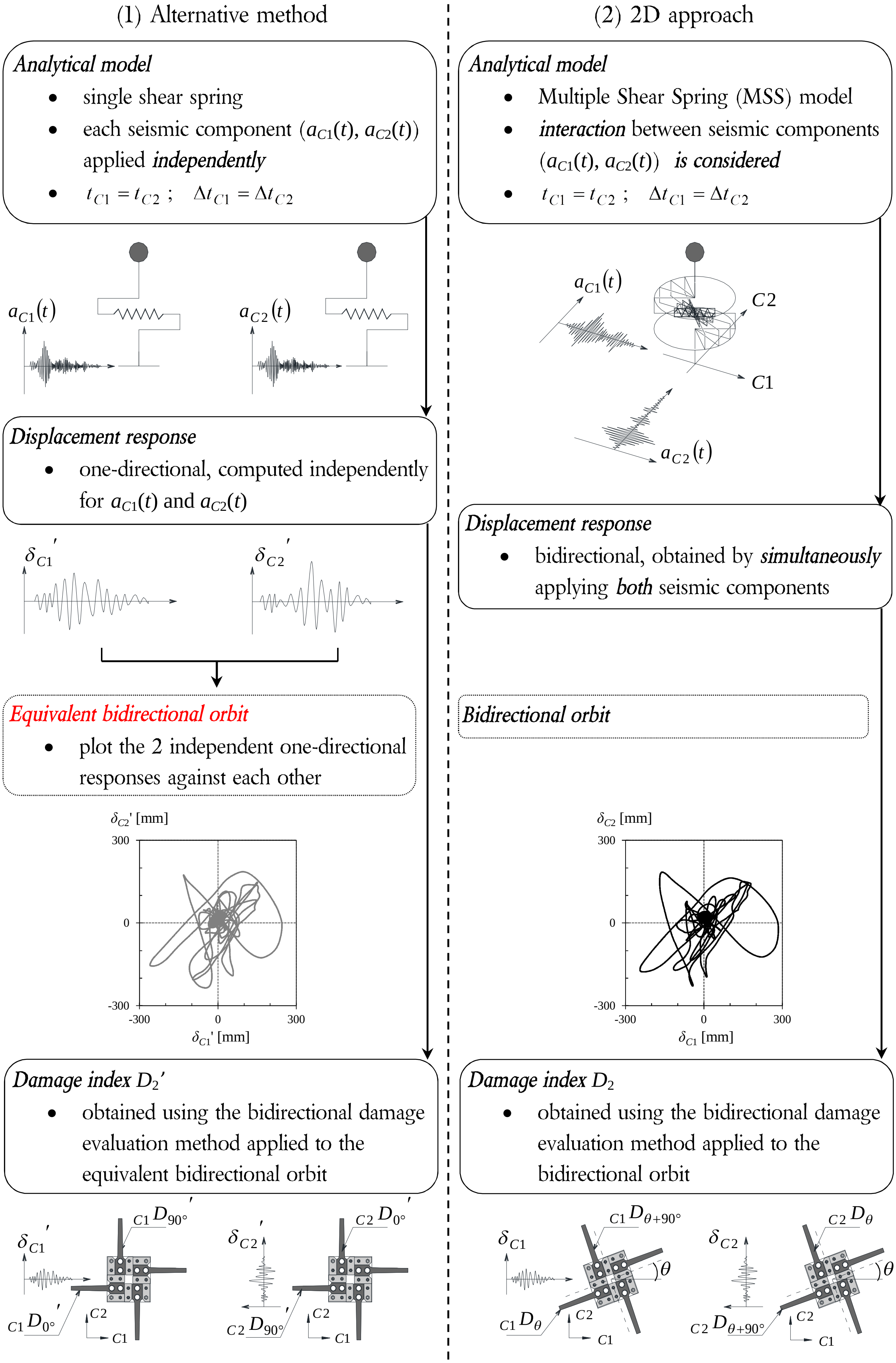

(1) Alternative method

Analytical model

- single shear spring
- each seismic component ($a_{C1}(t)$, $a_{C2}(t)$) applied *independently*
- $t_{C1} = t_{C2}$; $\Delta t_{C1} = \Delta t_{C2}$

Displacement response

- one-directional, computed independently for $a_{C1}(t)$ and $a_{C2}(t)$

Equivalent bidirectional orbit

- plot the 2 independent one-directional responses against each other

Damage index D_2'

- obtained using the bidirectional damage evaluation method applied to the equivalent bidirectional orbit

(2) 2D approach

Analytical model

- Multiple Shear Spring (MSS) model
- *interaction* between seismic components ($a_{C1}(t)$, $a_{C2}(t)$) *is considered*
- $t_{C1} = t_{C2}$; $\Delta t_{C1} = \Delta t_{C2}$

Displacement response

- bidirectional, obtained by *simultaneously* applying *both* seismic components

Bidirectional orbit

Damage index D_2

- obtained using the bidirectional damage evaluation method applied to the bidirectional orbit

Figure V-14. Difference between the alternative method (left) and bidirectional one (right).

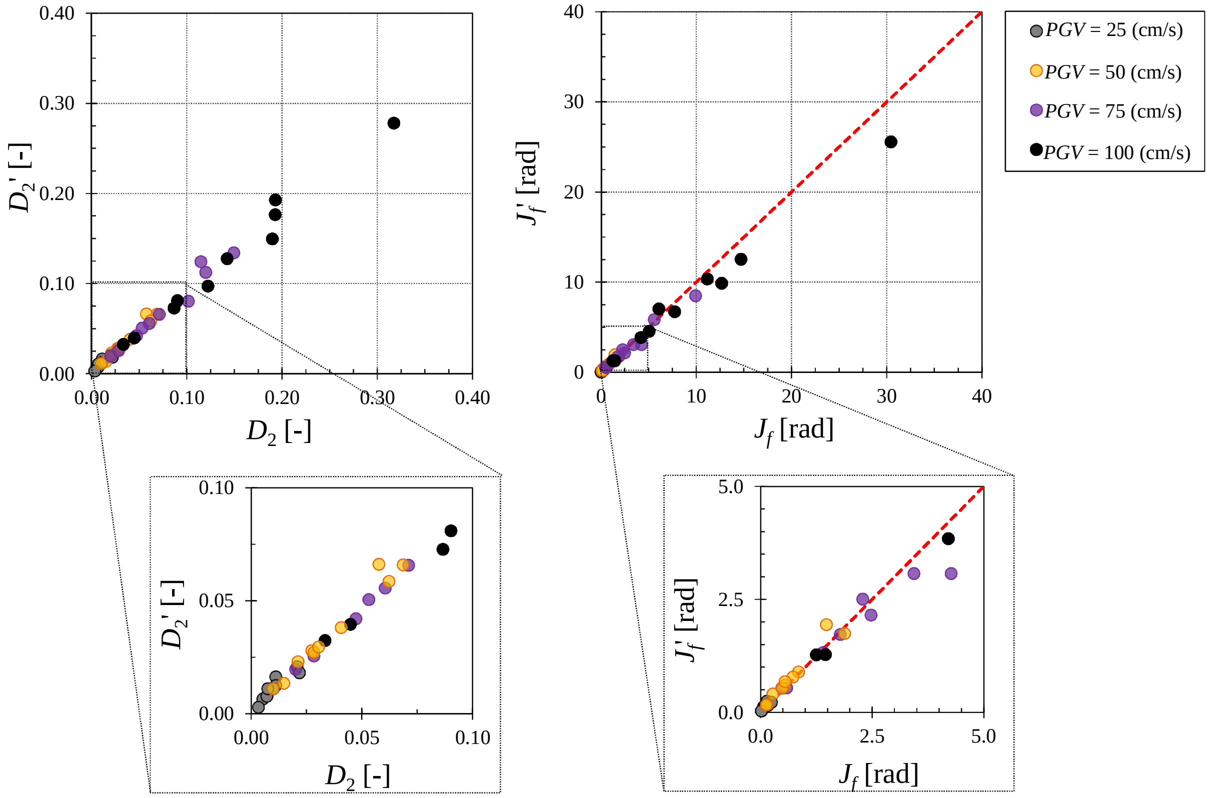

(a) Damage indices D_2 and D_2' (b) Sway-motion indices J_f and J_f'

Figure V-15. Comparison between the bidirectional indices D_2 and J_f obtained using the 2D approach and their equivalent values obtained by using the alternative approach D_2' and J_f'.

Further on, the comparison between the bidirectional maximum displacement of the isolation layer $R_{\max}$ and the computed values ${}_cR_{\max}$ obtained by employing Eq. (V.6), respectively the equivalent values obtained using the alternative approach $R_{\max}'$ is conducted. The results are plotted in Fig. V-16 for each of the considered values of PGV. It can be observed that the values provided by Eq. (V.6) are situated slightly more towards the conservative side than those of $R_{\max}'$, although the difference is not significant (less than 10%).

In Fig. V-17 are plotted the values of the damage ratio DR for 2D approach against those computed by employing Eq. (V.8) – DR_c –, respectively those obtained by following the alternative method (DR'). Here it can be noticed that the latter set of values – although providing quite accurate results for PGV levels 25 and 50(cm/s) – considerably underestimate the damage ($DR > DR'$) for the other two cases. This fact happens because the values of both D_2 and J_f and are underestimated (Fig. V-15). The reason for this difference between the yield displacements of the two considered analytical models (1D and 2D) is explained below.

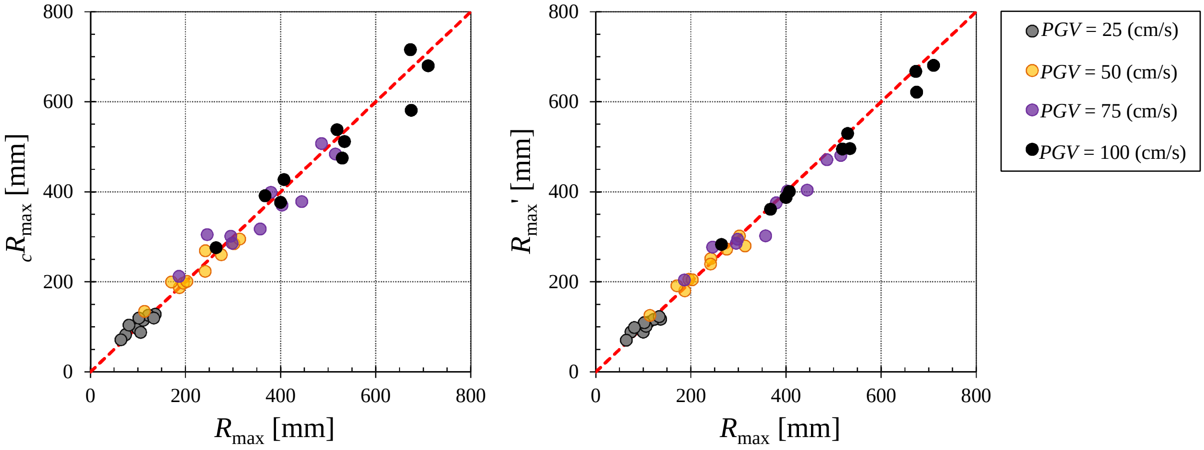

(a) Calculated values (Eq. (V.6)) (b) Equivalent values (alternative method)

Figure V-16. Comparison between R_{max} obtained using the 2D approach and calculated values $_cR_{max}$ (Eq. (V.6)), respectively equivalent values R_{max}'.

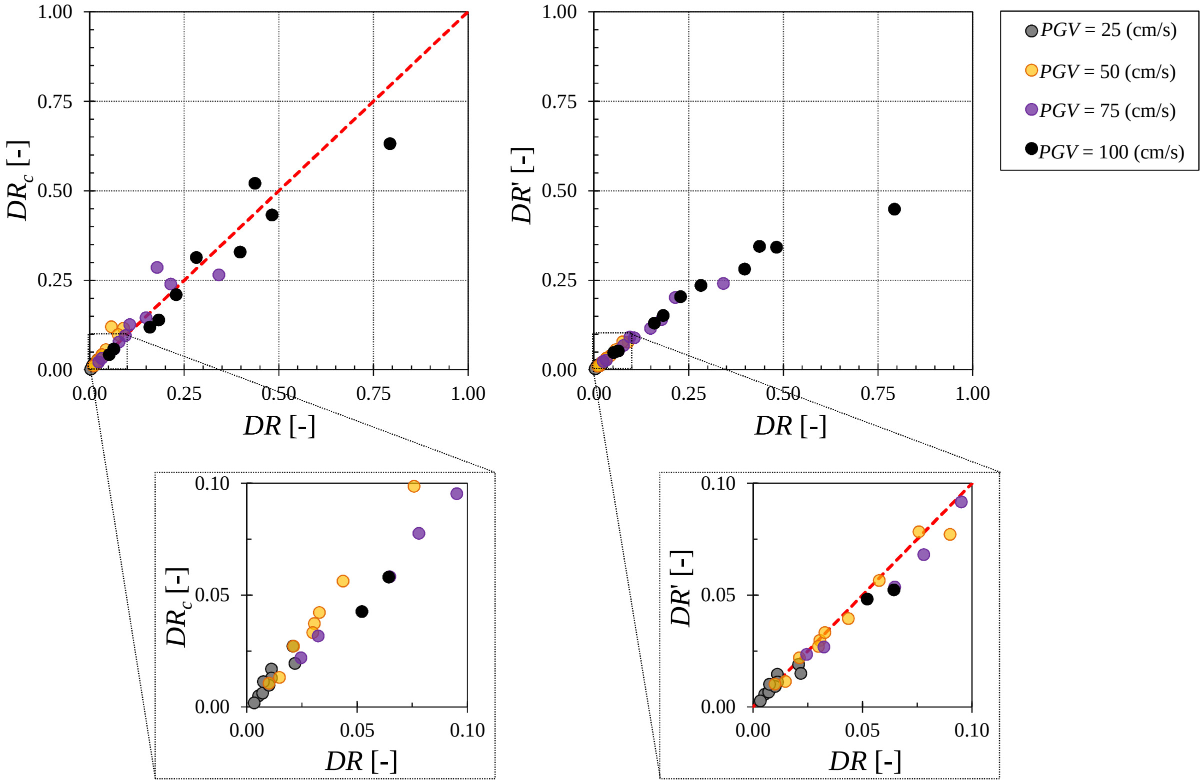

(a) Calculated values (Eq. (V.9)) (b) Equivalent values (alternative method)

Figure V-17. Comparison between damage ratio DR obtained using the 2D approach and calculated values DR_c (Eq. (V.9)), respectively equivalent values DR'.

The reason for which the values of both D_2 and J_f are underestimated when applying the alternative approach, in spite of the fact that the maximum displacement of the isolation layer is correctly estimated, needs to be clarified. Let us take for example the displacement orbits obtained for Loma Prieta (AG) and Tokachi-Oki (HC) earthquakes at PGV = 50, respectively 100(cm/s). In Fig. V-18 are plotted on the same graphics the equivalent displacement orbit obtained using the alternative approach and the bidirectional displacement orbit obtained for the 2D approach. Fig. V-18(a) shows the data corresponding to *PGV* = 50(cm/s), while Fig. V-19(b) that for *PGV* = 100(cm/s). The difference between the two sets of displacement orbits is given by the difference in the yield displacement of the damper considered by each model. For the 2D model, an MSS element is adopted, therefore the yield displacement of a single damper-spring element ${}_e\delta_y^d$ is obtained from the yield displacement of the damper δ_y^d by employing Eq. (V.11).

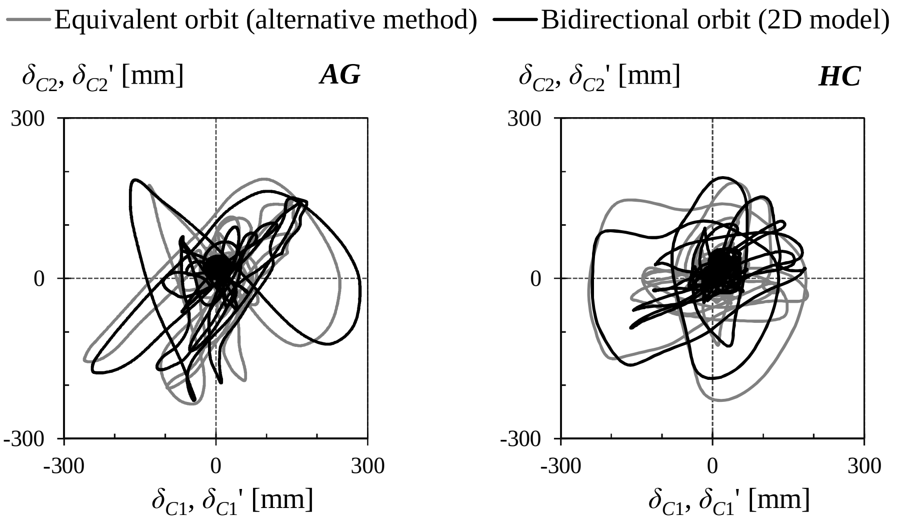

(a) *PGV* = 50(cm/s)

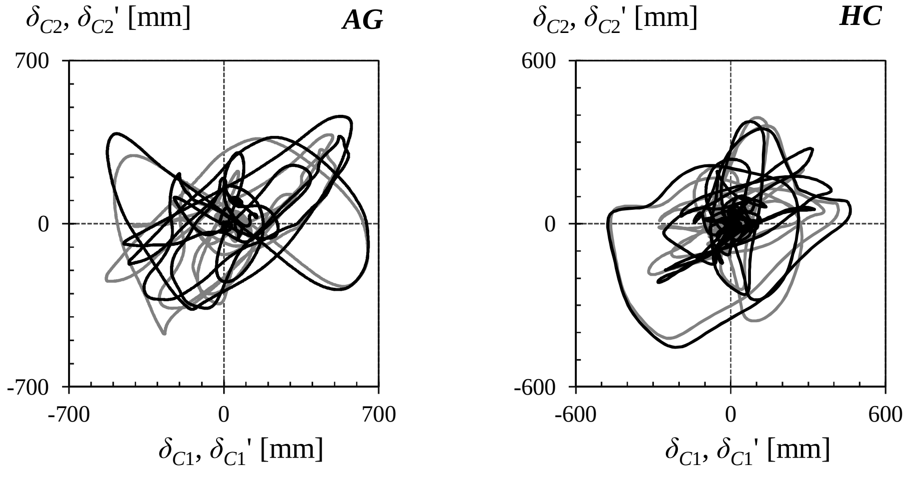

(b) *PGV* = 100(cm/s)

Figure V-18. Equivalent displacement orbit (alternative method - gray) vs. bidirectional displacement orbit (2D model – black).

$$ {}_e\delta_y^d = \delta_y^d \cdot \frac{\sum_{i=1}^{Ns} \cos^2 \theta_i}{\sum_{i=1}^{Ns} \left|\cos \theta_i\right|} \tag{V.11} $$

where ${}_e\delta_y^d$ is the yield displacement of a single damper-spring

δ_y^d is the yield displacement of the damper unit (equal to Q_y/k_e given in Table III-4)

N_s is the number of springs (16 in the present study)

θ_i is the angle made by each spring element with the abscissa.

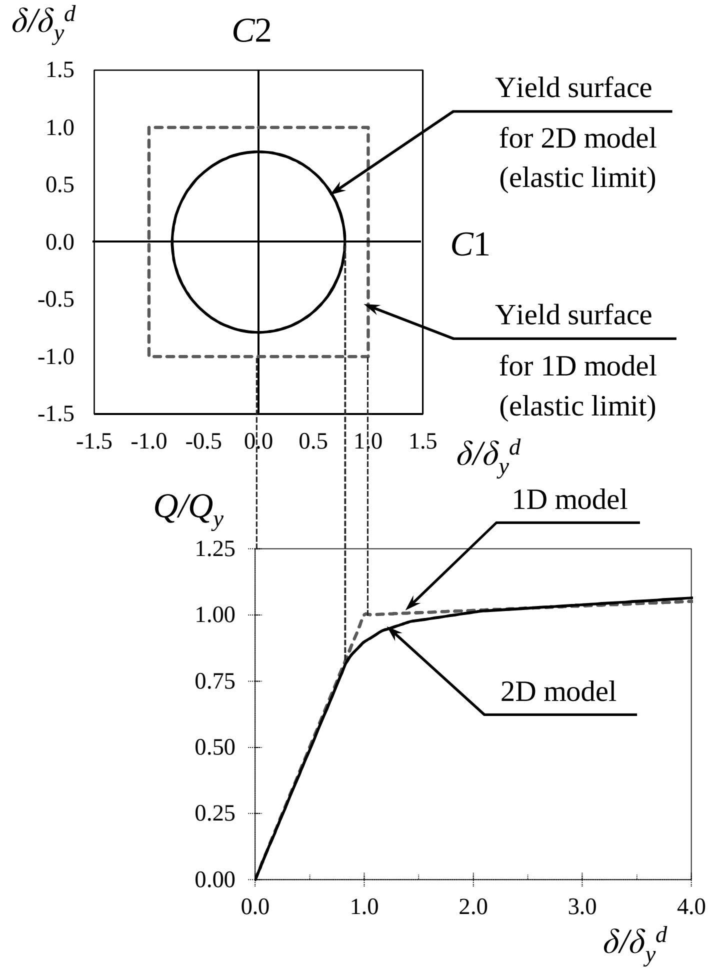

Figure V-19. Difference between the yield surface for 2D model and that for the alternative approach (1D model).

To get a clearer image on the reason why the values of D_2 and J_f are underestimated when applying the alternative approach, the yield surfaces for 1D and 2D models are plotted in Fig. V-19. The elastic limit of the MSS model is established based on the yield displacement of a single damper-spring element ${}_e\delta_y^d$. Considering the fact that in the present study 16 spring elements were used, it results that on the direction of the dominant seismic component *C1* , ${}_{e}\delta_{y}^{d}$ is equal to $0.79 \cdot \delta_{y}^{d}$. On the diagonal direction, the difference between the two yield displacements further increases. A smaller value of the yield displacement means that the 2D model reaches its plastic range earlier than the 1D model. This does not have a great impact on the value of the maximum displacement, which is reasonable if one were to think that the yield displacement is that corresponding to half a cycle. Contrary to this, for the case of the bidirectional cumulative damage index D_2 and sway-motion index J_f, because of their definition, the plastic deformations accumulate for large displacement responses, resulting in a significant impact on their values.

V.3.4. Remarks

In this section, preliminary analyses were conducted for *PGV* equal to 25, 50, 75 and 100(cm/s) using the 1D and 2D approaches described in the previous section. The main objective was to compare the two sets of results and assess whether the 1D approach evaluates the damage of a U-shaped steel damper on the unconservative side. To fulfill this goal, it had to be recognized that fracture limit is defined differently for the two approaches. Therefore, the damage ratio *DR* was proposed for the 2D approach, which is an indicator of how close to the interaction curve (fracture) is the point defined by (D_2, J_f). Furthermore, two methods to estimate the main bidirectional indices ($R_{\max}$, *DR*) using one-directional indices typically computed in design were investigated. The first method is based on fitting through the obtained data Eq. (V.6) for the maximum displacement, respectively Eq. (V.9) for the damage ratio *DR*. The second method – called here alternative method – is based on independently computing the displacement response of each seismic component using the 1D model, then regard the obtained data as an equivalent bidirectional orbit, and further calculate equivalent values for the bidirectional indicators J_f' , D_2' , $R_{\max}'$ and DR' . Below are listed the main remarks:

- The analytical results obtained using the 1D approach overestimate the safety margin against fracture when the seismic intensity is large (*PGV* = 75, 100(cm/s)), but provide satisfactory estimation of the damage for level L1 and L2.
- Eqs. (V.6) and (V.9) provide a more accurate prediction of the maximum displacement of the isolation layer and the damage ratio *DR* than the alternative method. This is explained by the difference of the yield displacement adopted by the two considered models (1D and 2D).

As a general remark, it is important to note that the direct prediction of the main bidirectional indices provides more reliable results when compared to their estimation using an equivalent bidirectional displacement derived by adopting 1D model for both seismic horizontal components.

V.4. One-directional IDA curves

In the previous section, preliminary analyses were conducted to compare the damage estimation of the 1D and 2D approaches and it was concluded that for large seismic intensities the 1D approach overestimates the safety margin against fracture. In this section, the main objective is to obtain a continuous relation between the damage indices and the seismic intensity starting from elastic range and ending with fracture. To this purpose, IDA is employed due to the reasons mentioned in ***Chapter IV***.

In technical literature there is a considerable number of studies applying IDA to single horizontal components of a ground motion in order to predict the capacity of the structure at different seismic intensity levels. In this section the one-directional IDA curves are obtained under the following hypotheses:

- To facilitate the comparison between the one-directional and bidirectional IDA curves, the former are obtained using the same values for the scale factors.
- The one-directional IDA curves do not necessarily reach the ultimate limit state. This happens because of the fact that the scale factors corresponding to the ultimate state of the bidirectional IDA curves do not always lead to $\delta_{\max}$ = 800(mm) and never lead to fracture of the damper (assumed to occur when D = 1.0, Table V-1).

In deriving the one-directional IDA curves, one has to recall that each horizontal component of the ground motion is applied independently. This means that the damage measure selected in ***Chapter IV***, namely the bidirectional cumulative damage index D_2, cannot be obtained and has to be replaced with the one-directional damage index D (Eq. (V.2)). Moreover, the intensity measure PGV_{gm} – adopted in ***Chapter IV*** for the bidirectional IDA curves specifically because of its ability to characterize the interaction between the two horizontal components – is not applicable here. For this reason, the peak ground velocity PGV corresponding to the horizontal component that gives the maximum damage index D was adopted. It is worth noting that, with very few exceptions, the maximum one-directional cumulative damage index is obtained for the horizontal component that has the largest PGV. In addition, in Table V-4 the values for PGV_{gm} and PGV for each component are listed in order to offer a general idea about their difference.

The one-directional IDA curves are plotted in Fig. V-20 for each of the considered values of the yield base shear coefficient α_s. The following observations are made:

- The ***waving pattern*** observed for some curves (*e.g.* Friuli – Tolmezzo (FTZ) for $\alpha_s = 0.010$ (Fig. V-20(a))) is caused by the fact after a certain threshold of the scale factor, the maximum damage is caused by the other horizontal component which has a different PGV.
- The curves become shorter as the yield base shear coefficient α_s increases.

A straightforward comparison between the one-directional and bidirectional IDA curves is not possible because different IMs and DMs are considered. Nevertheless, some basic differences can be pinpointed since the same scale factors were adopted. Among these differences, the values of the damage indices at ultimate limit state are of main interest. It is worth mentioning again the fact that the 1D IDA curves are stopped at the exact scale factors as the 2D IDA curves. For this reason, one can compare the values of D^{us} and D_2^{us}. In Fig. V-21 – where the lognormal probability density functions (PDF) of the two parameters are plotted – it can be observed that the PDFs for D_2^{us} are shifted to the right of those for D^{us}. This means that the bidirectional cumulative damage index at ultimate limit state is greater than the corresponding one-directional one. Their difference increases with the yield base shear coefficient; take for example the median value: the ratio between $\tilde{D}_2^{us}$ and $\tilde{D}^{us}$ increases from 1.44 for $\alpha_s = 0.010$, to almost 2.00 for $\alpha_s = 0.040$.

A more detailed comparison of D and D_2 is presented in Section V.4 where the safety margin against fracture is also evaluated.

Table V-4. Values of PGV_{gm} and PGV for the considered ground motions

Earthquake		Station		PGV_{gm}	PGV [cm/s]	
No.	Name	Full name	Abv.	[cm/s]	x dir.	y dir.
1	Tohoku	JMA Sendai	TSD	51.80	53.30	54.50
2		K-net Koriyama	TKY	52.40	43.60	60.40
3	Manjil	Abbar	MAB	43.78	42.50	52.10
4	Chi-Chi	TCU045	TC0	38.89	36.70	39.10
5		TCU129	TC1	47.34	55.40	51.00
6	Landers	Yermo Fire Station	LYF	36.89	51.40	29.7
7		Coolwater	LCW	34.64	25.60	42.30
8	Kobe	Nishi-Akashi	KNA	35.73	37.30	36.60
9		Shin-Osaka	KSO	32.82	37.80	27.90
10	Hector Mine	Hector	HMN	34.21	28.60	41.70
11	Duzce	Bolu	DBL	59.68	56.40	62.10
12	Cape Mendocino	Rio Dell Overpass	CMR	47.95	43.80	41.90
13	Loma Prieta	Gilroy Array #3	LPG	43.11	35.70	44.70
14	Northridge	Canyon Country - WLC	NCC	43.33	43.00	44.90
15	Superstition Hills	El Centro Imp. Co.	SHE	45.16	46.40	40.90
16	Imperial Valley	Delta	IVD	29.75	26.00	33.00
17	Friuli	Tolmezzo	FTZ	25.06	22.00	30.80

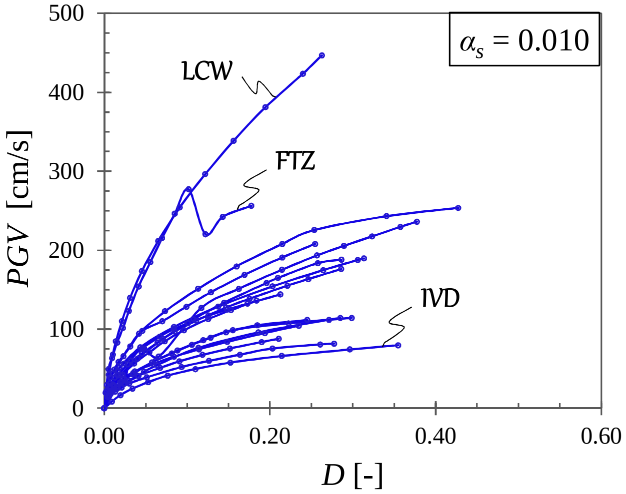

(a) $\alpha_s = 0.010$

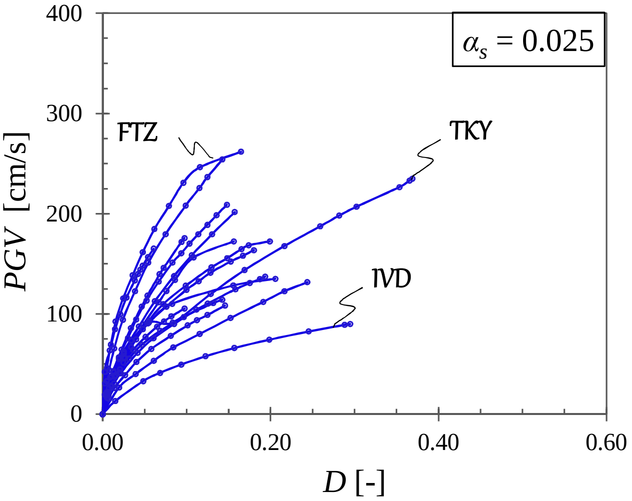

(b) $\alpha_s = 0.025$

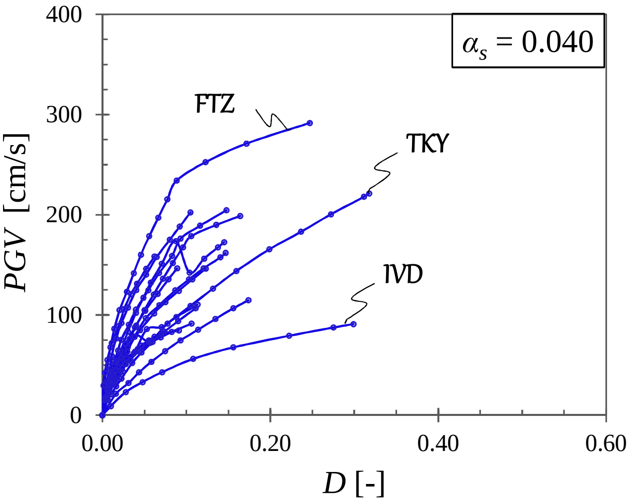

(c) $\alpha_s = 0.040$

Figure V-20. One-directional IDA curves. IM: *PGV* of the dominant horizontal component *CI*; DM: one-directional cumulative damage index *D*.

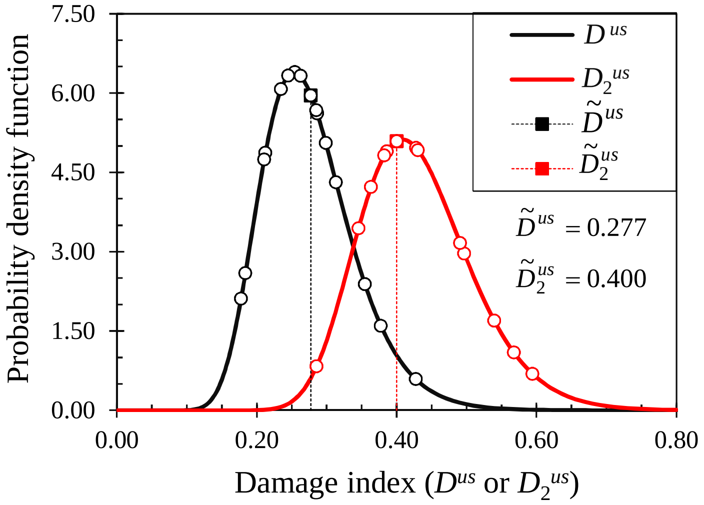

(a) $\alpha_s = 0.010$

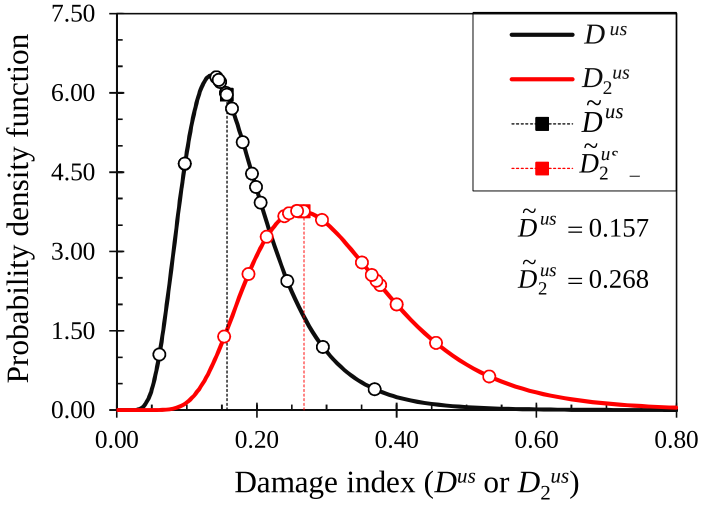

(b) $\alpha_s = 0.025$

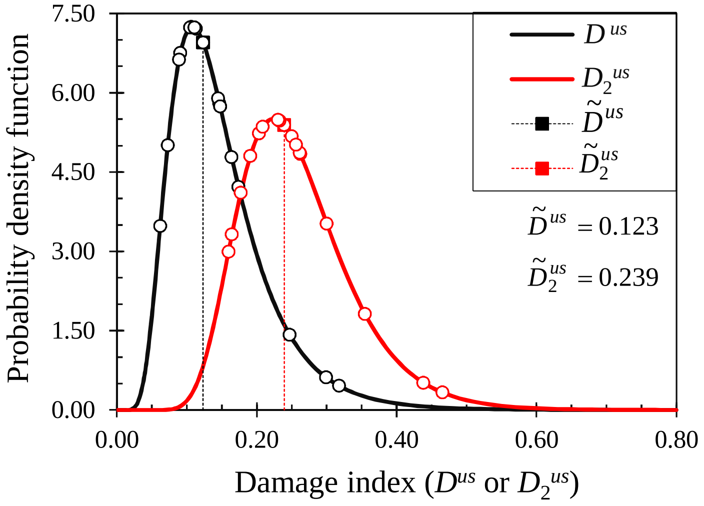

(c) $\alpha_s = 0.040$

Figure V-21. Probability distributions (lognormal) of the damage indices at ultimate limit state D^{us} (1D approach – black line) and D_2^{us} (2D approach – red line).

V.5. Comparison between one-directional and bidirectional approaches

The main purpose of this chapter is to quantitatively estimate the difference between the one-directional (D) and the bidirectional (D_2) cumulative damage indices in order to decide whether the typical design practices provide unconservative values that may endanger the structural safety of seismic isolated structures. To this purpose, in running the 1D analyses, the same scale factors as for the 2D analyses were adopted.

There are 3 main factors that affect the above-mentioned difference:

1. Analytical model.
2. Damage evaluation method.
3. Consideration of fracture of a damper.

The analytical model indirectly influences the difference between the two cumulative damage indices through the displacement response and is discussed in Section V.5.1. Moreover, it is closely related to the criterion considered for the fracture of the damper, in the sense that only the bidirectional model allows taking into account the reduction of the inelastic deformation capacity under bidirectional loading. The damage evaluation method has a direct impact on the difference between D and D_2 (Section V.5.2), while the criterion for considering fracture of the damper is directly related to the safety margin and whether the estimated values of the damage are situated on the conservative or unconservative side (Section V.5.3).

The last part of this chapter, Section V.4.3, focuses on the difference between D and D_2 at design specific seismic hazard levels (L1, L2 and L3), providing essential information to the structural designer.

V.5.1. Influence of analytical model

The considered analytical models affect the obtained results because the displacement response is different. Assessing the difference between the results obtained with the 1D model and those obtained for the 2D model is not an easy task. However, since the maximum displacement of the isolation layer is one of the most important parameters in designing a base-isolated structure, it was selected in the present study to conduct the comparison.

By comparing the values of the maximum displacement of the isolation layer obtained for the two considered approaches $\delta_{\max}$ (1D) and $R_{\max}$ (2D), the influence of the analytical model can be assessed. From the results obtained for the preliminary analyses conducted in Section V.3, it is expected that the values of $R_{\max}$ are greater than those of $\delta_{\max}$, which is confirmed in Fig. V-22 where the two quantities are plotted against each other. The gray zone represents the range in which the values of $\delta_{\max}$ are less than those of $R_{\max}$, or – in other words – the unconservative side. It can be observed that as the scale factor s_f increases (and, implicitly so do $\delta_{\max}$ and $R_{\max}$), the difference between the two quantities also increases. This is explained by the fact that the 2D model, due to the characteristics of the adopted MSS element, has a smaller yield surface than the 1D model, which means that it reaches earlier the plastic range. Therefore, as the seismic intensity increases, so does the influence of the plastic range as compared to the elastic one, and the displacements increase more rapidly with rather small increase of the shear force. Details about this issue were explained in Section V.3, were Eq. (V.6) was proposed to estimate the values of $R_{\max}$ based on those of $\delta_{\max}$ simply by multiplying with 1.10. It is clear from Fig. V-22, where Eq. (V.6) is also plotted, that this approach provides conservative values for only about half of the analytical data, the rest of the data being considerably underestimated. Given the fact that the maximum displacement of the isolation layer is one of the most important parameters used in design, this range cannot be considered satisfactory. Therefore a probabilistic method that can take into account the fact that the scatter of the data increases with the values of $R_{\max}$ and $\delta_{\max}$ is investigated next.

To analyze more closely the variation of the difference between $\delta_{\max}$ and $R_{\max}$, the lognormal probability density functions of the ratio $\delta_{\max}/R_{\max}$ were drawn through all the points obtained in the analyses, as shown in Fig. V-23. The minimum, maximum and median values are listed in Table V-5. The values of the ratio $\delta_{\max}/R_{\max}$ were found to vary between 0.58 and 1.13, depending on the ground motion. In addition, it is worth noting that the median values of the ratio $\delta_{\max}/R_{\max}$ are around 0.90, which agree with the results obtained in the preliminary analysis. Moreover, the scatter of the data slightly increases with the value of the yield base shear coefficient α_s, as indicated by the values of the coefficient of variation (COV) shown in Fig. V-23. The greater scatter presented by the currently analyzed data (Fig. V-22) by comparison to the results obtained in the preliminary analyses (Fig. V-7) is explained by the record-to-record variability and by the fact that the input waves were not normalized with respect to the *PGV* of the dominant component. In conclusion, the influence of analytical model on the value of the maximum displacement of the isolation layer increases with the intensity of the ground motion. Moreover, the record-to-record variability is also an important parameter affecting the above-mentioned difference.

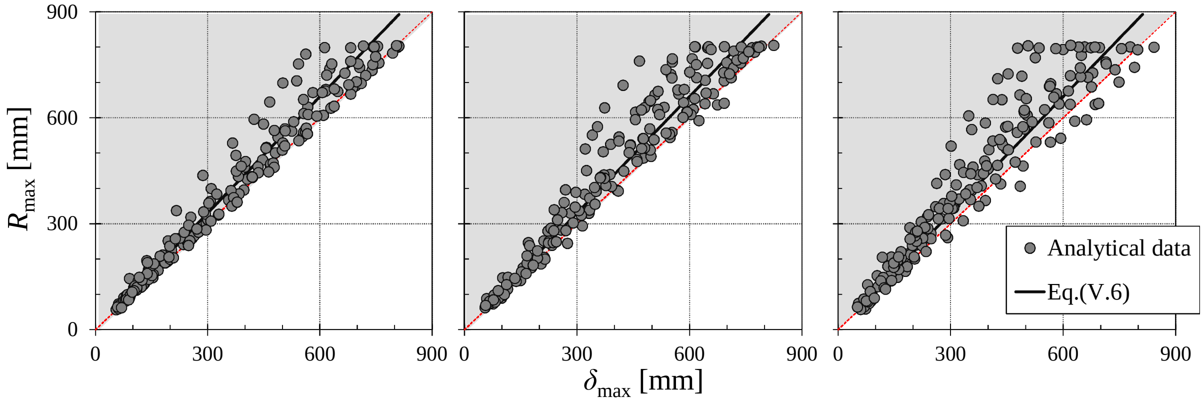

(a) $\alpha_s = 0.010$ (b) $\alpha_s = 0.025$ (c) $\alpha_s = 0.040$

Figure V-22. Maximum displacement of the isolation layer for 1D approach ($\delta_{\max}$) against that for 2D approach ($R_{\max}$).

Table V-5. Median, minimum and maximum values of ratio δ_{max}/R_{max}

α_s δ_{max}/R_{max}	0.010	0.025	0.040
min	0.63	0.60	0.58
median	0.95	0.91	0.87
max	1.13	1.13	1.12

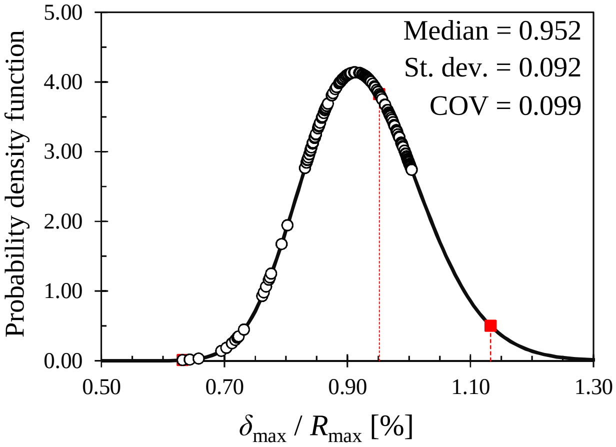

(a) $\alpha_s = 0.010$

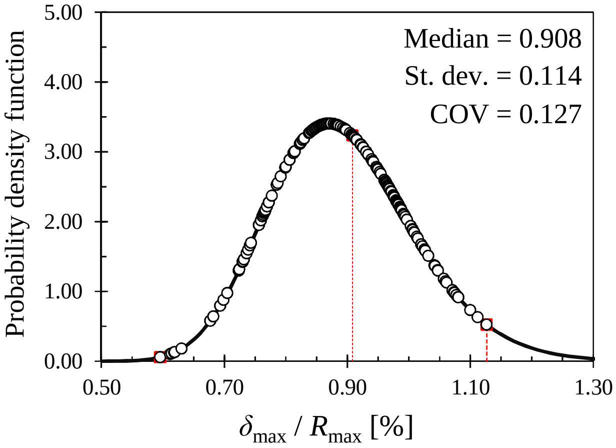

(b) $\alpha_s = 0.025$

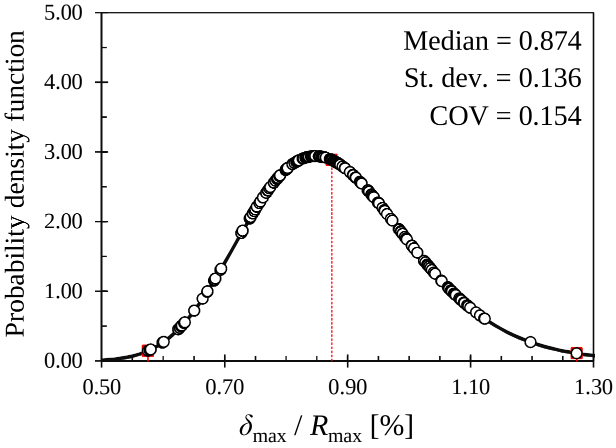

(c) $\alpha_s = 0.040$

Figure V-23. Probability distributions for D/D_2 . Median, minimum and maximum values.

To account for the record-to-record variability as well as for different levels of seismic intensity, the lognormal probability density functions of the $\delta_{\max}/R_{\max}$ ratio and their corresponding cumulative distribution functions are derived at constant increments of $\delta_{\max}$. The results are plotted in Fig. V-24 for each value of the yield base shear coefficient α_s, together with the curves for the median values, respectively median ±1 standard deviation values. It is worth mentioning that for $\delta_{\max}$ smaller than 100(mm), due to the fact that cubic spline was used as interpolation technique (see ***Chapter IV***) and the intercept has to be equal to 0, the resulting curves present an unstable behavior. For this reason, only the values obtained for $\delta_{\max}$ greater or equal to 100(mm) are shown in Fig. V-24. In addition, it can be observed that as a curve ends at $\delta_{\max}$ less than 800(mm), the median, respectively median ±1 standard deviation curves present sudden "jumps". This fact implies that – statistically speaking – the number of degrees of freedom of the sample decreases, therefore so does the reliability of the mentioned curves. Hence it is advised to neglect the last part of the curves, as discussed in this section.

Another important observation that can be drawn from Fig. V-24 is that the scatter of the data increases with α_s. This occurs because of the fact that for small values of α_s, the contribution of the damper with respect to that of the isolator is small (for $\alpha_s = 0.010$ the ratio between the shear force resisted by the damper to that resisted by the isolator is 3:22), therefore the difference between the yield displacements of the two considered models does not affect as much the displacement response. On the contrary, for larger values of α_s, the contribution of the damper increases (for $\alpha_s = 0.040$ it becomes 1:1). Therefore, to ensure that the estimated values of $R_{\max}$ as a function of $\delta_{\max}$ are situated towards the safe side regardless of the value of α_s, one should use the median –1 standard deviation curve of $\delta_{\max}/R_{\max}$ ratio. However, as mentioned above, the median –1 standard deviation curves become unstable as the number of degrees of freedom of the sample decreases, therefore only the values of $\delta_{\max}$ between 100 and 600(mm) are used to derive a set of formulae to estimate $R_{\max}$. These are given by Eq. (V.12), where the estimated values $R_{\max,eq}$ are expressed as power functions of $\delta_{\max}$. It is worth mentioning that for $\alpha_s = 0.025$ and $\alpha_s = 0.040$ the corresponding formulae for values of $\delta_{\max}$ between 500 and 600(mm) are traced significantly towards the conservative side. The results obtained with Eq. (V.12) ($R_{\max,eq}$) are plotted against the analytical values obtained for 2D approach ($R_{\max}$) in Fig. V-25. It can be easily observed that most of the values are now estimated on the conservative side.

$$R_{\max,eq} = 1.45 \cdot \delta_{\max}^{0.97} \qquad (\alpha_s = 0.010) \tag{V.12a}$$

$$R_{\max,eq} = 0.84 \cdot \delta_{\max}^{1.08} \qquad (\alpha_s = 0.025) \tag{V.12b}$$

$$R_{\max,eq} = 0.96 \cdot \delta_{\max}^{1.07} \qquad (\alpha_s = 0.040) \tag{V.12c}$$

where $\delta_{\max} \in [100, 600](\mathrm{mm})$.

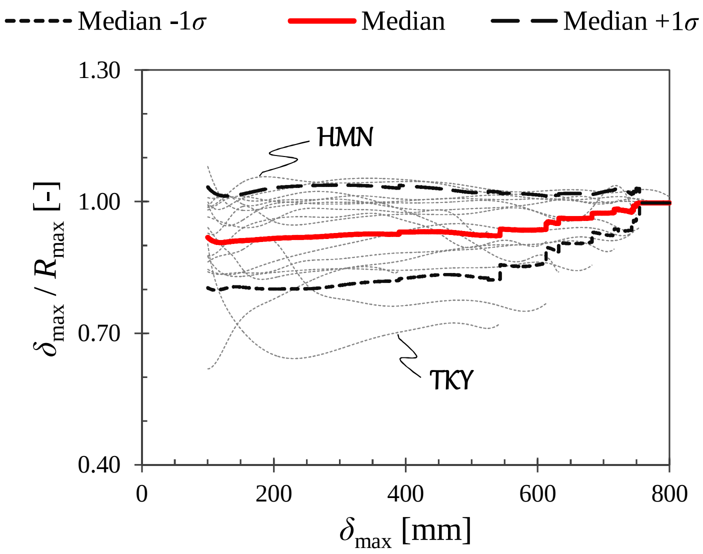

(a) $\alpha_s = 0.010$

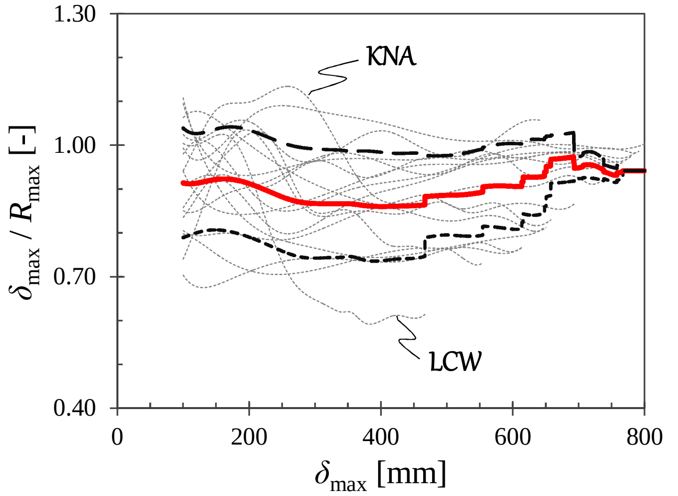

(b) $\alpha_s = 0.025$

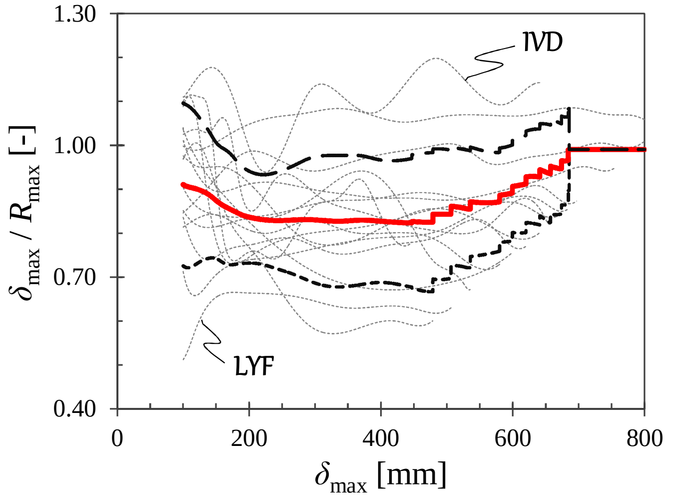

(c) $\alpha_s = 0.040$

Figure V-24. Variation of ratio $\delta_{\max}/R_{\max}$ with respect to the maximum one-directional displacement $\delta_{\max}$ $\left(\delta_{\max} \in [100, 800](\text{mm})\right)$.

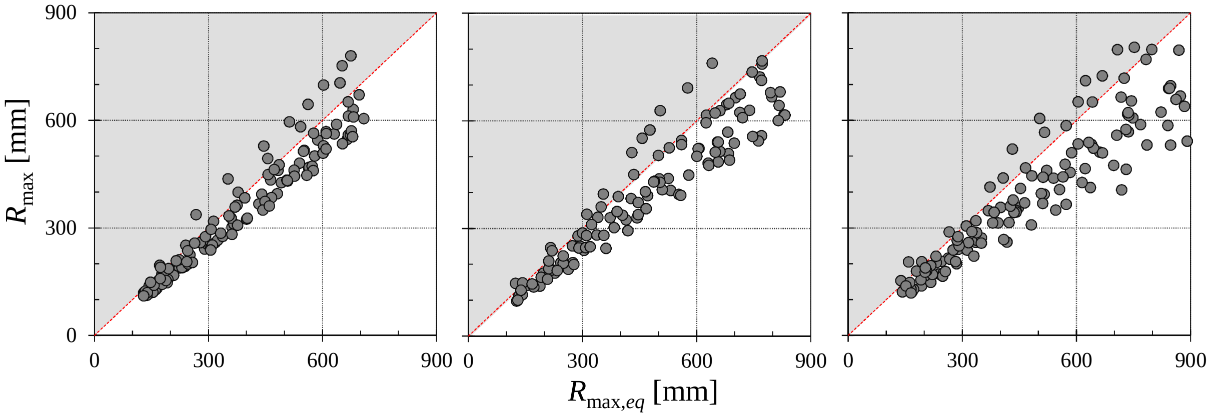

(a) $\alpha_s = 0.010$ (b) $\alpha_s = 0.025$ (c) $\alpha_s = 0.040$

Figure V-25. Relation between the analytic values of the maximum displacement of the isolation layer $R_{\max}$ (2D approach) versus the values $R_{\max,eq}$ estimated using $\delta_{\max}$ (Eq. (V.12)).

V.5.2. Influence of damage evaluation method

To quantitatively assess the difference between D and D_2, the ratio D / D_2 is computed function of the one-directional maximum displacement $\delta_{\max}$. The latter quantity was selected to be consistent with the proposed Eq. (V.12). The variation of D / D_2 with $\delta_{\max}$ for each ground motion, as well as the median, respectively median ±1.0σ (standard deviation) are shown in Fig. V-26. It should be noted that for small displacement amplitudes ($\delta_{\max}$ less than 100(mm)), the ratio D / D_2 is unstable, therefore its values are not plotted in Fig. V-26. Moreover, for $\delta_{\max}$ greater than 600(mm) a significant number of ground motions reach the interaction curve, hence their ultimate limit state. For these two reasons, in Fig. V-26 only the relevant portion of each curve, namely for $\delta_{\max}$ between 100 and 600(mm) is plotted.

Regarding Fig. V-26, the following observations are made:

- For almost all the cases, the ratio D / D_2 – expressed in percentage – is considerably less than 100(%). This means that the one-directional cumulative damage typically computed in design is evaluated on the unconservative side.
- The curves corresponding to the median, respectively median ±1.0σ, present sudden discontinuities at values of $\delta_{\max}$ where the last point of analysis is reached for a certain record (criterion for ultimate limit state is satisfied).
- The largest record-to-record variability as well as the smallest difference between D and D_2 was observed for the case with $\alpha_s = 0.010$.
- For $\delta_{\max}$ between 100 and 600(mm), all the curves corresponding to the median values resemble a cubic function.

The last observation suggests the fact that the ratio D / D_2 may be expressed as a cubic function of the one-directional maximum displacement $\delta_{\max}$ within the interval 100~600(mm). This range of $\delta_{\max}$ covers the majority of the situations encountered in design of seismic isolated structures, therefore it is considered to be sufficient. Furthermore, to obtain a dimensionless relation of D / D_2 function of $\delta_{\max}$, the latter is divided by the height h of the considered damper size (335(mm)). The results are shown in Eq. (V.13).

$$D/D_2 = -22.35 \cdot (\delta_{\max}/h)^3 + 77.98 \cdot (\delta_{\max}/h)^2 - 90.16 \cdot (\delta_{\max}/h) + 112 \quad (\alpha_s = 0.010) \qquad \text{(V.13a)}$$

$$D/D_2 = -19.67 \cdot (\delta_{\max}/h)^3 + 71.22 \cdot (\delta_{\max}/h)^2 - 95.35 \cdot (\delta_{\max}/h) + 119.52 \quad \begin{matrix} (\alpha_s = 0.025) \\ (\alpha_s = 0.040) \end{matrix} \qquad \text{(V.13b)}$$

where h is the height of a UD50 size damper (335(mm))

$\delta_{\max}$ ranges between 100 and 600(mm).

In Fig. V-28, the median curves for each considered value of the yield base shear coefficient α_s are plotted against the proposed cubic functions defined in Eq. (V.13). It can be observed that there is no significant difference the median curves for $\alpha_s = 0.025$ and $\alpha_s = 0.040$. For this reason, the same cubic function was used to approximate both of them (Eq. (V.13b)). By employing this equation, assuming that the maximum one-directional displacement $\delta_{\max}$ and its corresponding one-directional cumulative damage index D are known (these quantities are usually computed in design), an equivalent bidirectional damage index $D_{2,eq}$ can be obtained. The accuracy of Eq. (V.13) in estimating $D_{2,eq}$ is checked by plotting the obtained values against the analytical ones for the bidirectional cumulative damage index D_2 (Fig. V-28). It can be noticed that in the area where both indices are less than 0.200, the two set of values agree well, while outside this area, the plots are mostly situated on the unconservative side ($D_{2,eq} < D_2$). This is particularly true for $\alpha_s = 0.010$ and is directly related to the sway-motion index, as it can be observed in Fig. V-29 where the ratio $D_2 / D_{2,eq}$ is plotted against J_f. For each case, it can be observed that generally the values of $D_2 / D_{2,eq}$ are situated between 0.70 and 1.40 (with the exception of LCW). Moreover, as J_f becomes greater than 10(rad), the ratio $D_2 / D_{2,eq}$ increases, providing – thus – values on the unsafe side. This issue is addressed by considering more conservative values (based on median plus one standard deviation) for estimating the sway-motion index as a function of $\delta_{\max}$, as it is described in the following paragraphs.

Eq. (V.13) represents the first step towards finding an alternative method for estimating the performance of U-shaped steel dampers under bidirectional excitation using quantities typically obtained in design (in-plane frame analysis). The second step is to find an expression for the sway-motion index J_f function of the same one-directional displacement $\delta_{\max}$, allowing, thus, obtaining an equivalent value, $J_{f,eq}$. Further on, with the two sets of equations providing an estimation of the bidirectional parameters D_2 and J_f, the performance of the dampers under bidirectional excitation can be evaluated by plotting ($D_{2,eq}$, $J_{f,eq}$) against the limit states defined in ***Chapter IV***.

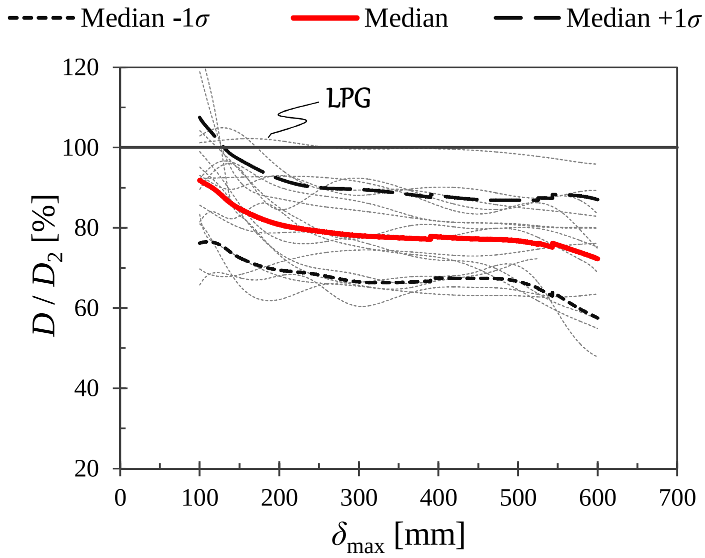

(a) $\alpha_s = 0.010$

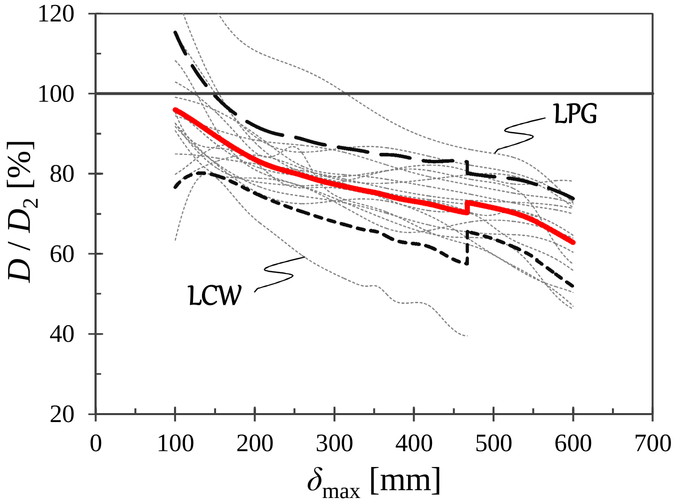

(b) $\alpha_s = 0.025$

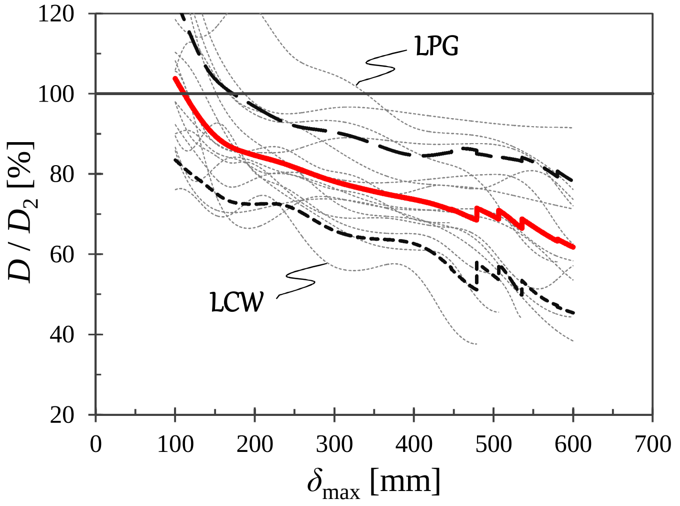

(c) $\alpha_s = 0.040$

Figure V-26. Difference between 1D (D) and 2D (D_2) damage indices plotted against the maximum one-directional displacement $\delta_{\max}$.

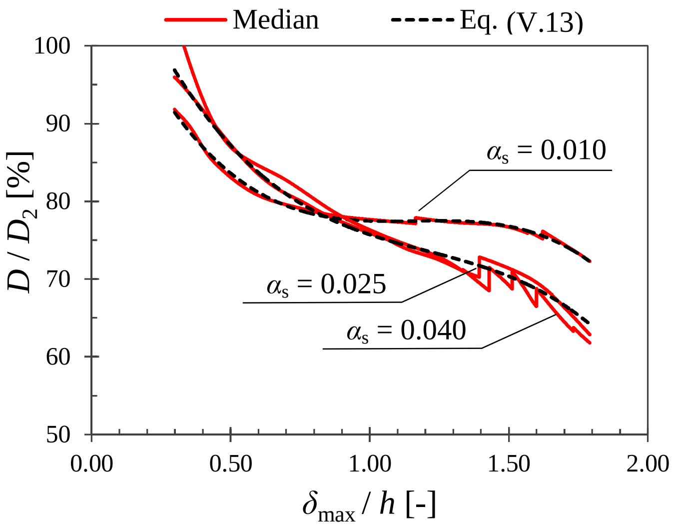

Figure V-27. Approximation of the median curves of ratio D / D_2 with quadratic functions using Eq. (V.13) (for $\delta_{\max} \in [100, 600](\mathrm{mm})$).

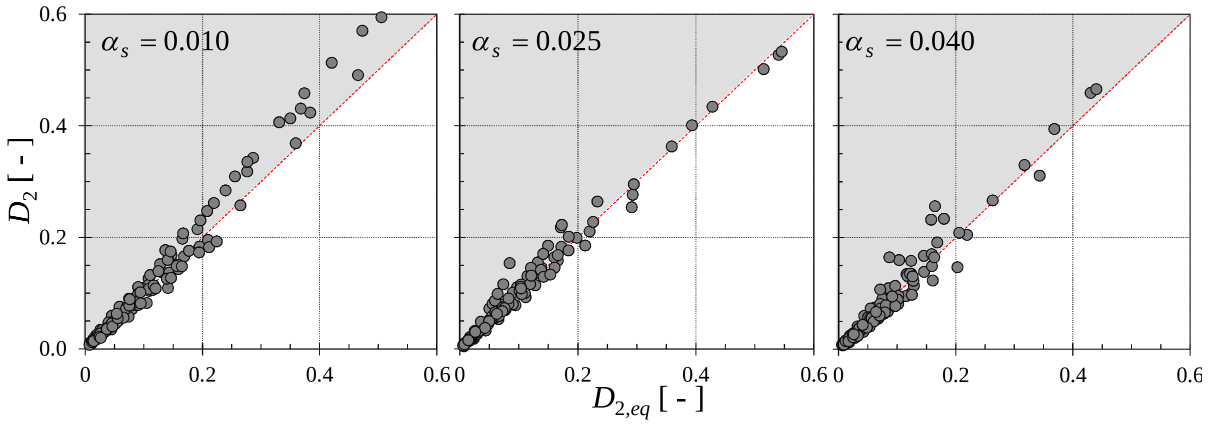

Figure V-28. Analytical values of the bidirectional cumulative damage index D_2 against the equivalent one $D_{2,\,eq}$ given by Eq. (V.13).

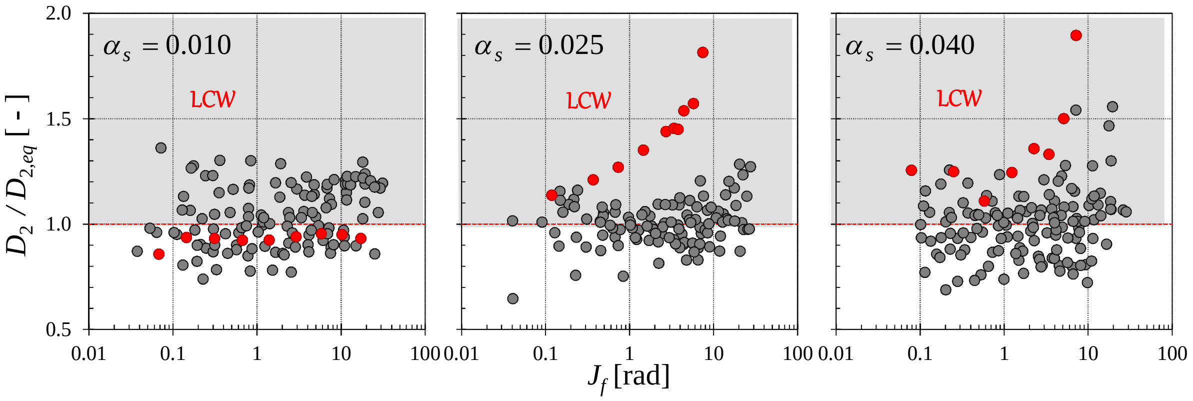

Figure V-29. Accuracy of regression formula (Eq. V.13) for the bidirectional cumulative damage index expressed with respect to the sway-motion index J_f.

The variation of the sway-motion index J_f with respect to the one-directional maximum displacement $\delta_{\max}$ is investigated next. The results for each ground motion and for each of the three considered values of α_s, together with their median, respectively median plus one standard deviation curves are shown in Fig. V-30. For values of $\delta_{\max}$ smaller than 100(mm), J_f is significantly smaller than 1.0(rad) and can, therefore, be neglected because in this range fracture is assumed to occur when D_2 = 1.0, which is highly unlikely to happen during a single or even several seismic events of moderate intensity.

To provide an overall conservative estimation of the performance of U-shaped steel dampers subjected to bidirectional loading using their one-directional response quantities, it is important to account for the fact that about half of the values for $D_{2,eq}$ are situated slightly towards the unconservative side. For this purpose, the median +2σ curves are selected to estimate J_f. These curves are plotted against the ratio between the one-directional maximum displacement $\delta_{\max}$ and the height of the damper element (Fig. V-31). As explained above, the considered values of $\delta_{\max}$ are between 100~600(mm) because in this interval the considered curves present a stable behavior. It was found that the median +2σ curves can be approximated by using power functions to compute an equivalent sway-motion index $J_{f,eq}$ as given in Eq. (V.14). These equations are also shown in Fig. V-31.

$$J_{f,eq} = 9.39 \cdot (\delta_{\max}/h)^{3.04} \qquad (\alpha_s = 0.010) \tag{V.14a}$$

$$J_{f,eq} = 6.05 \cdot (\delta_{\max}/h)^{2.93} \qquad (\alpha_s = 0.025) \tag{V.14b}$$

$$J_{f,eq} = 6.85 \cdot (\delta_{\max}/h)^{2.88} \qquad (\alpha_s = 0.040) \tag{V.14c}$$

where h is the height of a UD50 size damper (335(mm))
$\delta_{\max}$ ranges between 100 and 600(mm).

Fig. V-32 shows the analytical values of the sway-motion index J_f against the equivalent values $J_{f,eq}$ obtained using Eq. (V.14). One can notice that, with very few exceptions (for the 2 recordings of Tohoku earthquake), the plots are located considerably inside the conservative range. Combining this finding with the fact that the ultimate inelastic deformation capacity of U-shaped steel dampers under bidirectional loadings decreases as J_f increases, the overall performance of the dampers will most likely be evaluated on the conservative range in spite of the fact that $D_{2,eq}$ may be situated slightly towards the unsafe side. In fact, the latter aspect ensures that the bidirectional behavior is not estimated in an overly conservative way.

By intentionally providing conservative values for the sway-motion index, while keeping the median ones for the bidirectional cumulative damage index, the curve for a given ground motion described by ($D_{2,eq}$, $J_{f,eq}$) and plotted against the considered limit states will have a milder slope as compared to that given by (D_2, J_f). This can be observed in Fig. V-33, where an example of the analytical pairs (D_2, J_f) computed in ***Chapter IV*** and the equivalent pairs ($D_{2,eq}$, $J_{f,eq}$) are plotted for comparison, and it ensures that the performance of the dampers is estimated on the conservative side in terms of the considered performance levels. The results are summarized in Table V-6 which shows that the proposed equations (V.13, V.14) correctly estimate the performance level for 80.0% of the total number of analytical results.

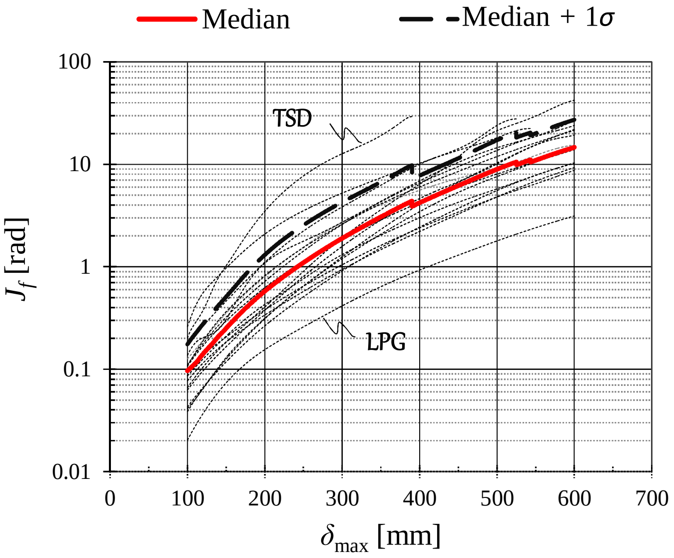

(a) $\alpha_s = 0.010$

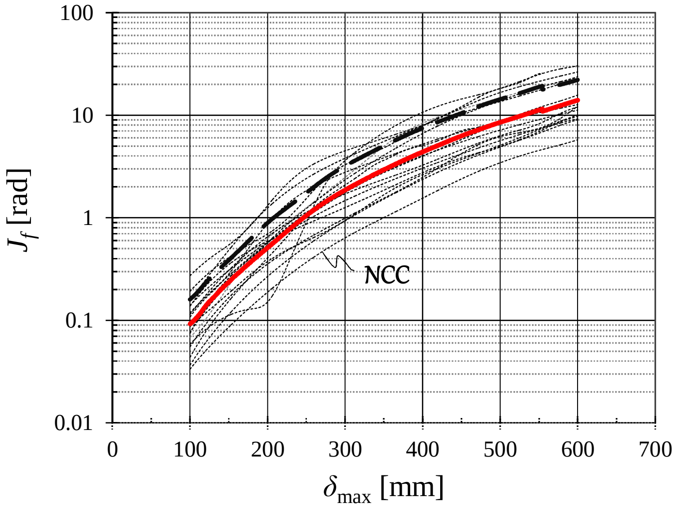

(b) $\alpha_s = 0.025$

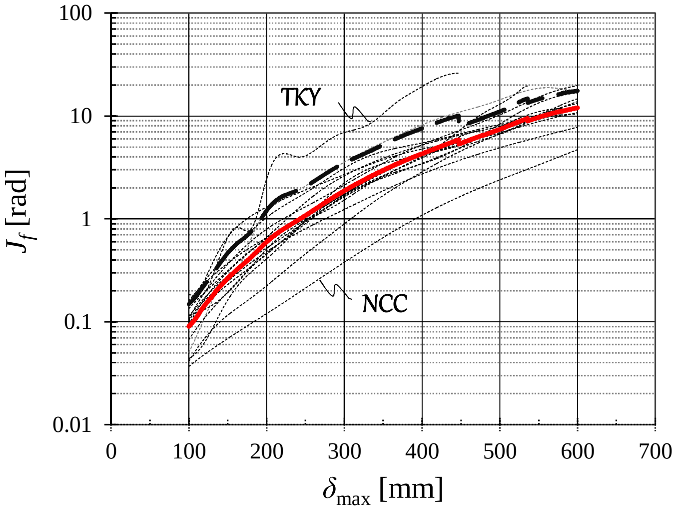

(c) $\alpha_s = 0.040$

Figure V-30. Variation of sway-motion index J_f with 1D maximum displacement $\delta_{\max}$ ($\delta_{\max} \in [100, 600]$(mm)).

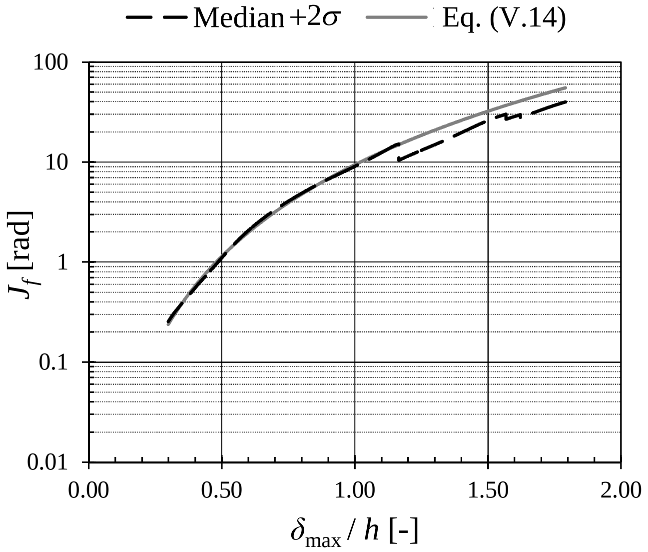

(a) $\alpha_s = 0.010$ (Eq. (V.14a))

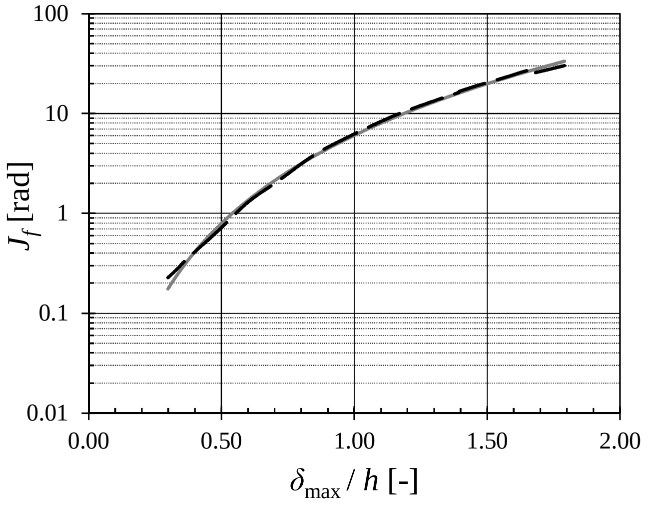

(b) $\alpha_s = 0.025$ (Eq. (V.14b))

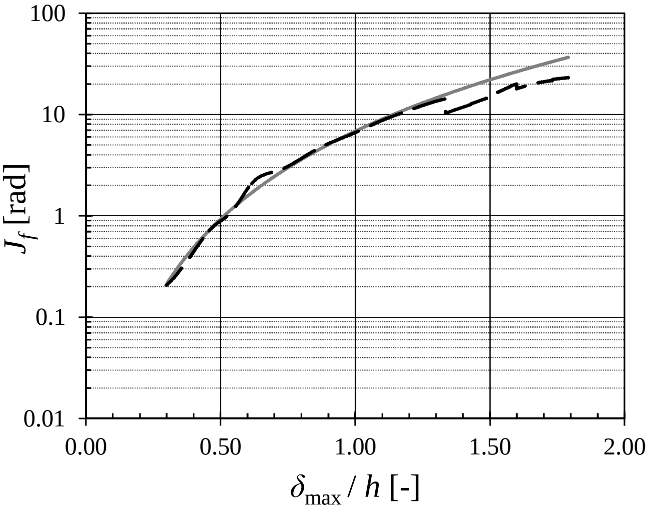

(c) $\alpha_s = 0.040$ (Eq. (V.14c))

Figure V-31. Approximation of the median +2σ curves of sway motion index J_f using Eq. (V.14) (for $\delta_{max} \in [100, 600]$(mm)).

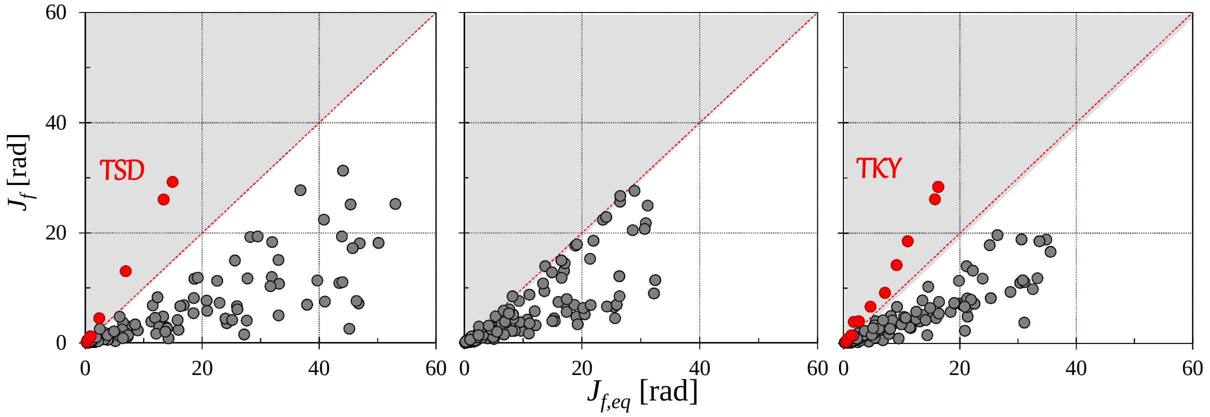

(a) $\alpha_s = 0.010$ (b) $\alpha_s = 0.025$ (c) $\alpha_s = 0.040$

Figure V-32. Analytical values of the sway-motion index J_f against the equivalent values ($J_{f,eq}$) given by Eq. (V.14).

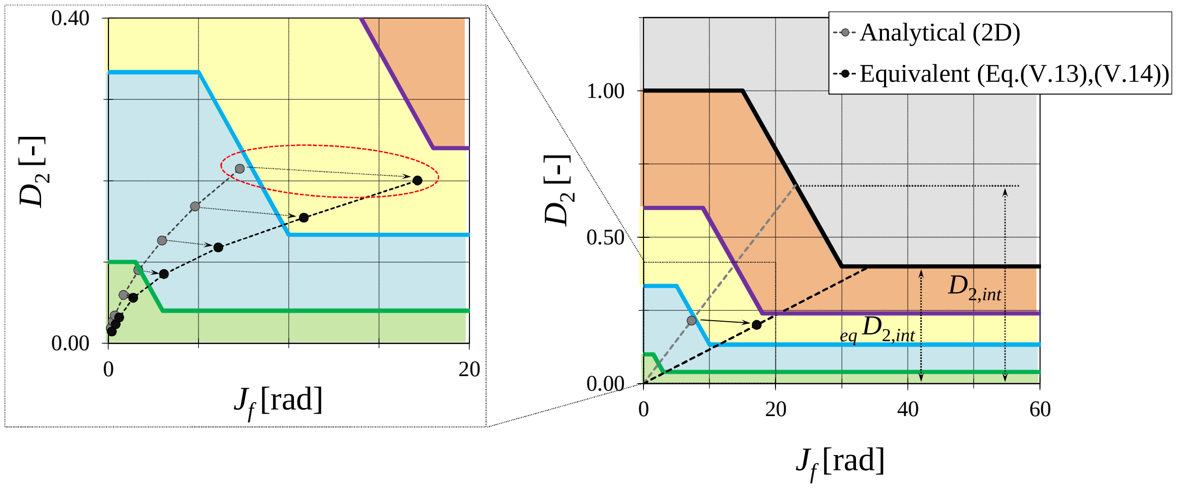

Figure V-33. Example of the difference between the analytical results (D_2, J_f) computed in ***Chapter IV*** and equivalent results ($D_{2,eq}$, $J_{f,eq}$) obtained with Eqs. (V.13) and (V.14).

Table V-6. Comparison between the performance obtained using the analytical data (D_2, J_f) for the 2D approach and those obtained by using Eqs. (V.13) and (V.14)

	Number of analytical points ($\delta_{\max} \in [100, 600]$(mm))									Total	
α_s	0.010			0.025			0.040			No. of points	Percentage [%]
Performance Level (**PL**)	***PL1***	***PL2***	***PL3***	***PL1***	***PL2***	***PL3***	***PL1***	***PL2***	***PL3***		
Underestimated	0	0	3	0	0	2	0	0	3	9	2.3
Same	46	27	22	39	39	19	59	46	14	306	80.0
Overestimated	17	12	2	13	6	0	15	3	0	53	17.7
Subtotal	129			120			141			390	100

V.5.3. Safety margin against fracture

As it was discussed in Section V.3, the safety margin against fracture is assessed by using the one-directional cumulative damage index D for 1D approach and the damage ratio DR (Eq. (V.7)) for 2D approach. Their ratio is computed and expressed in percentage against $\delta_{\max}$ (situated between 100 and 600(mm) as shown in Fig. V-35). The median, respectively median plus/minus one standard deviation curves are also shown. As a general observation, the damage ratio DR is significantly larger than the one-directional cumulative damage index D, especially for $\delta_{\max}$ greater than 200(mm). For example, the median value of DR can be as large as 3.80 times that of D. In addition, it can be noted that D and DR decrease as the yield base shear coefficient α_s increases. This is explained by the fact that the number of ground motions reaching the ultimate limit state by intersection with the interaction curve decreases with the increase of α_s. Adding to this the fact that in general the median values of D are usually less than 80% from those of D_2, one can easily understand that by adopting the 1D approach, the safety margin of U-shaped steel dampers is significantly overestimated.

To overcome this problem, first it was investigated whether the proposed Eqs. (V.13) and (V.14) for estimating the values of the cumulative bidirectional damage index D_2, respectively sway-motion index J_f, provide a conservative evaluation of the safety margin. Therefore, the equivalent values ($D_{2,eq}$, $J_{f,eq}$) were adopted to compute the equivalent damage ratio DR_{eq}. The results are compared to the values of DR obtained based on the bidirectional approach (Fig. V-34). In general, DR_{eq} provides conservative estimates of DR with a satisfactory accuracy. The highest correlation between DR and DR_{eq} is observed for $\alpha_s = 0.025$.

To apply the method described above for estimating the safety margin against fracture of the dampers when subjected to bidirectional loadings using one-directional indicators, knowing the value of the one-directional damage index D is a prerequisite. However, obtaining the value of D for the response displacement of an isolated structure subjected to seismic excitation is not a trivial task. Therefore a simple method for estimating the bidirectional damage that doesn't require knowing the value of D is preferable.

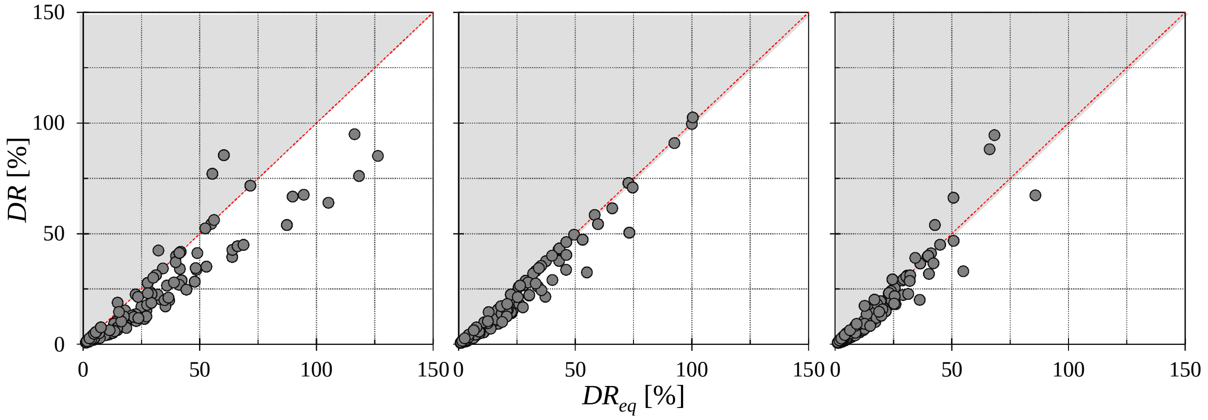

(a) $\alpha_s = 0.010$ (b) $\alpha_s = 0.025$ (c) $\alpha_s = 0.040$

Figure V-34. Comparison between the analytically obtained bidirectional damage ratio DR and the equivalent one DR_{eq} computed using Eqs. (V.13) and (V.14).

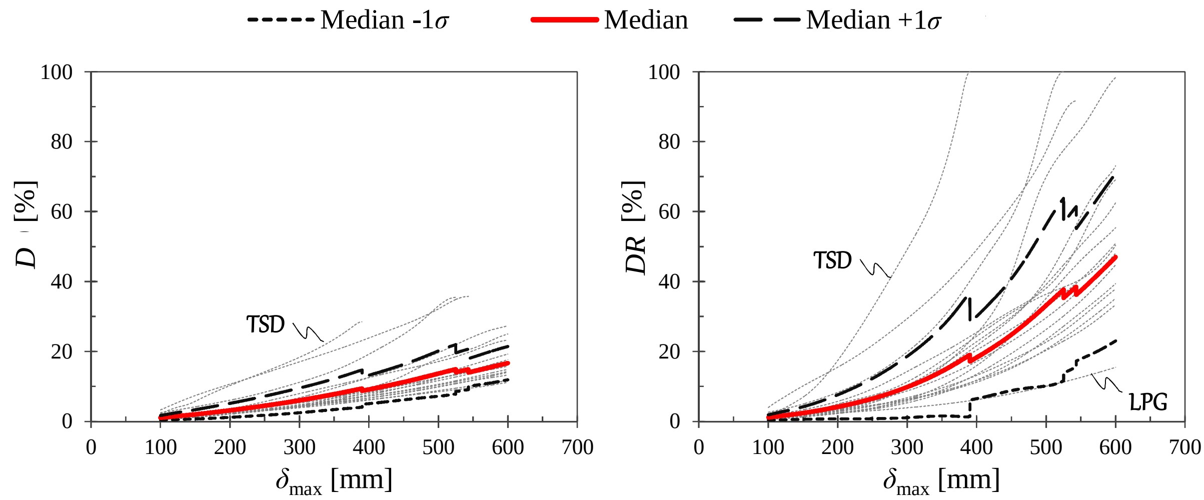

(a) $\alpha_s = 0.010$ – 1D approach (b) $\alpha_s = 0.010$ – 2D approach

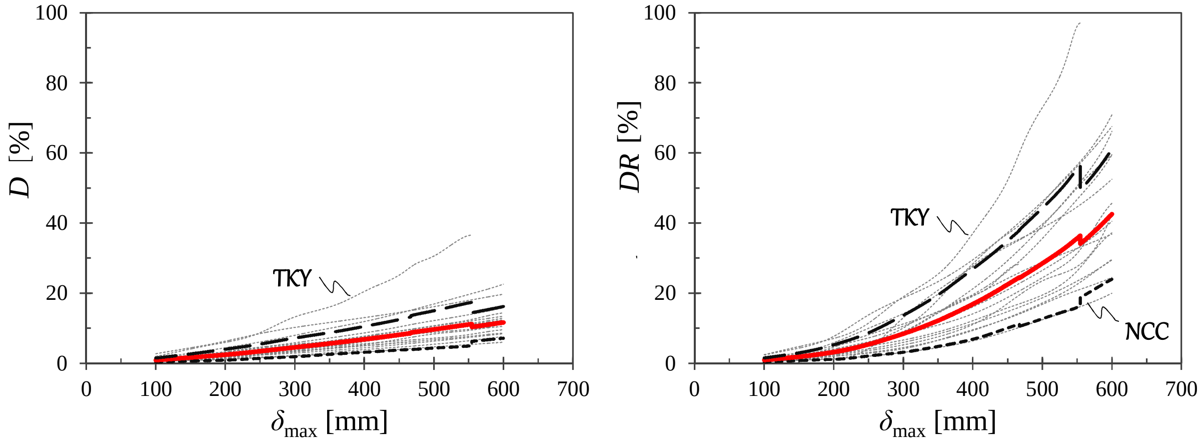

(c) $\alpha_s = 0.025$ – 1D approach (d) $\alpha_s = 0.025$ – 2D approach

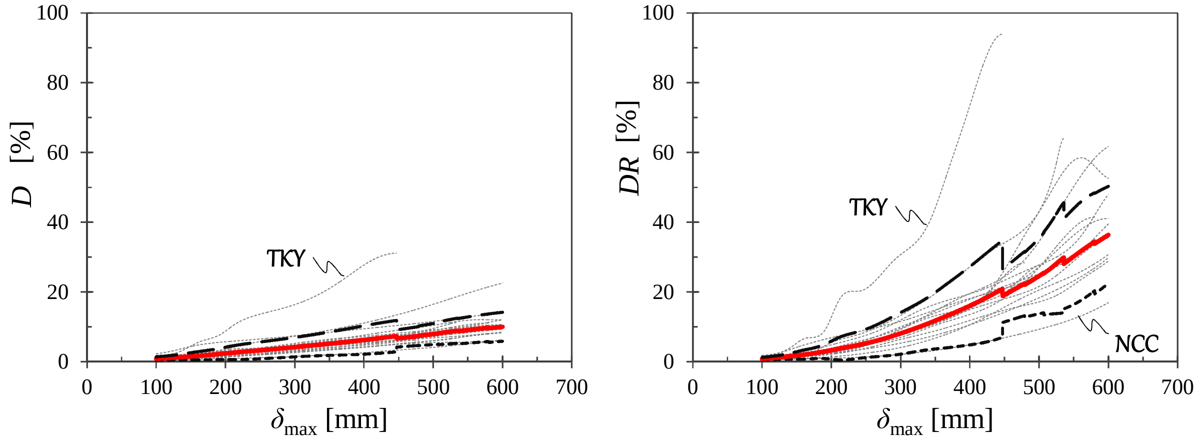

(d) $\alpha_s = 0.040$ – 1D approach (e) $\alpha_s = 0.040$ – 2D approach

Figure V-35. Damage ratio with respect to fracture limit: 1D approach (left), 2D approach (right) expressed against the $\delta_{\max}$ $(\delta_{\max} \in [100, 600](\text{mm}))$.

The second method investigated here is based on the same principle which was used to establish Eqs. (V.13) and (V.14), namely proposing an equation based on one of the reference curves (median, respectively median +/- one standard deviation as shown in Fig. V-35). The median plus one standard deviation curves were selected here and were approximated using power functions with respect to the ratio $\delta_{\max} / h$. Eq. (V.15) is, thus, proposed to estimate the values of the damage ratio *DR* using the maximum displacement of the isolation layer $\delta_{\max}$ computed in the 1D approach. This reduces significantly the overly estimated safety margin obtained using the conventional 1D approach (Fig. V-34(a), (c), (e)).

$$DR_{eq} = \left| \begin{array}{ll} 24.0 \cdot \left(\delta_{\max}/h\right)^{2.16} & \left(\alpha_s = 0.010, \alpha_s = 0.025\right) \\ 18.2 \cdot \left(\delta_{\max}/h\right)^{2.28} & \left(\alpha_s = 0.040\right) \end{array} \right. \tag{V.15}$$

where DR_{eq} (%) is the equivalent damage ratio expressing the safety margin against the fracture limit for 2D approach (DR_{eq} = 100(%) means that fracture is reached)

$\delta_{\max}$ ranges between 100 and 600(mm).

Eq. (V.15) is plotted against the median plus one standard deviation curves in Fig. V-36. It can be observed that for $\alpha_s = 0.010$ and $\alpha_s = 0.025$ the analytical curves are very close, therefore they are approximated using the same power function. To confirm that indeed Eq. (V.15) provides conservative results, in Fig. V-37 the obtained results (DR_c) are plotted on the abscissa against the analytical values of *DR*. It can be observed that most of the values are situated far inside the conservative range. Moreover, a significant scatter of the data can be noticed. By comparing Fig. (V-34) to Fig. (V-37), one can conclude that the first method which estimated the values of *DR* using a probabilistic approach for both bidirectional indices (D_2 and J_f) provides more accurate results.

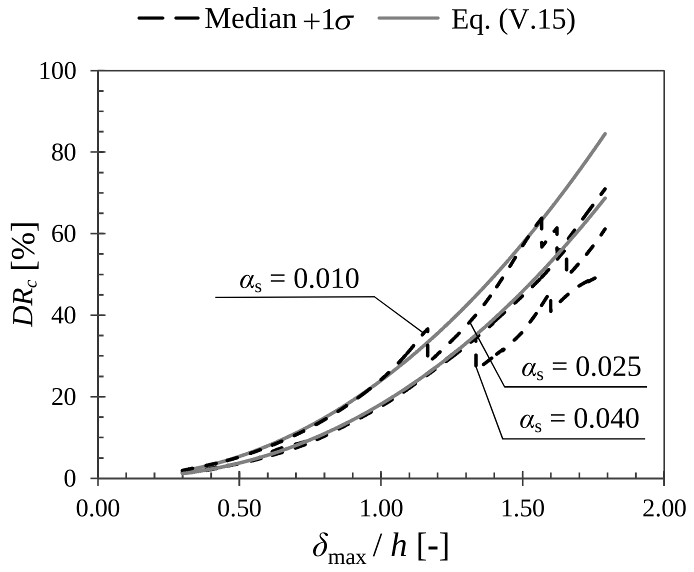

Figure V-36. Damage ratio *DR* for 2D approach (and approximation of the median plus one standard deviation curves using power functions: Eq. (V.15)).

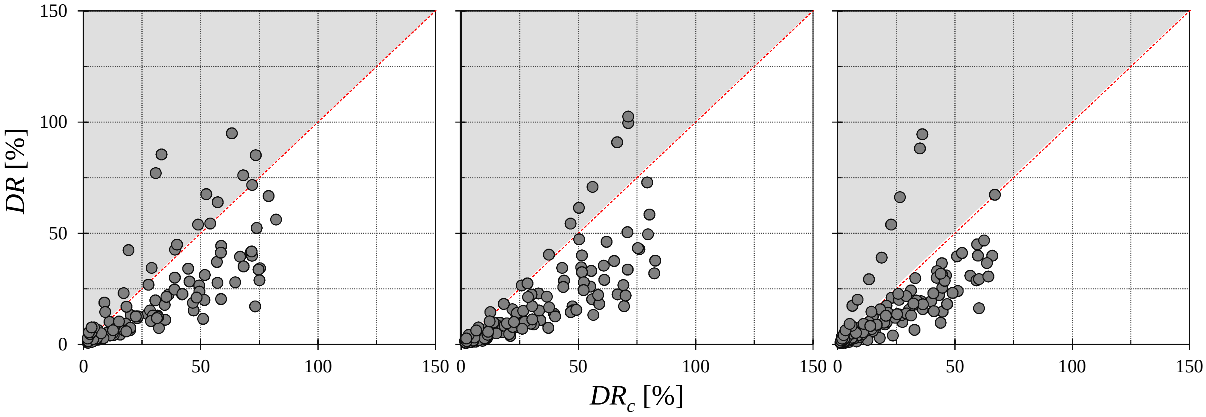

Figure V-37. Comparison between the analytically obtained bidirectional damage ratio *DR* and the calculated values DR_c using Eq. (V.15).

V.5.4. Comparison at design seismic hazard levels

In the previous sections, the main differences of the damage of U-shaped steel dampers obtained using 1D and 2D approaches have been investigated and quantitatively assessed. Moreover, the factors causing these differences were identified. In this section, a more detailed comparison considering the seismic intensity levels described in Section V.3 (*PGV* = 25, 50, 75, 100(cm/s)) is conducted. Furthermore, the suitability of the proposed equations Eqs. (V.12-15) for estimating the bidirectional behavior using the one-directional maximum displacement of the isolation layer $\delta_{\max}$ and the one-directional cumulative damage index *D* at the considered seismic levels is given particular attention.

Using the results obtained in this chapter and those obtained in the previous one, in Fig. V-38 are plotted the points corresponding to design seismic hazard level L1 (*PGV* = 25(cm/s)), L2 (*PGV* = 50(cm/s)), L3 (*PGV* = 75(cm/s)) and those corresponding to *PGV* = 100(cm/s). The left side of Fig. V-38 shows the dispersion of the considered points with respect to the proposed equation (Eq. (V.13)) for determining the equivalent bidirectional cumulative damage index $D_{2,eq}$. The fact that Eq. (V.13) was derived from the median curves is also reflected for the selected values of *PGV*. In the right side of Fig. V-38, the values of the sway-motion index J_f and Eq. (V.14) are plotted. It can be observed that almost all the points are situated on the conservative side, which is explained by the fact that Eq. (V.14) was defined to model the median + 2σ curves.

Eqs. (V.13) and (V.14) that give the equivalent indices $D_{2,eq}$ and $J_{f,eq}$ are further employed to estimate the damage ratio DR_{eq} of U-shaped steel dampers under bidirectional loading. The results are shown on the right side of Fig. V-29 plotted against the ratio between $\delta_{\max}$ and *h* (height of damper), while on the left side, the analytical values of *DR* are shown against the same ratio. Moreover, Eq. (V.15) is plotted for both cases. It can be noted that DR_{eq} has values that estimate those of *DR* with a higher accuracy, whereas Eq. (V.15) provides estimates *DR* too far within the conservative range.

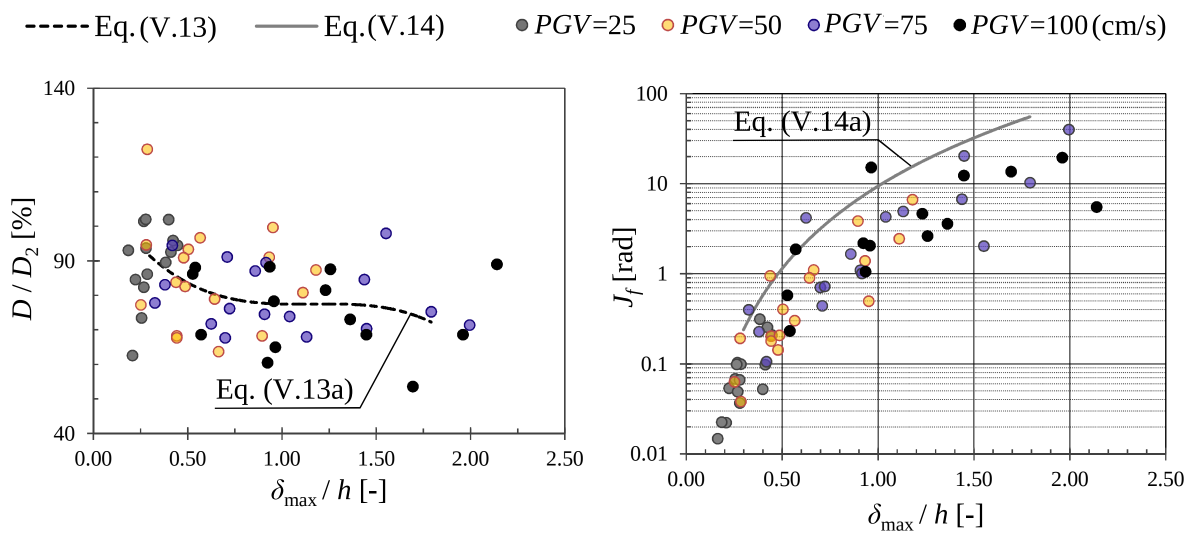

(a) $\alpha_s = 0.010$

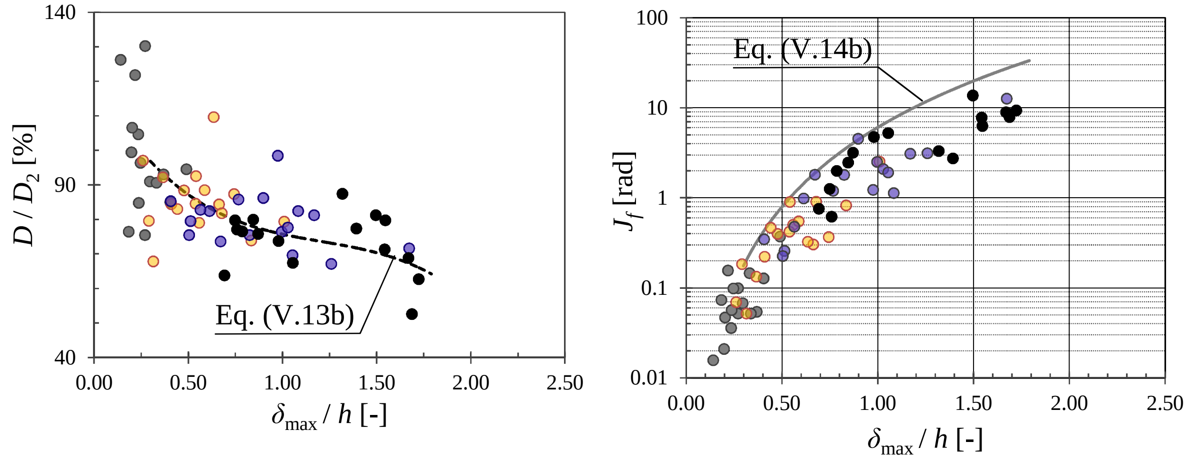

(b) $\alpha_s = 0.025$

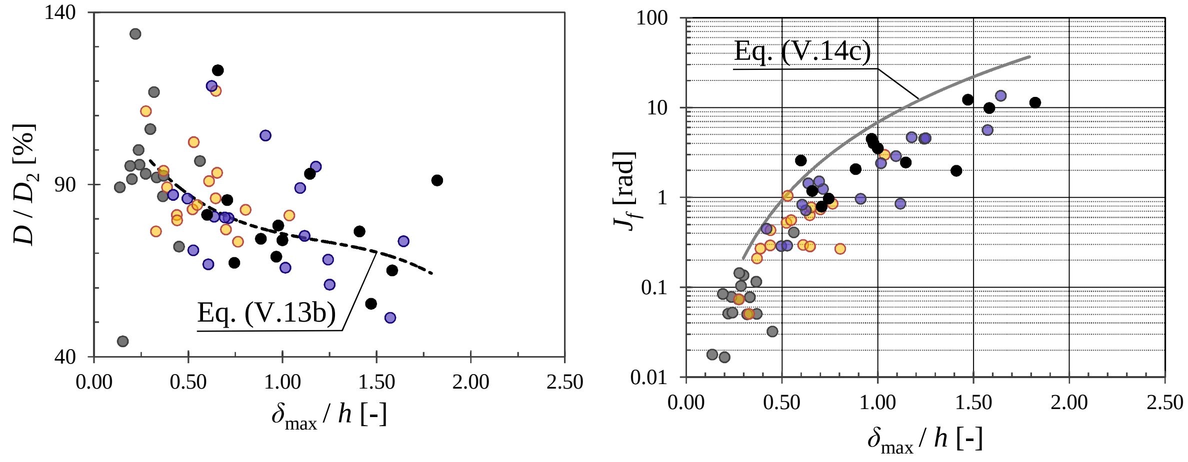

(c) $\alpha_s = 0.040$

Figure V-38. Analytical values obtained at *PGV* equal to 25, 50, 75, respectively 100(cm/s) plotted against the proposed equations (Eqs. (V.13) and (V.14)) for estimating the equivalent values ($D_{2,eq}$, $J_{f,eq}$).

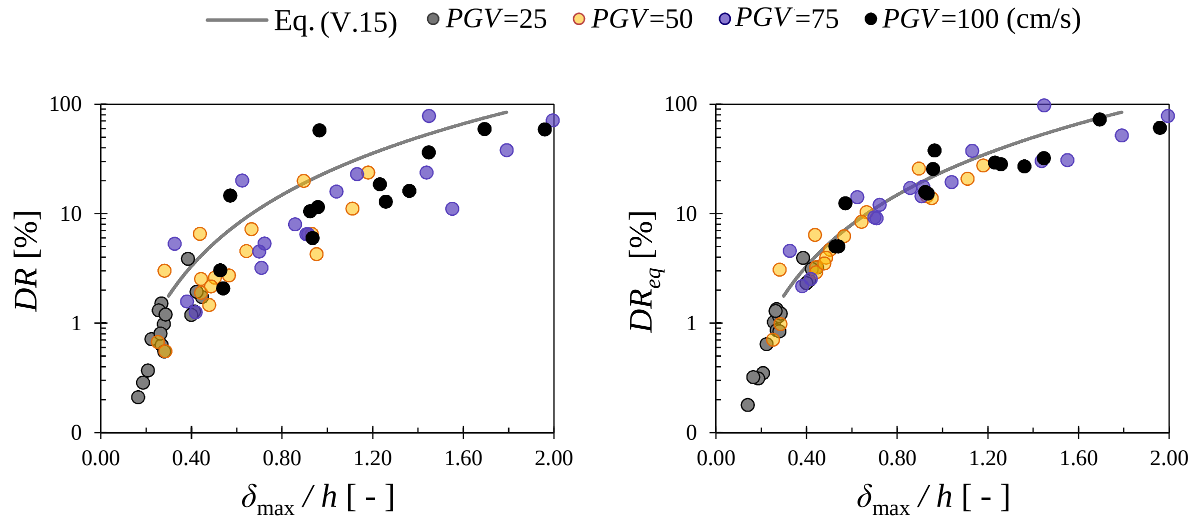

(a) $\alpha_s = 0.010$

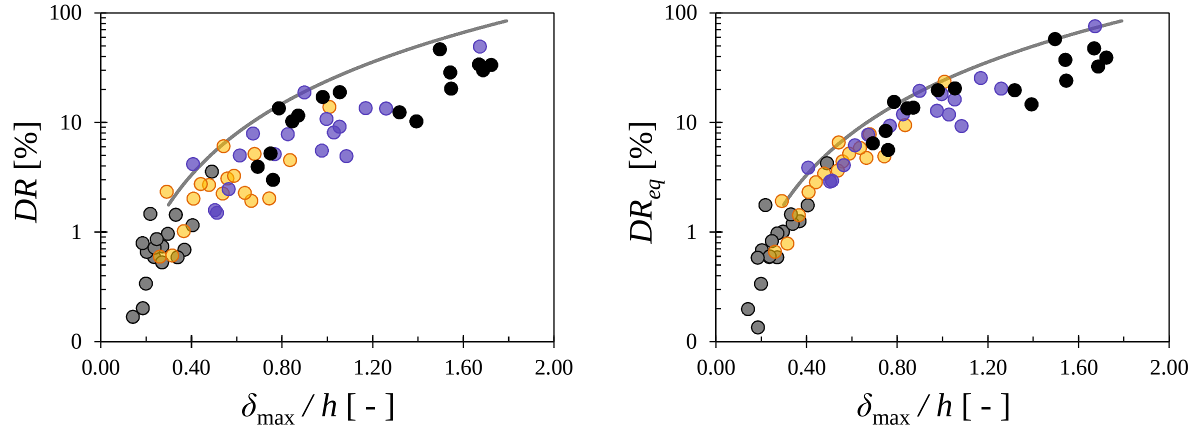

(b) $\alpha_s = 0.025$

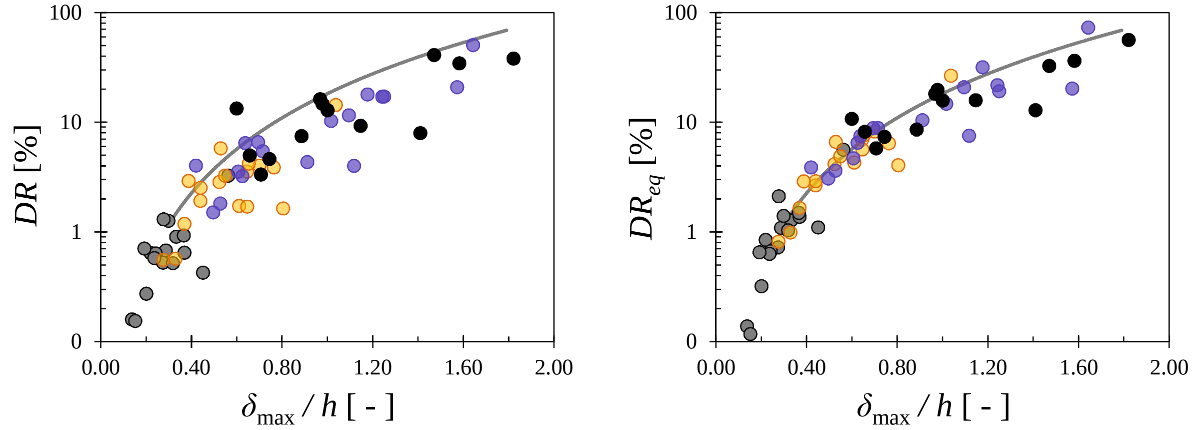

(c) $\alpha_s = 0.040$

Figure V-40. Analytical damage ratio *DR* under bidirectional excitation for *PGV* = 25, 50, 75, 100(cm/s) (left) and its equivalent values DR_{eq} obtained by applying Eqs. (V.13) and (V.14) (right).

V.6. Summary

In the present chapter, the results obtained using the bidirectional approach proposed by Kishiki *et al.* to estimate the damage of a U-shaped steel damper are compared to those computed following the typical design practices. The differences were quantitatively assessed and the factors influencing them were identified. The main conclusions are listed below:

1. The median values of the one-directional maximum displacement $\delta_{\max}$ are generally 10(%) smaller than those for 2D approach $R_{\max}$. Their difference increases with the scale factor, therefore a probabilistic approach was adopted to estimate the values of $R_{\max}$ as a function of $\delta_{\max}$. As a result, Eq. (V.12) was proposed.
2. The difference caused by the damage evaluation method (one- or bidirectional) is assessed by expressing the ratio D / D_2 (%) function of $\delta_{\max}$. It was found that the median curves are situated on the unconservative side, generally lower than 80%.
3. A method for determining an equivalent set of values ($D_{2,eq}$, $J_{f,eq}$) for the bidirectional cumulative damage index D_2 and sway-motion index J_f using the one-directional maximum displacement $\delta_{\max}$ was proposed (Eqs. (V.13), (V.14)). This method enables the structural engineer to verify the performance of the dampers under bidirectional loading using one-directional indices (D and $\delta_{\max}$) determined by conducting in-plane analysis.
4. As a result of the difference in the analytical model, damage evaluation method, and definition of fracture, the damage ratio DR expressed against the fracture limit for the 2D approach is significantly greater than that for 1D approach, going as high as 3.80 times. This means that the safety margin in the 1D approach is overestimated, leading to possibly dangerous situations where the dampers cannot fulfill their function. To avoid this problem, the value of DR is estimated using ($D_{2,eq}$, $J_{f,eq}$) (Eqs. (V.13), (V.14)) and the results agree well with the analytical ones obtained by employing the 2D approach. Thus, the safety margin for U-shaped dampers under random bidirectional loading is estimated in a much more realistic range without having to compute the indices D_2 and J_f.
5. For the design seismic hazard levels currently employed for seismic isolated structures in Japan, the performance of the U-shaped steel dampers can be estimated with a good accuracy using the one-directional indices D and $\delta_{\max}$.

References:

[V.1] National Institute for Land and Infrastructure Management (NILIM) and Building Research Institute (BRI), 2011. Summary of the Field Survey and Research on "The 2011 off the Pacific coast of Tohoku Earthquake" (the Great East Japan Earthquake), Response of seismically isolated buildings (accessed on December 6th 2013) http://www.kenken.go.jp/english/contents/topics/20110311/0311summaryreport.html;

[V.2] 吉敷 祥一，高山大，山田哲，Ene Diana，小西克尚，川村典久，寺嶋正雄 2012：水平 2 方向載荷下における繰り返し変形性能に関する実験 ：免震構造用 U 字形鋼材ダンパーの水平 2 方向特性(その 1)，日本建築学会構造系論文集 第 680 号, pp.1579-1588, 2012.10;

[V.3] Endo, T., Matsuishi, M., Mitsunaga, K., Kobayashi, K., Takahashi, K. 1974 Rainflow method, the proposal and the applications (in Japanese). *Bulletin of the Kyushu Institute of Technology Science and Technology*, ***28***, pp. 33–62;

[V.4] 日本建築学会 2013：免震構造設計指針;

[V.5] Yamaguchi, S., Wada, A. 1989. Current construction practice of base-isolated buildings in Japan, *ATC-15-2: 3rd US – Japan Workshop on the Improvement of Building Structural Design and Construction Practices*;

[V.6] 和田章，広瀬景一：2 方向地震動を受ける無限均等ラーメン構造の弾塑性応答性状，日本建築学会構造系論文報告集，第 399 号，pp.37-47，1989.5.

Chapter VI

Conclusions

VI.1. Summary

VI.2. Conclusions

VI.1. Summary

This research investigates the performance of U-shaped steel dampers as seismic isolation devices for base-isolated structures subjected to biaxial excitation. The methodology for damage evaluation proposed by Kishiki *et al.* was confirmed to be applicable for the purpose of the present research by conducting a set of dynamic tests with realistic displacement histories (***Chapter II***). An analytical model simulating the bidirectional response of an isolation layer by modeling the dampers as having bilinear restoring force characteristics was proposed (***Chapter III***). Using these results, extensive bidirectional nonlinear time-history analyses were conducted and the reliability of the dampers under various seismic hazard intensities was assessed by deriving fragility and IDA curves (***Chapter IV***). Lastly, the obtained analytical results were compared to those computed using the one-directional damage evaluation method adopted in the design recommendations for base-isolated structures in Japan. It was concluded that the one-directional approach underestimates the real damage level, therefore a set of equations was proposed to estimate the bidirectional damage level on the conservative side using one-directional indicators (***Chapter V***).

1. The bidirectional cumulative damage index D_2 and the sway-motion index J_f (proposed by Kishiki *et al.*) were confirmed to be suitable to estimate the damage of U-shaped steel dampers subjected to realistic bidirectional loadings.
2. The validity of the D_2^u – J_f interaction curve – proposed by Kishiki *et al.* as the upper limit of the damage a damper can take before reaching fracture – was confirmed for U-shaped steel dampers under realistic bidirectional loadings by conducting dynamic and quasi-static tests on full-scale specimens.
3. Insofar as the test results can indicate, it is highly unlikely that contact with the rest of the connection occurs during a single seismic event. Moreover, the possibility that a damper fractures during a single (strong) ground motion is also extremely small.
4. The effect of the loading speed on the behavior of the dampers under realistic bidirectional loading was found to be negligible in the considered range (maximum 3.00 γ/sec).
5. A bilinear hysteretic model was proposed for U-shaped steel dampers based on one-directional loading tests, and, in combination with a multiple shear spring (MSS) element, their force – deformation relations under bidirectional loadings were successfully simulated. The validity of the model was confirmed against the experimental data obtained in the dynamic tests.
6. Having established a methodology and an analytical model for U-shaped steel dampers as seismic isolation devices for base-isolated structures subjected to biaxial

excitation, their reliability under various seismic hazard intensities was assessed by deriving two sets of fragility curves. The first set relates the performance of the dampers to the selected seismic intensity – the geometric mean horizontal component of the peak ground velocity PGV_{gm}. The second set estimates the value of the maximum displacement of the isolation layer as a function of the same intensity measure PGV_{gm}. These are very important results because they allow the structural engineer to estimate the damage level of the dampers and the maximum displacement of the isolation layer under bidirectional loading without having to conduct any response analysis.

7. The normalized IDA curves were summarized by employing their median, respectively median plus/minus one standard deviation curves. By using the latter, the safety margin against the ultimate limit state of the dampers can be easily obtained for different seismic hazard levels.
8. The damage of the dampers presented a significant record-to-record variability, therefore adopting a probabilistic approach such as the one conducted in this study is of paramount importance.
9. The bidirectional approach for estimating the behavior of U-shaped steel dampers under bidirectional loading was compared to the one-directional approach usually adopted in the current design practice of base-isolated structures in Japan. By conducting a quantitative comparison between the two sets of results, the following conclusions were drawn:
   a. The maximum displacement of the isolation layer obtained using the bidirectional approach is about 10% greater than that estimated by adopting the one-directional one (median values). The difference increases with the seismic intensity.
   b. Generally, the one-directional damage index D is about 0.8 times the bidirectional one D_2.
   c. The safety margin against fracture of the dampers is severely overestimated (up to 3.8 times) when adopting the one-directional approach because the reduction of their ultimate inelastic capacity when subjected to bidirectional loading cannot be taken into consideration.

   Based on the above, it is concluded that in general the damage estimated using the one-directional approach is situated on the unconservative side. To account for this issue that can lead to dangerous situations under a very strong motion event, a set of formulae for deriving the bidirectional damage using one-directional indicators was proposed by employing a probabilistic approach.
10. The difference between the one- and bidirectional approaches at the design seismic hazard levels was investigated. For levels L1 (PGV = 25(cm/s)) and L2 (PGV =

50(cm/s)), due to the fact that the damage of the dampers is small compared to the fracture limit, either of the two approaches can be employed without causing any dangerous situations. However, for *PGV* = 100(cm/s), the safety margin is significantly overestimated when the one-directional approach is used. Hence it is advised that for special buildings that are required to resist extremely rare events without collapsing, either the set of proposed formulae that derive the bidirectional damage from one-directional indicators, or a complete bidirectional approach should be adopted to avoid unsafe design of the isolation layer.

VI.2. Conclusions

The key conclusions of the present research are:

- Under realistic large-amplitude displacement histories, U-shaped steel dampers have a stable behavior and are reliable even when subjected to several such loadings.
- Fragility curves that relate the damage level to the seismic intensity were derived, allowing the prediction of the bidirectional performance of the dampers.
- The one-directional damage evaluation approach typically adopted in the current design practice of seismic isolated structures in Japan generally provides values on the unconservative side. Although this fact does not significantly affect the estimated damage under seismic hazard levels L1 and L2 (because its values are usually less than 10% of the fracture limits), for stronger events, the safety margin against fracture is significantly overestimated. This leads to possibly dangerous situations.
- Based on a probabilistic approach, a set of equations that estimate the bidirectional damage using one-directional indicators is proposed. The advantages of employing these equations is that they generally provide conservative results, eliminating thus the potentially dangerous situations without requiring to conduct bidirectional response analyses which are not common in design practices.

Annex A

The present annex shows the experimental (*Chapter II*) and analytical (*Chapter III*) force – displacement relations of the first three loading cycles of the dynamically loaded specimens U1 through U4. For specimen U4, the first 5 cycles are shown because the first two are those corresponding to Ishinomaki hospital which have smaller displacements and do not produce significant damage.

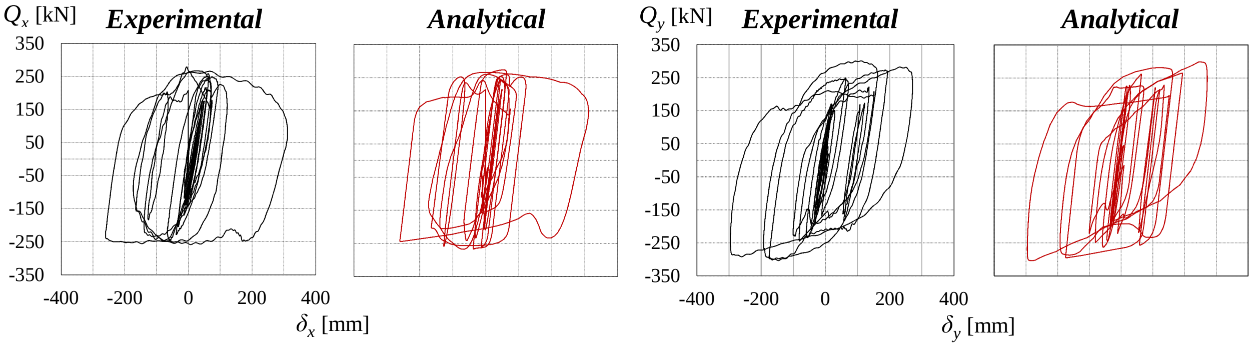

(a) *Takatori* – hysteresis on *x* direction (b) *Takatori* – hysteresis on *y* direction

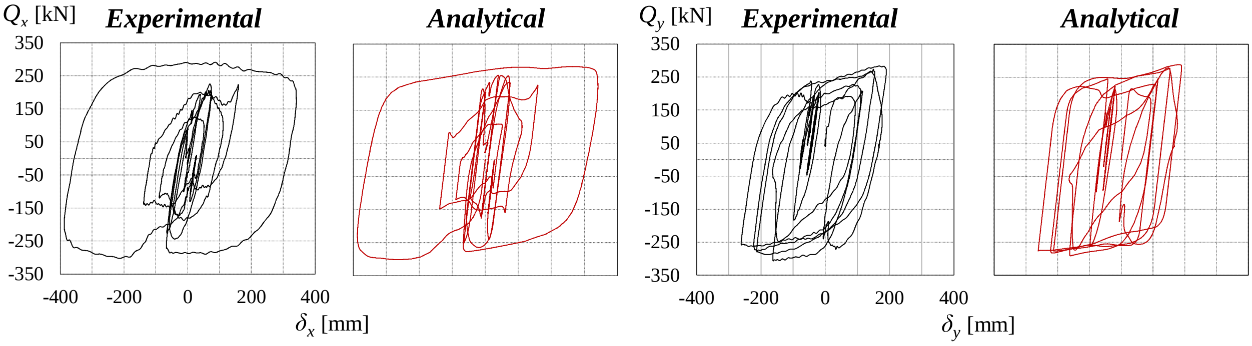

(c) *Hachinohe* – hysteresis on *x* direction (d) *Hachinohe* – hysteresis on *y* direction

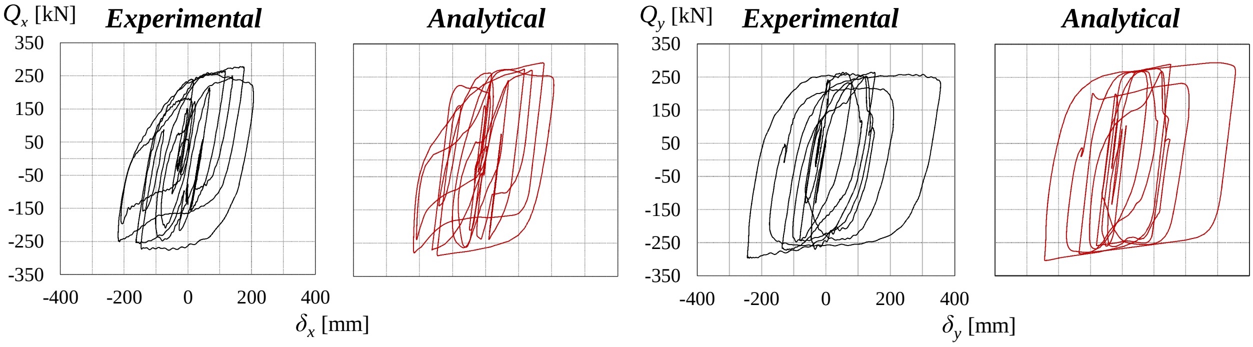

(e) *Chihuahua* – hysteresis on *x* direction (f) *Chihuahua* – hysteresis on *y* direction

Figure A1. Comparison between the analytical and experimental force – deformation relations for specimen U1 (first three displacement orbits)

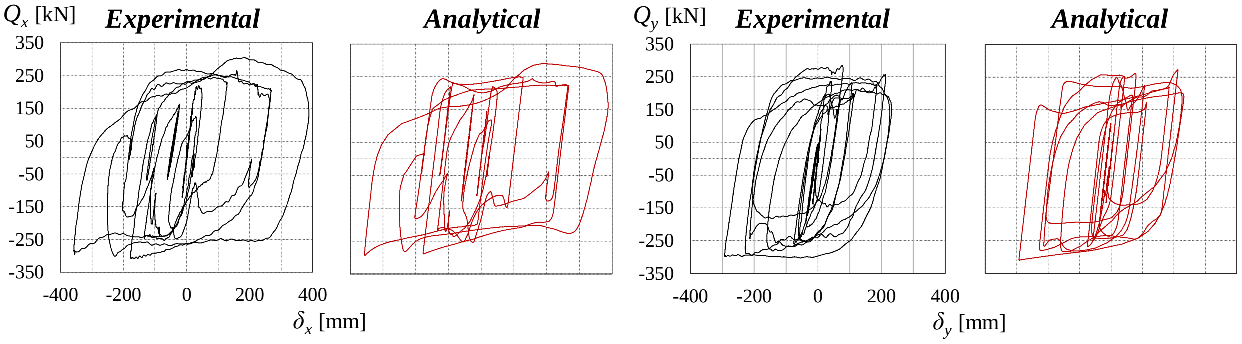

(a) *Agnews Hospital (1st)* – hysteresis on *x*　　(b) *Agnews Hospital (1st)* – hysteresis on *y*

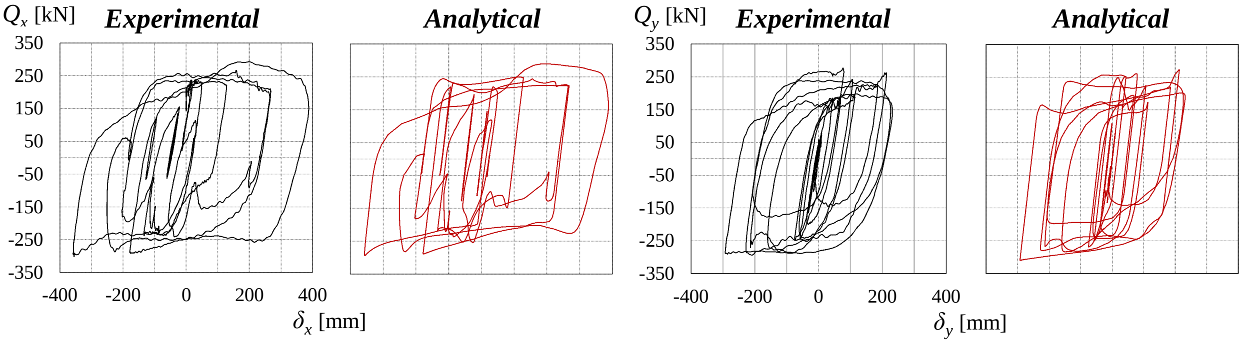

(c) *Agnews Hospital (2nd)* – hysteresis on *x*　　(d) *Agnews Hospital (2nd)* – hysteresis on *y*

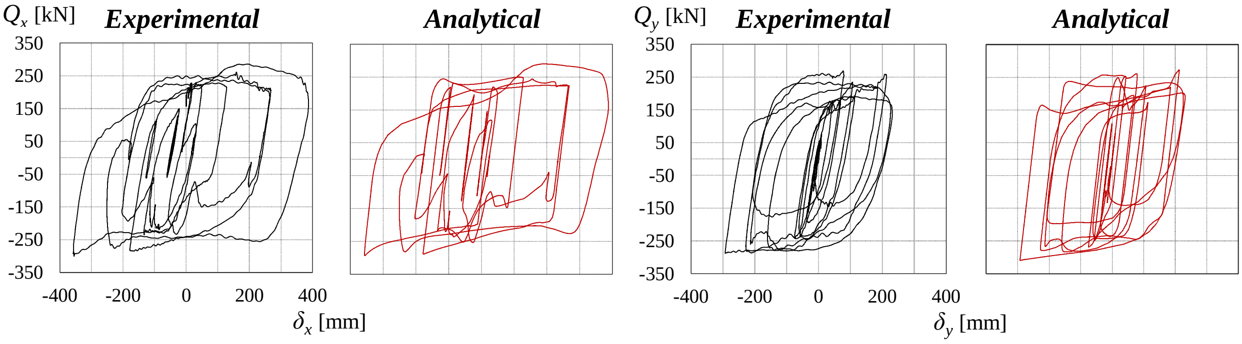

(e) *Agnews Hospital (3rd)* – hysteresis on *x*　　(f) *Agnews Hospital (3rd)* – hysteresis on *y*

Figure A2. Comparison between the analytical and experimental force – deformation relations for specimen U2 (first three displacement orbits)

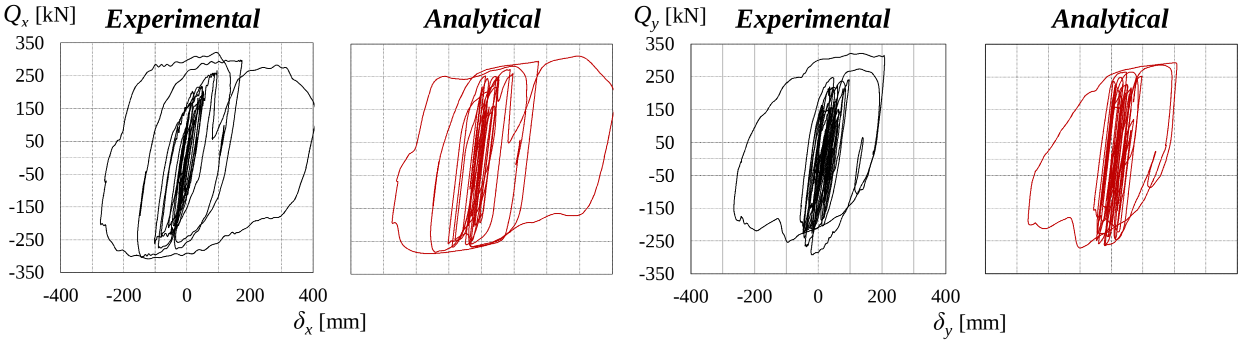

(a) *JMA Sendai (1st)* – hysteresis on x direction (b) *JMA Sendai (1st)* – hysteresis on y direction

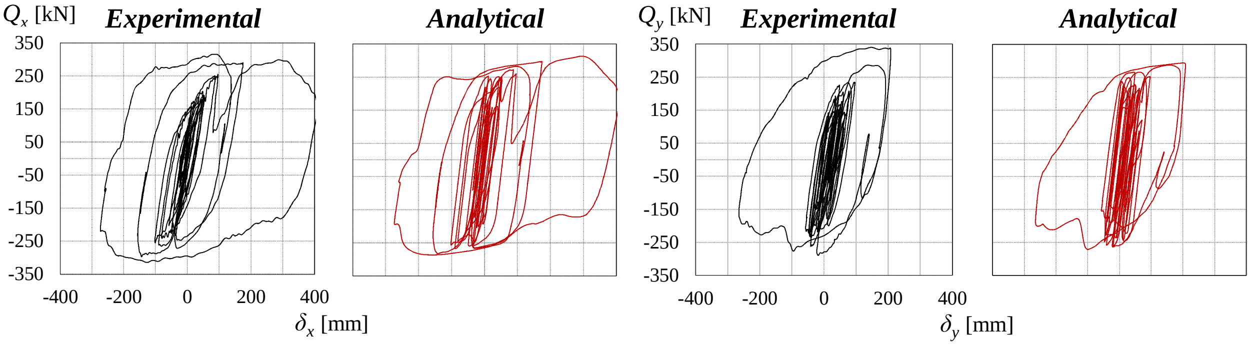

(c) *JMA Sendai (2nd)* – hysteresis on x direction (d) *JMA Sendai (2nd)* – hysteresis on y direction

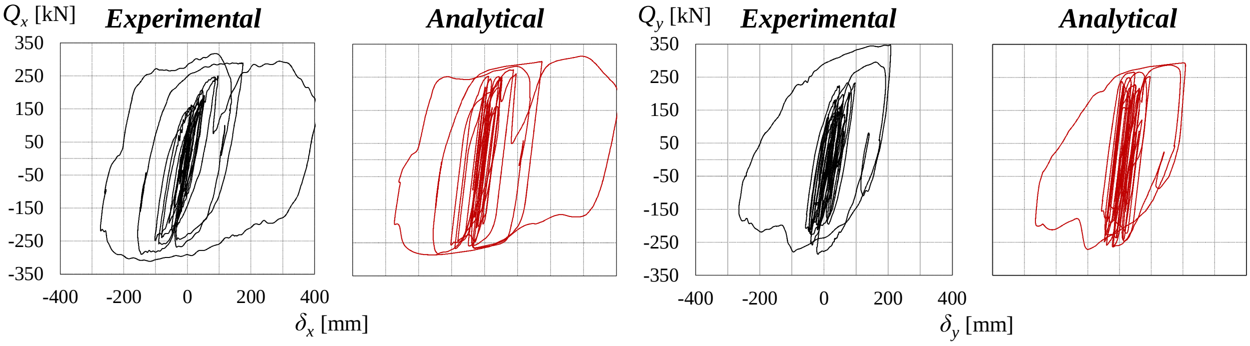

(e) *JMA Sendai (3rd)* – hysteresis on x direction (f) *JMA Sendai (3rd)* – hysteresis on y direction

Figure A3. Comparison between the analytical and experimental force – deformation relations for specimen U3 (first three displacement orbits)

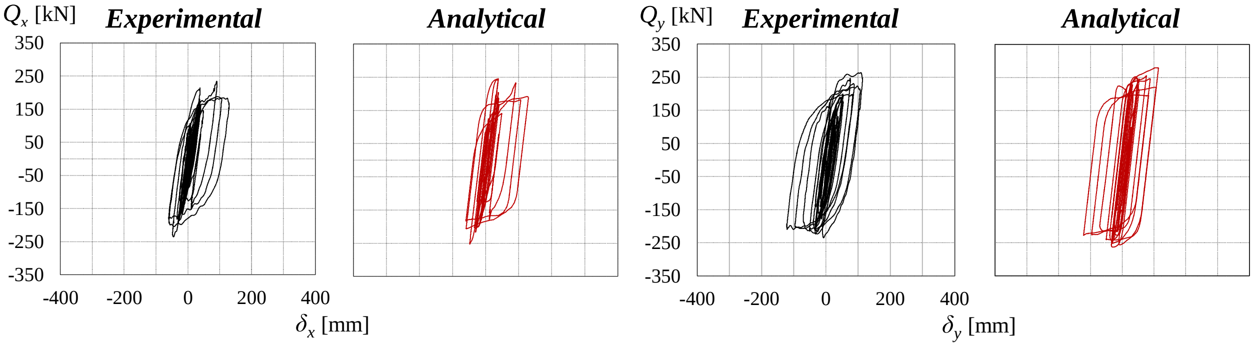

(a) *Ishinomaki hospital (1st)* – hysteresis on x (b) *Ishinomaki hospital (1st)* – hysteresis on y

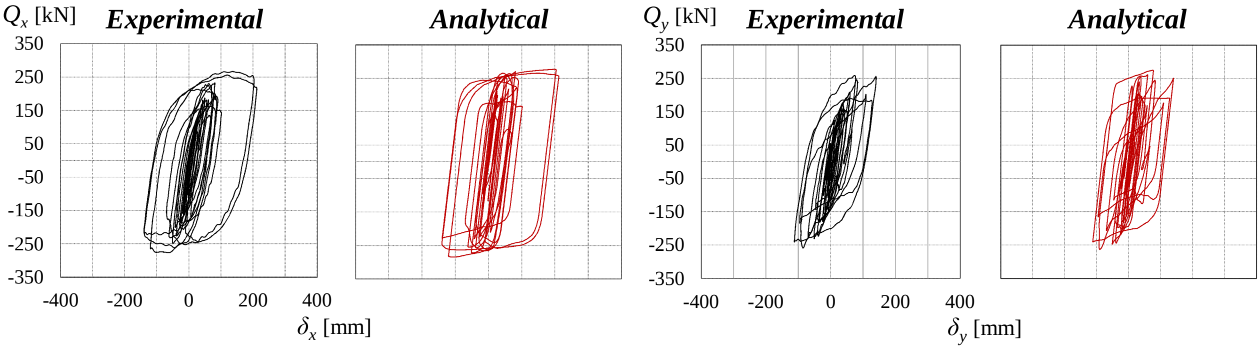

(c) *Ishinomaki hospital (2nd)* – hysteresis on *x*

(d) *Ishinomaki hospital (2nd)* – hysteresis on *y*

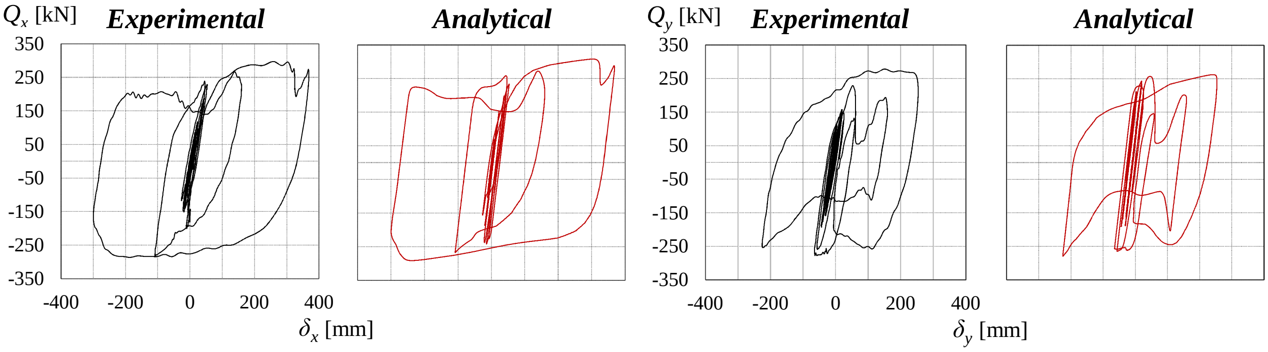

(e) *Sylmar – Olive View (3rd)* – hysteresis on *x*

(f) *Sylmar – Olive View (3rd)* – hysteresis on *y*

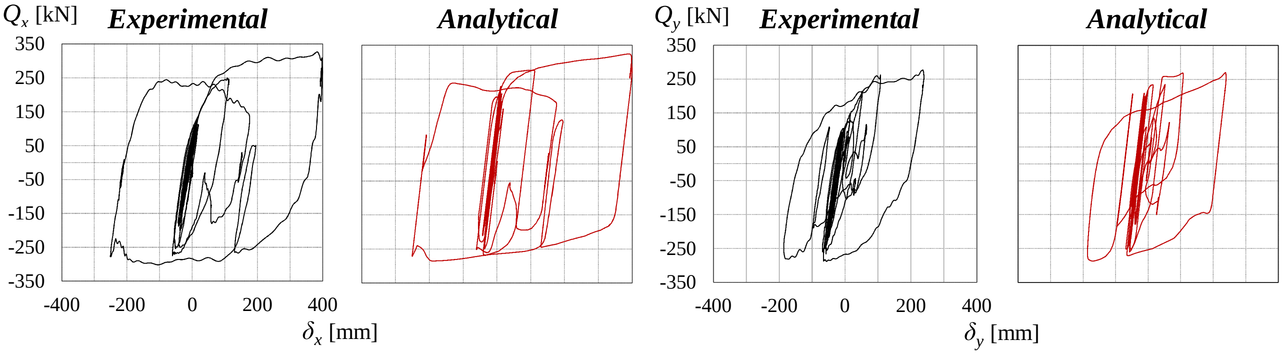

(g) *Newhall (4th)* – hysteresis on *x*

(h) *Newhall (4th)* – hysteresis on *y*

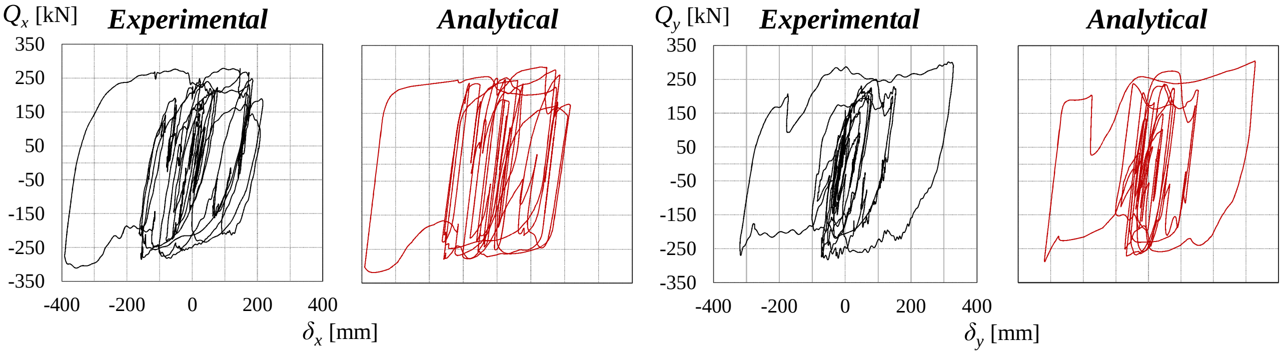

(i) *TCU078 (5th)* – hysteresis on *x*

(j) *TCU078 (5th)* – hysteresis on *y*

Figure A4. Comparison between the analytical and experimental force – deformation relations for specimen U4 (first five displacement orbits)

Annex B

The present annex lists details about the characteristics of the selected ground motions for conducting incremental dynamic analysis. The last column in Table B-1 shows references for other studies on base-isolated structures that have adopted the same ground motion.

Table B-1. Characteristics of the selected ground motions.

No.	Station		Lowest frequency [Hz] [1]		S_v [cm/s]		Reference
	Full name	Abv.	C1	C2	C1	C2	
1	JMA Sendai	TSD	–	–	54.4	55.7	–
2	K-net Koriyama	TKY	–	–	23.9	24.4	–
3	Abbar	MAB	0.130	0.130	62.0	66.0	[2]
4	TCU045	TC0	0.025	0.050	30.1	27.1	[3]
5	TCU129	TC1	0.038	0.038	75.9	58.4	–
6	Yermo Fire Station	LYF	0.070	0.070	59.9	51.4	[3]
7	Coolwater	LCW	0.125	0.125	28.4	23.6	[2], [4]
8	Nishi-Akashi	KNA	0.125	0.125	24.1	34.0	[3]
9	Shin-Osaka	KSO	0.125	0.100	31.4	28.5	[2]
10	Hector	HMN	0.025	0.038	28.6	39.0	[2]
11	Bolu	DBL	0.063	0.063	62.7	32.0	[3]
12	Rio Dell Overpass	CMR	0.070	0.070	21.2	20.0	[2], [4]
13	Gilroy Array #3	LPG	0.125	0.125	31.0	38.3	[3]
14	Canyon Country - WLC	NCC	0.063	0.125	32.0	32.4	[2]
15	El Centro Imp. Co.	SHE	0.125	0.125	79.4	59.3	[3]
16	Delta	IVD	0.063	0.063	53.1	64.8	[2]
17	Tolmezzo	FTZ	0.125	0.125	10.7	18.7	[2]

[1] Applied Technology Council, 2009. Quantification of building seismic performance factors. Federal Emergency Management Agency P695;

[2] Qu, Z., Kishiki, S., Nakazawa, T., 2013. Influence of isolation gap size on collapse performance of seismically isolated buildings, Earthquake Spectra 29 (4), pp. 1477-1494;

[3] 中澤俊幸，吉敷祥一，曲　哲，三好　新，和田　章．免震構造物における耐震安全性の確率論的評価に関する基礎検討，日本建築学会構造系論文集　第 76 巻　第 662 号，745-754, 2011 年 4 月；

[4] Bakshi, A., Mostafavi, S.A., 2014. Development of fragility curves for base isolated structures, Proceedings of the 9th International Conference on Structural Dynamics, EURODYN 2014, Porto, Portugal, June 30th – July 2nd 2014.